Study of the network formation of carbon nanotubes in epoxy matrices for electrical conductivity improvement

Vom Promotionsausschuss der

Technischen Universität Hamburg-Harburg

zur Erlangung des akademischen Grades

Doktor der Naturwissenschaften (Dr. rer. nat.)

genehmigte Dissertation

von

Dipl.-Phys. Josef-Zoltan Lott (geb. Kovacs)

aus

Temeschburg, Rumänien

2009

For Christina

Abstract

This thesis analyses the network formation of CNT in epoxy matrices using scanning electron microscopic (SEM), electrical, Raman spectroscopic and rheological techniques. Investigations are focused on the improvement of the electrical properties of the CNT/epoxy composites.

A non-destructive method called voltage (or charge) contrast SEM was developed for determining the real CNT shapes and distributions in a composite over several length scales. This knowledge is crucial for the interpretation of all upcoming experiments.

Conductivity measurements revealed two percolation thresholds, the lower one attributed to a kinetic and the higher one to a statistic network formation process. The kinetic percolation threshold was found to be sensitive to temperature and the shear forces present in the liquid composite. CNT with higher aspect ratios were found to have lower statistic and kinetic percolation thresholds, meaning that the influence of the aspect ratio on the kinetic percolation threshold is dominating the influence of shearing. Processing of the CNT/epoxy suspension with a calender was found to be disadvantageous for both, the percolation threshold and the maximum achievable composite conductivity.

Raman spectra were utilised to determine the temperature, orientation and stress state of CNT in epoxy resins. The waviness of some CNT types was shown to restrict determining the CNT orientation. Stresses induced by the thermal expansion coefficient of the matrix and their relief at the glass transition temperature could be monitored accurately by Raman spectroscopy. Simultaneous conductivity measurements revealed that the thermal stresses were not sufficiently high to affect the integrity of the established CNT network.

The CNT network formation in an epoxy liquid due to shear forces was studied under controlled conditions inside a rheometer. Rheological, electrical and optical parameters could be monitored and analysed simultaneously. Shearing with low shear rates was found to produce agglomerates while shearing with high shear rates destroyed them, both being reversible processes. The formation of electrically conductive networks was different for calendered and non-calendered CNT/epoxy suspensions. The calendered samples needed a pre-shearing step at high shear rates and a gradual lowering of the shear rate in order to establish a network.

In conclusion, CNT are ideal fillers for polymer composites used in antistatic and electromagnetic shielding applications. They yield high conductivities at low filler concentrations without the need to be perfectly dispersed in the matrix. Their agglomeration can be controlled most effectively by adjusting the suspension temperature.

Acknowledgments

Many people contributed to my doctoral thesis over the last five years. Especially, I would like to thank …

… my advisor, *Prof. Wolfgang Bauhofer*, for giving me the opportunity to work on this exciting topic, as well as for his guidance, support and motivation.

… *Prof. Karl Schulte* for offering me the support of his group and for co-reviewing the thesis.

… *Prof. Manfred Eich* for providing me with essential measurement equipment.

… *Prof. Jan Luiken ter Haseborg* for chairing the examination committee.

… former and present members of the research groups of Prof. Bauhofer and Prof. Eich: *Dr. Robert Schliewe, Roman Kubrin, Dr. Altan Yildirim, Dr. Alexander Petrov, Jan-Hendrik Wülbern, Jan Hampe, Gabriele Birjukov, Christine Kunstmann, Stefan Schön, Michael Seiler, Dr. Michael Hossfeld, Iris Bucher, Carola Micheelsen, Dr. Matthias Schwarz, Dr. Markus Schmidt;* those in the research group of Prof. Schulte: *Alejandra de la Vega, Dr. Bodo Fiedler, Dr. Florian Gojny, Dr. Malte Wichmann, Sam Buschhorn, Dr. Kirsten Prehn, Dr. Luis Prado, Dr. Leif-Ole Meyer, Dr. Eduard Ilinich, Jan Sumfleth, Florian Gehrig, Lars Böger, Hella Wilde, Ingrid Hoffmann, Dr. Georg Broza, Dr. Hans Wittich*; as well as other colleagues virtually affiliated with our group: *Martin Sussiek and Dr. Mathias Nolte* for their kind assistance and inspiring conversations.

Table of Contents

1 Introduction

Nowadays, polymers are widespread in industrial applications due to the possibility to adjust their electrical, chemical and mechanical properties over a wide area. In most cases tailoring of material properties is achieved by blending the polymer with additives. For example, electrically conductive filler particles can increase the conductivity of a polymer from initially 10^{-12} S/m to 10^4 S/m. The resulting filler/polymer composites are used in aviation, packaging, construction and automotive engineering for antistatic and electromagnetic shielding applications. Problems in these applications arise from the high filler concentration which deteriorates the mechanical and optical properties and from particle sedimentation in the liquid polymer resulting in a filler (and thus composite property) gradient. In industry, the former problem is solved by using high aspect ratio fillers–such as fibres–because the filler concentration needed to reach a certain composite conductivity scales inversely with the particle aspect ratio. The latter problem is solved by using nanoscaled fillers–such as carbon black–because the sedimentation rate scales with the particle radius. An approach that gets rid of both problems at the same time is to use carbon nanotubes (CNT) as fillers. They possess aspect ratios as high as 10,000 and simultaneously are nanosized (diameters of 1-50 nm).

This thesis deals with the formation, analysis and manipulation of CNT networks suspended in epoxy matrices. Investigations are focused on the improvement of the electrical properties of the CNT/epoxy composites. The goal is to understand the influence of various parameters–such as CNT type, synthesis method, treatment, dimensionality and concentration, as well as polymer type and suspension processing method–on the electrical properties of the composites.

The thesis spreads over various research fields which were first enhanced individually, tailored to CNT/epoxy composite requirements and then combined to improve the overall understanding of CNT network formation mechanisms. For this reason the thesis is structured in an unusual way. Each research field is discussed in an individual section including motivation, state-of-the-art of science and technology, description of experimental procedures, discussion of the results and conclusion. Details to the materials and their properties are presented in Section 2.

Section 3 deals with the scanning electron microscopy (SEM) analysis of CNT/epoxy composites. Knowledge about the distribution and shape of the CNT within the epoxy is crucial for the interpretation of all upcoming experiments. Therefore, a special technique called voltage (or charge) contrast SEM is developed and applied to visualize CNT that are located *inside* the polymer.

Section 4 covers the electrical characterisation of the produced composites and is the main section of this thesis. It comprises an extensive literature review which condenses a comprehensive collection of published data in order to extract general dependencies of the electrical characteristics on the above mentioned parameters. However, it is favourable to vary each parameter individually while keeping all others constant. This approach is followed in the presented experiments where the CNT type, synthesis method, dimensionality and concentration as well as the suspension processing method is successively varied.

Raman spectroscopy on CNT and CNT/epoxy composites is discussed in Section 5. The idea is (a) to map the distribution and orientation of CNT within the polymer on the micro-scale and (b) to use the CNT as internal stress sensors during and after the polymer curing reaction. For both tasks, appropriate CNT types need to be identified that exhibit an intense Raman

2

signal and allow a vanishingly small amount of CNT to be monitored in a liquid or solid polymer matrix.

Section 6 introduces a rheometer that allows applying controlled shear states to the CNT/epoxy suspension in order to analyse the influence of shear forces on the CNT network formation. The rheometer is unique in the sense that the CNT/epoxy suspension can be analysed rheologically, optically and electrically at same time.

A summary and outlook is given in Sections 7 and 8.

2 Materials

2.1 Epoxy resin systems

Epoxy resins belong to the class of thermosetting plastics. The curing process transforms the epoxy resin into a plastic by forming a three dimensional network of covalent bonds. Curing is initiated through heat and/or curing agents (hardeners). A thermoset material cannot be melted and re-shaped after curing.

Due to the three dimensional network, the mechanical properties of thermosets are generally superior to those of thermoplastic materials. Moreover, thermosets possess good insulating and adhesive properties, are resistant to most chemicals and have high thermal stability. Therefore, they are commonly used as adhesive, coating or matrix for structural composites for airplanes, boats, electronic devices and industrial floors.

Four different epoxy systems were used in this thesis, all based on a bisphenol-A epoxy resin (BPA) and an amine curing agent. The epoxy-amine chemistry was chosen because its curing mechanism is well known [1,2]. The characteristics of the studied systems are shown in Table 2-1. For the electrical conductivity and rheology analyses (Sections 4 and 6), only the LY556/XB3473 system was used. The E20/XB3473 system was additionally used for the scanning electron microscopy analyses (Section 3), while the LY564/A2954 and L135/H137 systems were additionally used for the Raman spectroscopy analyses (Section 5). A polyether siloxane copolymer (Tego Wet 280) obtained from Degussa, Tego Coating & Ink Additives (Germany) was added to the epoxy systems used in Section 3 in order to improve the wettability of the glass substrates.

Table 2-1 Characteristics of the investigated epoxy systems.

System	LY556/XB3473	E20/XB3473	LY564/A2954	L135/H137
Company	Huntsman Advanced Materials, Belgium	Cognis, Germany / Huntsman, Belgium	Huntsman Advanced Materials, Belgium	Bakelite MGS Kunstharzprodukte, Germany
Chemical origin of epoxy/hardener	BPA/aromatic amine	BPA/aromatic amine	BPA/cycloaliphatic amine	BPA/linear aliphatic amine
Mix ratio [parts by weight]	100:23	100:24	100:35	100:30
Initial viscosity at RT [mPa s]	5,200-6,000	3,000-8,000	500-700	700-1,100
Cure schedule	2 h @ 120 °C 2 h @ 140 °C 2 h @ 180 °C	2 h @ 120 °C 2 h @ 140 °C 2 h @ 180 °C	1 h @ 80 °C 2 h @ 140 °C	24 h @ 23 °C
Thermal expansion coefficient [K^{-1}]	$56\text{-}65 \cdot 10^{-6}$		$70\text{-}75 \cdot 10^{-6}$	

2.2 Carbon Nanotubes

Carbon nanotubes (CNT) were observed already in 1953 by Davis et al. [3], in 1976 by Oberlin et al. [4] and in 1982 by Nesterenko et al. [5]. The breakthrough of this carbon allotrope however came with Iijima's publication in 1991 [6]. CNT consists of sp^2-hybridised carbon atoms, just like graphite. CNT can be thought of as a cylinder consisting of rolled-up graphite layers. One layer constitutes single-wall nanotubes, two layers double-wall nanotubes and multiple layers multi-wall nanotubes. The way how these layers are rolled up–characterised by the chiral vector–defines the electrical properties of CNT. On turn, their high aspect ratio and crystalline perfection are responsible for their exceptional mechanical strength. The high research effort on carbon nanotubes is motivated by these material properties, which are comparable with or even exceed those of the best performance materials known to date (Table 2-2).

Chemical vapour deposition (CVD) is the most common production method for CNT. All CNT types used in this thesis were produced by the CVD process. This method comprises the decomposition of different hydrocarbons–such as benzene (C_6H_6), pentane (C_5H_{12}), acetylene (C_2H_2), methane (CH_4)–over different catalysts–such as Fe, Co, Ni–at temperatures between 500 and 1200 °C. The CVD method can be varied with respect to the way the catalyst is introduced into the furnace: either deposited on a substrate (then called catalytic CVD, or CCVD) or as an aerosol/floating catalyst (then called aerosol CVD, or ACVD). Another variant referes to the way the produced CNT are collected and extracted from the furnace. If the catalyst was sputtered onto the substrate or the aerosol sediment to a substrate, a carpet of well-aligned CNT grows, sticks to the substrate and needs to be scratched off. If the catalyst is loosely deposited on the substrate in a fixed-bed or fluidized-bed reactor, the CNT grow entangled, but can be removed much easier from the bed which can be re-used. A vertical reactor does not need a substrate, the CNT simply move downwards with the gas stream and leave the reactor. They grow entangled.

Table 2-2 Comparison of experimentally determined carbon nanotube properties with other high-performance materials.

Material property	Carbon nanotube	Reference	Best performance known to date
Dimension	1-10 nm		45 nm (Structure in Intel Core2 Duo processor)
Electrical conductivity (room temperature)	$3 \cdot 10^6$ S/m	[7]	$6 \cdot 10^7$ S/m (Silver)
Electrical current density	10^9 - 10^{10} A/cm^2	[8]	10^7 A/cm^2 (Copper)
Thermal conductivity (room temperature)	3,000 W/m·K	[9]	3,320 W/m·K (Diamond)
Elastic modulus	0.9-1.9 TPa	[10]	0.5 TPa (Tungsten carbide)
Tensile strength	11-63 GPa	[11]	3.5 GPa (Kevlar)
Specific surface area	948 m^2/g	[12]	500 m^2/g (Activated carbon)
Density	1.4 g/cm^3		2.7 g/cm^3 (Aluminium)

2.2.1 Nanocyl CNT

Nanocyl CNT are multi-wall carbon nanotubes that were produced by catalytic chemical vapour deposition (CCVD) in a fixed-bed reactor. They were supplied by Nanocyl S.A. (Belgium) and used as received. The average inner and outer diameter were specified as 4 and 15 nm, respectively, with lengths up to 50 µm and carbon purity exceeding 95% (<5% iron catalyst). The scanning electron microscopy image (Figure 2-1) shows a typical cluster of as-received CNT, which had to be broken up via shearing. This procedure tends to fracture the CNT due to their entanglement, thus an average length of 15 µm was assumed throughout these experiments.
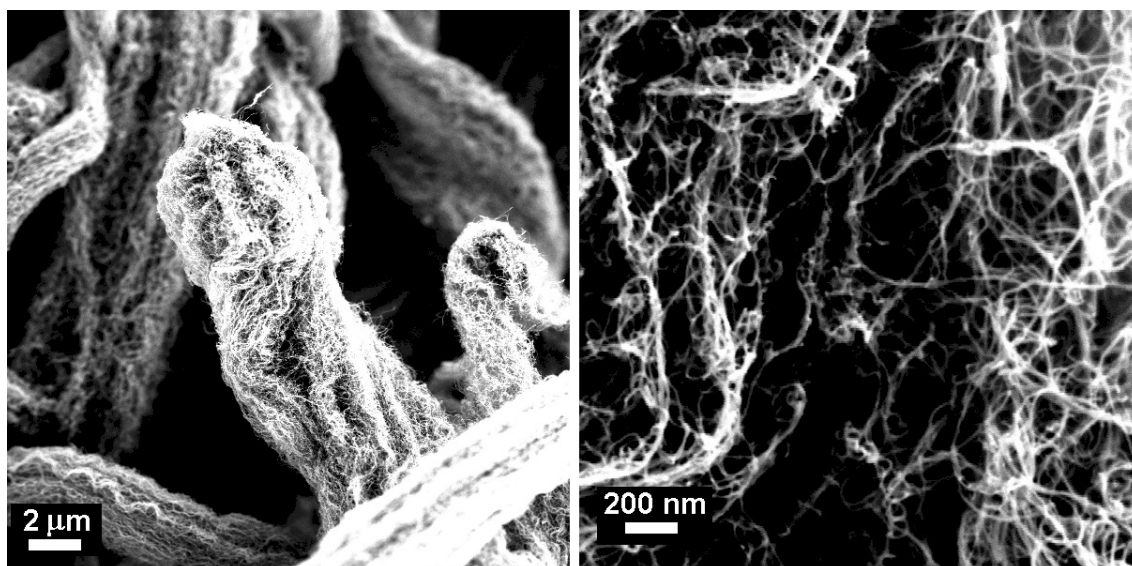
Figure 2-1 SEM images of a cluster of CCVD-grown multi-wall carbon nanotubes as supplied. Typical lengths / diameters / aspect ratios of the CNT are ~ 15 µm / 15 nm / ~ 1,000.

2.2.2 ACVD-aligned-grown CNT

ACVD-aligned-grown CNT are multi-wall carbon nanotubes that were produced in-house via aerosol chemical vapour deposition (ACVD) [13]. Toluol (C_7H_8) was used as carbon feedstock and ferrocene ($Fe(C_5H_5)_2$) as catalyst and carbon feedstock. They were injected into a gas stream of argon and hydrogen

which entered the furnace (heated to 760°C). Quartz plates were positioned inside the furnace and the CNT grew straight away from them forming carpets of well-aligned, non-entangled CNT (Figure 2-2). After 1 h of growth, the CNT had a typical length, diameter and aspect ratio of 50 µm, 80 nm and 625, respectively.
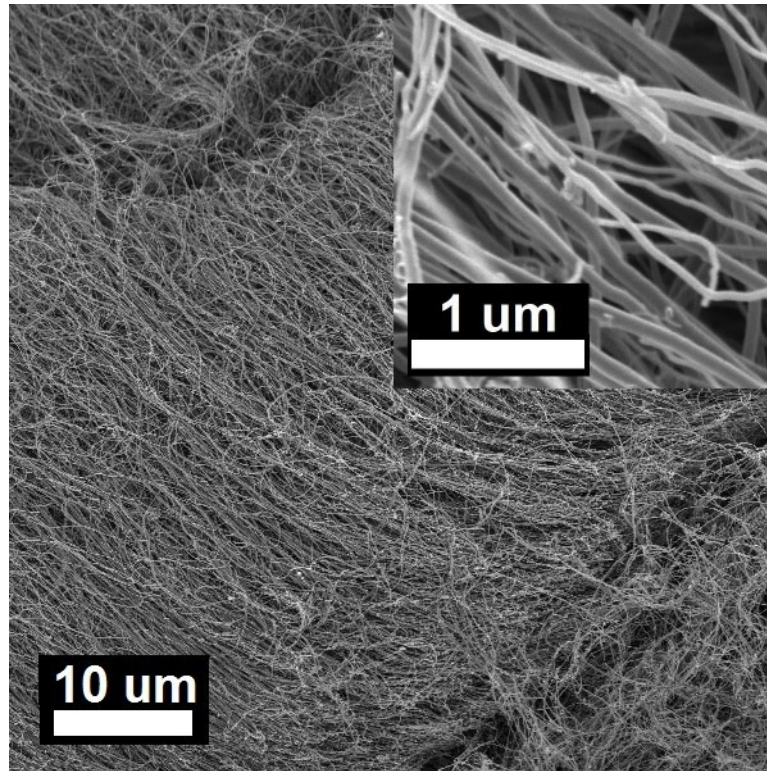
Figure 2-2 SEM images ACVD-aligned-grown multi-wall carbon nanotubes. Typical lengths / diameters / aspect ratios of the CNT are 50 µm / 80 nm / 625.

2.2.3 CCVD-aligned-grown CNT

CCVD-aligned-grown CNT are multi-wall carbon nanotubes that were produced in-house via catalytic chemical vapour deposition (CCVD) [14,15]. The method comprises the evaporation of a 1 nm layer of iron catalysts onto a 3 µm silica layer situated on a silicon wafer. The wafer was then transferred to the furnace which was heated to 725°C. Subsequently, the catalyst layer was activated by a H_2-plasma and growth of the CNT started as soon as acetylene (C_2H_2) was introduced into the furnace. The CNT grew straight away from the wafer forming carpets of well-aligned, non-entangled CNT (Figure 2-3). After 1 h of growth, the

CNT had a typical length, diameter and aspect ratio of 100 µm, 12 nm and 8,300, respectively.
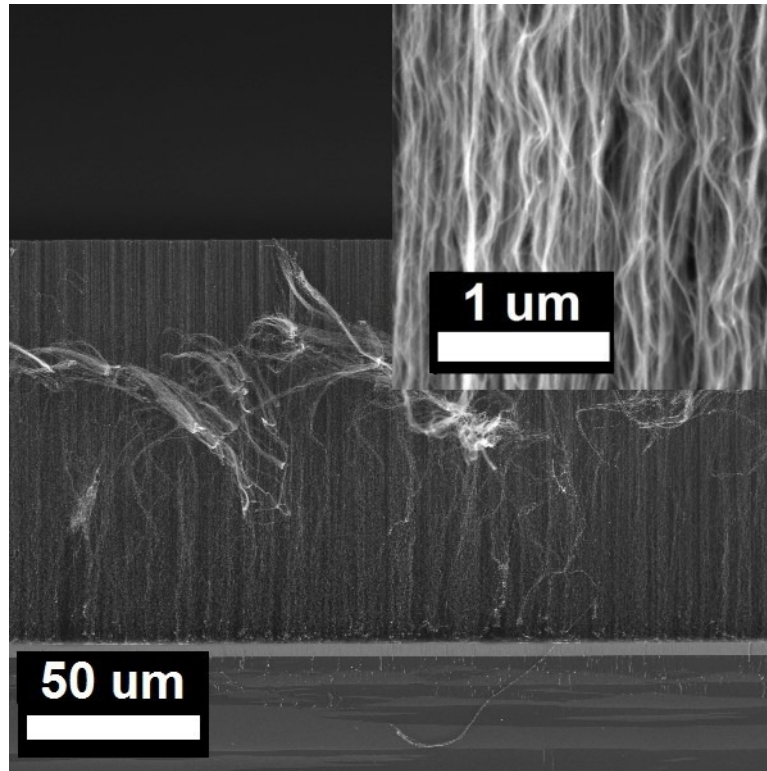
Figure 2-3 SEM images CCVD-aligned-grown multi-wall carbon nanotubes. Typical lengths / diameters / aspect ratios of the CNT are 100 µm / 12 nm / 8,300.

2.2.4 Elicarb SWCNT

Elicarb SWCNT are single-wall carbon nanotubes that were produced by chemical vapour deposition using a vertical reactor. They were supplied by Thomas Swan & Co. Ltd. (UK) and were used as-received. Carbon purity ranged between 70 and 90%. The average diameter of an individual SWCNT was specified to be 2 nm with lengths of some microns. However, the SWCNT were entangled, forming ropes of several tens to thousands of individual tubes.

3 Scanning electron microscopy analyses

Polymer composites containing nanoscaled filler particles have been investigated for decades. However, since the discovery of carbon nanotubes (CNT) [3-6] the interest is growing considerably. Many theories and explanations on CNT properties and their transfer into the composite thereby rely on assumptions of certain particle shapes and distributions. These assumptions were supported–if at all–by optical micrographs [16-29], atomic force microscopy [30,31], scanning electron microscopy (SEM) studies restricted to sample surfaces (due to etching, conductive coating or choice of detector) [32-52] and transmission electron microscopy (TEM) images [53-67].

TEM usually examines samples on a sub-micron scale; the resolution of optical images (~ 0.2 μm) impedes the visualization of individual CNT. All other aforementioned methods analyse merely the surface of a sample. For non-sputtered samples, and with the proper choice of electron detector, SEM can be effectively utilised to characterise CNT nanocomposites in nearly all length scales: from TEM to light microscopy. Moreover, it permits a simultaneous shallow insight into the sample [68,69]. The technique is based on sensing potential variations on the sample surface that were caused by electron charging. This contrast effect was known as early as 1957 [70] and was termed "voltage contrast". A discussion on this technique was conducted by Chung et al. [71] in 1983 who monitored carbon black fillers. It was continued by Loos et al. [72] in 2005 and Dikin et al. [73] in 2006, both of whom analysed CNT. Lillehei et al. contributed a NIST practice guide in 2005 on how to characterize the dispersion of CNT in a polymer matrix [74]. Voltage contrast images of CNT were already published before 2005 [75-79] and also thereafter [80-82], unfortunately without going in depth into the procedure to obtain such images.

The first theoretical model that described time dependent charging phenomena in insulators irradiated by an electron beam was presented in 1995 [83]. It modelled the dynamics of a double-layer (one layer directly below the sample surface and one deeper inside the sample) as a sum of different currents to and from these layers. Other groups improved this model by taking into account elastic and inelastic scattering, diffusion, recombination and deposition for each electron impinging the sample [84-86]. This allowed the simulation of three dimensional charge distributions inside homogeneous insulators.

This section intends to supply detailed information on the way to visualize CNT in insulating matrices. Subsequently, the effect of various SEM parameters as well as requirements on sample conductivity and SEM detector type are illustrated by imaging CNT/epoxy composites. The aim is to provide knowledge about this non-destructive technique for determining real particle shapes and distributions in a composite over several length scales. Recently introduced methods that could provide similar information–the automated nanotomography [87] and focused-ion-beam [88]–are destructive techniques.

3.1 Principles of image generation

This section briefly summarizes the basic principles of image generation in a scanning electron microscope [68,69]. The challenge in interpreting voltage contrast images is discussed in the following sub-sections. The electrons that contribute to image formation split up into two major classes. Backscattered electrons (BSE) are electrons of the incident beam that escape the specimen as a result of multiple elastic scattering and which frequently retain nearly all their initial energy. Secondary electrons (SE) are specimen electrons having a small amount of kinetic energy (< 50 eV, with the most probable energy of 3-5 eV) and are produced during the inelastic collisions of the beam electrons. The beam electrons pass through the specimen surface, scatter and thereby generate so-called SE1. Those beam electrons that are scattered back to the surface produce so-called SE2 before emerging as BSE.

14

The detector used throughout this thesis is situated inside the beam focusing lens and therefore is referred to as "through-the-lens" or InLens detector. Only secondary electrons leaving the sample near to the electron beam impact area are intercepted by the weak electrical field present at the sample surface, accelerated to a high energy by the electrostatic lens field (+8 kV) and focused on the annular InLens detector above the final lens [89,90]. SE1 and a few SE2 are the only electrons that fulfil this conditions, thus, an InLens detector is monitoring mainly the SE1.

The other detector used for comparison is the widespread Everhart-Thornley detector (in the following referred to as ET) which is placed beside the specimen. A positive bias of 400 V facilitates the collection of low energy electrons, no matter where and in which direction they are leaving the specimen. In addition, it also monitors all BSE that leave the sample with trajectories towards the ET. Thus, the ET signal is composed of different types of electrons which have various spatial distributions (influencing the signal resolution) and contribute with different intensities to the total signal (influencing the contrast).

An image generated by SE represents a mix of topographic contrast (enhanced SE emission at tilted surfaces or at small particles and edges), material contrast (increasing BSE generation with increasing atomic number) and magnetic/ electric contrast. The contribution of electric and magnetic fields to the image contrast is very complex since interactions of the fields at the sample surface with all other fields present within the sample [91] and in the specimen chamber [92] have to be considered. These interactions were analysed long time ago for fields of the ET detector. However, comparable information for the InLens detector is not available in literature.

The image resolution is determined by the SE emission area. For SE1 this area is simply the incident beam cross-sectional area, while for SE2 it is the area defined by the projection of the incident beam interaction volume onto the

surface. The incident beam electrons penetrate a volume which extends up to $0.6\,R_{KO}$ laterally (for light element samples) and up to R_{KO} in depth. The electron range within a sample was derived by Kanaya and Okayama [68] as

$$R_{KO}[\mu m] = \frac{0.0276\,A_r[\text{g/mole}]}{Z^{0.89}\,\rho[\text{g/cm}^3]}\,E^{1.67}\,[\text{keV}] \qquad \textbf{Eq. 3-1}$$

where E is the beam energy; A_r is the atomic weight, Z the atomic number and ρ the density of the specimen; the brackets indicate the respective units. Within the interaction volume, these electrons scatter and generate SE which, due to their low energy, not always leave the sample. In fact, only SE within a maximum depth of ~ 50 nm can be emitted and reach a detector [68,93]. However, this value could be altered if opposite charges are present inside and onto the sample through electric field enhanced SE emission [93,94]. The image resolution is determined by the sample area belonging to a single picture element size (pixel). The SE1 emission area (diameter of ~ 2 nm) equals one pixel at a magnification of approximately 200,000× while the SE2 emission area (radius $0.6\,R_{KO} \approx 1\,\mu m$ for light element samples and 10 keV beam energy) equals one pixel already at ~ 200×. The respective SE emission area limits the image resolution at higher magnifications, while the respective pixel area limits the resolution at lower magnifications.

3.2 Experimental procedure

Samples containing 0.1-1 wt% Nanocyl CNT were prepared by mixing epoxy resin (LY556 or E20) and CNT primarily with a dissolver disk (2,000 rpm for 2 h) and then with a three roll calender (5 μm gap size) [95,96]. The suspension collected from the rolls was filled in small bottles and immediately stored in a refrigerator to prevent re-agglomeration of the CNT. Each bottle was consecutively removed from the refrigerator and heated to room temperature before 23 wt% of XB3473 hardener and 1 wt% of Tego Wet 280 wetting agent

were added. The suspension was mixed manually and subsequently centrifuged (4,000 rpm) or exposed to vacuum (for 1 h) to remove the air bubbles. The dispersion was spin-coated onto glass substrates at 5,000-9,000 rpm for 1 min using a Convac TSR 48 spin-coater. The samples were cured on a hot-plate or in an oven at 120-150°C for 6-48 h. Film thicknesses were then determined with a Sloan Dektak 3030 ST surface profilometer and ranged between 8 and 30 μm. Extensive scanning electron microscopy analyses were conducted on LEO 1530 FE-SEM using two detectors. One is situated inside the beam focusing lens (called InLens) and monitors only SE1 [68,69] which are attracted by an electrostatic lens field of 8 kV [89,90]. The ET detector was operated with a positive bias of 400 V and is sensitive to both, SE1 and SE2. The films were analysed without applying surface etching or conductive layer coating techniques. The SEM parameters were as follows: working distance of 2-4 mm, aperture of 20-30 μm, acceleration voltage of 0.2-20 kV, magnification of 500×-500,000× with respect to a 1024×768 pixel image and scanning speed of 20 sec/frame.

3.3 Visualization of filler particles within a polymer matrix

SEM images of Nanocyl CNT deposited on a glass substrate and covered with a thin gold layer are presented in Figure 3-1a,c. Bright structures attributed to the topographic contrast of the CNT are clearly visible. Spin-coated Nanocyl CNT/epoxy composites were covered with gold and analysed in Figure 3-1b,d. Areas where the gold layer was scratched away reveal bright structures. However, no bright structures are visible in regions where the gold layer is intact. The only possible conclusion is that in this case the bright structures are not due to topographic contrast, thus the CNT visible in Figure 3-1b,d are not located on top of the composite. Material and magnetic contrast can be excluded as CNT and epoxy mainly consist of carbon which is non-magnetic. It seems that different electrical conductivities of the CNT and the epoxy matrix produce an electrical contrast that can be monitored with SEM.
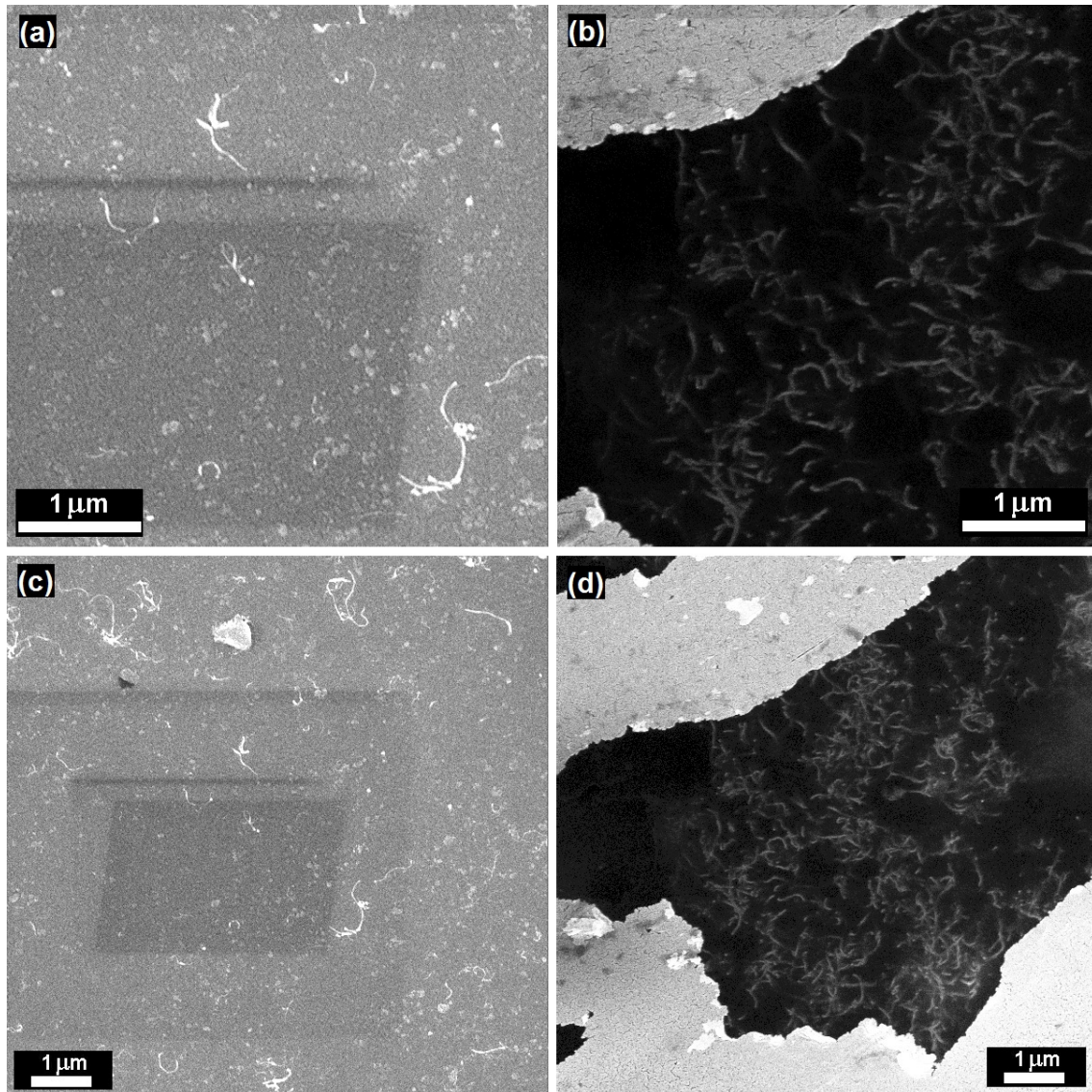
Figure 3-1 (a,c) Nanocyl CNT deposited on a glass substrate and covered with a gold layer. (b,d) The gold layer on top of a Nanocyl CNT/epoxy composite was scratched away and reveals the embedded CNT. SEM images were taken with the InLens detector at (a,b) 50,000× and (c,d) 25,000× magnification.

Figure 3-2 presents two SEM images of the same area on a cryo fractured specimen (note the ditches that are visible in both pictures); one image recorded with the ET detector (Figure 3-2a) and the other with the InLens detector (Figure 3-2b). Bright structures are visible only in Figure 3-2b and are attributed to CNT. Figure 3-2a seems to be dominated by topographic contrast, but no CNT are visible here, meaning that they are inside of the polymer rather

than on the surface. It is important to note that the resolution of SE2 at 10 kV is around 2 μm (due to the large electron emission area with radius $\approx 0.6\,R_{KO}$) while the ditch visible in Figure 3-2a is resolved on a sub-micron scale. This means that even with the ET detector mainly SE1 are monitored. This is not surprising when considering that the SE1:SE2 emission ratio in carbon element samples is 5:1 [68].
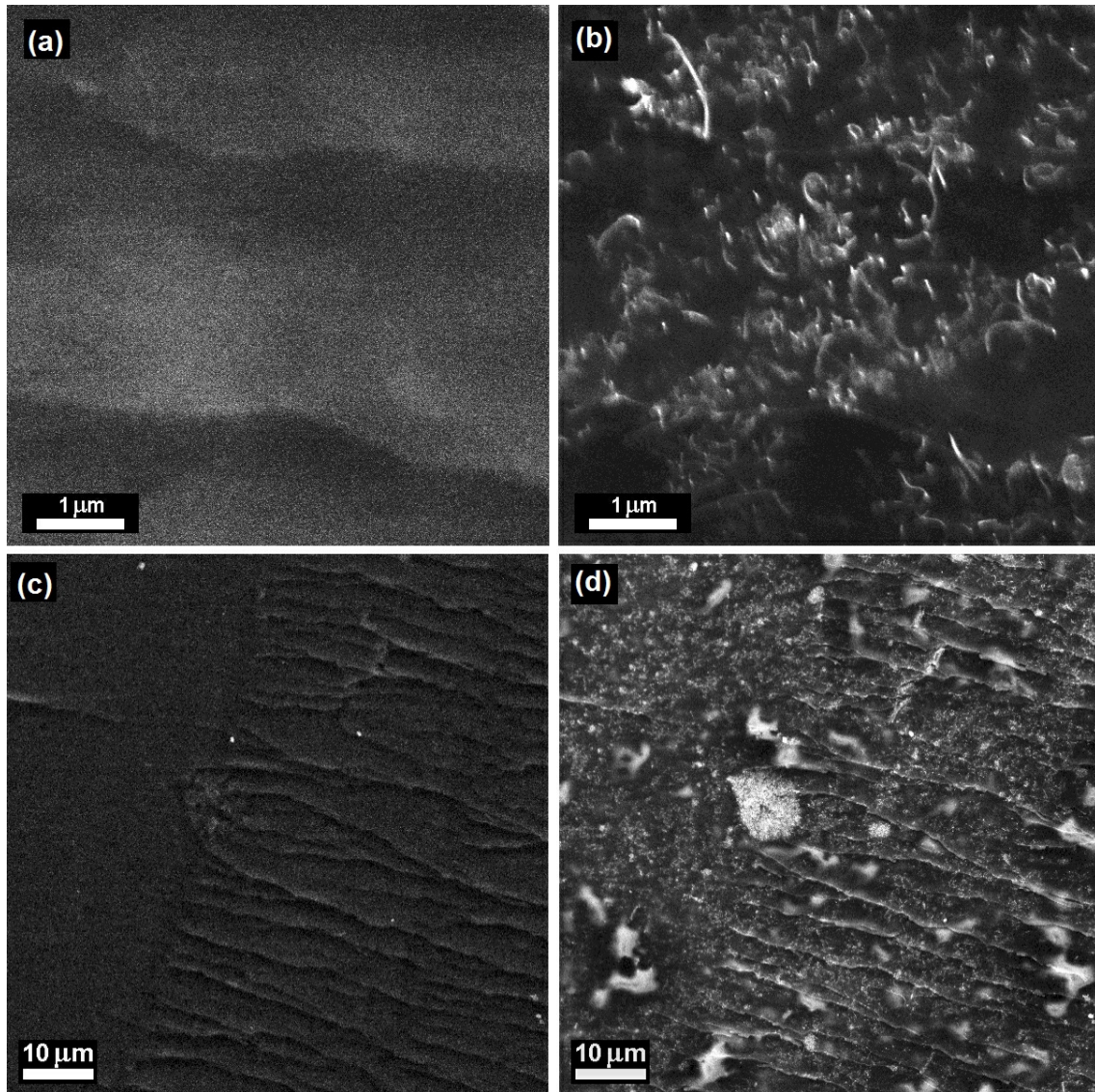
Figure 3-2 Cryo fractured surface of a composite containing 1 wt% Nanocyl CNT dispersed in LY556. Images were recorded with (a,c) the ET detector and (b,d) the InLens detector at 10 kV acceleration voltage and magnification of (a,b) 25,000× and (c,d) 2,000×.

But why are CNT visible in Figure 3-2b and not in Figure 3-2a (working distances up to 16 mm were examined) although SE1 are monitored in both cases? Besides topographic contrast, only voltage contrast is present due to potential differences between the insulating polymer and the metallic CNT. This contrast is present in both images, but it seems to influence only the SE1 signal recorded by the InLens detector. Dotan [97] finds the same effect and uses it deliberately to avoid charge influences in the ET signal. However, this does not mean that ET detectors in general are not capable to sense these slight charges on a sample surface, as Loos et al. [72,78] demonstrated by using an Environmental SEM (ESEM) from FEI Company. We were able to take similar images with the ET detector of a JSM-840A SEM from Jeol. The InLens detector from Hitachi SEM devices is also sensitive to voltage contrast [76,77,81,82], but at the same time, it seems to be immune to excessive surface charging. Thus, as long as the electric field influence for new detector (InLens) or microscope types (ESEM, LVSEM) are not explored, attention has to be paid to the choice of the detector [98].

3.4 Dispersion quality analyses by means of voltage contrast

Three series of pictures recorded with the InLens detector are presented in Figure 3-3 to Figure 3-5. They show zooming out sequences from high to low magnification without changing the scanning position on the three samples (the white squares denote the area of the preceding zoom step). The first sample displays a homogeneous and dense CNT layer (Figure 3-3) while the second and third ones exhibit close-meshed (Figure 3-4) and wide-meshed (Figure 3-5) network structures (note that all pictures in Figure 3-5 are shifted by one zooming step when compared to Figure 3-3 and Figure 3-4). It should be also noted that all CNT visible in the figures are distributed within ~ 50 nm of sample depth, which is much smaller than the sample thicknesses. These series of images point out a new way for analysing the quality of CNT dispersions over several length scales, from tens of nanometres to some hundred micrometers.
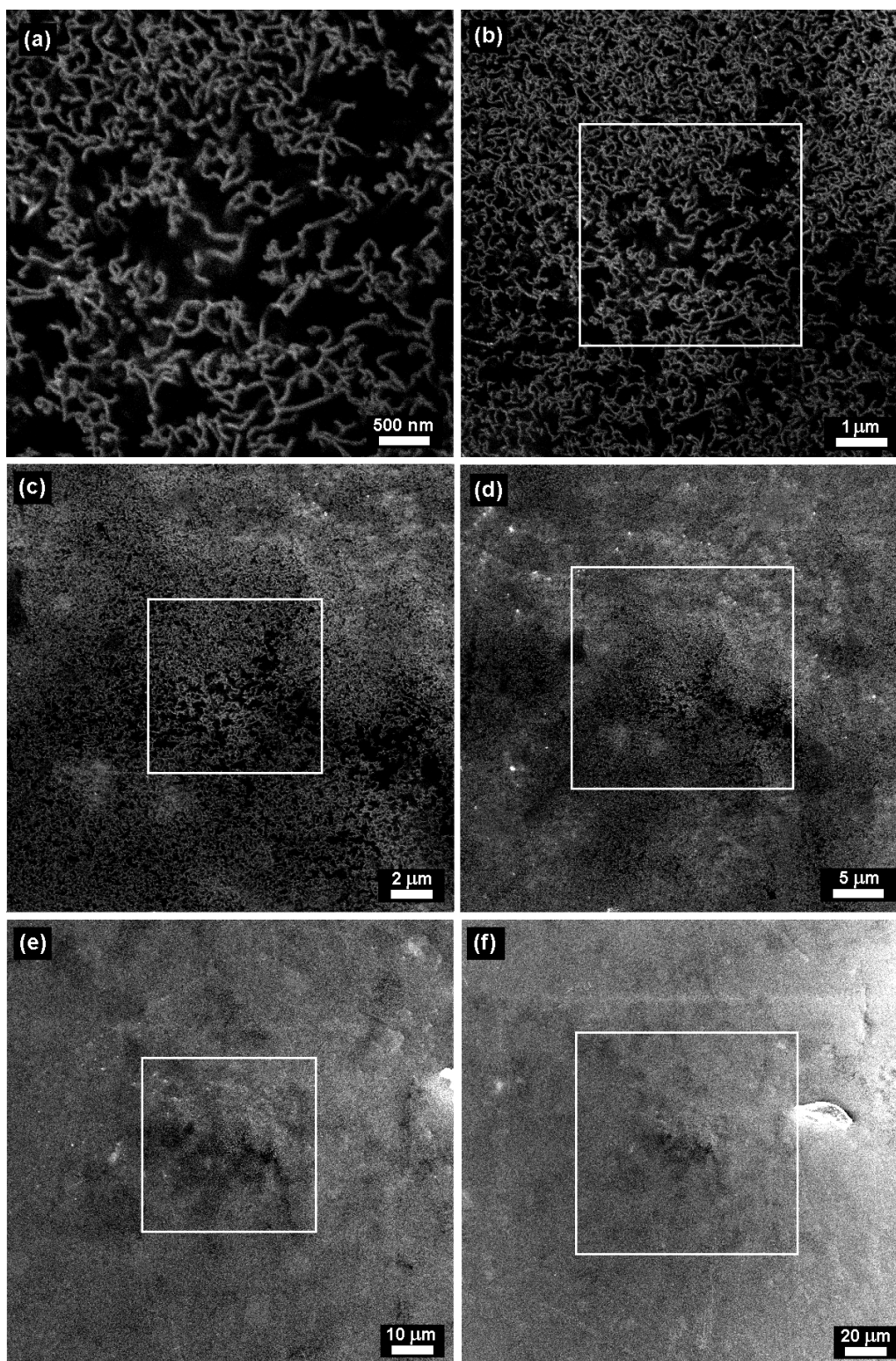
Figure 3-3 Spin-coated composite (14 µm film thickness) containing 1 wt% Nanocyl CNT in E20 resin recorded at 10 kV acceleration voltage and different magnifications: (a) 50,000×, (b) 25,000×, (c) 10,000×, (d) 5,000×, (e) 2,000× and (f) 1,000×.

Figure 3-4 Spin-coated composite (26 μm film thickness) containing 1 wt% Nanocyl CNT in E20 resin recorded at 20 kV acceleration voltage and different magnifications: (a) 50,000×, (b) 25,000×, (c) 10,000×, (d) 5,000×, (e) 2,000× and (f) 1,000×.

Figure 3-5 Spin-coated composite (20 μm film thickness) containing 1 wt% Nanocyl CNT in LY556 resin recorded at 10 kV acceleration voltage and different magnifications: (a) 25,000×, (b) 10,000×, (c) 5,000×, (d) 2,000×, (e) 1,000× and (f) 500×.

The comparison of Figure 3-4 and Figure 3-5 suggests that increased charging of the matrix and subsequent image whitening take place in areas where the CNT concentration drops below a certain level. The influence of these charged areas can increase substantially and thereby outshine the signal of the CNT. Imaging of CNT at high acceleration voltages was possible down to a CNT concentration of 0.5 wt% (corresponding to a conductivity of $\sim 10^{-2}$ S/m) for good dispersions. However, lower CNT concentrations and poorly dispersed CNT can also be analysed when low acceleration voltages are used, as will be reported in Section 3.6.

3.5 The influence of SEM parameters on the voltage contrast

Figure 3-6 shows high magnification SEM images of the same sample recorded at different acceleration voltages. For low acceleration voltages (0.2-0.7 kV) the CNT appear bright with the polymer being dark. The contrast nearly vanishes around 0.7 kV (not shown) and subsequently inverts, displaying dark CNT surrounded by bright polymer. It should be noted that the boundaries of contrast changing are not defined merely by the acceleration voltage, as dark CNT are visible at 1 kV and bright ones at 1.5 kV too. Interestingly, the CNT start changing contrast from edge to centre. The contrast reaches a maximum around 1.5 kV and then starts decreasing again until it vanishes at around 2 kV (not shown), inverts and again reveals bright CNT with a dark polymer (4-20 kV). Similar analyses were conducted on a fixed region of the sample but–unlike the results reported in [72]–no additional CNT appeared with increasing acceleration voltage. This is consistent with SEM theory which indicates a maximum depth of SE emission of ~ 50 nm for light element samples [68,93]. However, this value could be altered due to electric field enhanced SE emission if opposite charges are present inside and onto the sample [93,94].

Figure 3-6 Spin-coated composite (14 µm film thickness) containing 1 wt% Nanocyl CNT in E20 resin (same sample as in Figure 3-3) recorded at 25,000× magnification and different acceleration voltages: (a) 0.5 kV, (b) 1 kV, (c) 1.5 kV, (d) 4 kV, (e) 6 kV and (f) 15 kV.

In fact, Figure 3-6 also visualizes another important feature of SEM. The charging of the sample by the incident electron beam–which in the end produces the voltage contrast needed for imaging–can be manipulated through the acceleration voltage. The total electron emission yield of a sample is depending on the beam energy and can even increase above unity [69]. This means that a sample can be charged positively or negatively or can remain uncharged if a proper acceleration voltage is chosen. For low acceleration voltages the total electron emission yield is smaller than unity, meaning the sample charges negative. Increasing the beam energy increases also the emission yield, which crosses unity at an energy usually denoted by E1 (generally below 1 keV) and starts charging the sample positive. In this energy region, the incident electrons excite efficiently many SE near the surface which then can all leave the sample. With increasing energy most SE are excited deeper and can no longer leave the sample. Hence, the emission yield starts to decrease, crosses unity at an energy usually denoted by E2 (generally 0.5-2 keV for light element materials) and now charges the sample negative again. The acceleration voltages, where contrast is lost, are in the right regions to be assigned to E1 (= 0.7 keV) and E2 (= 2 keV), meaning that negative sample charging is obviously monitored below E1, positive charging between E1 and E2, and again negative charging above E2 in Figure 3-6.

The explanation given above is based on analyses of electric field interactions between sample surface charges and ET detectors, which were already conducted decades ago and do not necessarily apply to InLens detectors. Furthermore, sample charging must be understood in terms of relative charge densities, which are affected by additional parameters. The equilibrium density of charges depends on the relationship of the electron dose to the discharging capability of individual sample regions [69]. The dose itself depends on the scanning density (magnification) and scanning speed (beam dwell time per area).
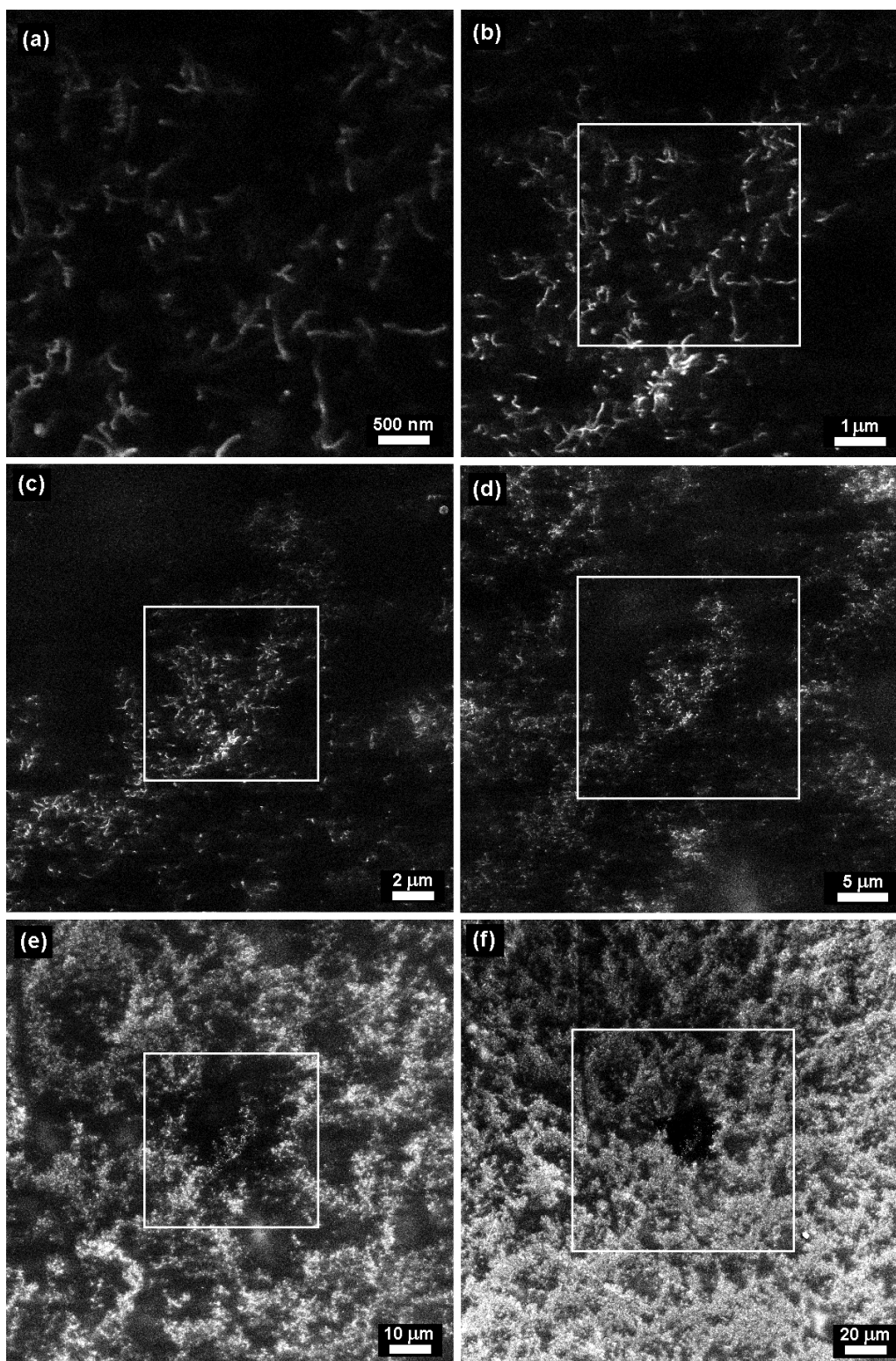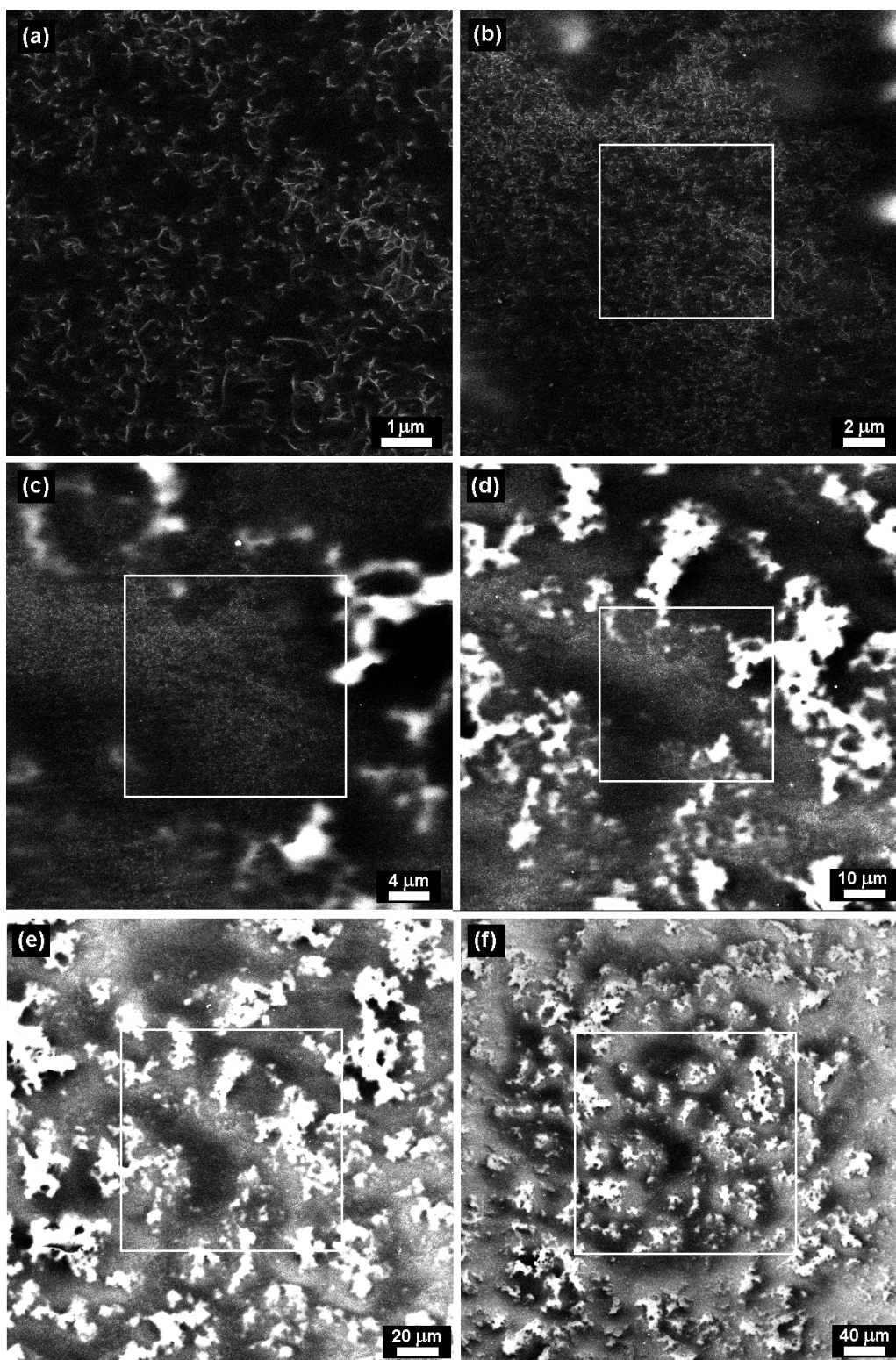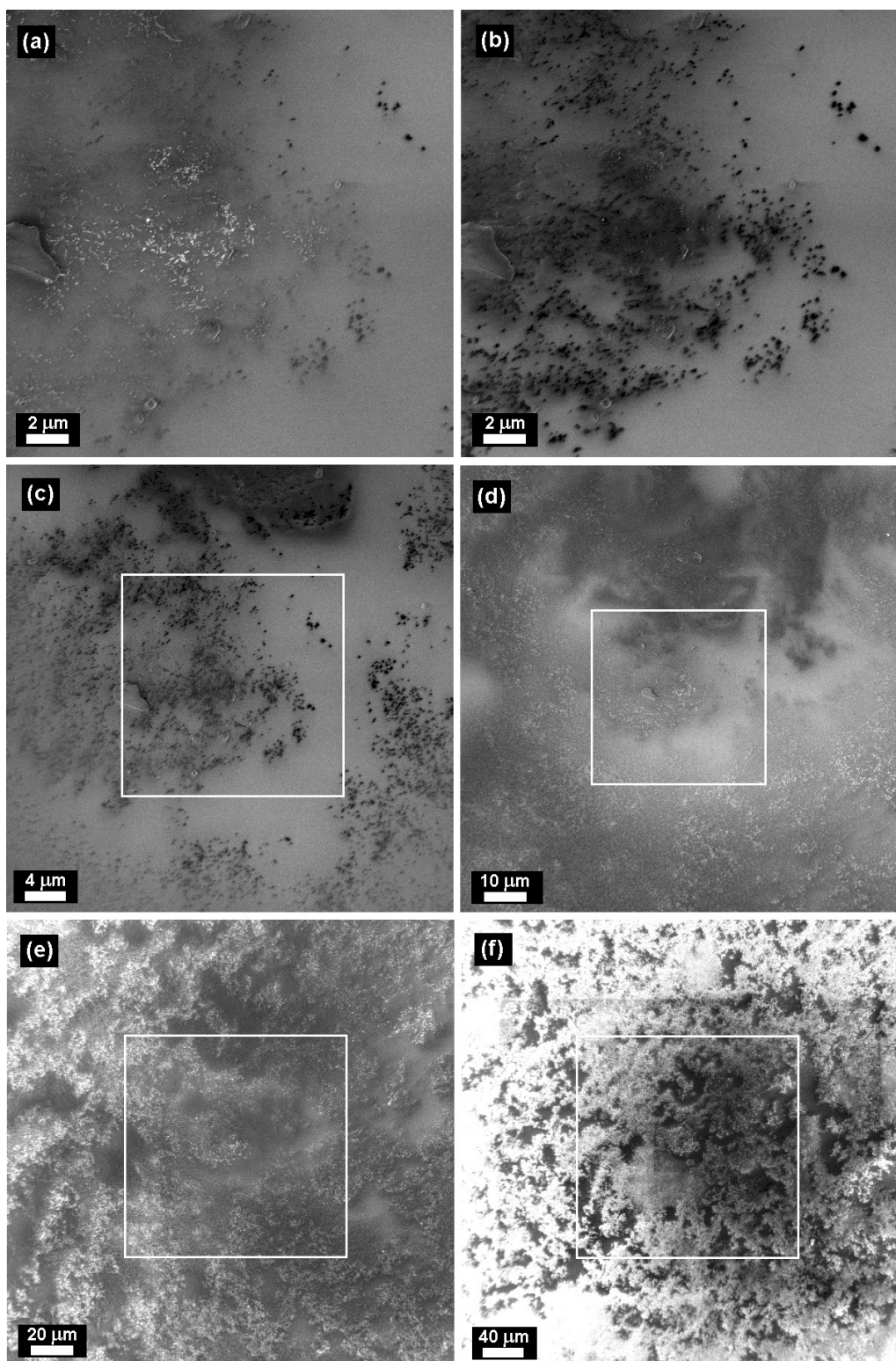
Figure 3-7 The first (a) and third (b-f) scans of a spin-coated composite (10 µm film thickness) containing 1 wt% Nanocyl CNT in LY556 resin recorded at 0.5 kV acceleration voltage and various magnifications: (a,b) 10,000×, (c) 5,000×, (d) 2,000×, (e) 1,000× and (f) 500×.
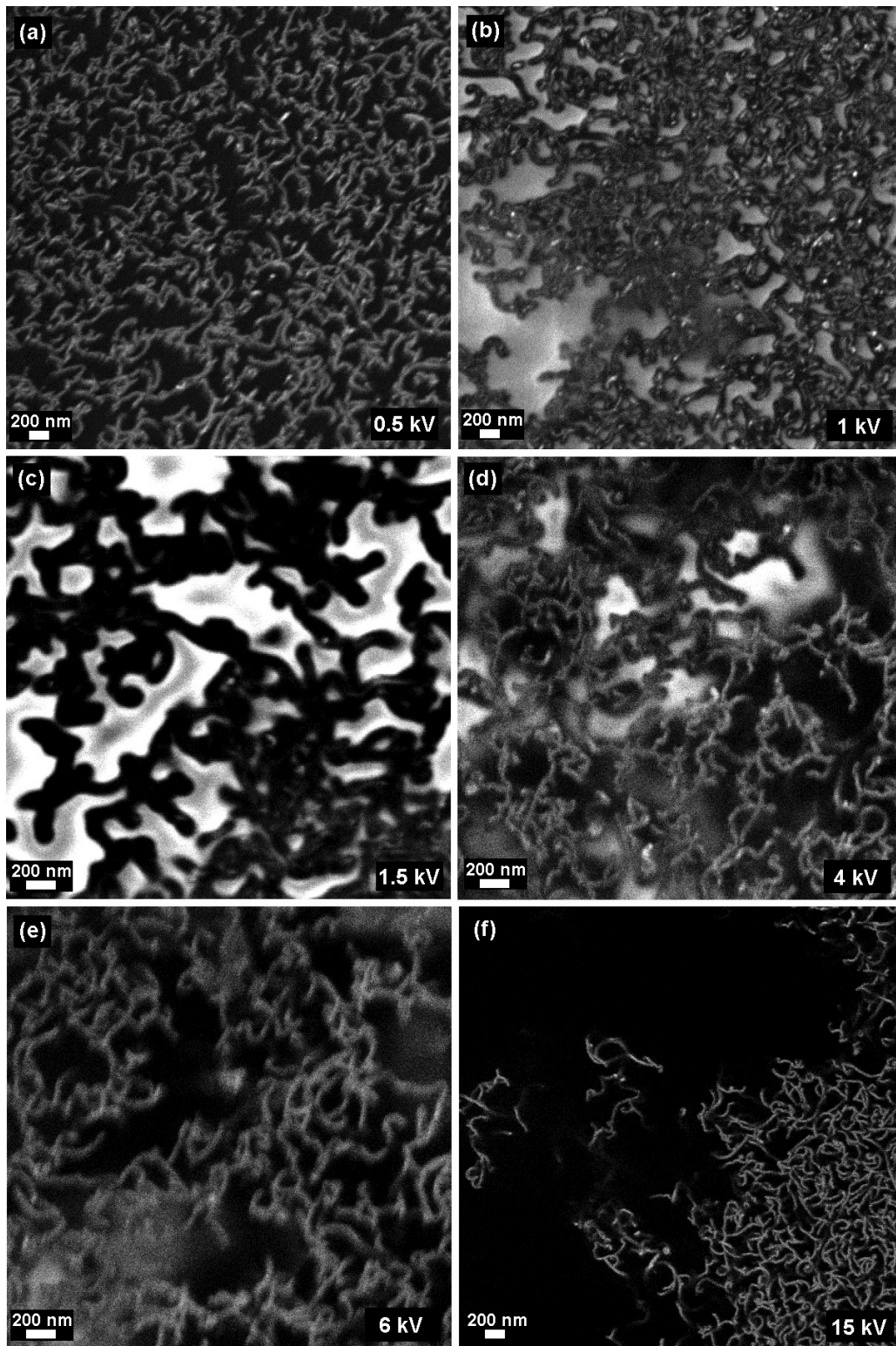
Figure 3-8 Spin-coated composite (26 μm film thickness) containing 1 wt% Nanocyl CNT in E20 resin (same sample as in Figure 3-4) recorded at 0.6 kV acceleration voltage, 25,000× magnification and different beam dwell times: (a) 800 ns, (b) 400 ns and (c) 100 ns.

These dependencies are visualized in Figure 3-7 and Figure 3-8 using low acceleration voltages. The first scan of a sample at 0.5 kV acceleration voltage leads to bright CNT (Figure 3-7a), while scanning the same area several times turns the CNT into dark ones (Figure 3-7b). With increasing scanning speed (~ 2 sec/frame) the CNT immediately appear bright again (not shown). The same effect is observed when zooming out from this region, even though scanning slowly and multiple times again (Figure 3-7c-f). Similarly, Figure 3-8 shows that a long beam dwell time yields dark CNT while a short time leads to bright ones. Here, the frame scanning speed (e.g. 800 ns × 1024 × 768 = 630 μs) was much shorter than in the other experiments, so that multiple frames were integrated in order to get a total scanning time of ~ 20 sec. This contrast reversal is encountered only when scanning (a) regions of poor CNT homogeneity or too low overall CNT concentration (< 0.5 wt%) (b) at high magnifications and low acceleration voltages (< 1 kV). This clearly demonstrates the sensitivity of the charge density distribution on the electron dose. It should be noted that scanning the sample in Figure 3-7 at high acceleration voltages (~ 10 kV) yields–for each magnification–images similar to the ones presented in Figure 3-5.

3.6 SEM analyses of poorly conductive composites

Poorly conductive samples or regions can also be analysed with SEM if low acceleration voltages are used. Gojny et al. [80] recently demonstrated this by recording high magnification images of a composite with only 0.1 wt% CNT. High and low magnification SEM images of a spin-coated film with the same CNT concentration are displayed in Figure 3-9. The CNT change their appearance from bright to dark within a single scan (Figure 3-9a) which illustrates again the complexity of the charging mechanism. In the subsequent zooming out steps (Figure 3-9b-d) large, dark areas of charging artefacts appear. Nevertheless, most CNT remain visible–mainly as bright dots–so that their macroscopic distribution can be monitored even for this low filler concentrations.
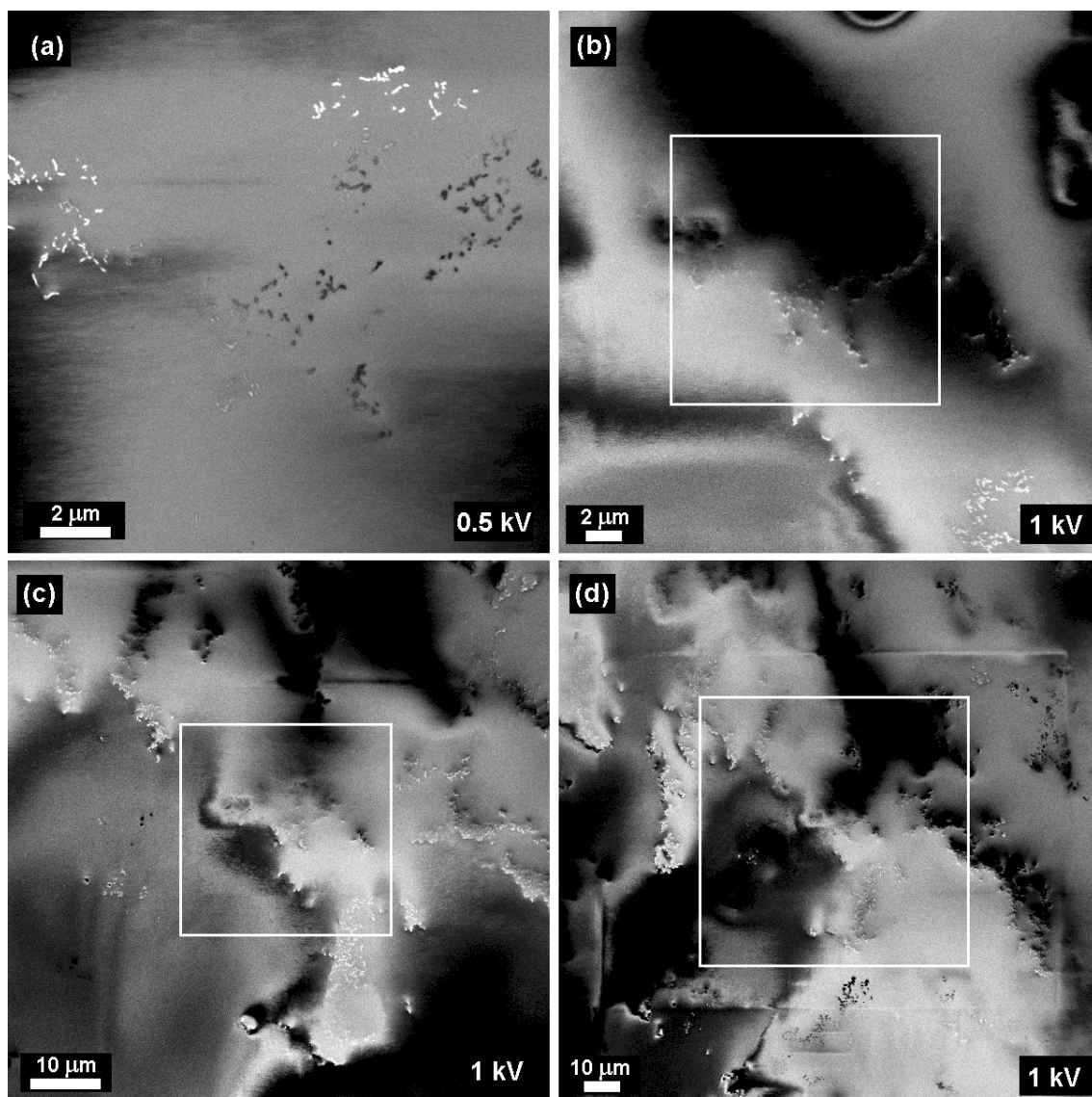
Figure 3-9 Spin-coated composite (8 µm film thickness) containing 0.1 wt% Nanocyl CNT in E20 resin recorded at different magnifications: (a) 10,000×, (b) 5,000×, (c) 2,000× and (d) 1,000×.

3.7 High magnification imaging of individual CNT

Figure 3-10 demonstrates the capability of an InLens detector of resolving individual CNT at magnifications usually encountered in a transmission electron microscope (TEM) analysis. The observed structures are individual CNT with their initial diameter (~ 15 nm) approximately doubled by charging effects. The CNT appear to be curly and entangled (Figure 3-10a) as expected due to the

large-scale production CCVD-technique and even exhibit coil spring-like structures (Figure 3-10b). It is pointed out that such high magnifications introduce an immense dose into the sample leading–in this case–to irreversible damaging (whitening of the whole area) within two slow scans (20 sec/frame).

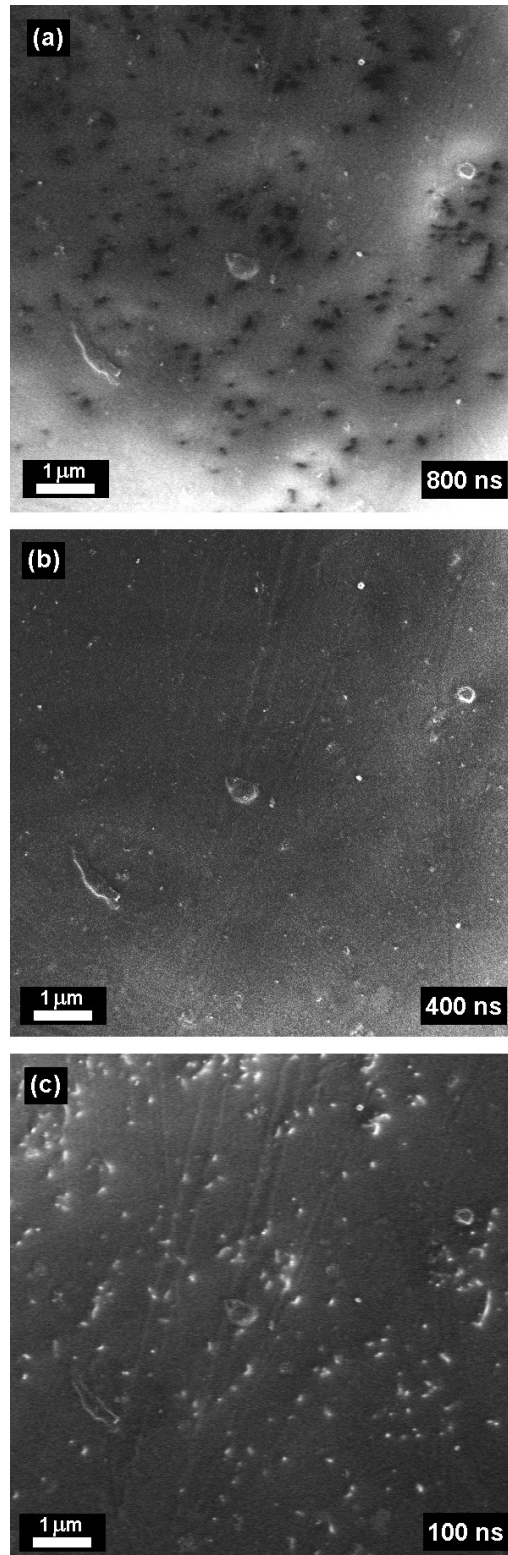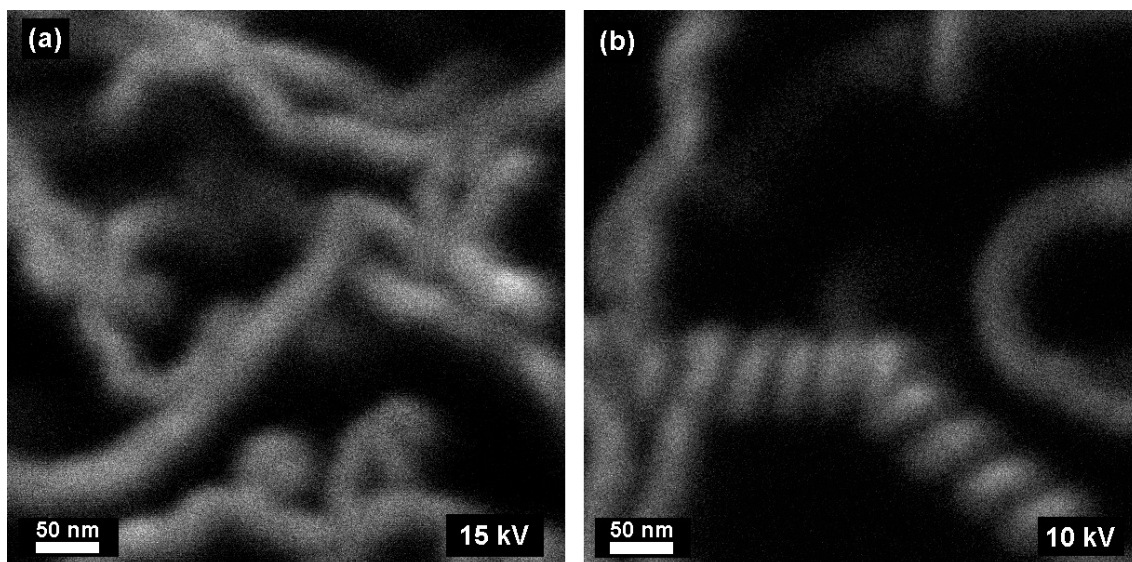**Figure 3-10** Individual Nanocyl CNT within a spin-coated composite (14 µm film thickness) containing 1 wt% Nanocyl CNT in E20 resin (same sample as in Figure 3-3) visualized at an extremely high magnification (500,000×) and an acceleration voltage of (a) 15 kV and (b) 10 kV.

3.8 Imaging of electric field induced CNT networks

For this analysis gold electrodes were evaporated to the glass substrates before spin-coating the dispersion. During the whole curing process, an AC electric field of 70 V/mm at 100 Hz was applied. Voltage contrast SEM images of the cured composite containing 0.7 wt% CNT are presented in Figure 3-11. One electrode is located below the CNT visible in the upper half of the images while the electrode gap is situated below the black network visible in the lower half of the images. With a constant potential above the electrode, all CNT remain randomly distributed and individually visible. However, the electric field between the electrodes forces the individual CNT to migrate laterally to form thick

columns, as already stated in [82]. The complete absence of individual CNT lets the polymer between these columns charge up electrically and produce white artefacts. Obviously, the columns are not located near the composite surface as it is not possible to resolve any CNT within them. As expected, the degree of column alignment with the electric field is poor at such high CNT concentrations (0.7 wt%).
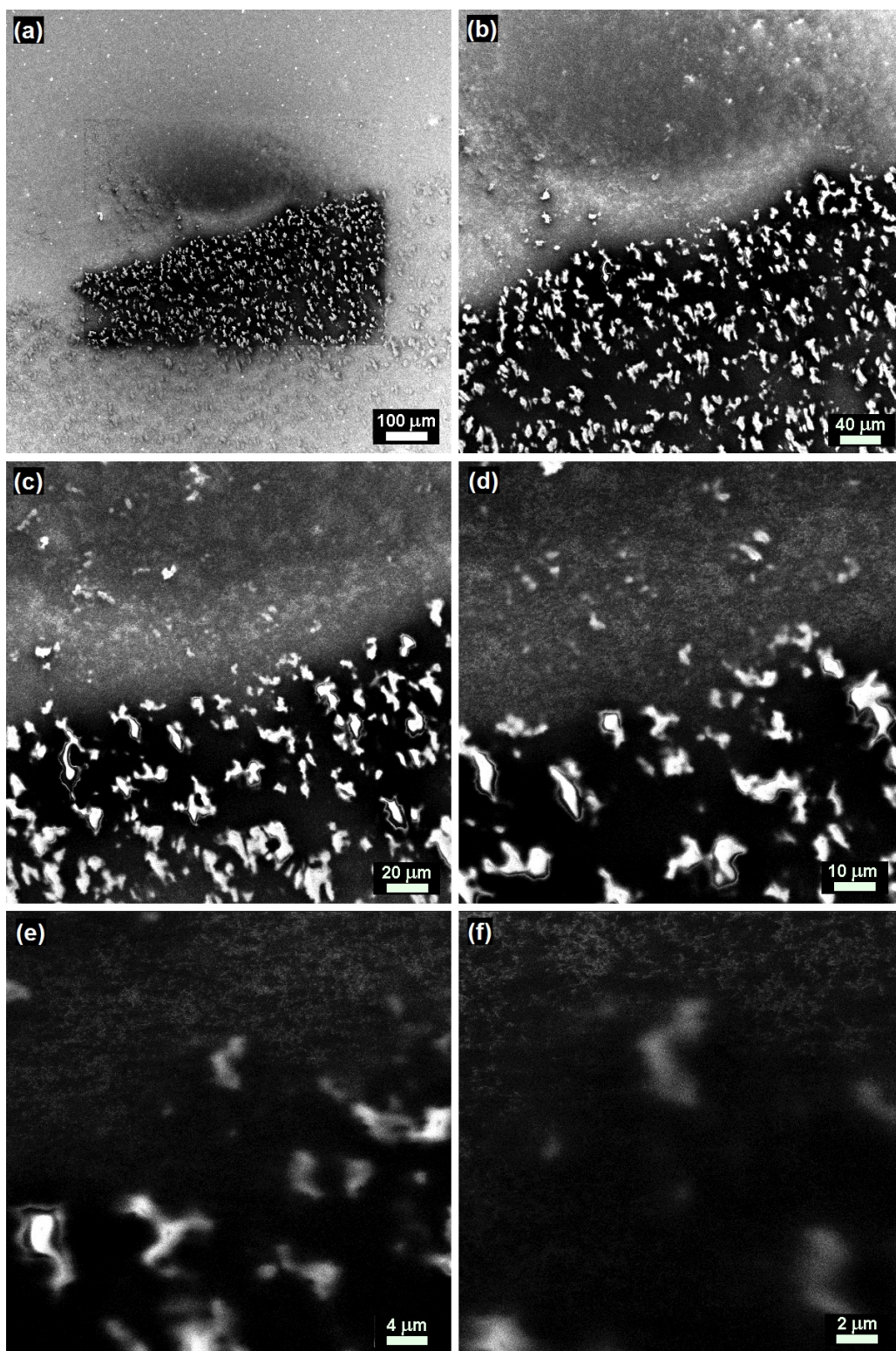
Figure 3-11 Spin-coated composite containing 0.7 wt% Nanocyl CNT in LY556 resin recorded at 10 kV acceleration voltage and different magnifications: (a) 200×, (b) 500×, (c) 1,000×, (d) 2,000×, (e) 5,000×, (f) 10,000×.

3.9 Summary and conclusion

The technique of CNT visualization within polymers with SEM was discussed in detail in order to enable the analysis of filler distributions inside of polymers at several length scales. The key for this task seems to be (a) the detection of secondary electrons (SE1) excited in the electron beam impact area, and (b) the use of an appropriate detector which is sensitive to slight charges on sample surfaces. The quality of filler particle dispersion can be monitored accurately at high acceleration voltages (~ 10 kV) when the sample conductivity is at least 10^{-2} S/m (thus, 0.5 wt% CNT in this case) and at low voltages (0.5-1 kV) even for lower conductivities.

SEM pictures of CNT in insulating matrices were taken by exploiting the voltage (or charge) contrast. The effect of several parameters (such as magnification, scanning speed, acceleration voltage, sample conductivity and dispersion quality) on the voltage contrast were investigated. The results show that increasing the acceleration voltage does not increase the CNT sampling depth. Secondary electrons have energies up to 50 eV and can only leave the sample when excited within a depth of ~ 50 nm. Therefore, only limited information about the three-dimensional organization of CNT in a matrix can be obtained.

4 Electrical conductivity analyses

Conductive filler particles in an insulating matrix are able to lower the overall resistivity by several orders of magnitude when a network develops throughout the matrix. The transition from an insulating to a conducting composite as a function of filler concentration is known as percolation, and the critical concentration at which this sudden increase in conductivity occurs is called percolation threshold.

In the case of carbon nanotubes (CNT) as filler particles, the electrical performance of a composite is influenced by a series of parameters such as CNT entanglement state, synthesis method, treatment and dimensionality, as well as polymer type, dispersion quality and composite preparation method. Numerous publications were recently reviewed in order to extract general dependencies of the percolation threshold, the scaling law exponent and the maximum conductivity upon the above mentioned parameters [99]. These findings are summarized in Section 4.1.

In a systematic approach to investigate the mentioned dependencies, each parameter should be varied individually while keeping all others constant. The experiments discussed in Sections 4.3-4.8 follow this approach by varying synthesis method, entanglement state and dimensionality of the CNT, as well as sample preparation methods (stirring/calendering and additional slow stirring step prior to curing [29]). Untreated CNT and a single polymer matrix are used throughout the experiments.

However, the mere existence of a particle network does not guarantee good conductivity if the contact resistance between the individual filler particles is too high. Therefore, a simple relation between sample conductivity and filler content

including the contact resistances is derived in Section 4.9. The calculations are applied to published conductivity results in order to correlate the contact resistance values to different filler parameters, polymer materials and processing conditions.

Besides shear forces, a CNT network can also be established by electric fields. CNT and polymer type again have a strong impact on the final composite performance (Section 4.10).

4.1 Literature review

Electrical percolation in mixtures of electrically conducting and non-conducting materials is a widely investigated field which has been covered in several textbooks [100,101]. The observation of a conductivity threshold in CNT/polymer composites [102] has triggered world-wide activities in this area. A recent synopsis has been given by Winey et al. [103].

By now, 256 publications[1] report on the electrical percolation threshold of CNT in different polymer systems. The variation of many parameters like CNT type, synthesis method, treatment and dimensionality as well as polymer type and dispersion method, however, impedes a thorough understanding of the processes involved. This section condenses a comprehensive collection of published data in order to extract general dependencies of the percolation threshold, the scaling law exponent and the maximal conductivity on the above mentioned parameters.

4.1.1 Percolation thresholds – kinetic and statistical

Since the early observation of percolation-dominated electrical conductivity in a CNT/PmPV composite by Coleman et al. [102] more than 30 polymer matrices have been investigated with respect to percolation of CNT filler loading.

---

[1] Search results at http://apps.isiknowledge.com/ with key words „nanotube* electr* percolat* threshold* polymer*" (27. March 2009)

36

Table 4-1 represents a comprehensive collection of published data in this field. The table is organized as follows: the polymer matrices in column 1 are arranged alphabetically, the data for a given polymer are arranged with increasing percolation threshold. The acronyms used to denote the polymers are defined below the table. Type (single-/double-/multi-wall), synthesis method (arc discharge, chemical vapour deposition, laser vaporization), manufacturer, state (entangled or non-entangled), additional treatment (purification, functionalization) and aspect ratio of the CNT are given in columns 2-5 as far as the information is available from the publications. In columns 6 and 7, dispersion method and solvent in the case of solution processing are specified. Finally, electrical characteristics like percolation threshold ϕ_C, critical exponent t and maximum observed conductivity σ_{max} are listed in columns 8-10. All thresholds and filler concentrations are given in weight percent (wt%). Wherever the original data are given in vol%, we use the conversion relations vol% = wt% for single-wall carbon nanotubes (SWCNT) and vol% = 2 wt% for multi-wall carbon nanotubes (MWCNT) independent of the polymer matrix. The inaccuracies resulting from this simplification have no significant effect on the interpretation of the experimental results.

Table 4-1 Summary of the experimental parameters of all reviewed publications, arranged alphabetically with respect to the polymer matrices, the data for a given polymer arranged with increasing percolation threshold. The acronyms are explained in the list of abbreviations at the end of the thesis.

Matrix	Filler	State	Treatment	r	Solution	Dispersion	ϕ_C [wt%]	t	σ_{max} [S/m]	Ref.
ASTAA	SWCNT (HiPco®), Rice Univ.	e	HCl	-	C_4H_9NO	sonicated, stirred	0.035	-	1E-7 @ 0.08 wt%	[104]
Epoxy	MWCNT (CVD)	ne	-	200	-	heat sheared	0.0021	1.8	1E-3 @ 0.01 wt%	[17]
Epoxy	MWCNT (CVD)	ne	-	8000	-	stirred, heat sheared	0.0024	1.6	4E+0 @ 0.62 wt%	[105][2]
Epoxy	MWCNT (CVD)	ne	-	340	-	heat sheared	0.0025	1.2	2E+0 @ 1 wt%	[32]
Epoxy	MWCNT (CVD)	ne	-	1000	-	heat sheared	0.0025	-	4E-1 @ 0.5 wt%	[51]
Epoxy	MWCNT (CVD)	ne	-	860	-	heat sheared	0.0039	1.7	2E-4 @ 0.01 wt%	[17]
Epoxy	SWCNT (Laser), Rice Univ.	e	purified	400	C_6H_8O	sonicated, cured without	0.005	2.7	2E-2 @ 0.1 wt%	[33]
Epoxy	SWCNT (HiPco®), Carbon Nanot.	e	purified	150	C_6H_8O	sonicated, cured without	0.009	3.1	1E-5 @ 0.04 wt%	[33]
Epoxy	MWCNT (CVD)	ne	-	625	-	stirred, heat sheared	0.0099	2.8	2E+0 @ 1 wt%	[105][2]
Epoxy	SWCNT (Laser), Rice Univ.	e	purified	400	C_6H_8O	sonicated, cured with	0.01	1.6	5E-3 @ 0.4 wt%	[33]
Epoxy	MWCNT (CVD), Nanocyl	e	-	1000	-	stirred, heat sheared (slowly)	0.011	1.7	4E-1 @ 1 wt%	[29][3]
Epoxy	MWCNT (CVD)	ne	-	8300	-	stirred	0.012	2.5	4E+0 @ 0.62 wt%	[105][2]
Epoxy	SWCNT (HiPco®), Carbon Nanot.	e	purified	150	C_6H_8O	sonicated, cured with	0.023	3.2	2E-4 @ 0.2 wt%	[33]
Epoxy	MWCNT (CVD), Nanocyl	e	-	1000	-	stirred, heat sheared (medium)	0.024	1.7	3E-1 @ 1 wt%	[29][3]
Epoxy	MWCNT (CVD), Hyperion Catal.	e	-	100	C_2H_6O	sonicated, stirred	0.03	-	5E-1 @ 0.15 wt%	[16]
Epoxy	MWCNT (CVD), Nanocyl	e	-	1000	-	calendered, stirred	0.03	-	1E-2 @ 0.3 wt%	[106]
Epoxy	MWCNT (CVD), Iljin Nanotech.	e	HNO$_3$, centrifuged, C_3H_6O	1000	OP	sonicated	0.034	1.7	1E-1 @ 2 wt%	[79]
Epoxy	SWCNT (Arc), Carbon Solutions	-	-	-	C_3H_6O	sonicated, stirred	0.04	1.7	1E+1 @ 4 wt%	[107]
Epoxy	SWCNT (CVD), Thomas Swan	-	-	1000	-	calendered, stirred	0.04	-	1E-3 @ 0.4 wt%	[106]
Epoxy	MWCNT (CVD), Iljin Nanotech.	e	H$_2$O$_2$/NH$_4$OH, centrifuged, C_3H_6O	1000	OP	sonicated	0.042	1.8	1E+0 @ 2 wt%	[79]
Epoxy	SWCNT (CVD), Thomas Swan	-	-	-	C_2H_6O, NaOH	sonicated, heat sheared	0.05	-	3E-2 @ 0.5 wt%	[108]
Epoxy	SWCNT (Arc), Iljin Nanotech.	e	thermal oxidation, chemical treatment	5000	C_2H_6O	sonicated, vacuum pumped	0.074	1.3	1E-3 @ 0.2 wt%	[109]
Epoxy	MWCNT (CVD), Nanocyl	e	-	1000	-	stirred, heat sheared (fast)	0.08	2.0	4E-2 @ 0.6 wt%	[29][3]
Epoxy	SWCNT (CVD)	-	HCl	-	H_2O	stirred	0.08	-	2E-2 @ 0.4 wt%	[110]
Epoxy	MWCNT (CVD)	ne	-	625	-	stirred	0.088	3.1	1E-1 @ 1 wt%	[105][2]
Epoxy	SWCNT (HiPco®), Rice Univ.	e	HCl	-	-	sonicated	0.1	-	-	[27]
Epoxy	MWCNT (CVD), Iljin Nanotech.	e	-	1000	C_3H_6O	sonicated	0.1	-	2E-1 @ 1 wt%	[111]
Epoxy	MWCNT (CVD), Nano Carbon T.	-	-	100	-	stirred	0.1	1.8	1E+2 @ 15 wt%	[112]

[2] See also Section 4.6
[3] See also Section 4.3

38

Matrix	Filler	State	Treatment	r	Solution	Dispersion	ϕ_C [wt%]	t	σ_{max} [S/m]	Ref.
Epoxy	DWCNT (CVD), Nanocyl	e	-	1000	-	calendered, stirred	0.15	-	1E-2 @ 0.6 wt%	[106]
Epoxy	SWCNT (CVD), Thomas Swan	-	-	-	-	ball milled, heat sheared	0.23	-	1E-3 @ 0.5 wt%	[108]
Epoxy	MWCNT (CVD), Nanocyl	e	NH$_2$-functionalized	-	-	calendered, stirred	0.25	-	5E-4 @ 0.4 wt%	[106]
Epoxy	DWCNT (CVD), Nanocyl	e	NH$_2$-functionalized	-	-	calendered, stirred	0.25	-	3E-4 @ 0.6 wt%	[106]
Epoxy	MWCNT (CVD), Iljin Nanotech.	e	UV/O$_3$	1000	C$_3$H$_6$O	sonicated	0.27	-	2E-2 @ 1 wt%	[111]
Epoxy	SWCNT (HiPco®), Carbon Nanot.	e	-	-	-	PMMA removal, Epoxy infiltrat.	0.3	-	5E-1 @ 3 wt%	[113]
Epoxy	SWCNT (CVD)	-	-	-	C$_2$H$_6$O	sonicated, stirred	0.3	1.4	1E-2 @ 2.5 wt%	[114]
Epoxy	MWCNT (CVD)	ne	-	300	-	sonicated, stirred	0.35	-	2E-4 @ 1 wt%	[115]
Epoxy	MWCNT (CVD), Iljin Nanotech.	e	-	1000	-	stirred	0.4	-	2E-2 @ 1 wt%	[111]
Epoxy	MWCNT (CVD)	e	-	400	CH$_4$O	stirred	0.5	-	5E+0 @ 3 wt%	[116]
Epoxy	SWCNT (Arc), Aldrich	e	-	1000	-	manually mixed	0.6	-	1E-2 @ 14 wt%	[117]
Epoxy	MWCNT (CVD), Shenzhen Nanot.	e	-	100	C$_3$H$_6$O	stirred	0.6	2.9	5E-3 @ 10 wt%	[118]
Epoxy	MWCNT (CVD)	-	-	500	CH$_4$O	stirred, hot pressed	0.7	-	5E+0 @ 4 wt%	[19]
Epoxy	SWCNT (Arc), Carbon Solutions	e	HNO$_3$	-	C$_3$H$_6$O	sonicated, stirred	1	2.4	1E-1 @ 7.5 wt%	[107]
Epoxy	MWCNT (CVD)	e	-	80	CH$_4$O	stirred, filtrated	1.5	-	1E-3 @ 3 wt%	[116]
Epoxy	MWCNT (CVD), Sun Nanotech	-	-	-	-	sonicated, stirred	2	-	5E-5 @ 5.5 wt%	[119]
Epoxy	MWCNT (CVD)	-	HNO$_3$	20	C$_3$H$_6$O	sonicated, stirred	3.5	-	1E-5 @ 8 wt%	[120]
Epoxy	MWCNT (Arc), Aldrich	e	-	100	-	manually mixed	4	-	1E-3 @ 16 wt%	[117]
Epoxy	MWCNT (CVD)	-	-	20	C$_3$H$_6$O	sonicated, stirred	5	-	2E-5 @ 20 wt%	[121]
Epoxy	MWCNT (CVD)	-	HNO$_3$	20	C$_3$H$_6$O, Tergitol	sonicated, stirred	5	-	1E-5 @ 8 wt%	[120]
Epoxy	MWCNT (CVD), Arkema	e	-	-	-	calendered, vacuum stirred	< 0.5	-	3E-2 @ 2 wt%	[122]
P(BuA)-Latex	SWCNT (Arc)	e	PVA-functionalized	-	H$_2$O	sonicated	0.27	-	5E+0 @ 1 wt%	[123]
P(BuA)-Latex	MWCNT (CVD)	e	HNO$_3$	100	H$_2$O, SDBS	sonicated	0.36	1.7	1E+1 @ 6 wt%	[124]
P(BuA)-Latex	MWCNT (CVD)	e	HNO$_3$	100	H$_2$O, SDBS	sonicated, freeze dried, hot pressed	0.9	3.9	1E-1 @ 6 wt%	[124]
P(BuA)-Latex	MWCNT (CVD)	-	-	-	H$_2$O, SDS	sonicated, centrifuged, stirred	2.5	-	1E+1 @ 15 wt%	[35]
P3HT	MWCNT (CVD), Nanocyl	e	-	100	CHCl$_3$	sonicated, CH$_4$O (coagulation)	0.1	1.7	5E-1 @ 20 wt%	[125]
P3OT	SWCNT (Arc), CarboLex	e	HCl, centrifuged	100	CHCl$_3$	sonicated, spin coated	4	2.0	5E-2 @ 35 wt%	[126]
P3OT	SWCNT (Arc), CarboLex	e	-	100	CHCl$_3$	sonicated, spin coated	11	2.0	1E-3 @ 35 wt%	[126]
PA-6	MWCNT (CVD), Nanocyl	e	-	1000	H$_2$O, Na-AHA	sonicated, dried, extruded, hot pressed	2.5	-	3E-2 @ 4 wt%	[127]
PA-6	MWCNT (CVD), Hyperion Catal.	e	-	-	-	extruded	7	-	1E+1 @ 16 wt%	[58]
PANI	SWCNT (HiPco®), Carbon Nanot.	e	-	-	-	sonicated	0.3	2.1	3E+3 @ 15 wt%	[128]
PANI	SWCNT (HiPco®), Carbon Nanot.	e	-	-	C$_8$H$_{10}$	sonicated	0.3	2.1	3E+2 @ 20 wt%	[128]
PANI	SWCNT (Laser), Carbon Nanot.	e	-	-	C$_8$H$_{10}$	sonicated	0.3	2.1	3E+2 @ 20 wt%	[128]
PANI	MWCNT, Conyuan Biochem.	-	-	500	-	blended, compressed	4	-	1E+3 @ 80 wt%	[129]
PAT	MWCNT (CVD)	ne	HNO$_3$, CHCl$_3$	200	C$_6$H$_{12}$, CHCL$_3$	sonicated	12	2.6	5E+1 @ 35 wt%	[130]
PBT	SWCNT (HiPco®), Carbon Nanot.	e	oxidized	-	-	sonicated, extruded	0.2	-	1E-8 @ 0.2 wt%	[131]
PC	SWCNT (HiPco®), Carbon Nanot.	e	PEE-functionalized	-	CHCl$_3$	shaken, sonicated	0.1	2.8	5E+2 @ 7 wt%	[39]
PC	SWCNT (HiPco®), Carbon Nanot.	e	-	-	-	extruded	0.3	-	1E-1 @ 1 wt%	[132]

Matrix	Filler	State	Treatment	r	Solution	Dispersion	ϕ_C [wt%]	t	σ_{max} [S/m]	Ref.
PC	SWCNT (Arc)	e	-	-	C_6H_8O, $CHCl_3$, C_2H_6O	sonicated, filtrated, hot pressed	0.5	-	3E+1 @ 17 wt%	[133]
PC	SWCNT (HiPco®)	e	-	-	C_6H_8O, $CHCl_3$, C_2H_6O	sonicated, filtrated, hot pressed	0.5	-	1E+1 @ 1 wt%	[133]
PC	SWCNT (HiPco®)	e	-	-	-	extruded	0.5	-	1E-1 @ 2 wt%	[133]
PC	MWCNT (CVD), Nanocyl	e	-	100	-	extruded, hot pressed	0.5	-	3E+1 @ 5 wt%	[134]
PC	MWCNT (CVD), Tsinghua-Nafine (1st charge)	e	-	100	-	extruded, hot pressed	1	-	3E+1 @ 5 wt%	[134]
PC	MWCNT (CVD), Hyperion Catal.	e	-	1000	-	extruded	1	3.8	5E+0 @ 3 wt%	[135]
PC	MWCNT (CVD), Hyperion Catal.	e	-	100	-	extruded	1.44	2.1	2E+0 @ 5 wt%	[136]
PC	SWCNT (Arc)	e	-	-	-	extruded	1.9	-	1E-1 @ 10 wt%	[133]
PC	SWCNT (Arc)	e	-	-	$CHCl_3$	sonicated, extruded	1.9	-	1E-1 @ 4 wt%	[133]
PC	SWCNT (Arc)	e	-	-	-	extruded	2.5	-	1E-1 @ 7 wt%	[132]
PC	MWCNT (CVD)	e	HCl	1000	-	extruded	5	-	1E-4 @ 15 wt%	[137]
PC	MWCNT (CVD), Tsinghua-Nafine (2nd charge)	e	-	100	-	extruded, hot pressed	5	-	3E-7 @ 5 wt%	[134]
PC	MWCNT (CVD), Hyperion Catal.	e	-	100	-	extruded	1 - 2	-	1E+1 @ 15 wt%	[36]
PC	SWCNT (HiPco®), Carbon Nanot.	e	annealed, $SOCl_2$, centrifuged	-	-	extruded	-	-	1E-1 @ 1 wt%	[132]
PC	SWCNT (Arc)	e	annealed, $SOCl_2$, centrifuged	-	-	extruded	> 5	-	1E-1 @ 7 wt%	[132]
PCL	SWCNT (HiPco®), Carbon Nanot.	e	purified	-	C_7H_8, ADA	sonicated	0.09	1.5	1E-3 @ 3 wt%	[138]
PCL	MWCNT (CVD), Iljin Nanotech.	e	-	1000	-	sonicated, stirred	1.5	-	1E+1 @ 7 wt%	[139]
PCL	MWCNT (CVD), Iljin Nanotech.	e	HNO_3, filtrated	1000	-	sonicated, stirred	4	-	1E+0 @ 7 wt%	[139]
PE/UHMW	MWCNT (CVD)	ne	-	100	H_2O, SDS	sonicated, dry mixed, hot pressed	0.045	2.6	5E+1 @ 1 wt%	[140]
PE/UHMW	MWCNT (CVD)	-	NaOH, HCl	100	-	stirred, hot pressed	0.07	2.1	1E-2 @ 0.7 wt%	[141]
PE/UHMW	SWCNT (Arc), CarboLex	e	-	-	C_6H_8O	sonicated, dry mixed, hot pressed	0.09	2.3	5E-2 @ 2 wt%	[140]
PE/UHMW	MWCNT (CVD)	-	NaOH, HCl	100	-	stirred	0.14	1.8	1E-1 @ 0.7 wt%	[141]
PE/UHMW	MWCNT (CVD)	ne	-	100	C_6H_8O	sonicated, dry mixed, hot pressed	0.19	2.7	1E+2 @ 1 wt%	[140]
PE/UHMW	SWCNT (Arc), CarboLex	e	-	-	C_2H_6O	sonicated, dry mixed, hot pressed	0.25	2.2	5E-1 @ 3 wt%	[140]
PE/UHMW	MWCNT (CVD)	ne	-	5000	-	dry mixed, hot pressed	0.28	2.7	1E+1 @ 1 wt%	[140]
PE/UHMW	SWCNT (Arc, high-grade)	e	-	-	-	dry mixed, hot pressed	0.6	2.2	5E-2 @ 3 wt%	[140]
PE/UHMW	SWCNT (Arc, low-grade)	e	-	-	-	dry mixed, hot pressed	1.1	2.3	5E-1 @ 3 wt%	[140]
PE/UHMW	SWCNT (Arc), CarboLex	e	-	-	-	dry mixed, hot pressed	1.2	2.2	5E-3 @ 3 wt%	[140]
PE/UHMW	MWCNT (CVD), Hyperion Catal.	e	-	1000	$C_{10}H_{18}$	mixed, hot pressed	1.2	2.0	1E+2 @ 100 wt%	[142]
PE/LD	MWCNT (CVD)	e	HCl/HNO_3, centrifuged	1000	-	ball milled, hot pressed	2	-	3E+0 @ 10 wt%	[143]
PE/HD	SWCNT (HiPco®), Carbon Nanot.	e	purified	-	H_2O, SDS	sonicated, centrifuged, sprayed, extruded	4	-	5E-1 @ 6 wt%	[144]
PE/MD	MWCNT (CVD), Sun Nanotech	-	HCl	100	-	extruded	7.5	-	1E-2 @ 10 wt%	[31]

40

Matrix	Filler	State	Treatment	r	Solution	Dispersion	ϕ_C [wt%]	t	σ_{max} [S/m]	Ref.
PE/LD	MWCNT (CVD), Shenzhen Nanot.	e	-	100	C_8H_{10}	sonicated, melt mixed	15	-	5E-6 @ 30 wt%	[145]
PEO	MWCNT (CVD), Nano-Lab	-	-	1000	H_2O, GA	sonicated, stirred, electrospinned	0.45	1.3	-	[146]
PEO	MWCNT (CVD)	-	HNO_3	-	C_3H_8O	stirred	15 - 50	-	7E+2 @ 50 wt%	[147]
PET	SWCNT (Arc), CarboLex	e	-	1000	-	extruded, hot pressed	0.7	-	1E-4 @ 2 wt%	[148]
PET	MWCNT (CVD), Shenzhen Nanot.	e	HCl	1000	ODCB-C_6H_6O	sonicated	0.9	2.2	3E-2 @ 9 wt%	[64]
PFA	MWCNT (CVD), Showa Denko	-	anneal	30	-	sonicated, stirred, doctor blade	8	-	1E+1@ 15 wt%	[149]
PI	SWCNT (Laser), Rice Univ.	e	-	300	C_6H_8O	sonicated, stirred	0.05	1.5	1E-4 @ 1 wt%	[150]
PI	MWCNT (CVD), Hyperion Catal.	e	-	1000	C_4H_9NO	sonicated, stirred	0.3	1.6	1E+1 @ 7.4 wt%	[151]
PI	MWCNT (CVD), Sun Nanotech	-	H_2SO_4/HNO_3, centrifuged	100	C_4H_9NO	sonicated	9.5	-	2E-3 @ 12 wt%	[50]
PLA/HC	MWCNT, CNT Co. Ltd.	-	-	100	-	extruded	-	-	-	[152]
PLA/LC	MWCNT, CNT Co. Ltd.	-	$C_4H_2O_3$	100	-	extruded	0.3	-	-	[152]
PLA/LC	MWCNT, CNT Co. Ltd.	-	-	100	-	extruded	0.6	-	-	[152]
PMMA	MWCNT (CVD)	ne	-	-	$C_8H_{18}O_4$	stirred, spin coated	0.084	1.8	2E+2 @ 1 .5wt%	[153]
PMMA	MWCNT, NanoLab	-	-	1000	$C_2HF_3O_2$, C_4H_8O	sonicated	0.12	-	8E-1 @ 1.5 wt%	[154]
PMMA	SWCNT (HiPco®), Carbon Nanot.	e	$SOCl_2$	-	$CHCl_3$	stirred	0.17	2.2	1E+4 @ 10 wt%	[155]
PMMA	SWCNT (HiPco®), Carbon Nanot.	e	-	-	$CHCl_3$	stirred	0.17	1.3	2E+3 @ 10 wt%	[155]
PMMA	MWCNT (CVD), Iljin Nanotech.	e	-	-	C_7H_8	sonicated, stirred	0.2	2.3	1E+2 @ 10 wt%	[156]
PMMA	SWCNT (Arc)	e	-	-	C_7H_8	sonicated	0.33	2.1	5E+1 @ 8 wt%	[157]
PMMA	SWCNT (HiPco®), Rice Univ.	e	HCl, CH_4O, annealed	45	C_6H_8O	sonicated, H_2O (coagulation), hot pressed	0.37	-	5E-2 @ 2 wt%	[158]
PMMA	SWCNT (HiPco®), Rice Univ.	e	HCl	-	C_6H_8O	sonicated, H_2O (coagulation), hot pressed	0.39	2.3	1E-3 @ 2 wt%	[25]
PMMA	SWCNT (Arc)	e	HNO_3	1000	C_6H_8O	sonicated, wet-stretched, hot pressed	0.5	-	1E-1 @ 7 wt% (parallel)	[159]
PMMA	SWCNT (Arc)	e	HNO3	1000	C_6H_8O	sonicated, wet-stretched, hot pressed	0.5	-	1E-5 @ 7 wt% (perp.)	[159]
PMMA	MWCNT, Aldrich	-	C_6H_8O, $C_2HF_3O_2$, centrifuged	100	$C_2HF_3O_2$, C_4H_8O	sonicated	0.65	-	8E-2 @ 1.5 wt%	[154]
PMMA	SWCNT (HiPco®), Rice Univ.	e	HCl, CH_4O, annealed	-	C_6H_8O	sonicated, H_2O (coagulation), hot pressed	1.3	-	1E-2 @ 2 wt%	[24]
PMMA	MWCNT (CVD), Sun Nanotech	-	annealed, HCL	300	C_7H_8	sonicated	4	-	5E-3 @ 20 wt%	[160]
PMMA	MWCNT (CVD), Sun Nanotech	-	annealed, HCL	300	$CHCl_3$	sonicated	7	-	5E-4 @ 20 wt%	[160]
PMMA	MWCNT (CVD), Sun Nanotech	-	annealed, HCL	300	C_3H_6O	sonicated	10	-	1E-4 @ 20 wt%	[160]
PMMA	SWCNT (HiPco®), Aldrich	e	$SOCl_2$	-	$CHCl_3$	shaken, sonicated	< 0.1	-	5E+1 @ 0.5 wt%	[161]
PMMA-Latex	SWCNT (Arc), CarboLex	e	-	-	H_2O, SDS	sonicated, centrifuged, hot pressed	0.7	2.0	1E-1 @ 1.5 wt%	[78]
PmPV	MWCNT (Arc)	e	-	-	C_7H_8	sonicated	0.06	1.4	1E-5 @ 4 wt%	[162]
PmPV	MWCNT (Arc)	e	-	25	C_7H_8	sonicated	7.5	-	2E-3 @ 35 wt%	[161]
PmPV	MWCNT (Arc)	e	-	-	C_7H_8	sonicated, spin coated	8	-	3E+0 @ 36 wt%	[102]
PP	MWCNT (CVD)	ne	-	1000	-	extruded	0.07	-	-	[21]
PP	MWCNT (CVD)	-	-	-	-	sonicated, extruded	0.4	-	1E-1 @ 0.07 wt%	[163]

Matrix	Filler	State	Treatment	r	Solution	Dispersion	ϕ_C [wt%]	t	σ_{max} [S/m]	Ref.
PP	MWCNT, Nanostr. and Amorph. Mat. Inc.	-	-	-	-	extruded (high shear), hot pressed	0.44	-	2E+0 @ 9 wt%	[164]
PP	MWCNT (CVD), Iljin Nanotech.	e	H_2SO_4/HNO_3, filtrated	1000	-	extruded, hot pressed	1.5	-	2E-1 @ 5 wt%	[57]
PP	MWCNT (CVD)	-	HF, HCl	-	-	extruded, hot pressed	2	-	5E-1 @ 10 wt%	[165]
PP	MWCNT, Nanostr. and Amorph. Mat. Inc.	-	-	-	-	extruded (low shear), hot pressed	2.62	-	1E-4 @ 2.6 wt%	[164]
PPV	SWCNT (Laser)	e	-	-	-	sonicated	1.8	2.0	1E+3 @ 64 wt%	[47]
PS	SWCNT (HiPco®), Carbon Nanot.	e	PEE-functionalized	-	$CHCl_3$	shaken, sonicated	0.05	1.5	7E+0 @ 7 wt%	[39]
PS	MWCNT (CVD), Arkema	e	-	60	C_6H_8O	sonicated, stirred	0.16	-	-	[166]
PS	SWCNT (HiPco®), Carbon Nanot.	e	PmPV-functionalized	230	$CHCl_3$	stirred, sonicated, hot pressed	0.17	2.0	3E-5 @ 1.5 wt%	[167]
PS	SWCNT (CoMoCAT®), Southwest Nanotech.	e	PmPV-functionalized	222	$CHCl_3$	stirred, sonicated, hot pressed	0.17	4.1	7E-7 @ 1.5 wt%	[167]
PS	SWCNT (Arc), CarboLex	e	annealed	-	$C_6H_4Cl_2$	sonicated, stirred	0.27	2.0	1E-3 @ 1 wt%	[168]
PS	SWCNT (Laser), NASA	-	PmPV-functionalized	223	$CHCl_3$	stirred, sonicated, hot pressed	0.3	2.0	5E-8 @ 2 wt%	[167]
PS	SWCNT (HiPco®), Carbon Nanot.	e	HNO_3	122	C_3H_7NO	stirred, sonicated, hot pressed	0.4	2.9	1E-5 @ 6 wt%	[167]
PS	SWCNT (CoMoCAT®), Southwest Nanotech.	e	HNO_3	136	C_3H_7NO	stirred, sonicated, hot pressed	0.4	4.5	3E-7 @ 4 wt%	[167]
PS	SWCNT (Arc), CarboLex	e	-	-	$C_6H_4Cl_2$	sonicated, stirred	0.44	3.6	3E-6 @ 2 wt%	[168]
PS	MWCNT (CVD)	ne	-	1000	-	extruded	0.45	-	-	[21]
PS	SWCNT (Laser), NASA	-	HNO_3	148	C_3H_7NO	stirred, sonicated, hot pressed	0.5	4.8	2E-6 @ 6 wt%	[167]
PS	MWCNT (CVD), Iljin Nanotech.	e	HNO_3, HCl	-	-	sonicated	0.8	-	1E-2 @ 2 wt%	[169]
PS	BMWCNT (Arc)	e	C_3H_6O, filtrated	-	C_7H_8	sonicated, hot pressed	< 12	-	1E+4 @ 25 wt%	[170]
PS	MWCNT (Arc)	e	C_3H_6O, filtrated	-	C_7H_8	sonicated, hot pressed	< 12	-	3E+2 @ 25 wt%	[170]
PS-Latex	SWCNT (Arc), CarboLex	e	-	-	H_2O, SDS	sonicated, centrifuged, hot pressed	0.28	1.6	1E+0 @ 1.5 wt%	[78]
PS-Latex	SWCNT (Arc), CarboLex	e	-	1000	H_2O, SDS	sonicated, centrifuged, hot pressed	1.5	4.9	5E-3 @ 5 wt%	[171]
PS-Latex	MWCNT (CVD), Nanocyl	e	-	-	H_2O, SDS	sonicated, centrifuged, hot pressed	1.5	-	1E+0 @ 5 wt%	[172]
PS-Latex	SWCNT (Arc), CarboLex	e	-	-	H_2O, GA	sonicated, centrifuged, hot pressed	-	-	1E-6 @ 3 wt%	[78]
PU	MWCNT (CVD), Iljin Nanotech.	e	oxidized	1000	MEK, BKC	sonicated, stirred, calendered	0.018	1.5	8E+0 @ 8 wt%	[173]
PU	MWCNT (CVD), Iljin Nanotech.	e	2 h HNO_3, filtrated	1000	MEK, BKC	sonicated, stirred, calendered	0.54	1.3	1E-2 @ 5 wt%	[174]
PU	MWCNT (CVD), Iljin Nanotech.	e	2 h H_2SO_4/HNO_3, filtrated	1000	MEK, BKC	sonicated, stirred, calendered	0.58	1.1	1E-1 @ 5 wt%	[174]
PU	MWCNT (CVD), Iljin Nanotech.	e	3 h H_2SO_4/HNO_3, filtrated	1000	MEK, BKC	sonicated, stirred, calendered	0.63	1.3	2E-2 @ 5 wt%	[174]
PU	MWCNT (CVD), Iljin Nanotech.	e	1 h H_2SO_4/HNO_3, filtrated	1000	MEK, BKC	sonicated, stirred, calendered	0.69	1.0	5E-3 @ 5 wt%	[174]
PU	MWCNT (CVD), Iljin Nanotech.	e	4 h H_2SO_4/HNO_3, filtrated	1000	MEK, BKC	sonicated, stirred, calendered	0.7	1.0	2E-3 @ 5 wt%	[174]
PU	MWCNT (CVD), Iljin Nanotech.	e	4 h HNO_3, filtrated	1000	MEK, BKC	sonicated, stirred, calendered	0.7	1.0	9E-4 @ 5 wt%	[174]
PU	MWCNT (CVD), Iljin Nanotech.	e	3 h HNO_3, filtrated	1000	MEK, BKC	sonicated, stirred, calendered	0.77	1.0	5E-4 @ 5 wt%	[174]

Matrix	Filler	State	Treatment	r	Solution	Dispersion	ϕ_C [wt%]	t	σ_{max} [S/m]	Ref.
PU	MWCNT, Applied Science	-	-	100	C_4H_8O	stirred	1	3.1	2E+3 @ 15 wt%	[45]
PU	MWCNT (CVD), Iljin Nanotech.	e	1 h HNO_3, filtrated	1000	MEK, BKC	sonicated, stirred, calendered	1.04	1.1	5E-4 @ 5 wt%	[174]
PVA	MWCNT, Ahwahnee Techn. Inc.	ne	H_2SO_4/HNO_3, filtrated	-	C_6H_8O	sonicated, stirred, electrospinned	0.2	-	1E+1 @ 5 wt%	[175]
PVA	MWCNT (CVD), Hyperion Catal.	e	H_2SO_4/HNO_3, filtrated	-	H_2O	stirred	< 10	-	1E+2 @ 60 wt%	[176]
PVA-Latex	SWCNT (HiPco®), Carbon Nanot.	e	-	-	H_2O, GA	sonicated, stirred, filtrated	0.038	1.9	2E+1 @ 4 wt%	[59]
PVC	MWCNT (CVD), TMSpetsmash	-	-	1000	-	stirred, grinded, hot pressed	0.094	3.3	1E-2 @ 1.4 wt%	[177]
PVDF	SWCNT, Carbon Nanotech.	-	H_2SO_4	1000	C_6H_8O	spin coated	0.02	-	3E-4 @ 0.05 wt%	[178]
PVDF	MWCNT (CVD), Aldrich	-	-	-	-	extruded (high shear), hot pressed	1.5	-	5E+0 @ 4 wt%	[179]
PVDF	MWCNT (CVD), Aldrich	-	-	-	-	extruded (low shear), hot pressed	2.5	-	5E+0 @ 4 wt%	[179]
PVDF	MWCNT	-	-	-	C_6H_8O	sonicated, hot pressed	3.2	0.9	2E-4 @ 4 wt%	[180]
PVDF	MWCNT, Chengdu Organic Chem	-	H_2SO_4/HNO_3	1000	C_2H_6O	sonicated, cold pressed, heated	7.6	3.2	6E-2 @ 20 wt%	[181]
S-I-Latex	SWCNT (CoMoCAT®), Southwest Nanotech.	e	HF, filtrated	2000	H_2O, AIBN, C_5H_8, SDBS, $C_{16}H_{34}$	sonicated, stirred (miniemulsion)	0.2	7.3	1E-4 @ 3 wt%	[182]
S-I-Latex	SWCNT (CoMoCAT®), Southwest Nanotech.	e	HF, filtrated	2000	H_2O, AIBN, C_5H_8, SDBS	sonicated, stirred (macroemulsion)	0.2	7.6	5E-5 @ 3 wt%	[182]
SPPA	MWCNT	-	-	-	-	sonicated	3.5	-	2E-1 @ 20 wt%	[183]
UPR	MWCNT (CVD)	-	annealed	-	-	sonicated, magnetic field	< 1	-	1E-1 @ 1 wt% (parallel)	[184]
UPR	MWCNT (CVD)	-	annealed	-	-	sonicated, magnetic field	< 1	-	5E-3 @ 1 wt% (perpendicular)	[184]
VE	MWCNT (CVD)	-	NaOH, HCl, K_2MnO_4	-	-	sonicated, stirred	< 0.5	-	4E-2 @ 2 wt%	[185]
VMQ	MWCNT	-	APTS-functionalized	500	-	hot pressed	2.4	2.9	4E-4 @ 5 wt%	[186]

Inspection of Table 4-1 clearly shows a large spread in the number of investigations for different polymer matrices. For 16 polymers listed in the table a single publication was available while 26 papers referring to an epoxy matrix could be included. This imbalance has to be taken into account when evaluating Table 4-1 with respect to percolation thresholds ϕ_C. This fact is visualized in Figure 4-1, which shows the minimum observed ϕ_C together with the number of publications for each polymer matrix. We notice that for all $\phi_C > 0.3\,$wt% no more than two papers could be exploited. This finding supports the idea that with optimized dispersion methods a threshold $\phi_C \approx 0.1\,$wt% might be obtainable for nearly any CNT/polymer system. For a statistical distribution of filler particles, the excluded volume concept [187,188] gives $\phi_C^{vol} \approx (2r)^{-1}$ or $\phi_C^{wt} \approx r^{-1}$ in the limit of large aspect ratios (Section 4.1.3). A typical aspect ratio $r \approx 1,000$ for CNT reproduces the above mentioned value of 0.1 wt%. This value thus could be related to the statistical percolation threshold (Section 4.3). As long as not extremely high aspect ratios are involved ($r \gg 1,000$, see Sections 4.6 and 4.7), thresholds significantly lower than $\phi_C \approx 0.1$ wt% can be attributed to kinetic percolation (Section 4.3). In kinetic percolation, the particles are free to move and thereby can form a conducting network at much lower particle concentrations. Particle movement can be caused by diffusion, convection, shearing, or external fields.
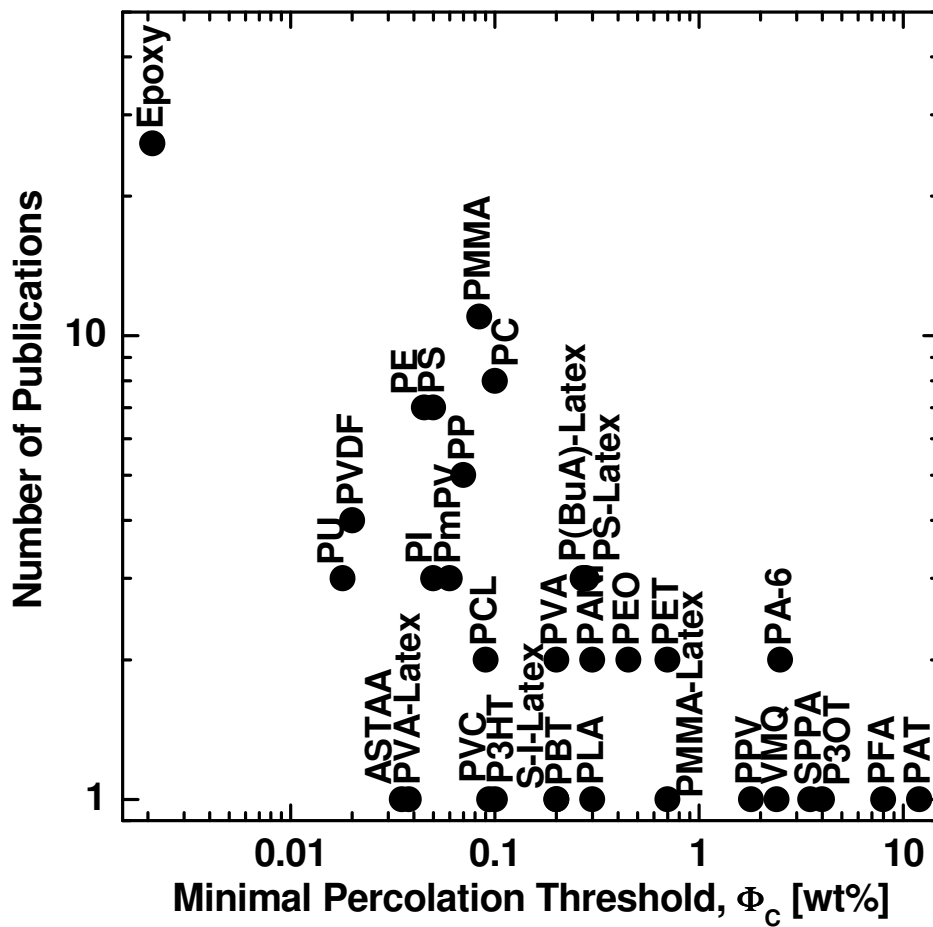
Figure 4-1 Plot of the total number of publications per polymer system versus the minimum percolation threshold achieved with the respective system.

Contradicting results have been published concerning the dependence of the percolation threshold on the aspect ratio. According to the excluded volume analysis of Celzard et al. [187] the threshold of a fibre suspension should decrease with increasing aspect ratio. The results presented in Section 4.6 and [116] indeed yield a decreasing percolation threshold with increasing CNT length while Martin et al. [17] find an increasing threshold with increasing CNT length. This inconsistency may be solved by considering the type of the respective percolation thresholds. Bai et al. [116] most likely obtained statistical thresholds while Martin et al. definitely achieved kinetic percolation. Since all theoretical analyses so far ignore the movement of filler particles, they can only predict the dependence of the statistical percolation threshold on the filler

aspect ratio. However, it is shown in Section 4.6 that the aspect ratio is dominating over the shear influence even for the kinetic percolation threshold–which still contradicts the findings in [17].

The effect of CNT alignment on percolation conductivity in SWCNT/PMMA composites has been investigated by Du et al. [158]. The SWCNT were aligned by melt fibre spinning, various levels of alignment could be obtained by controlling the extensional flow in the spinning process. As a function of alignment the conductivity exhibits power-law behaviour. Highest conductivities occur for slightly aligned, rather than isotropic CNT. A theoretical investigation of the effects of CNT alignment on percolation resistivity using Monte Carlo simulations was recently published by Behnam et al. [189]. He concluded that minimum resistivity occurs for a partially aligned rather than a perfectly aligned CNT film.

4.1.2 Maximum conductivity

Maximum conductivities of 10,000 S/m have been reported for PMMA containing 10 wt% $SOCl_2$ treated SWCNT [155], of 3,000 S/m for PANI filled with 15 wt% SWCNT [128], and of 2,000 S/m for PU with 15 wt% MWCNT [45].[4] The percolation thresholds found for the above mentioned systems, i.e., 0.17 wt%, 0.3 wt%, and 1 wt%, respectively, suggest a correlation between threshold and maximum conductivity. Indeed, this finding seems to be true especially for composites based on the same matrix system, as shown in Figure 4-2. The data for each matrix had to be subdivided into sets of similar maximum CNT concentrations, as the maximum concentrations and thus the maximum conductivities evaluated in the publications vary considerably even for similar percolation thresholds. Within each data set, an indirect proportionality between the maximum conductivities and the percolation thresholds can be identified.

---

[4] Even higher conductivities can be found in publications that do not analyse the electrical percolation threshold or that report on conductive polymer matrices like protonated PANI. These publications are not considered in our review.
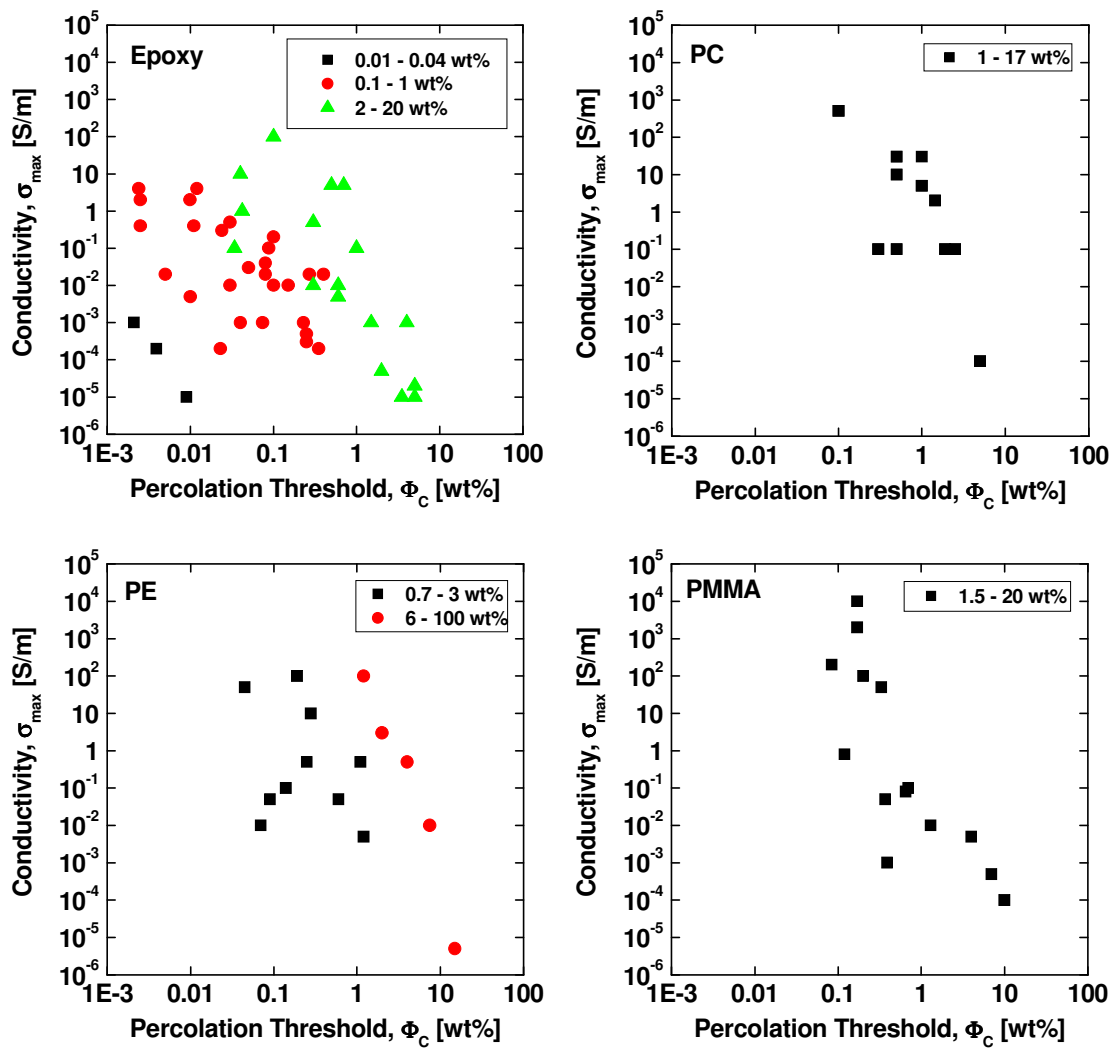
46

Figure 4-2 Maximum conductivities versus percolation thresholds for various matrices, subdivided into data sets of similar maximum CNT concentrations.

In Figure 4-3 the maximum conductivities of all reviewed data are plotted versus their respective filler concentration values. It is pointed out that the maximum conductivities of Figure 4-3 refer to the maximum values reported in a given publication. In general, these values are significantly lower than conductivities obtained at the maximum attainable concentrations with a respective polymer and processing method.
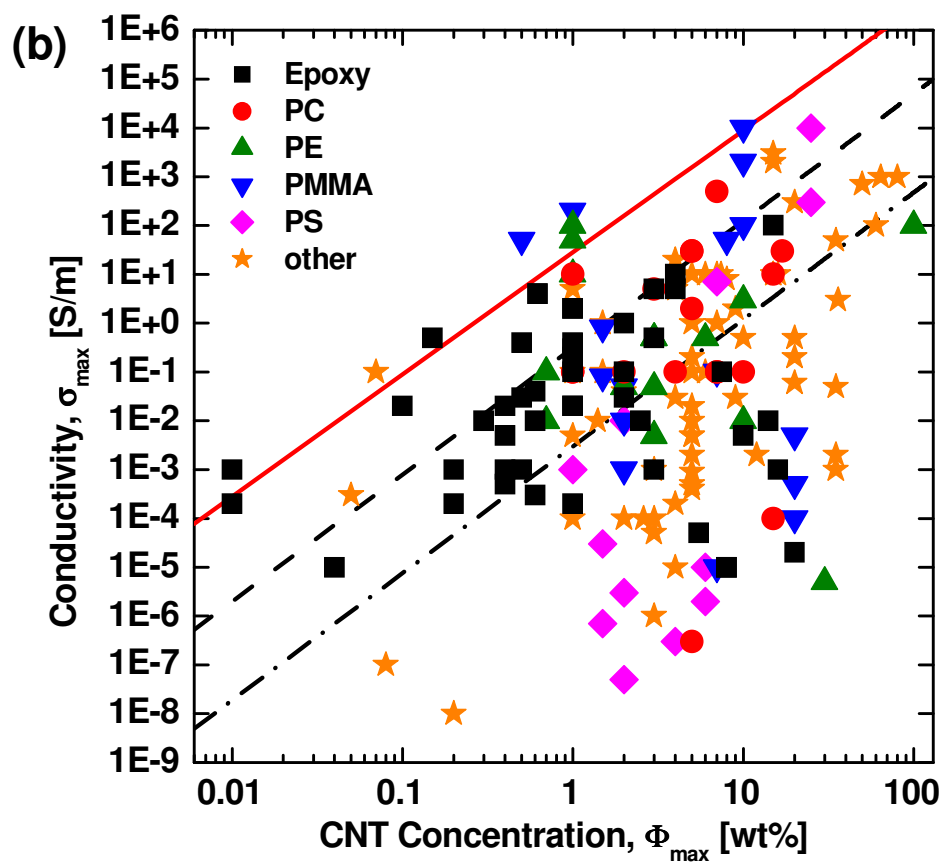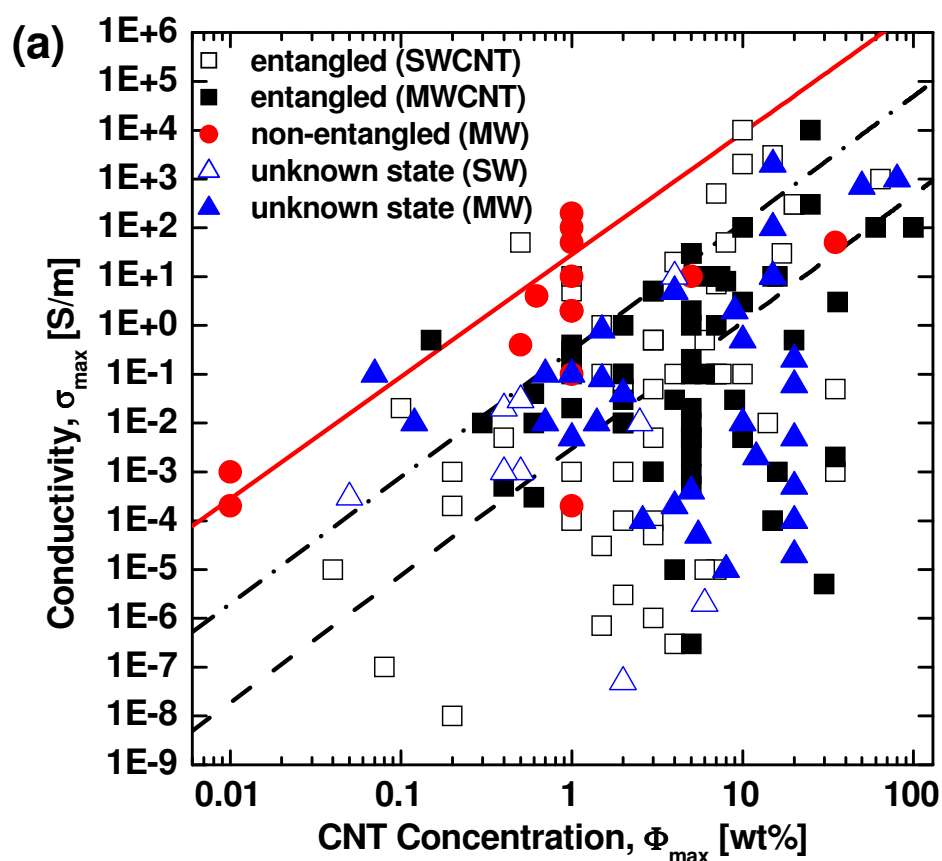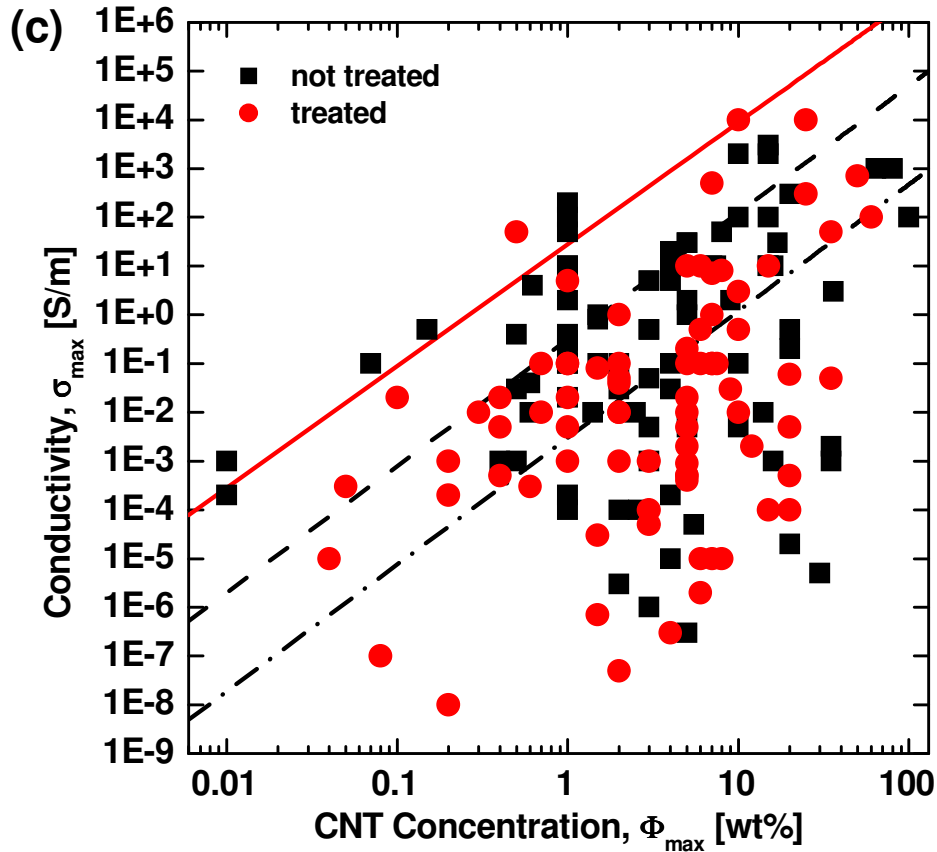
Figure 4-3 Comparative log-log plot of maximum conductivity versus respective CNT concentration for all the data in Table 4-1, differentiated by (a) CNT type, (b) matrix type and (c) CNT treatment. The dash-dotted line denotes the dependence $\sigma = 5 \cdot 10^4 \phi^{2.6}$ S/m found for the Nanocyl CNT composites (Section 4.6) while the solid line indicates a similar dependence $\sigma = 3 \cdot 10^6 \phi^{2.5}$ S/m found for CCVD-aligned-grown CNT composites (Section 4.6). All data below the dashed line ($\sigma = 500 \phi^{2.6}$ S/m for low conductive CNT) are most likely dominated by tunnelling between the CNT.

The data points spread over a wide conductivity and concentration range, but mainly stay below the dash-dotted line. There are some exceptions, most of them at concentrations above 10 wt%, where a homogeneous suspension probably is not reached. The dash-dotted line denotes the dependence $\sigma = 5 \cdot 10^4 \phi^{2.6}$ S/m found for the Nanocyl CNT composites (Section 3.6) above

the statistical threshold. This line seems to represent the maximum achievable conductivities for entangled MWCNT, which are widespread in composite research as their production is fast and cheap. CCVD-aligned-grown CNT composites (Section 3.6) show similar power law dependencies above the statistical percolation threshold, the conductivities however are shifted upwards by a factor of 60 (solid line). These findings along with the results of other groups on various matrix systems (see Table 4-1) suggest that non-entangled MWCNT give much higher composite conductivities than entangled ones. This difference can be explained in two alternative ways. Either the entangled MWCNT could not be dispersed homogeneously and therefore their intrinsic conductivity σ_0 cannot be extracted from a formula of the type $\sigma \approx \sigma_0 \phi^t$, or the intrinsic conductivities of entangled and non-entangled MWCNT truly differ by a factor of 60 (possibly because the straight growing non-entangled MWCNT are less defective).

Taking 500 S/m as a lower conductivity limit for highly defective MWCNT we still find many reported data below the dashed line ($\sigma = 500 \phi^{2.6}$ S/m). In these cases, tunnelling through polymer barriers between CNT most probably takes place. According to Connor et al. [190] tunnelling between CNT separated by a thin isolating layer should lead to a dependence of the form $\ln \sigma \sim -\phi^{-1/3}$ between DC conductivity and filler load. A number of investigations seem to confirm this relation. However, as discussed in Section 4.4, an unambiguous determination of the exponent is not possible. The mechanism of charge transport in CNT/polymer composites has also been addressed by temperature dependent conductivity measurements. Kim et al. [156] have fitted their experimental results to different theoretical dependencies derived by Mott [191] and by Sheng et al. [192] based on variable range hopping in the former case and fluctuation induced tunnelling in the latter. Again, a definite conclusion seems difficult.

A comparison of the shift (from one line to another) attributed to different intrinsic CNT conductivities with the conductivity scattering below the dashed line suggests that polymer tunnelling barriers have a dominant effect on the overall composite conductivity. Definite conclusions on how to avoid this polymer sheathing [193] and maximize conductivity cannot be drawn from the analysed data. The best dispersions not necessarily seem to lead to the highest conductivities as good dispersions usually imply the formation of a polymer layer around each CNT (Section 4.5). It seems that solvent processing techniques [153] or shear induced re-aggregation (Section 4.3) sometimes improve the electrical performance of composites by preventing an overall sheathing or reducing the sheath thickness, respectively. However, nanotube type (SWCNT or MWCNT), treatment (purification, oxidation) and matrix type generally do not show a clear impact on the maximum conductivity (Figure 4-3).

4.1.3 Percolation theory

Percolation is described by many theories using different approaches. Some of them take into account the dependence of the percolation threshold on the filler shape [194], size [195] or aspect ratio [187], based upon an excluded volume approach [188] of infinitely thin particles. Another approach considers the dependency on the orientation of finitely thick sticks [196]. These statistical theories generally assume a random filler particle distribution and are static theories because they do not include the possibility of particle movement through the matrix. They predict thresholds that are orders of magnitude higher than found in many experiments [16,17,32]. All these experiments have in common that they were performed on systems where the matrix possesses a fluid state of low viscosity (< 1 Pas) during processing. In this state, particle manipulation is possible via shear forces [17,32] and electric fields [18] which promote the formation of a network at filler contents as low as 0.002 wt% [17]. Such low percolation thresholds are no longer statistic but dynamic and have to be described by dynamic colloid theory [197].

The concept of excluded volume has proven to be a powerful method to estimate the percolation threshold of composites containing statistically dispersed non-spherical particles. The concept is based on the idea that the threshold is not linked to the true volume of the filler particles but rather to their excluded volume V_{ex}. The excluded volume is defined as the volume around an object in which the centre of another similarly shaped object is not allowed to penetrate [198]. $<V_{ex}>$ represents the excluded volume of an object averaged over the orientational distribution characterizing the system objects. For randomly oriented cylinders with volume $V = d^2 \ell \pi / 4$ and high aspect ratio $r = \ell / d$, Celzard et al. [187] and Balberg et al. [188] estimate $<V_{ex}> \approx d\ell^2 \pi / 2$, leading to

$$\phi_C^{vol} \sim V / <V_{ex}> \approx d /(2\ell) = 0.5 / r \qquad \textbf{Eq. 4-1}$$

Saar et al. [194] use the excluded volume approach to derive for prolate ellipsoids and prisms of aspect ratio $r > 50$ the dependence

$$\phi_C^{vol} \approx 0.6 / r \qquad \textbf{Eq. 4-2}$$

Foygel et al. [199] and Néda et al. [200] performed Monte Carlo simulations for cylinders yielding the same dependence in the limit of high aspect ratios. Néda et al. claim that Celzard et al. [187] and Balberg et al. [188] erroneously calculated the average of $\sin\gamma$ (γ being the angle between two randomly positioned cylinders) to be $\pi / 4$ while it should be $2 / \pi$ instead. This would yield $<V_{ex}> \approx 4d\ell^2 / \pi$ and $\phi_C^{vol} \approx 0.6 / r$.

From electron microscopy investigations it became evident that CNT embedded in a polymer matrix generally are curved or wavy rather than straight [201]. The effect of waviness on percolation has been addressed by a couple of authors

using different theoretical approaches [112,202-204]. They all come to the conclusion that the percolation threshold increases with increasing waviness of the CNT. However, in all calculations the increase in ϕ_C remains well below a factor of 2 which means that the effect of waviness can be considered small in the context of Table 4-1.

Frequently, CNT are dispersed in form of bundles. The effect of bundles on percolation has been calculated by Grujicic et al. [205]. As expected, the percolation threshold increases with increasing bundle radius.

Statistical percolation theory predicts conductivity σ to scale as $\sigma = \sigma_0 \left(\phi - \phi_C \right)^t$ with filler concentration ϕ. Usually, experimental results are fitted by plotting $\log \sigma$ vs. $\log \left(\phi - \phi_C \right)$ and incrementally varying ϕ_C until the best linear fit is obtained [162]. The critical exponent t is expected to depend on the system dimensionality with calculated values of $t \approx 1.33$ in two and $t \approx 2$ in three dimensions [100,101]. A value of $t \approx 3$ has been obtained for a Bethe lattice and within mean field theory whereas a value of $t \approx 2.5$ has been derived within a continuum model, the "Swiss cheese model" [100], which simulates distributed bond strengths or contact resistances. Similar results have been achieved by Balberg [206] allowing a non-random distribution of voids in random void models of continuum percolation. Recently, Balberg et al. [207] pointed out that the effective medium approach (EMA) yield for a three-dimensional particle distribution local exponents of t which vary, depending on their position $\phi - \phi_C$, between 2 and the order of 10.

As shown in Figure 4-4, fits to experimental data for CNT/polymer composites yield values of t predominantly in the range from 1 to 3 peaking around $t = 1.8$. The above mentioned theories relate increasing values of t to increasing tunnelling barriers between the fillers which would lead to low maximum composite conductivities. As visible in Figure 4-4a, such a dependency is not found in the evaluated publications. Experiments presented in Sections 4.3 and

4.8 carried out with the same system suggest a change in t from low values (~ 1.7) in the case of low (kinetic) percolation thresholds to high values (~ 2.5) in the case of higher (statistical) ones. However, Figure 4-4b does not reflect such a relation between the percolation threshold and the magnitude of t.
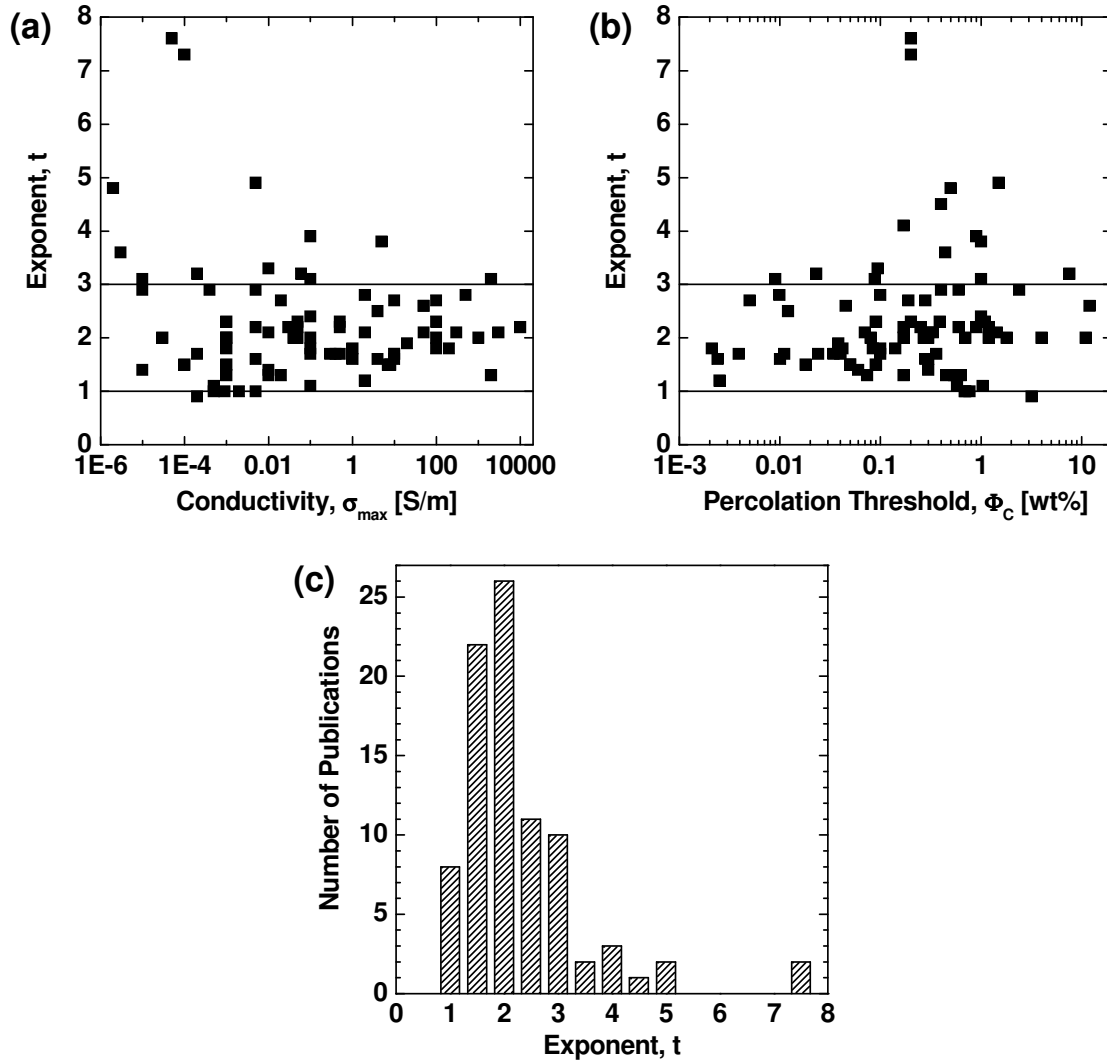

Figure 4-4 Plot of the power law exponent t as a function of (a) the maximum conductivity and (b) the percolation threshold for all data in Table 4-1. The horizontal lines denote $t = 1$ and 3. (c) A histogram of t values.

It seems rather complicated to extract geometrical information about the CNT network from experimentally determined values of t. Such a procedure generally seems to be not justified. First of all, scaling is limited to a

concentration range very close to the percolation threshold. However, this range of validity has not been examined in detail for CNT/polymer composites. In addition, the results of statistical percolation theory are derived for ideal systems which contain a homogeneous dispersion of identical particles. Due to the spread in CNT properties, i.e., length, diameter, chirality, entanglement and waviness, CNT/polymer composites are far away from being ideal systems. A further complication arises from the fact that low thresholds are likely to be kinetically produced, which makes the application of statistical percolation theory questionable.

Modelling of kinetic percolation requires complex and time-consuming calculations. Rahatekar et al. [208] applied dissipative particle dynamics (DPD) to investigate the dynamic behaviour of an assembly of oriented fibres suspended in a viscous medium. After establishing the structural arrangement the fibre network impedance was assessed using Monte Carlo simulations. Wescott et al. [209] used DPD simulations to investigate methods of controlling the assembly of percolating networks of CNT in thin films of block copolymer melts. For suitably chosen parameters the CNT were found to self-assemble. Finally, Tozzi et al. [210] employed particle-level simulations [211] to investigate the time evolution of the microstructure and the electrical conductivity of CNT suspensions in shear flow. The simulations allow control of numerous properties, including the matrix viscosity, CNT aspect ratio, shape, flexibility, and interaction forces. All these approaches are important steps towards a better understanding of kinetic percolation.

4.1.4 Summary and conclusion

181 experimental results on electrical percolation of CNT in polymer composites published in 109 articles were reviewed. The following conclusions can be drawn from these data:
- o Regarding minimum percolation thresholds and maximum conductivities, no decisive influences of type and production method of CNT, type of polymer and dispersion method could be identified.

- An indirect proportionality seems to exist between the percolation threshold and the maximum conductivity attained for given CNT concentrations and polymer matrices.
- Non-entangled MWCNT give conductivities 60 times higher than the usual entangled MWCNT from industrial mass production. Conductivity values below $\sigma = 500\phi^{2.6}$ S/m are indicative of polymer tunnelling barriers between CNT.
- Many polymer composites seem to reproduce the theoretically predicted dependence of the percolation threshold on the aspect ratio $\phi_C^{wt} \approx r^{-1}$, provided that their filler particles are homogeneously distributed (statistical percolation).
- Deviating results with higher ϕ_C suggest that the filler particles were not dispersed homogeneously, while lower ϕ_C indicates the flocculation of homogeneously dispersed particles (kinetic percolation).
- Regarding the contradiction between the experimental results from Martin et al. [17] and the above mentioned theoretical prediction, it is concluded that kinetic percolation cannot be described with statistical percolation theory. However, results that will be presented in Section 4.6 indicate that the aspect ratio is dominating over the shear influence even for the kinetic percolation threshold.
- The magnitude of the percolation theory scaling law exponent t could not be related to any other parameter extracted from the articles. It is believed that no reliable geometrical information about the CNT network can be extracted from most of the experimentally determined values of t.

4.2 Experimental procedure

4.2.1 Composite processing

4.2.1.1 Nanocyl CNT composites

Samples of varying Nanocyl CNT concentrations (0.008-1 wt%) in LY556/ XB3473 epoxy were produced in the following way. A master batch of epoxy resin containing a high CNT concentration was prepared with a dissolver disk rotating at 2,000 rpm for 2 h at room temperature. Approximately 30 g of this dispersion was poured into a small cup. The appropriate amount of hardener (mixing ratio of 23:100 parts by weight of hardener:resin) was added and the suspension was subsequently processed in three different ways. The filler concentration in the remaining master batch was then lowered adding pure resin and again stirred for 30 min at 2,000 rpm. A suspension of 30 g was again extracted, and the procedure described above was repeated several times. The first sample set was stirred at 500 rpm for 10 min at 80 °C, then poured into aluminium moulds and further stirred at 50 rpm for 5 min at 80 °C (in the following referred to as the slow stir sample set). The second set of samples was only stirred at 500 rpm for 10 min at 80 °C and afterwards left untouched in the aluminium moulds for 5 more min (medium stir samples). The third sample set was stirred at 2,000 rpm for 15 min at room temperature (fast stir samples) and then poured into aluminium moulds. Brass electrodes (17 mm width, clamped in 1.8 mm distance and dipped 10 mm deep into each portion) were additionally dipped into the suspension to monitor the conductivity while curing proceeded. All samples were cured in an oven at 120 °C.

After curing, two specimens ($8\times18\times4$ mm^3) were cut out from each slow and medium stirred sample. The 8×18 mm^2 sides were polished, coated with conductive silver paint and contacted for conductivity measurements. The embedded brass electrodes were used as contacts for the fast stir samples. For optical analysis slices were cut out from all three sample sets and polished down to a thickness of only 0.5 mm.

4.2.1.2 ACVD-aligned-grown CNT composites

Samples of varying ACVD-aligned-grown CNT concentrations (0.006-1 wt%) in LY556/XB3473 epoxy were produced via the master batch process. This involves dispersing the highest possible concentration of CNT into the epoxy resin with a dissolver disk rotating at 2,000 rpm for 2 h at room temperature. The resulting suspension was poured into two bottles. The suspension of the second bottle was then processed with a three roll calender [95,96]. These samples were labelled as "calender". Approximately 7 g of each suspension was poured into a vial and the appropriate amount of hardener was added (23:100 parts by weight of hardener:resin). Each suspension with hardener was stirred for 5 min, centrifuged at 3,500 rpm for 1 min (to remove air bubbles) and then poured into four cavities (15 mm diameter, 5 mm depth) located within a PTFE block. This block ensured a homogeneous heat-up process in order to avoid any convection, which would cause shearing and thus uncontrolled CNT re-agglomeration. Unintended shearing during sample preparation (stirring of hardener, pouring, etc.) however did not promote re-agglomeration below a suspension temperature of 50°C. The block was heated to 100°C, and then the suspensions of two cavities were manually sheared for 5 min at 60 rpm (the conductivity results were later averaged and referred to as the slow stir samples). The suspensions in the other two cavities were left untouched; therefore they are referred to as the no-stir samples (again with averaged conductivities). Finally the samples were cured in an oven at 120°C. The filler concentration in the initial bottles was then lowered adding pure resin and the resulting suspension was stirred again for 30 min at 2,000 rpm. Then the process described above was repeated several times.

After curing, the samples were removed from the cavities, polished and contacted for conductivity measurements by coating with conductive silver paint and contacted for conductivity measurements. For optical analyses the samples were later polished down to a thickness of 0.2 mm.

4.2.1.3 CCVD-aligned-grown CNT composites

Samples of various CCVD-aligned-grown CNT concentrations (0.001-0.6 wt%) in LY556/XB3473 epoxy were produced and analysed in the same way described for the ACVD-aligned-grown CNT in Section 4.2.1.2, however without calendering half of the suspension and by averaging three samples instead of two.

4.2.2 Conductivity measurement

Electrical measurements were performed in AC mode using a HP 4284A LCR meter at room temperature with a voltage amplitude of 1.4 V over a frequency range from 20 Hz to 1 MHz. The AC conductivity $\sigma(\omega)$ and the relative static permittivity ε_r of the sample were recorded by a LabVIEW-based data acquisition software. They were calculated from the complex admittance $Y^*(\omega)$ by modelling the sample (with electrode area A and distance s) as a parallel circuit of resistance R and capacitance C

$$Y^*(\omega) = Y'(\omega) + iY''(\omega) = \frac{1}{R} + i\omega C = \sigma(\omega)\frac{A}{s} + i\omega\varepsilon_0\varepsilon_r\frac{A}{s} \qquad \textbf{Eq. 4-3}$$

The AC conductivity $\sigma(\omega)$ usually was constant up to at least 1 kHz, thus, the value at 100 Hz was considered to be equivalent to the DC conductivity σ. The calibration of the LCR meter was regularly checked with a standard resistance (100 Ω).

4.2.3 Electric field alignment

Electric fields were utilized to align CNT suspended in a liquid epoxy. The setup consisted of two electrodes separated by an insulating space holder at one end while the other end was dipped into the CNT/epoxy suspension. The electrodes were connected to a self-built AC voltage amplifier delivering voltages up to 700 V_{p-p}, thus 250 V_{rms} at frequencies between 10 Hz and 1 kHz.

4.3 Kinetic and statistical percolation thresholds

The conductivity values of the Nanocyl CNT composites (see Section 4.2.1.1 for the processing conditions) are summarized in a log-log plot in Figure 4-5. The values for the lowest concentrations are limited by the measurement range of the LCR meter ($\sim 3 \cdot 10^{-9}$ S/m). A scaling law of the form $\sigma = \sigma_0 (\phi - \phi_C)^t$ is fitted to the results by plotting $\log \sigma$ vs. $\log (\phi - \phi_C)$ and incrementally varying ϕ_C until the best linear fit is obtained (Figure 4-6) [162].
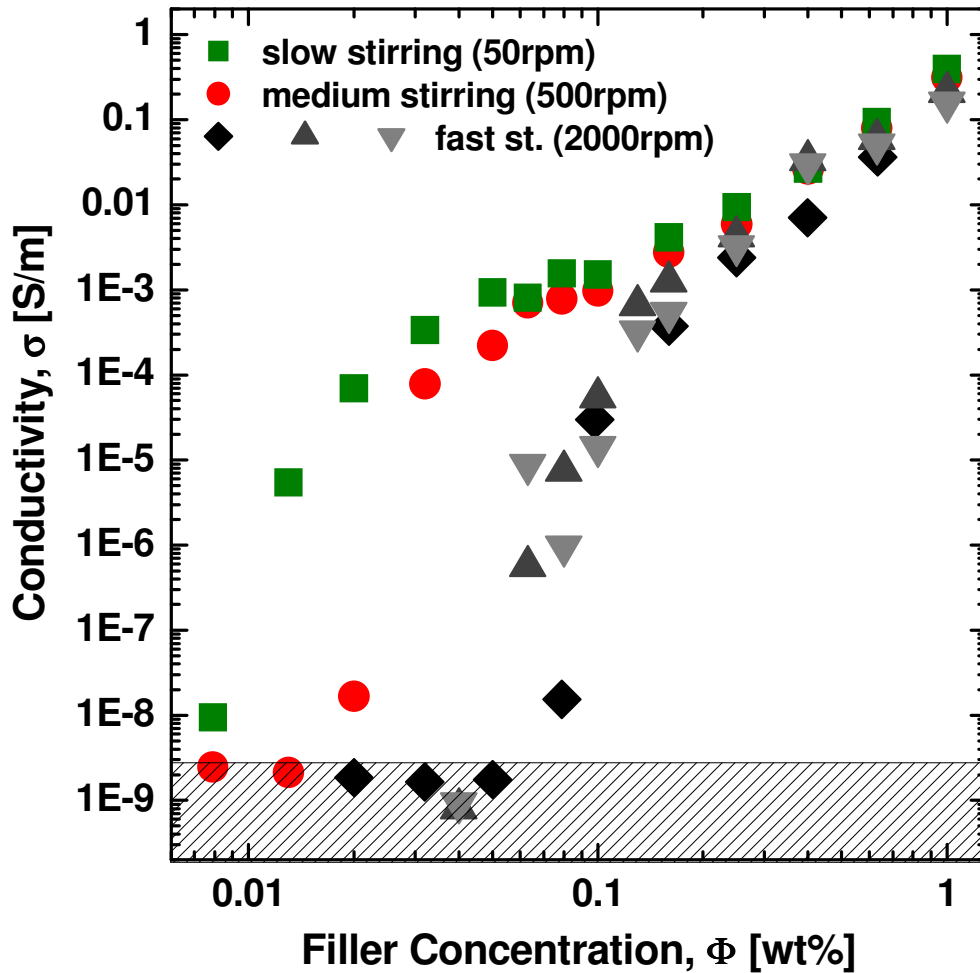
Figure 4-5 Comparative log-log plot of the Nanocyl CNT/LY556/XB3473 composite conductivity as a function of the CNT weight fraction for the three different sample preparation methods: slow (50 rpm), medium (500 rpm), and fast (2,000 rpm) stirring of the dispersion prior to curing.
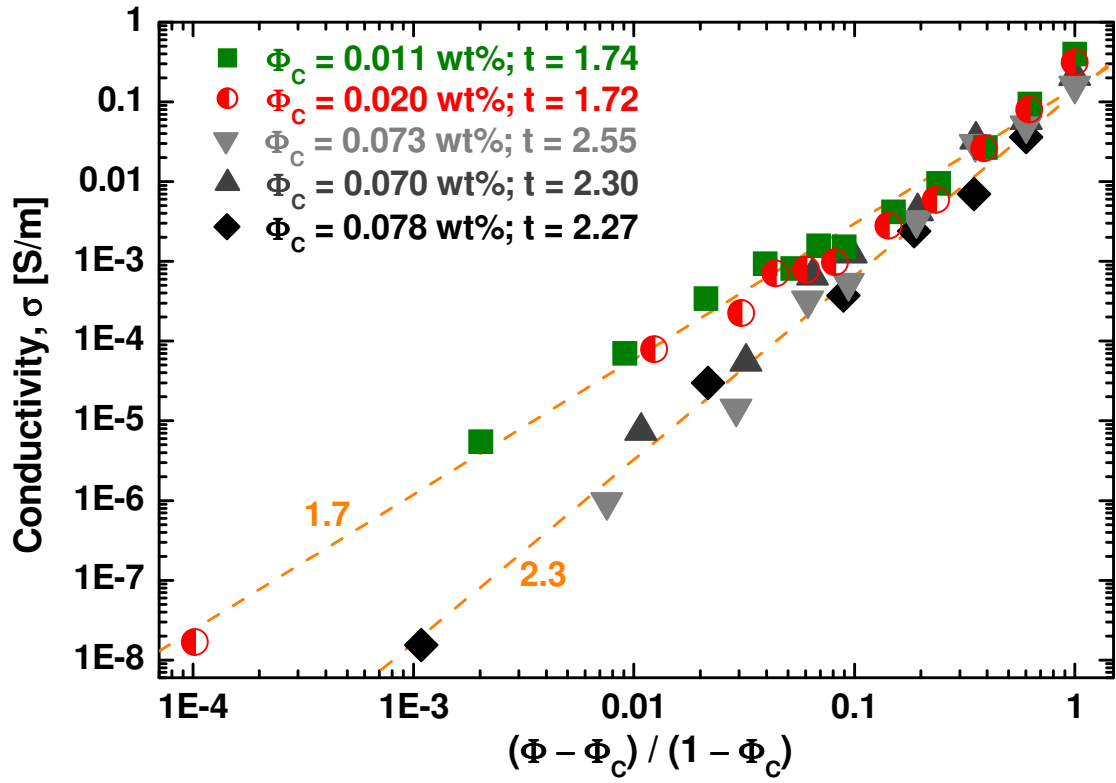
Figure 4-6 Logarithmic plot of conductivity vs. reduced mass fraction of the Nanocyl CNT/LY556/XB3473 composites presented in Figure 4-5.

For the slow stir samples the percolation threshold ϕ_C is 0.011 wt% while for the medium stir samples it is 0.020 wt%. These values are comparable with the threshold found in previous experiments (0.03 wt%) performed with similarly entangled CNT [16] but are one order of magnitude higher than achievable with aligned CNT [32]. Above the percolation threshold, a conductivity plateau develops for both sets and sustains until 0.1 wt% (Figure 4-5). Here, a crossover from saturation to power-law behaviour is clearly visible. While investigations of Sandler et al. [32] on a similar system already suggest both, the plateau and the onset of a slope crossover in their conductivity plot, unambiguous evidence is provided through these measurements for the first time. This is made possible by the large number of measurements over a wide range of concentrations with smaller incremental steps than previously considered. The three fast stir samples yield thresholds around 0.074 wt%.

Two types of percolation thresholds seem to exist in the Nanocyl CNT composites, which could be a characteristic feature of all composite materials that possess a fluid state of low viscosity during processing. The higher threshold is determined by statistical percolation theory and is unchangeable by processing methods. The lower one can vastly be shifted down to lower concentrations by stimulating particle flocculation and network formation.

Evidence is provided through comparison of the conductivity measurements in Figure 4-5 with the light microscopy images in Figure 4-7. For each preparation method the emergence of flocks and the formation of a kind of superstructure are detectable. It is obvious that they appear at the same concentrations where the conductivity increases by several orders of magnitude. Both, the emergence of flocks and the steep conductivity increase, occur at lower filler concentrations (0.011 wt% and 0.020 wt%) than predicted by percolation theory for statistically distributed particles (Eq. 4-1: $\phi_C^{wt} \approx r^{-1} \approx 0.1$ wt% for the Nanocyl CNT with aspect ratio $r \approx 1{,}000$). This theoretical value represents the lower limit where a conducting network develops due to contacts between homogenously dispersed, immobile particles. At this point flocculation cannot further improve the conductivity, or particle rearrangement cannot even occur due to lowered particle mobility through the established network. Right below this point the superstructure of flocks is able to retain a certain level of conductivity (plateau), and above this point conductivity increases solely due to the generation of additional paths that connect opposite sample sites (power-law dependence). This point at 0.1 wt% seems to represent the real statistical percolation threshold for the Nanocyl CNT composites. The thresholds at lower concentrations (0.011, 0.020 and 0.074 wt%) are additional, kinetic percolation thresholds of this system. For the fast stir samples, both thresholds are too close to each other to be distinguishable.

Even the exponents of the scaling laws (Figure 4-6) differ for the kinetic and statistical percolation. For the kinetic percolation (slow and medium stir samples) values around $t = 1.7$ are found. The threshold of the three fast stir samples is

close to the statistical one and yield exponents around 2.37. A similar behaviour can be found for the computer simulations performed by Lebovka et al. [212]. They used a two-dimensional diffusion-limited aggregation model (DLA) with mobile and immobile seeds, the mobile ones performing random walks until they come in contact with one of the growing clusters or seeds. The percolation behaviour for the case that all seeds are immobile yields an exponent $t = 1.33$ and is equivalent to the model of random percolation in two dimensions [100,101]. With decreasing number of immobile seeds the established network gets more and more fractal and the percolation threshold decreases. Simultaneously, a transition from $t = 1.33$ to higher values is detected in the logarithmic plot of conductivity vs. reduced mass fraction, similar to the behaviour visible in Figure 4-6. It seems that in three dimensions the exponent $t \approx 1.7$ represent a kinetic/fractal network while $t \approx 2.5$ indicates a statistical/homogeneous one. It should be noted that above 0.1 wt% all samples follow a power law behaviour between $\sigma \sim \phi^{2.6}$ and $\sigma \sim \phi^{2.9}$, which will be further used for the contact resistance calculations presented in Section 4.9.

But which mechanism is responsible for the different flocculation intensities for the composites? Diffusion, convection, van der Waals and Coulomb forces can be excluded as they are present in all samples and should initiate identical flocculation all-over. The only difference arises from the variation of the stirring rates and temperatures after hardener addition. Thus, shear forces at low viscosities seem to be the only promoter of flocculation, at least regarding the short time period (1 h) until polymer gelation. The significance of shearing was demonstrated in experiments [213] as well as in simulations [211], where Klingenberg et al. further predict a strong dependence of flocculation on the stiffness and shape of the filler particles and the friction forces between them.

The presented results–the kinetic percolation, the conductivity plateau and the universal behaviour above the statistical percolation threshold–were recently reproduced in various systems consisting of MWCNT/chloroform and SWCNT/chloroform [214].
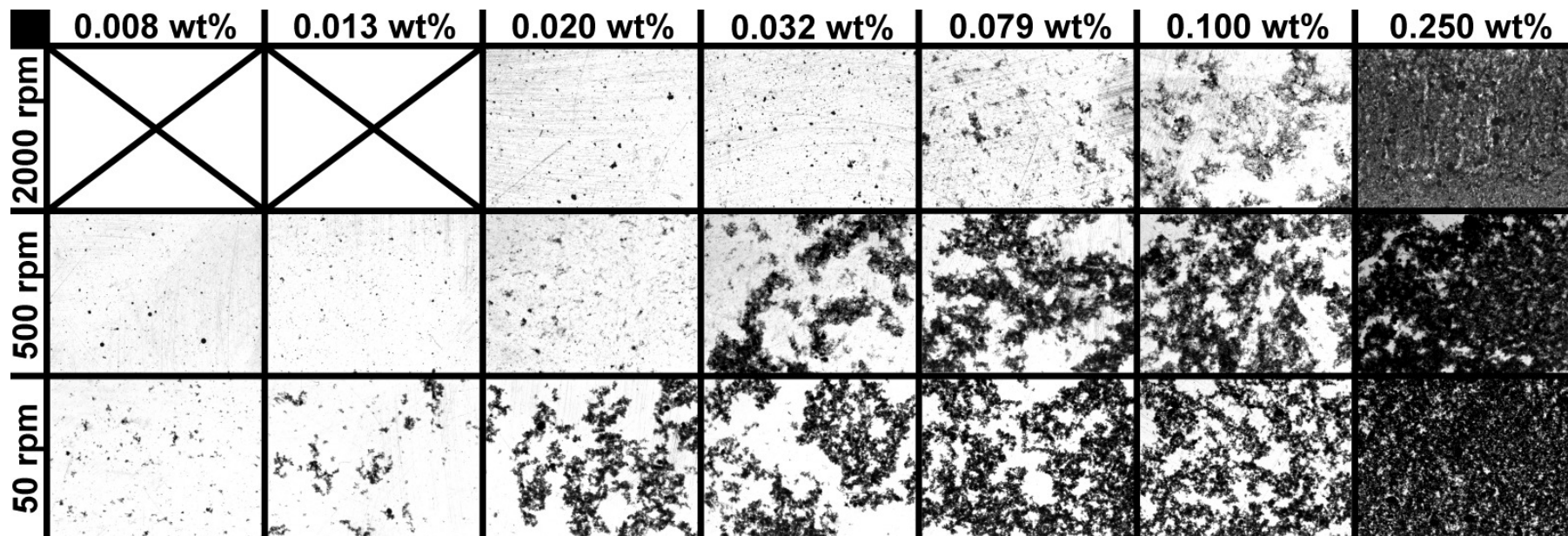
Figure 4-7 Light microscopy images (7.5 mm width and 5.5 mm height) of 0.5 mm thick Nanocyl CNT/LY556/XB3473 composites from each preparation method (rows) and with different CNT concentrations (columns).

4.4 Charge transport through the CNT network

Statistical percolation theory does not directly describe the conductivity increase due to the percolation behaviour of conductive particles, but merely the amount of particles of a given size needed to form infinite clusters of particles which are in contact with each other. However, these particles could comprise an insulating layer of a certain thickness, which finally determines the magnitude of the conductivity improvement through percolation.

In this context, conductivity below the percolation threshold is sometimes explained by tunnelling conduction between homogeneously distributed particles not yet in physical contact–yielding the proportionality $\log \sigma \sim \phi^{-1/3}$ [162,215]. This argument is not valid for the Nanocyl CNT/LY556/XB3473 composites discussed in the previous section as here all homogeneity is lost while lowering the threshold by as much as a factor of 10. Nevertheless, the corresponding plot of the results of Section 4.3 (Figure 4-8a) is worth being discussed. All samples show above 0.2 wt% the mentioned proportionality which is however lost below 0.1 wt%. While this result suggests tunnelling conduction above statistical percolation threshold rather than below it, possible limitations of this analysis are now emphasized. First of all, it is not clear whether a deviation from the given proportionality indicates a change in the conduction mechanism or simply the transition to an inhomogeneous particle distribution. Moreover, the plots of $\log \sigma$ vs. $\phi^{-1/2}$ or $\phi^{-1/4}$ yield a comparable linear fit (Figure 4-8b,c).

The contact resistances between adjacent CNT will be determined from a simplified model in Section 4.9.
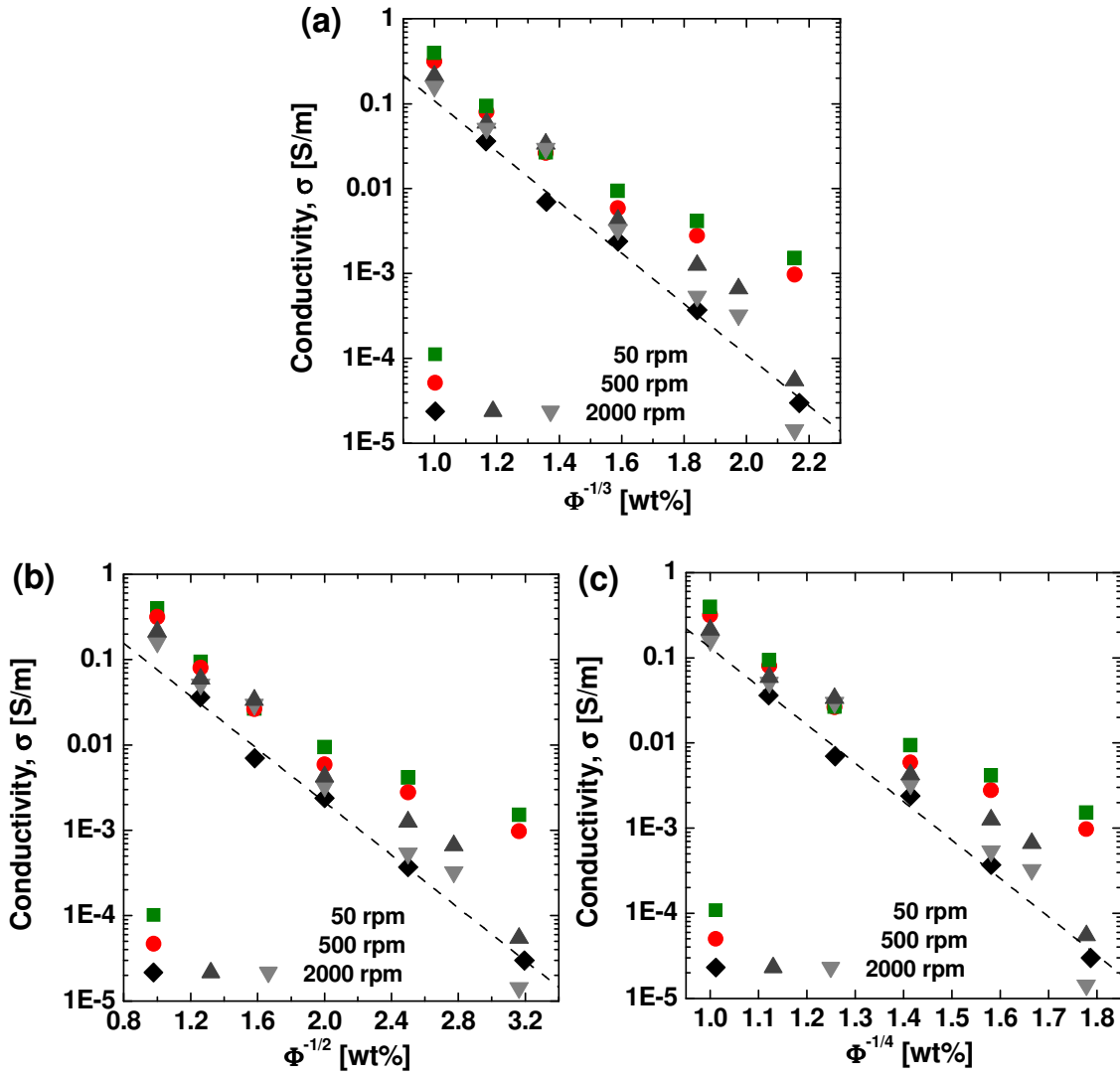
Figure 4-8 Plot of the conductivity data from Figure 4-5 as a function of (a) $\phi^{-1/3}$, (b) $\phi^{-1/2}$ and (c) $\phi^{-1/4}$.

4.5 Influence of calendering

In this set of experiments, ACVD-aligned-grown CNT were used and the sample preparation method was varied (for details see Section 4.2.1.2). The suspension was processed with a dissolver disk and partly calendered thereafter. The suspensions were then partly exposed to slow shearing and left partly unagitated. The conductivities of the resulting four sample sets are plotted in Figure 4-9. The sample set that was not calendered and not sheared exhibits

a threshold $\phi_C = 0.09\,\mathrm{wt\%}$, which–according to statistical percolation theory (Eq. 4-1: $\phi_C^{wt} \approx r^{-1}$)–indicates that the CNT are expected to have a mean aspect ratio $r \approx 1,000$. Indeed, the initial aspect ratio of the CNT is close to this value, so we conclude that the observed/apparent percolation threshold equals the statistical/intrinsic value of the percolating system [29,216]. According to these results and the optical micrographs in Figure 4-10, the dissolver disk is able to optimally disperse aligned-grown CNT and the PTFE block prevents efficiently convection and thus CNT re-agglomeration.
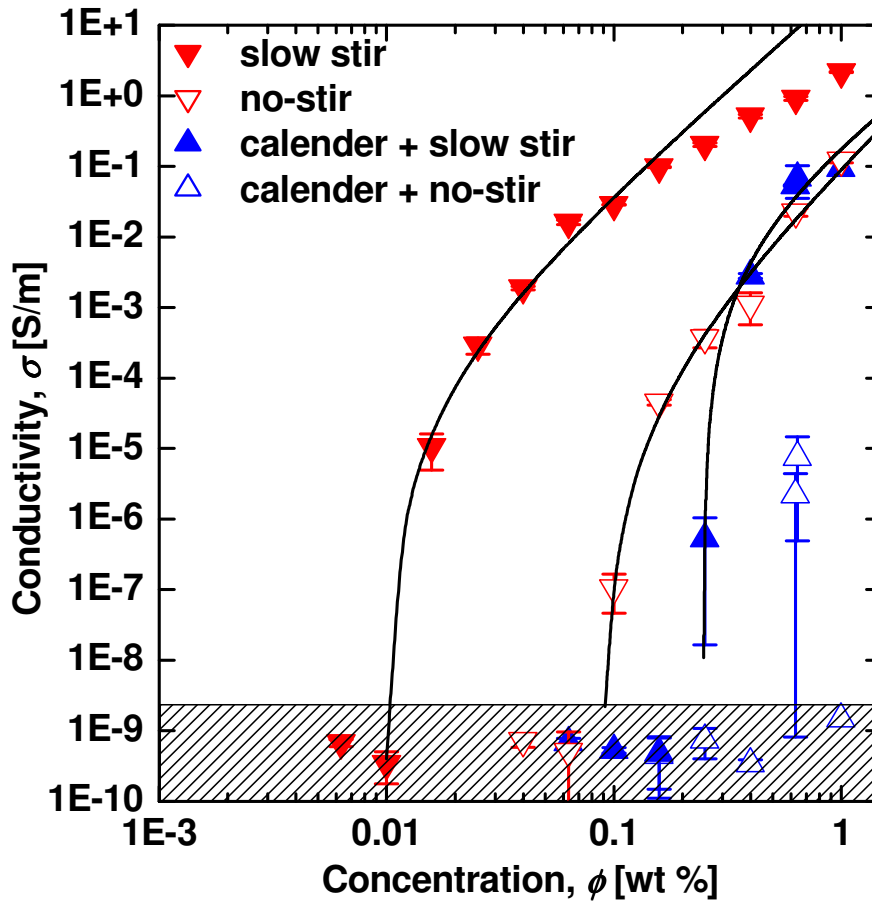
Figure 4-9 Log-log plot of conductivity vs. ACVD-aligned-grown CNT weight fraction in the LY556/XB3473 epoxy system for the four sample preparation methods. The power law fit to the slow stir, no-stir and calender + slow stir data are $\sigma = 2 \cdot 10^7 (\phi - 0.000099)^{2.84}$, $\sigma = 2 \cdot 10^5 (\phi - 0.00088)^{3.13}$ and $\sigma = 10^4 (\phi - 0.00248)^{2.32}$, respectively.
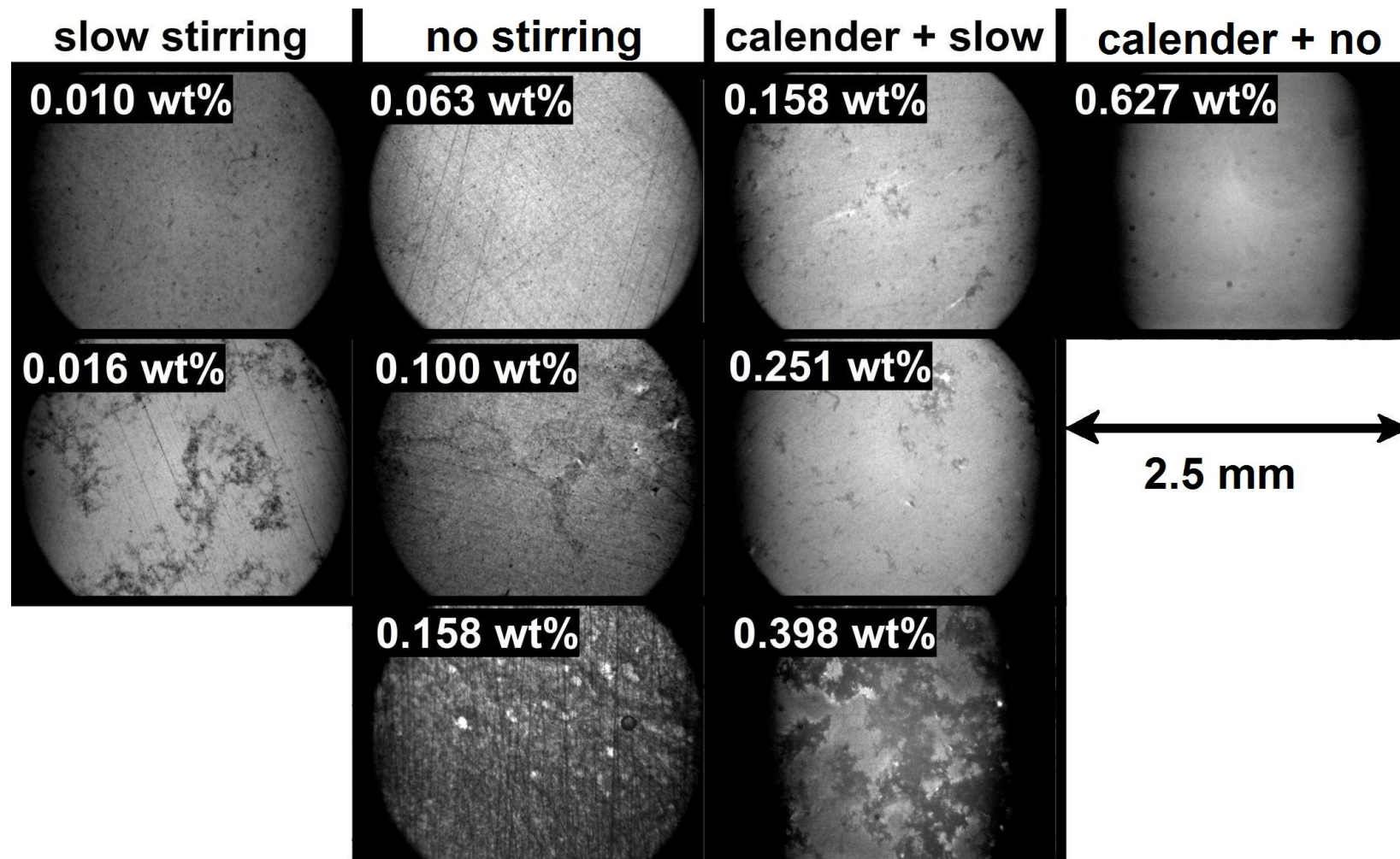
Figure 4-10 Optical micrographs of samples from each preparation method (columns) and varying ACVD-aligned-grown CNT weight fraction (rows) in the LY556/XB3473 epoxy system.
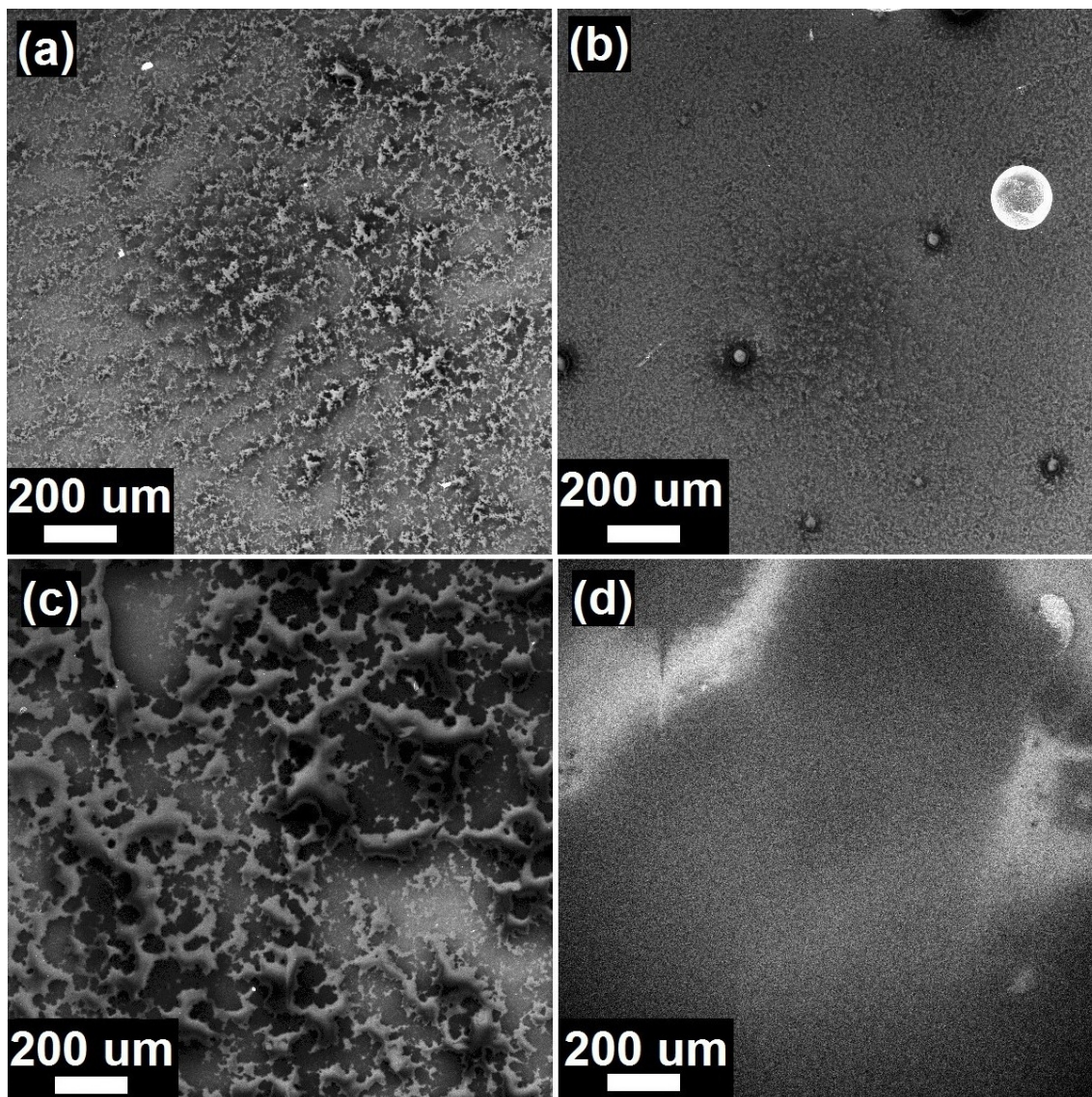
Figure 4-11 Charge contrast SEM-images of (a) slow stir, (b) no-stir, (c) calender + slow stir and (d) calender + no-stir samples containing 0.63 wt% ACVD-aligned-grown CNT in the LY556/XB3473 epoxy system.

As soon as CNT re-agglomeration is induced by modest shear forces the conductivity starts increasing. This effect was described in detail in Section 4.3. We now proceed to the discussion of the calendered sample set that was not stirred slowly. A percolation threshold can hardly be determined in this case, one of two samples always exhibits insulating behaviour nearly for all CNT concentrations. Unfortunately, the second sample with 1 wt% CNT cracked when removing it from the PTFE block cavity, but the other sample was

insulating even at this high concentration. The statistical percolation threshold of this sample set seems to be located above 0.6 wt%, maybe even above 1 wt%.

Two reasons for this finding could be identified. The three roll calender could be able to separate the CNT and sheath [193] them with a layer of insulating matrix more efficiently than the dissolver disk. The matrix layer could then be too thick (~ 2 nm) to allow tunnelling conduction between adjacent CNT even at concentrations above 0.6 wt%. Charge contrast SEM-analyses [201] seem to support this conclusion as it was not possible to produce a contrast between conducting and insulating regions in the calender + no-stir samples while it was possible in all other samples (Figure 4-11). This would mean that having the best CNT dispersion quality is not favourable for electrical conductivity applications.

The second reason could be the fracturing of CNT during the calendering process. This could have lowered their aspect ratio and thereby increased their statistical percolation threshold. To verify this assumption, the hydrodynamic forces exerted on the CNT during calendering are estimated. A setup is selected where a single CNT is clamped on one end while the hydrodynamic force F^{hyd} acts as a line load on it. This setup definitely overestimates the real forces on a single CNT suspended in the matrix. At the same time it represents an underestimation for the concentrated master batch suspension because interactions with other CNT are not considered. The resulting bending moment M is then defined as

$$M = \frac{\ell}{2} F^{hyd} = \frac{\ell}{2} \eta \, \dot{\gamma} \, \ell \, d = \frac{\eta \, \dot{\gamma} \, \ell^2 d}{2}$$
Eq. 4-4

with the matrix viscosity $\eta = 10 \, \mathrm{Pa\,s}$, CNT length $\ell = 50 \, \mu m$ and CNT diameter $d = 80 \, nm$. The highest shear rate $\dot{\gamma} = 300{,}000 \, \mathrm{s^{-1}}$ is found within the 5 μm gap of the calender rolls (the fastest rotating at 180 rpm, all having a diameter of

120 mm) [217]. With the second moment of area $I = \pi d^4 / 64$ for a CNT with negligible inner diameter (as checked by TEM analyses), the resulting tensile stress in the outer layer of our multi-wall nanotube is

$$\frac{M}{I}\frac{d}{2} = \frac{16\,\eta\,\dot{\gamma}\,\ell^2}{\pi\,d^2} = \frac{16\,\eta\,\dot{\gamma}}{\pi}\,r^2 = 6\,\text{TPa} \qquad\qquad \textbf{Eq. 4-5}$$

This tensile stress exceeds the experimentally determined tensile strengths for the outer layer of a multi-wall nanotube (11-63 GPa [11]) as well as the CNT fracture stress derived from molecular mechanics simulations (80 GPa [218]) by two orders of magnitude. It seems that the CNT could have easily been fractured in the calender. In order to support this conclusion, a second estimate is performed based on simulation results of fibres in a viscous fluid subjected to a laminar shear flow [219]. Yamamoto et al. derived a condition for fibre fracture as a result of the bending stress imparted by the fluid after bending deformation of a fibre with Young's modulus E and aspect ratio r:

$$\frac{\eta\,\dot{\gamma}}{E} \approx 100\,\frac{\ln(2r)-1.75}{2\,r^4} \qquad\qquad \textbf{Eq. 4-6}$$

Young's moduli of 270-950 GPa [11] yield values between 10^{-6} and 10^{-5} for the left side of the equation, while an aspect ratio $r = 625$ yields 10^{-9} for the right side. According to this estimate, the bending stress exceeds the CNT Young's modulus by 3-4 orders of magnitude, again indicating CNT breakage.

But to what extent does the calender break the CNT? A statistical percolation threshold of 0.6-1 wt% suggests the final aspect ratio to be around 60.[5] This indicates a decrease of r by one order of magnitude. Interestingly, with this reduction in aspect ratio both estimated stresses–the tensile (being proportional

---

[5] This result could not be proved by TEM analyses due to the huge nanotube diameter of 80 nm.

to r^2) as well as the bending one (being proportional to r^4)–would decrease below the respective critical value for CNT and thus would stop breaking them. This could be a new method for adjusting the length of CNT in a composite with a calender. Further investigations are however necessary to support these statements.

4.6 Influence of shear forces and CNT on the percolation threshold

The potential of shear forces to significantly lower the percolation threshold has been demonstrated in Section 4.3. There, highly entangled Nanocyl CNT were used in the LY556/XB3473 epoxy system (for details see Section 4.2.1.1). The samples that were stirred with 50 rpm at elevated temperatures are reprinted here in Figure 4-12 (Nanocyl slow stir). Three sample sets that were submitted to the initial high speed mixing (2,000 rpm) without further shearing were averaged to give the Nanocyl no-stir results. The conductivities of the CCVD-aligned-grown CNT/LY556/XB3473 samples (see Section 4.2.1.3 for the processing conditions) are also plotted in Figure 4-12. The non-calendered ACVD-aligned-grown CNT/LY556/XB3473 epoxy system from Figure 4-9 represent the third CNT type analysed in this section. All percolation parameters are summarized in Table 4-2.

The thresholds ϕ_C of the no-stir samples coincide with values expected for statistically distributed particles of the respective aspect ratio (Eq. 4-1: $\phi_C^{\mathrm{wt}} \approx r^{-1}$). The Nanocyl and the ACVD-aligned-grown CNT both have $r \approx 600$ - $1,000$ and $\phi_C \approx 0.08\,\mathrm{wt\%}$ while for the CCVD-aligned-grown CNT we find $r \approx 8,300$ and $\phi_C \approx 0.01\,\mathrm{wt\%}$. These seem to be the statistical percolation thresholds of the composites. These thresholds can be further lowered through shear forces, giving rise to lower, kinetic percolation thresholds. Most interestingly, the factors between statistical and kinetic thresholds are rather similar for all three CNT types regardless of their huge differences in aspect ratio and entanglement

72

state. Thus, the influence of the aspect ratio on the kinetic percolation threshold is dominating the influence of shearing. This conclusion is in contradiction to results presented in [17] where shorter CNT are found to have a lower kinetic percolation threshold than longer CNT of same thickness. Comparing CNT of similar aspect ratios (ACVD-aligned-grown and Nanocyl) it is concluded that the entanglement state influences neither the kinetic nor the statistical percolation thresholds.
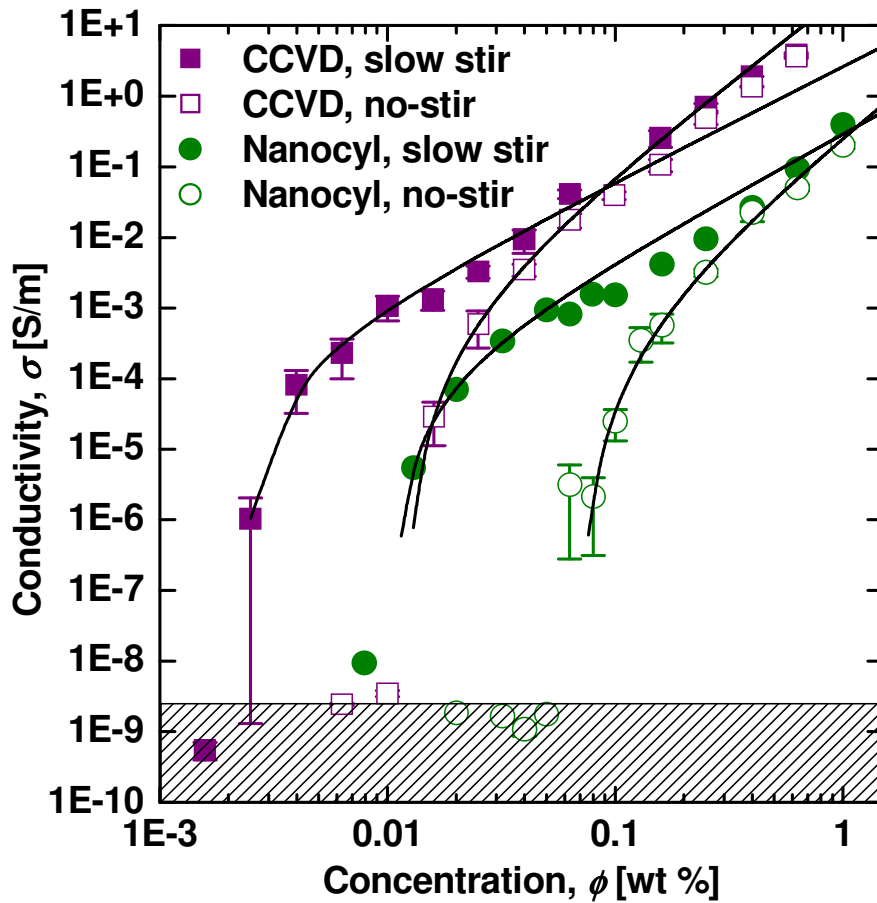

Figure 4-12 Log-log plot of conductivity vs. CNT weight fraction for the CCVD-aligned-grown and the Nanocyl CNT, each dispersed in the LY556/XB3473 epoxy system. The power law fit to the CCVD slow stir and no-stir data are $\sigma = 5 \cdot 10^3 (\phi - 0.000024)^{1.63}$ and $\sigma = 3 \cdot 10^6 (\phi - 0.00012)^{2.48}$, respectively. The power law fit to the Nanocyl slow stir and no-stir data are $\sigma = 10^3 (\phi - 0.00011)^{1.77}$ and $\sigma = 5 \cdot 10^4 (\phi - 0.00070)^{2.59}$, respectively.

Table 4-2 Scaling law $\sigma = \sigma_0(\phi - \phi_C)^t$ fitted to the data points between ϕ_C and $10\phi_C$ for the three CNT types. The percolation thresholds ϕ_C are given in absolute values and the intrinsic CNT conductivities σ_0 in S/m. The factor between ϕ_C (slow stir) and ϕ_C (no-stir) as well as the CNT dimensions are also summarized.

$\phi_C < \phi < 10\phi_C$	ACVD-aligned-grown CNT	Nanocyl CNT	CCVD-aligned-grown CNT
slow stir	$\sigma = 2 \cdot 10^7(\phi - 0.000099)^{2.84}$	$\sigma = 10^3(\phi - 0.00011)^{1.77}$	$\sigma = 5 \cdot 10^3(\phi - 0.000024)^{1.63}$
no-stir	$\sigma = 2 \cdot 10^5(\phi - 0.00088)^{3.13}$	$\sigma = 5 \cdot 10^4(\phi - 0.00070)^{2.59}$	$\sigma = 3 \cdot 10^6(\phi - 0.00012)^{2.48}$
factor between ϕ_C (slow stir) and ϕ_C (no-stir)	8.9	6.4	5.1
CNT aspect ratio, r	625	~ 1,000	8,300

Table 4-3 Scaling law $\sigma = \sigma_0 \phi^t$ fitted to the data points between 0.2 wt% and 1 wt% for the three CNT types. The percolation thresholds ϕ_C are given in absolute values and the intrinsic CNT conductivities σ_0 in S/m.

$0.002 < \phi < 0.01$	ACVD-aligned-grown CNT	Nanocyl CNT	CCVD-aligned-grown CNT
slow stir	$\sigma = 5 \cdot 10^3 \phi^{1.68}$	$\sigma = 9 \cdot 10^4 \phi^{2.70}$	$\sigma = 10^5 \phi^{1.98}$
no-stir	$\sigma = 2 \cdot 10^7 \phi^{4.12}$	$\sigma = 2 \cdot 10^5 \phi^{2.96}$	$\sigma = 3 \cdot 10^5 \phi^{2.20}$

4.7 Influence of shear forces and CNT on the maximum conductivity

This section compares the same composites that were analysed in the previous section, this time regarding maximum achievable conductivities. The influence of shear forces is different below and above the statistical percolation threshold. Above, shear forces have no effect on the conductivities of the CCVD-aligned-grown and the Nanocyl CNT/epoxy composites (Figure 4-12). Conductivity follows a scaling law behaviour ($\sigma = \sigma_0 \phi^t$) with similar parameters for both slow stir and no-stir preparation methods (Table 4-3). However, for the ACVD-aligned-grown CNT shearing seems to increase the conductivity by 1-2 orders of magnitude. Further experiments are necessary to confirm this finding and to assess the role of the CNT thickness–being the only parameter that differs from both other CNT types.

Below the statistical threshold, shear forces increase the conductivity of all composites by at least 5 orders of magnitude. For the CCVD-aligned-grown and the Nanocyl CNT/epoxy composites a constant conductivity of ~ 10^{-3} S/m is sustained in a narrow concentration region around the statistical percolation threshold (Figure 4-12). A more detailed explanation to this so-called plateau can be found in Section 4.3. It is surprising that neither the non-entangled state nor the higher aspect ratio of the CCVD-aligned-grown CNT seem to be able to widen the plateau. This is linked to the factors between statistical and kinetic percolation thresholds, which were found to be similar for both CNT types as well. Another surprising result is that the conductivity level corresponding to this plateau does not seem to be affected from changing the properties (aspect ratio, entanglement state) of the CNT. In contrast, the non-entangled state or/and the higher aspect ratio do increase the conductivity by 1-2 orders of magnitude at high concentrations (Figure 4-12).

4.8 Influence of synthesis method on the intrinsic CNT conductivity

It might be expected that the production method should have a strong impact on the intrinsic conductivities of the CNT. From the various scaling laws fitted at different concentration regions in the previous sections, the intrinsic conductivities of the ACVD-aligned-grown, CCVD-aligned-grown and Nanocyl CNT are now determined. The assumption is, of course, that these values should not differ between slow stirred and no-stirred samples. The scaling law fitted near the percolation threshold however yields extremely differing parameters (Table 4-2). While the variation of the exponent t can be traced back to different network types (fractal/kinetic: $t \sim 1.7$; homogeneous/statistical: $t \sim 2.5$; see Sections 4.1.3 and 4.3), the variation of the prefactor σ_0 should have another origin. Both parameters are very sensitive to the fitting procedure (described in [162]) and vary substantially when altering the number of data points to be fitted. Only data points that are near the percolation threshold (e.g. within one decade) should be used for the fit because data points far above it usually exhibit a different behaviour (Section 4.3). There, the CNT concentration is so high that it does not allow the CNT to rearrange upon shearing. This homogeneous CNT distribution yields–except for the ACVD-aligned-grown samples–more consistent fitting parameters for the slow stirred and no-stirred samples (Table 4-3). The exponent t scatters around the homogeneous/statistical value of 2.5. According to the prefactors, the intrinsic conductivities of the CCVD-aligned-grown and the Nanocyl CNT are very similar, around 10^5 S/m. As already stated, the ACVD-aligned-grown CNT behave–for reasons which are not yet fully understood–different, leading to huge discrepancies between the fit parameters for the slow stirred and no-stirred samples; nevertheless, their conductivities also scatter around this decade.

4.9 Inter-particle contact resistances

4.9.1 Theory

In this section an extremely simplified model of percolated particles is derived on the basis of the model presented by Ruschau et al. [220]. The goal is to relate the sample conductivity (that can be measured) to the inter-particle contact resistance within the polymer (that cannot be measured, but ultimately limits charge transport). The model describes homogenously dispersed, immobile particles that are presumed to be rigid and of cylindrical shape. The network they build is modelled through n parallel paths bridging the sample, each consisting of m sticks and m contacts. The number of parallel connections of single paths bridging the sample is defined as

$$n = \frac{V_{all}}{mV_{one}} = \frac{\phi_{vol}V_{sample}}{mV_{one}} \approx \frac{\rho_{matrix}\phi_{wt}}{\rho_{all}}\frac{V_{sample}}{mV_{one}} \qquad \textbf{Eq. 4-7}$$

with the volume of all particles V_{all}, the sample volume V_{sample} and the volume of a single particle V_{one}. The approximation of the filler volume fraction

$$\phi_{vol} = \frac{V_{all}}{V_{sample}} = \frac{1}{1+\dfrac{\rho_{all}}{\rho_{matrix}}\left(\dfrac{1}{\phi_{wt}}-1\right)} = \frac{\dfrac{\rho_{matrix}}{\rho_{all}}\phi_{wt}}{1-\phi_{wt}\left(1-\dfrac{\rho_{matrix}}{\rho_{all}}\right)} \approx \frac{\rho_{matrix}}{\rho_{all}}\phi_{wt} \quad \textbf{Eq. 4-8}$$

produces an error equal to $\phi_{wt}\left(1-\dfrac{\rho_{matrix}}{\rho_{all}}\right)$, with the matrix density ρ_{matrix} and particle density ρ_{all}. All matrix:filler density ratios encountered in this thesis, as well as in the references analysed in the next section, are around 1:2. For $\rho_{all} \approx 2\rho_{matrix}$ and $\phi_{wt} < 10$ wt% the error stays below 5%. The filler weight fraction is the only controllable parameter and therefore subsequently used

(without index). The number of particles and inter-particle contacts within a single path is conveniently defined as

$$m = \frac{s}{\ell} \frac{1}{\phi^x}$$

<div align="right">Eq. 4-9</div>

which is proportional to the sample thickness s and inversely proportional to the particle length ℓ and filler weight fraction ϕ. The latter dependence expresses the fact that paths usually do not bridge the sample in a straight way. The lower the filler concentration is, the longer the paths are. Only for a filler concentration of 100 wt% will all paths reduce to the minimum number of particles s/ℓ that are necessary to bridge the distance s. The exponential dependence on ϕ is solely supported by the experimentally found power law above the statistical percolation threshold. Therefore, the magnitude of the exponent x will always be adjusted according to the respective experimental results. Setting up the equations for parallel $\left(R_{\text{sample}}^{-1} = \sum_{n} R_{\text{path}}^{-1} \right)$ and series resistances $\left(R_{\text{path}} = \sum_{m} R + R_{\text{C}} \right)$ within a sample yield the relation

$$\sigma \approx \frac{2\ell}{\pi d^2} \frac{\phi^{2x+1}}{R + R_{\text{C}}}$$

<div align="right">Eq. 4-10</div>

where d and R are the diameter and resistance of a single particle, respectively, and R_{C} is the resistance of its contact to the next particle. In short, the procedure for assessing R_{C} consists of equating $2x+1$ with the slope of the log σ vs. log ϕ plot above the percolation threshold and then solving Eq. 4-10 with the help of the known parameters: individual particle size and resistance, as well as conductivity and concentration values corresponding to a single data point.

4.9.2 Application to various composite materials

The above calculations are now applied to conductivity data presented in Section 4.6 as well as to published data that provided both, information about their filler sizes and enough conductivity values above their statistical percolation threshold. All relevant parameters and the resulting contact resistance magnitudes are summarized in Table 4-4.

Three of the analysed results ([19], [221] and the ACVD-aligned-grown CNT from Section 4.5) yield particle contact resistances of the same magnitude as the respective resistances of the individual filler particles used, namely $6.4\,k\Omega$ [222,223] for a single CNT and several MΩ [221] for a pure PPy coated cellulose particle. It is remarkable that all filler particles with big diameters give low contact resistances, no matter what type of filler, matrix or processing method is used. The second set of published data ([224], [110], the Nanocyl and the CCVD-aligned-grown CNT from Section 4.6) exhibit a contact resistance in the region of 10^5-$10^6\,\Omega$, thus 100-1,000 times larger than the intrinsic CNT resistance. Again, neither the type of CNT or polymer nor the processing method seems to have a noticeable impact on the contact resistance magnitude. Finally, the high contact resistance in the case of the PmPV matrix [161] can be explained with the helical structure of the polymer chains which presumably wrap the CNT and–having a diameter of 2 nm– impedes electron tunnelling between them.

One reason for the restricted possibility of data comparison definitely is the simplicity of the presented model, which does not include the real state of the dispersion, e.g. the magnitude of particle agglomerates, the degree of particle wetting through the matrix and the real particle shape. However, including these parameters into the model simultaneously requires the publication of corresponding SEM and TEM analyses to provide these data. With an improved model and enough data points above the respective statistical percolation thresholds it should be possible to analyse the dependence on different filler particles, matrices and preparation methods.

Table 4-4 Summary of the experimental parameters of conductivity measurements found in literature with the resultant values needed for assessing the contact resistance R_C. Question marks indicate particle sizes that had been guessed (according to the percolation threshold) due to the lack of sufficient information.

Filler	Matrix	Preparation method	ϕ_C	$r = \ell / d$	$2x + 1$	R_C	Ref.
MWNT (CVD)	PC	Extruded and compression moulded	1.4 wt%	$80 = \dfrac{1\,\mu m}{13\,nm}$	2.2	$10^6\ \Omega$	[224]
MWCNT (Arc discharge)	PmPV	Filler and matrix sonicated in toluene	7.5 wt%	$25 = \dfrac{500\,nm}{20\,nm}$	4.9	$10^8\ \Omega$	[161]
MWNT (CVD)	Epoxy	Filler dispersed in methanol, composite cured under pressure	0.7 wt%	$150 = \dfrac{15\,\mu m\,?}{100\,nm}$	3.1	$10^3\ \Omega$	[19]
PPy coated cellulose	Latex	Stirred, freeze dried, moulded	3 vol%	$13 = \dfrac{2\,\mu m}{160\,nm}$	2.5	$10^7\ \Omega$	[221]
SW- and DWCNT (CCVD)	Epoxy	Filler dispersed in water, composite cured in Teflon mould	0.08 wt%	$667 = \dfrac{2\,\mu m\,?}{3\,nm}$	3.3	$10^5\ \Omega$	[110]
Nanocyl CNT	Epoxy	Stirred, cured in metal mould	0.07 wt%	$1{,}000 = \dfrac{15\,\mu m}{15\,nm}$	3.0	$10^5\ \Omega$	[105][6]
ACVD-aligned-grown CNT	Epoxy	Stirred, cured in PTFE mould	0.09 wt%	$625 = \dfrac{50\,\mu m}{80\,nm}$	4.1	$10^3\ \Omega$	[105][6]
CCVD-aligned-grown CNT	Epoxy	Stirred, cured in PTFE mould	0.01 wt%	$8{,}300 = \dfrac{100\,\mu m}{12\,nm}$	2.2	$10^6\ \Omega$	[105][6]

[6] See also Section 4.6

4.10 Electric field induced CNT network formation

Martin et al. [18] have shown that the formation of CNT networks can be induced by the application of an external electric field. Thus, electric fields not only align CNT but also enhance the attractive forces between neighbouring CNT. The growth of the network starts at the positive electrode indicating that CNT are negatively charged in an epoxy/amine hardener system. As has been shown for carbon black/epoxy composites, the chemical nature of the hardener mainly determines the charge of the filler particles [225]. AC fields are more effective than DC fields in the sense that the conductivity of samples cured in an AC field is one order of magnitude higher than for DC fields. Martin et al. [18] used CNT concentrations of up to 0.02 wt% and electric field strengths up to 20 V/mm yielding a maximum composite conductivity around $3 \cdot 10^{-4}$ S/m.

The formation of AC electric field induced aligned SWCNT percolative columns between electrodes has also been observed by Park et al. [82]. They used 0.03 wt% SWCNT in UDMA/HDDMA and found the conductivity to saturate at 10^{-4} S/m with field strengths of 33 V/mm, while the best performance was found for field frequencies of 100 Hz. Conductivity anisotropies of 10^4 were obtained at field strengths of 44 V/mm.

In this thesis, the CNT concentration is extended up to 0.08 wt% and the electric field strengths up to 60 V/mm (Figure 4-13). The conductivities of the cured samples saturate at $\sim 10^{-2}$ S/m as a function of field strength and as a function of filler concentration. The saturation is consistent with the results of Park et al. [82]: it also takes place around 30 V/mm, but at much higher conductivities. This could be due to the different CNT and/or polymer type that have been used. MWCNT and/or epoxy seem to be favourable when establishing a conducting network via electric fields. The saturation at high CNT concentrations is equivalent to the transition from kinetic to statistical percolation. When approaching statistical percolation (~ 0.08 wt% for the

Nanocyl CNT composites), the CNT mobility is reduced and the effect of the electric field vanishes. Compared with shear percolated composites–which yield a plateau at ~ 10^{-3} S/m (Figure 4-12)–the absolute conductivities of AC field percolated samples are up to one order of magnitude higher.
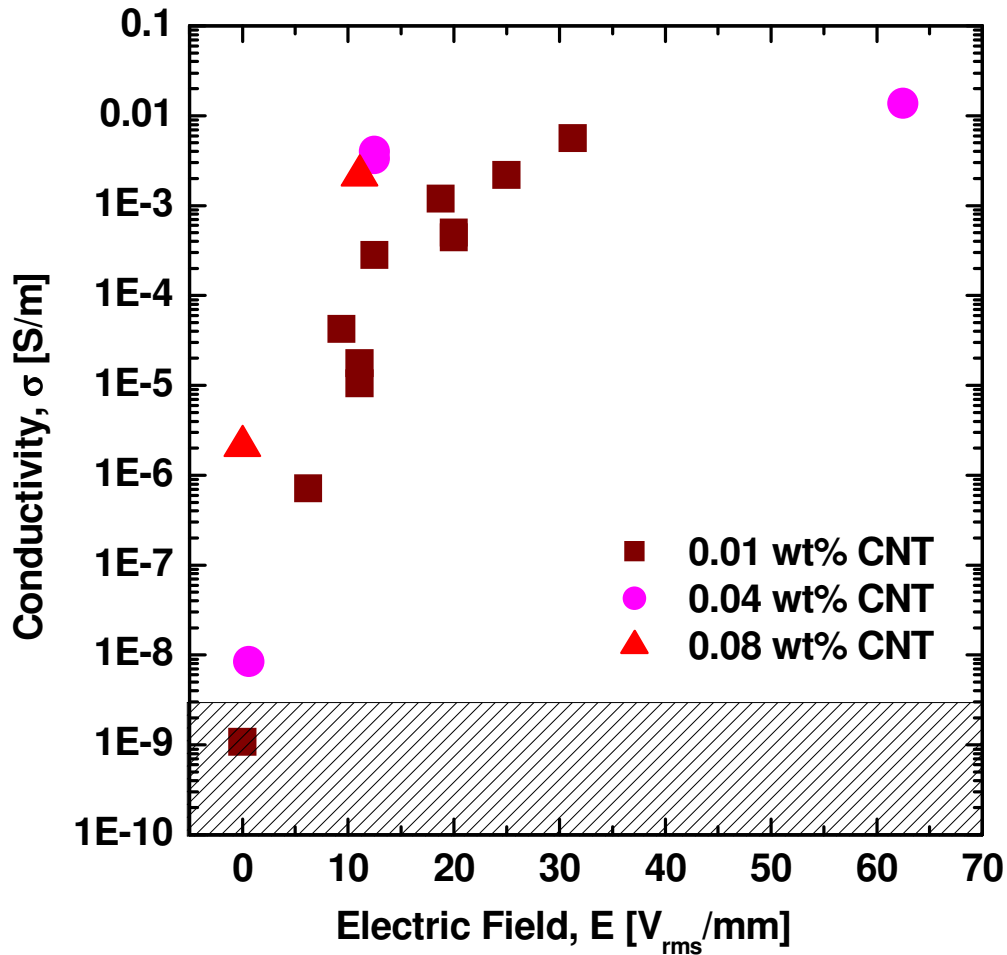

Figure 4-13 Plot of the Nanocyl CNT/LY556/XB3473 composite conductivity for various CNT concentrations after exposure to different AC field strengths at frequencies of 100 Hz during the curing time.

4.11 Summary and conclusion

Conductivity measurements over up to three decades of filler concentration with narrow increments revealed two percolation thresholds, the lower one attributed to a kinetic and the higher one to a statistic network formation process. A conductivity plateau was detected and was attributed to the presence of a superstructure of flocculated filler particles. The onset of this flocculation was controlled by coarsely adjusting the stirring rate and temperature during the final mixing step.

The influence of shear forces on the electrical properties of a composite can only be assessed in comparison with a setup where shear forces (e.g. through convection or extrusion) can be completely excluded. Taking care of this, for all CNT types a comparable influence of shear forces on the kinetic percolation threshold is found. CNT with higher aspect ratios were found to have lower statistical and kinetic thresholds. Thus, the influence of the aspect ratio on the kinetic threshold is dominating the influence of shearing, which is in contradiction to [17].

While the entanglement state of the CNT does not influence the kinetic or statistical percolation threshold, it (or the higher aspect ratio) seems to increase the conductivities considerably at high CNT concentrations. In contrast to this, shearing was not able to increase the conductivities at high concentrations.

From scaling laws fitted above the statistical percolation threshold it is concluded that all analysed synthesis methods yield CNT with intrinsic conductivities around 10^5 S/m.

It seems that the extremely high shear forces generated in a calender are able to separate the CNT efficiently and to sheath them with a thick layer of insulating matrix, which deteriorates the electrical performance of the composite. At the same time, the CNT are most probably broken down to an aspect ratio of ~ 60, as is indicated by the position of the statistical percolation threshold.

A simple geometrical model was developed to fit the power law dependence of conductivity above the statistical percolation threshold and to derive the magnitude of an individual inter-particle contact resistance. Filler particles with huge diameters (80-160 nm) seem to yield the lowest contact resistances, which are of the same magnitude as the intrinsic particle resistances.

Electric fields seem to be more efficient than shear forces in establishing a conducting network.

5 Raman spectroscopy analyses

The network formation process of carbon nanoparticles suspended in a polymer and exposed to electric fields was extensively analysed [18,225-228]. However, due to their small size, only agglomerated nanoparticles could be visualised. The SEM technique introduced in Section 2 allows to monitor nanosized particles, but only if the polymer they are dispersed in is already cured. Therefore, no information on the behaviour of individual nanoparticles during curing is accessible. As far as carbon nanotubes (CNT) are concerned, they fortunately exhibit a pronounced Raman signal due to their high crystallinity (Section 5.2) [229,230]. A vanishingly small amount of CNT can still be identified in a liquid or solid polymer matrix. Raman spectroscopy even allows detecting and studying single isolated CNT.

Raman spectroscopy has become one of the main characterisation tools for CNT. It provides information about their electronic states, phonon dispersion, geometry, defect concentration, doping level, temperature, orientation and stress state [229,230]. This thesis focuses only on the three last-mentioned characteristics of CNT.

Various CNT types were analysed in order to select one with high Raman signal intensity to be used in the polymer matrix (Section 5.3). The CNT Raman signal was then utilised to determine the sample temperature with respect to the laser intensity (Section 5.4). A laser intensity which does not heat up the composite too much had to be selected for the analyses of polymer curing processes (Section 5.6). The potential and accuracy in monitoring the CNT orientation with Raman spectroscopy was assessed in Section 5.5. And finally, chemically and thermally induced stresses in CNT/polymer composites during and after the curing process were analysed using the CNT as stress sensors (Section 5.6).

5.1 Experimental procedure

Raman spectra were recorded with a Horiba Jobin Yvon HR800 spectrometer (800 mm focal length spectrograph) using a He-Ne laser of 632.817 nm wavelength and 20 mW power. The laser was focused to an area of 2.3 µm in diameter by a 50× long working distance objective. The laser power could be lowered with neutral grey filters. The Raman signal from the focus was collected with the same objective in backscattering mode and directed to a diffraction grating (600 grooves per mm) and from there to a CCD detector (1024×256 pixel, each of 26 µm length). The spectrograph has a dispersion of 2 nm/mm, yielding a spectral resolution of 0.052 nm per pixel or 1.3 cm^{-1} per pixel, respectively. The spectrum acquisition time varied between 1 s and 15 min, depending on the filter used. A programmable oven (Linkam THMS600) could be attached to the spectrometer to monitor the Raman spectra during polymer curing cycles. The calibration of the spectrometer was regularly checked with a silicon crystal, (100) surface, which gives a strong peak at 520.7 cm^{-1}.

5.2 Raman spectra of CNT and peak fitting procedure

A typical Raman spectrum of CNT consists of four main bands [231,232], as shown in Figure 5-1. The radial breathing mode (RBM) at $v \sim 200\,\mathrm{cm}^{-1}$ corresponds to a collective radial displacement of the carbon atoms. It has a linear dependence on the CNT diameter and allows the determination of diameter and chirality [233]. The D-band ($v \sim 1,300\,\mathrm{cm}^{-1}$) is attributed to the in-plane breathing vibrations of carbon hexagons that are actually Raman in-active. However, structural defects in the graphite lattice enable a double-resonant process that makes these vibrations Raman active and dispersive [234]. The G-band ($v \sim 1,600\,\mathrm{cm}^{-1}$) is composed of tangential graphite lattice vibrations of various symmetries. Semiconducting and metallic CNT thereby exhibit different band shapes [235], originating from a diameter independent and a diameter dependent peak (with different dependencies for semiconducting and metallic CNT) [236]. The G'-band ($v \sim 2,600\,\mathrm{cm}^{-1}$)–sometimes called D*-band–is the

second harmonic of the D-band and is Raman active even without defects in the graphite lattice [237].
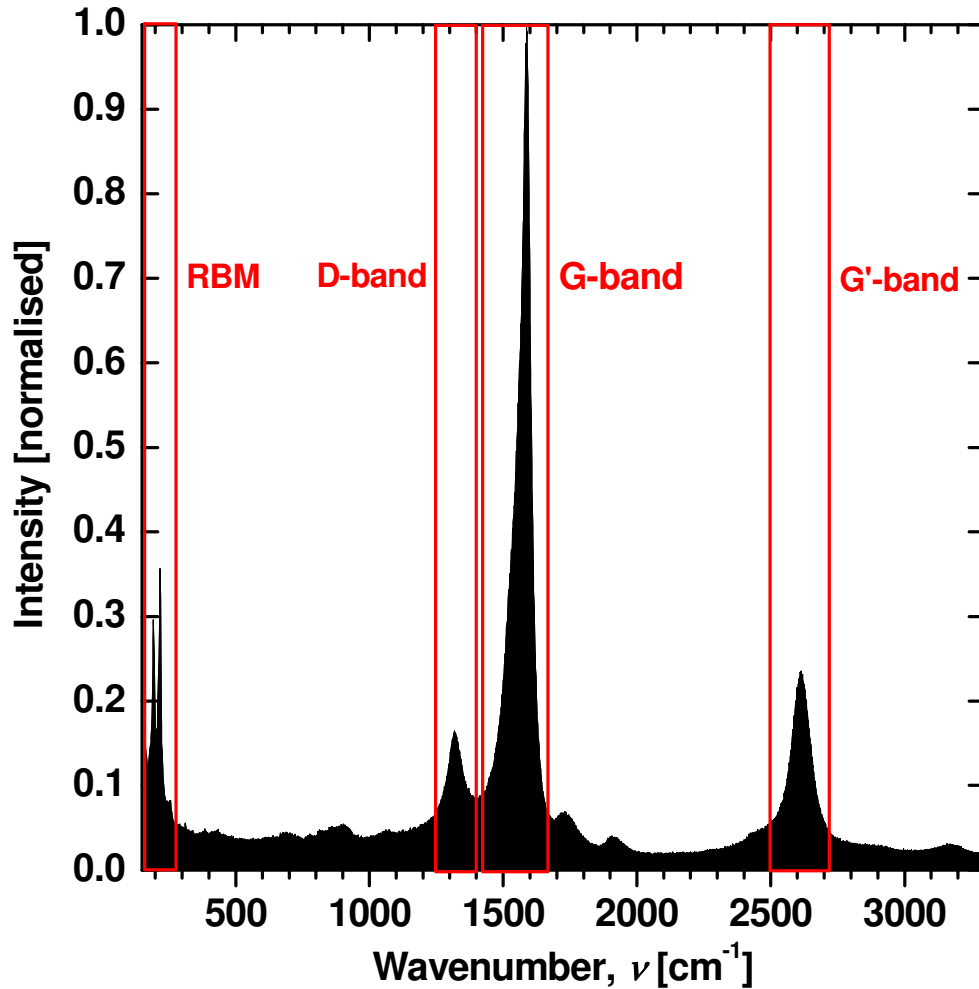

Figure 5-1 Raman spectrum of Elicarb SWCNT (see Section 2.2.4) with the characteristic vibration bands marked.

As the G-band is the only stable band concerning its intensity while all others can vary with e.g. laser intensity (due to changing graphitization degree), spectra are always normalised (Figure 5-1, Figure 5-6) or compared (Figure 5-4) with respect to the G-band. Moreover, when intensities of different bands need to be compared with each other (Section 5.4), the quantum efficiency of the CCD for the different wavelengths (Figure 5-2) has to be taken into account.

Relative Wavenumber, Δv [cm^{-1}]
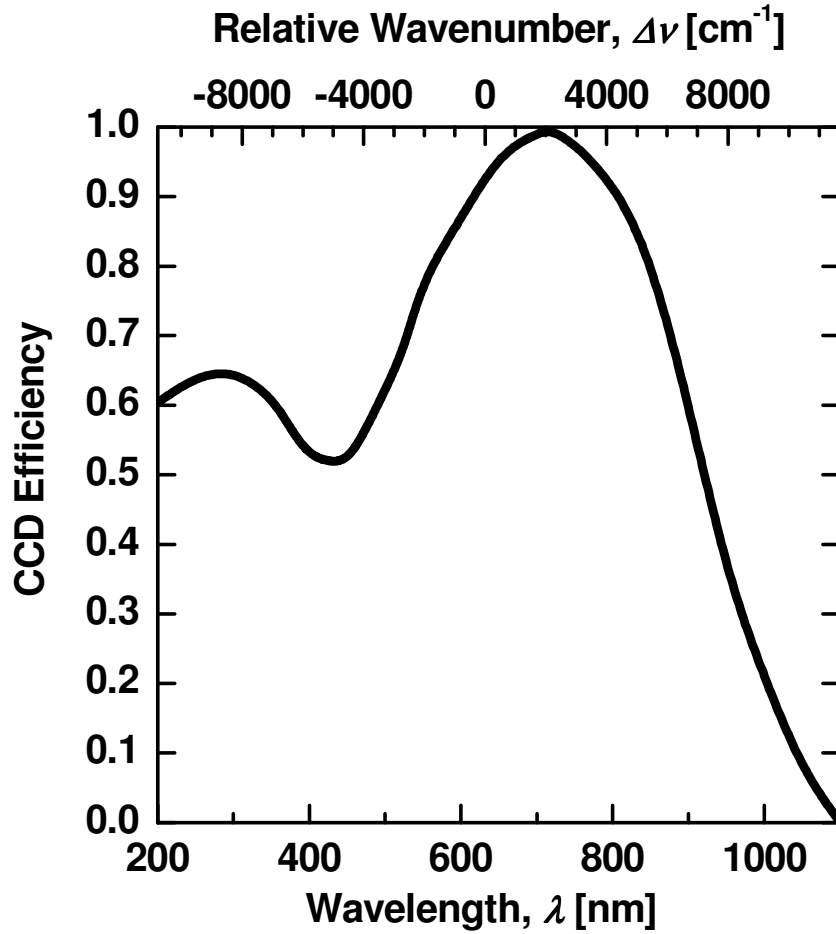
Figure 5-2 Quantum efficiency curve of the CCD vs. wavelength. The upper scale translates wavelength to wavenumber (relative to the 632.817 nm laser wavelength) according to the formula $\Delta v[\text{cm}^{-1}] = \frac{10^7}{\lambda^2[\text{nm}]} \Delta\lambda[\text{nm}]$. Negative relative wavenumbers represent an anti-Stokes shift of the laser wavelength to higher energies while positive ones denote a Stokes shift to lower energies. Relative wavenumbers are used throughout this thesis without explicitly noting it.

The band positions are determined by fitting one or two Lorentzian-Gaussian functions using the Raman spectrometer software LabSpec 4.18. Each band is extracted individually from the spectrum and a linear background is subtracted. The D-band of the Elicarb SWCNT (see Section 2.2.4) for instance is fitted with one function centred at ~ 1325 cm^{-1}, the G-band with two at ~ 1565 cm^{-1} and

1595 cm^{-1}, and the G'-band with two at ~ 2485 cm^{-1} and 2625 cm^{-1}. For the analyses however, only the positions of the dominant peaks of the G- and G'-band at 1595 and 2625 cm^{-1} are considered. Spectra of other CNT types are similarly fitted according to their respective peak frequencies.

5.3 Raman signal efficiency of various CNT
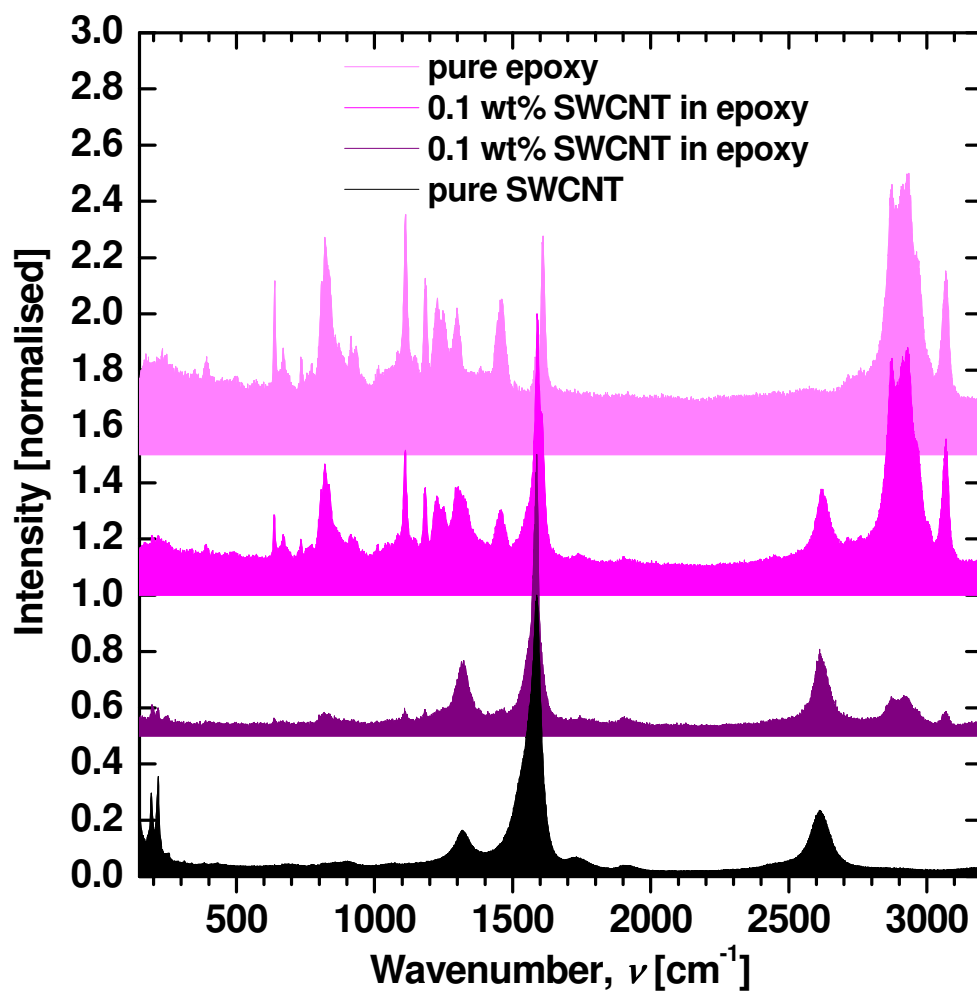
Figure 5-3 Raman spectra of pure Elicarb SWCNT, 0.1 wt% Elicarb SWCNT suspended in LY556/XB3473 epoxy (regions rich and poor in CNT) and pure LY556/XB3473 epoxy.
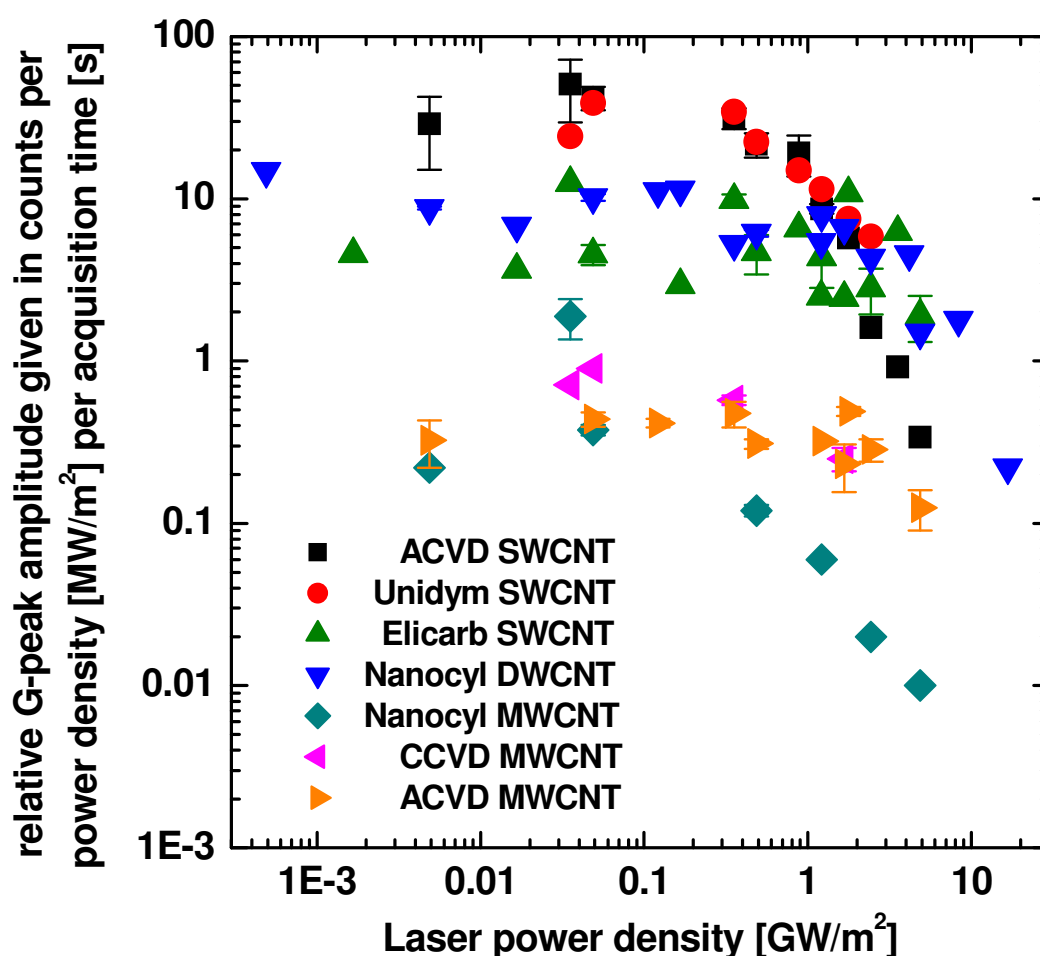
Figure 5-4 Raman signal efficiency of various CNT in dependence of the laser energy density in the focus. It should be noted that the laser energy density in the abscissa is given in GW/m^2 while the value that enters the relative G-peak amplitude calculation for the ordinate is taken in MW/m^2.

Analysing CNT/epoxy composites with extremely low CNT concentrations (e.g. 0.1 wt%) requires the use of CNT that produce the most intensive Raman signal, otherwise the signal of the composite will be dominated by the epoxy resin (Figure 5-3) and/or the acquisition time for a spectrum will be too long.

The Raman signal efficiency analysis consists of exposing CNT powder to the laser light, taking a Raman spectrum, fitting the G-peak and plotting its amplitude vs. the laser power density in the focus (Figure 5-4). In order to make

the analysis independent of the experimental parameters, the relative G-peak amplitude (the amplitude divided by the laser power density and the spectrum acquisition time) was used. The laser power density thereby is determined by the laser, the neutral grey filter and the objective. Losses due to the optical components were not considered.

As seen in Figure 5-4, SWCNT provide the most efficient Raman signal, particularly those produced by aerosol chemical vapour deposition (ACVD) [238] and by the HiPco process (Unidym Inc., USA). Despite their lower efficiency (~ 5 times) Elicarb SWCNT (see Section 2.2.4) were used in Section 5.4 and 5.6, as they were available in sufficient amount. All three MWCNT types used in the experiments in Section 4 exhibit a Raman signal even 20 times lower than the Elicarb SWCNT. Most CNT show a decreasing Raman signal for high laser power densities which is attributed to CNT heating and decomposition.

5.4 Temperature determination

The first measure when working with heat sensitive CNT/epoxy composites and a laser is to determine to what extent the laser heats up the composite. As the epoxy resin is transparent for the laser wavelength, heating predominantly takes place via the CNT. Therefore, Elicarb SWCNT (see Section 2.2.4) were exposed to different laser intensities between 0.01 and 100% of the maximum input (Figure 5-5a). The actual temperature T of the CNT was calculated from the anti-Stokes ($I_{\text{anti-Stokes}}$) to Stokes (I_{Stokes}) intensity ratio of the G- and D-bands [239]

$$\frac{I_{\text{Stokes}}}{I_{\text{anti-Stokes}}} = \left(\frac{\nu_i - \nu_p}{\nu_i + \nu_p}\right)^4 \exp\left(\frac{hc\nu_p}{k_B T}\right) \qquad \textbf{Eq. 5-1}$$

where ν_i and ν_p are the wavenumbers of the incident laser and that of the excited phonon, respectively, h is the Planck constant, c the light velocity and

k_B the Boltzmann constant. The different efficiencies of the detector at the Stokes and anti-Stokes band wavelengths were corrected using the quantum efficiency curve (Figure 5-2).

A linear relationship between temperature and band position is found in Figure 5-5a for temperatures up to ~ 400 °C. The higher scattering of the measured positions after 25% of the total laser power can be attributed to the onset of a "purification" and defect-healing process of the CNT [240,241]. At such high temperatures an irreversible decrease of the disorder parameter I_D / I_G was observed (not shown), I_D being the D-band intensity and I_G that of the G-band. The slopes for all three band dependences on temperature are determined up to 400 °C (inset in Figure 5-5a) and are found to be in accordance with those reported in literature [242].

Speculations exist whether it is reasonable to apply the Stokes/anti-Stokes method for temperature determination of CNT. For example, the authors in [243] argue that such a procedure is not possible, because both signals come from different types of CNT located in the laser focus. In this thesis, both the Stokes and anti-Stokes G-bands were found to have the same shape, coming from semiconducting SWCNT in resonance with the laser (Figure 5-6) [235,236].

To further test the reliability of the Stokes/anti-Stokes method, the SWCNT are heated using a programmable oven while keeping the laser intensity constant at 1% (Figure 5-5b). It can be seen that generally there exists a good correspondence between the programmed temperature (abscissa) and the one determined via the Stokes/anti-Stokes ratio (inset). The poor consistency at low temperatures is due to the low anti-Stokes band intensities which allow a less accurate peak fitting. The slopes of both curves also compare well with each other, except for the G'-band, which is double as high in the laser-heating experiment (Figure 5-5a) as in the stage-heating one (Figure 5-5b). Since the G'-band is commonly understood as the overtone of the D-band, the results obtained with the first method are considered to be the correct ones.
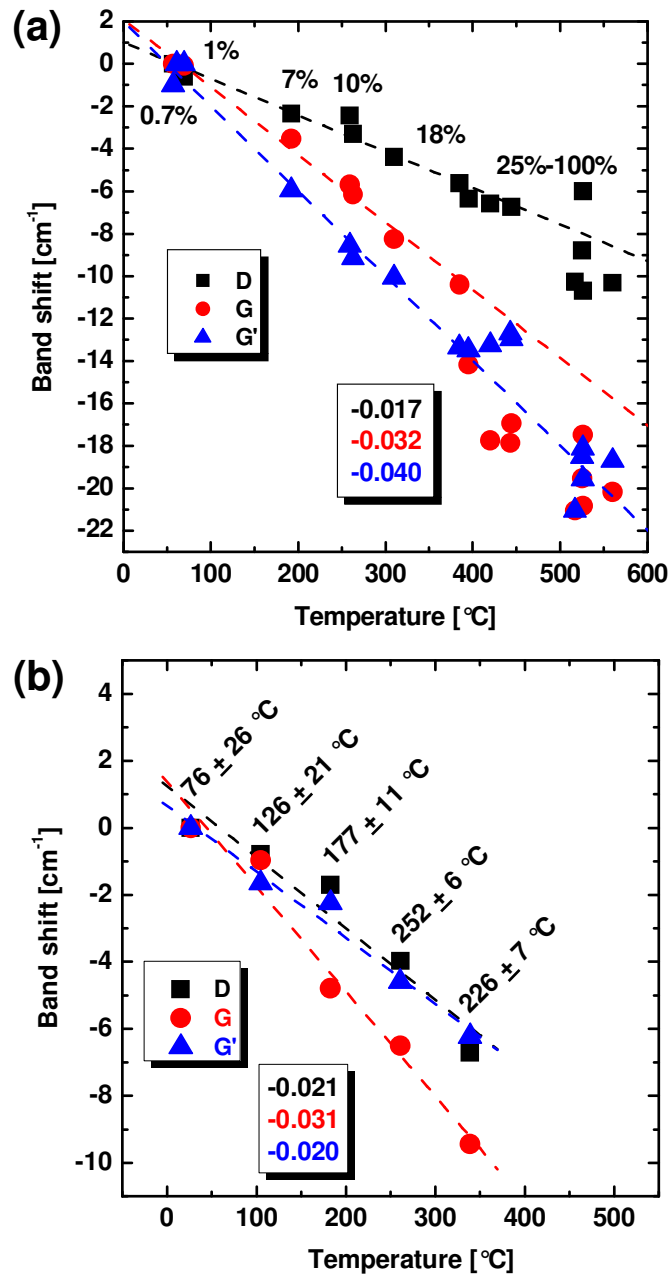
Figure 5-5 Temperature dependence of the Raman bands of Elicarb SWCNT. The inset display the slopes (in $cm^{-1}K^{-1}$) of this dependence. (a) The temperature was adjusted by varying the laser intensities (in % of the total intensity) and was determined by the Stokes/anti-Stokes ratio. (b) The laser intensity was kept constant at 1% while the temperature was adjusted by the oven (abscissa) and crosschecked with the Stokes/anti-Stokes ratio method from the D- and G-bands (the inset displays mean temperatures and standard errors).
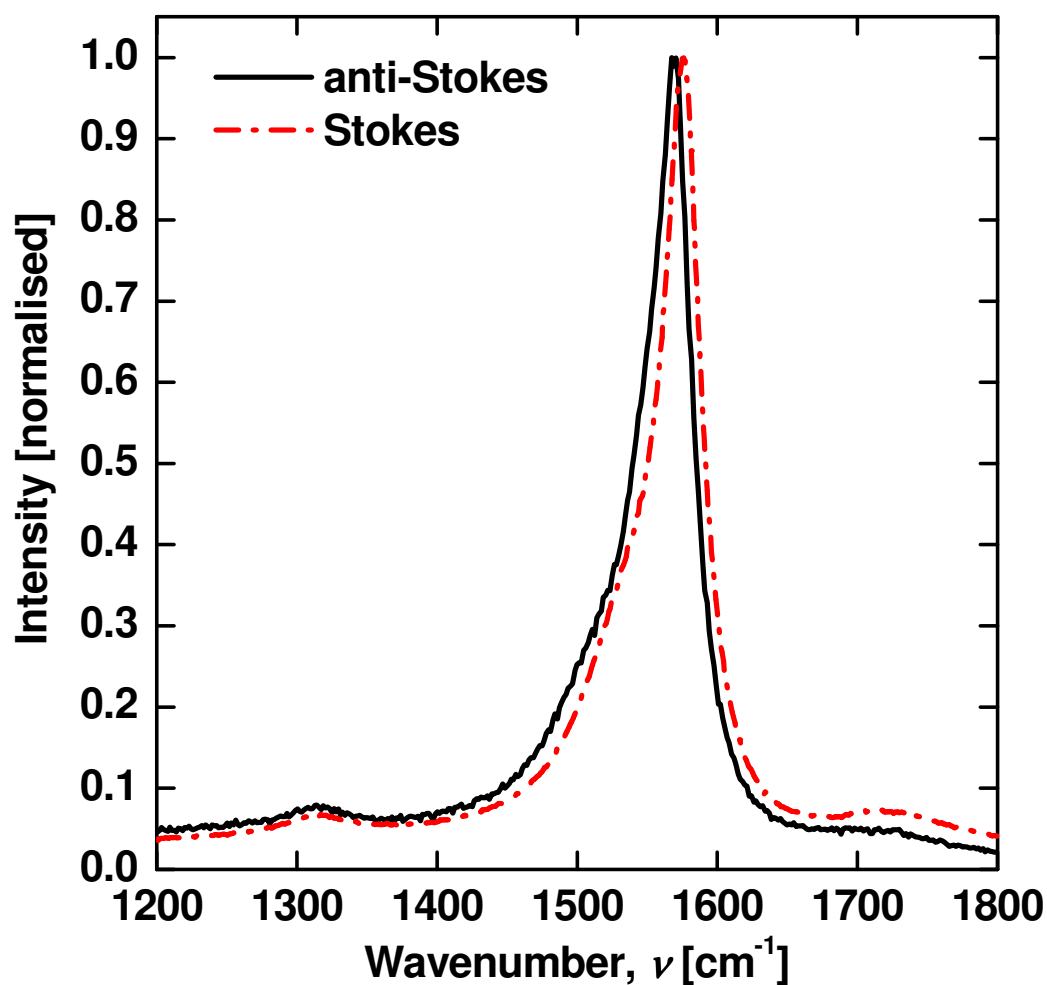
Figure 5-6 Normalised Stokes and anti-Stokes G-bands of Elicarb SWCNT plotted with positive wavenumber values for the anti-Stokes signal too.

5.5 Monitoring the orientation of CNT

The Raman signal intensity strongly depends on the angle between laser polarisation and CNT main axis [244-250]. This dependency can be used to determine the orientation of CNT within a polymer matrix and thus monitor and quantify CNT alignment due to e.g. electric fields (Section 4.10).
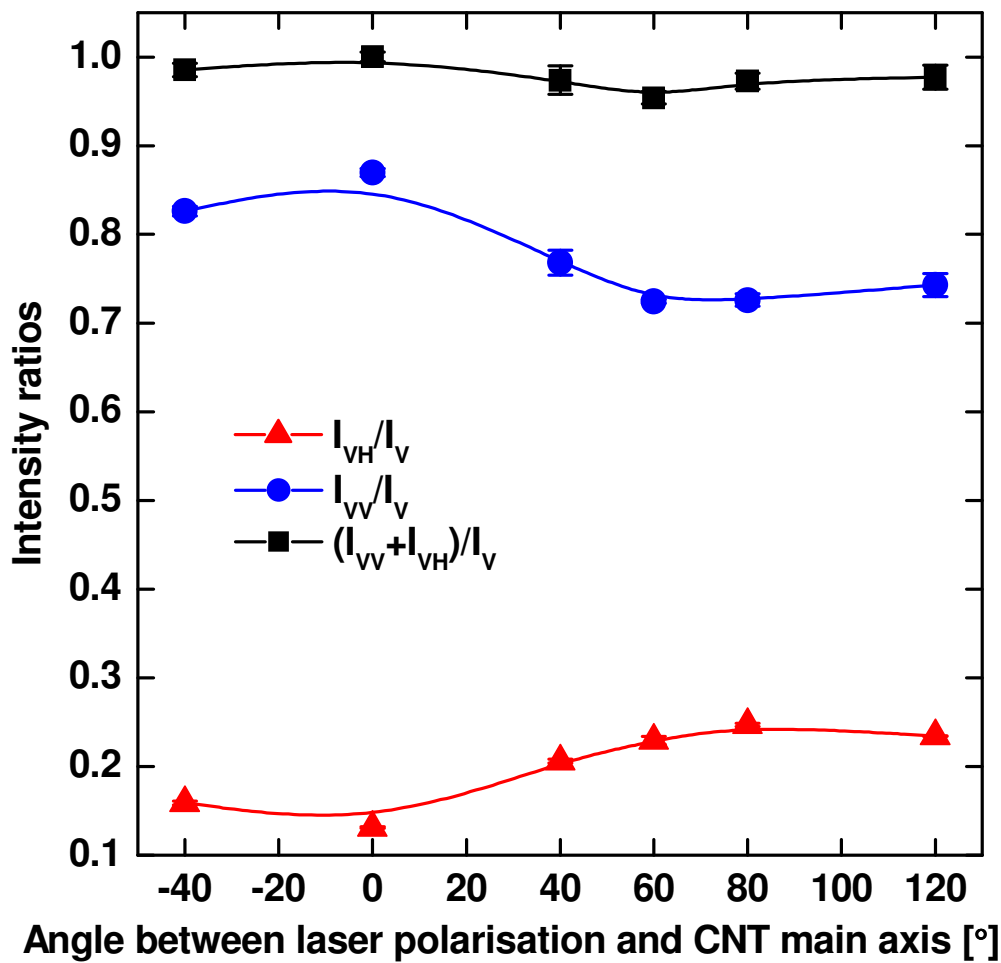
Figure 5-7 Raman intensity (mean of D-, G- and G'-peak height) of the CCVD-aligned-grown CNT (see Section 2.2.3) vs. the angle between laser polarisation and CNT main axis. The VH setup denotes the vertically polarised laser and the horizontally polarized analyser, while in the VV setup the polarisation analyser is also polarized vertically. V denotes that no polarisation analyser was used.

Polarised Raman spectroscopy is first tested on a sample of perfectly aligned CNT–on the CCVD-aligned-grown CNT introduced in Section 2.2.3. In order to analyse the same spot on the sample, the laser polarisation is rotated and not the sample. However, it should be avoided to direct light of different polarisation to the grating because this would result in intensity variations of the diffracted light. The solution is to position a half-wave plate so that both the laser light passes it on his way to the sample as well as the Raman signal on his way from the sample to the grating [244]. The half-wave plate is able to rotate the

polarisation of the laser light–which is vertically polarised initially (thus labelled V)–to any desirable angle. The emitted Raman signal–although depolarised to a certain extent (see I_{VH} / I_V ratio in Figure 5-7)–is then rotated back by the half-wave plate. A polarisation analyser in front of the grating takes care to let only Raman signals which are polarised parallel to the incident laser light reach the grating (this setup is often called VV-configuration in literature).

The Raman signal intensity as a function of the angle γ between laser polarisation and the CCVD-aligned-grown CNT main axis is determined by taking the mean normalised height of the fitted D-, G- and G'-peaks (Figure 5-8). The first observation is that all peaks show the same dependence on γ, as already anticipated and confirmed by others [247,249]. The second observation is that they follow neither the intensity evolution predicted by non-resonant bond-polarization theory (dash-dotted line in Figure 5-8a: $I \sim (3\,(\cos\gamma)^2 - 1)^2$) [245] nor that predicted by resonant theory (dash-dotted line in Figure 5-8b: $I \sim (\cos\gamma)^4$) [246].

One explanation could be the shape of the CCVD-aligned-grown CNT. Inspecting their high magnification SEM image (Figure 2-3) reveals that they are not straight but wavy. Therefore, Raman signal contributions are expected from segments of the CNT that have a different orientation than the overall CNT, e.g. -45° and +45°. Contributions from such segments are simulated in Figure 5-8 (dashed curves) with half of the intensity of the original theoretical (dash-dotted) curves. Interestingly, summing up all three curves for each theory yield much better fits to the experiment (continuous lines in Figure 5-8). However, the contributions from non-resonant theory fit the experimental data better, suggesting that phonons were excited non-resonantly in the CCVD-aligned-grown CNT. There exist polarised Raman studies on CNT which seem to be excited non-resonantly [247,249], but there also exist some studies which show resonant excitation of the CNT [248,250].
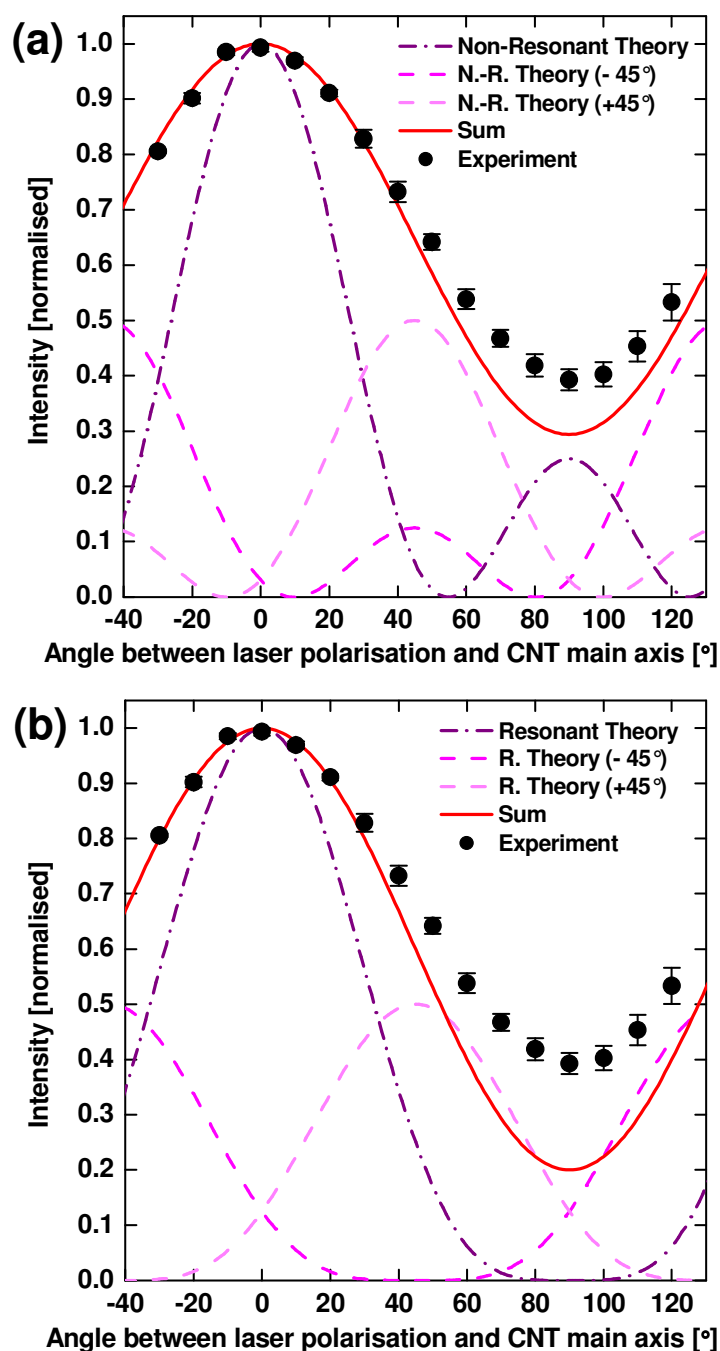
Figure 5-8 Experimental results (circles) of the Raman intensity (mean of D-, G- and G'-peak height) of the CCVD-aligned-grown CNT (see Section 4.2.1.3) vs. the angle between laser polarisation and CNT main axis. The dash-dotted lines denote the expected Raman intensity evolution according to (a) non-resonant theory and (b) resonant theory. The dashed lines are halved in intensity and shifted by -45° or +45° with respect of the particular theory. The continuous lines are the normalised sums of the shown dashed and dash-dotted lines.

Jorio et al. [244] find a similar Raman intensity evolution with polarisation angle as presented in Figure 5-8 and give another explanation. They believe that the presence of neighbouring isolated SWCNT or of multiple walls in a MWCNT leads to superimposed signals which prevent the Raman intensity from vanishing for laser polarisations perpendicular with respect to the CNT main axis. This would explain the results presented in [247,249] even without drawing the conclusion that the CNT were excited non-resonantly. However, with this explanation, it is not clear why the Raman intensity can vanish for the SWCNT bundle analysed in [248].

The presented results show that more analyses are necessary before being able to reliably determine the CNT orientation in a polymer matrix. It is important to known whether the CNT are excited resonantly or non-resonantly before interpreting the experimental data [249]. Furthermore, straight CNT should be used to avoid contributions from CNT segments that are not parallel to the CNT main axis.

5.6 Sensing stresses in CNT/epoxy composites

5.6.1 Motivation

The motivation for these analyses was the observation of conductivity drops at the end of the curing cycles of various nanoparticle/epoxy composites [226]. It seems that composites with filler concentrations below the percolation threshold that were exposed to electric fields during their curing cycles are affected predominantly (Figure 5-9). The assumption is that stresses are built up in the composite during the curing process and finally disrupt some of the established conductive paths.
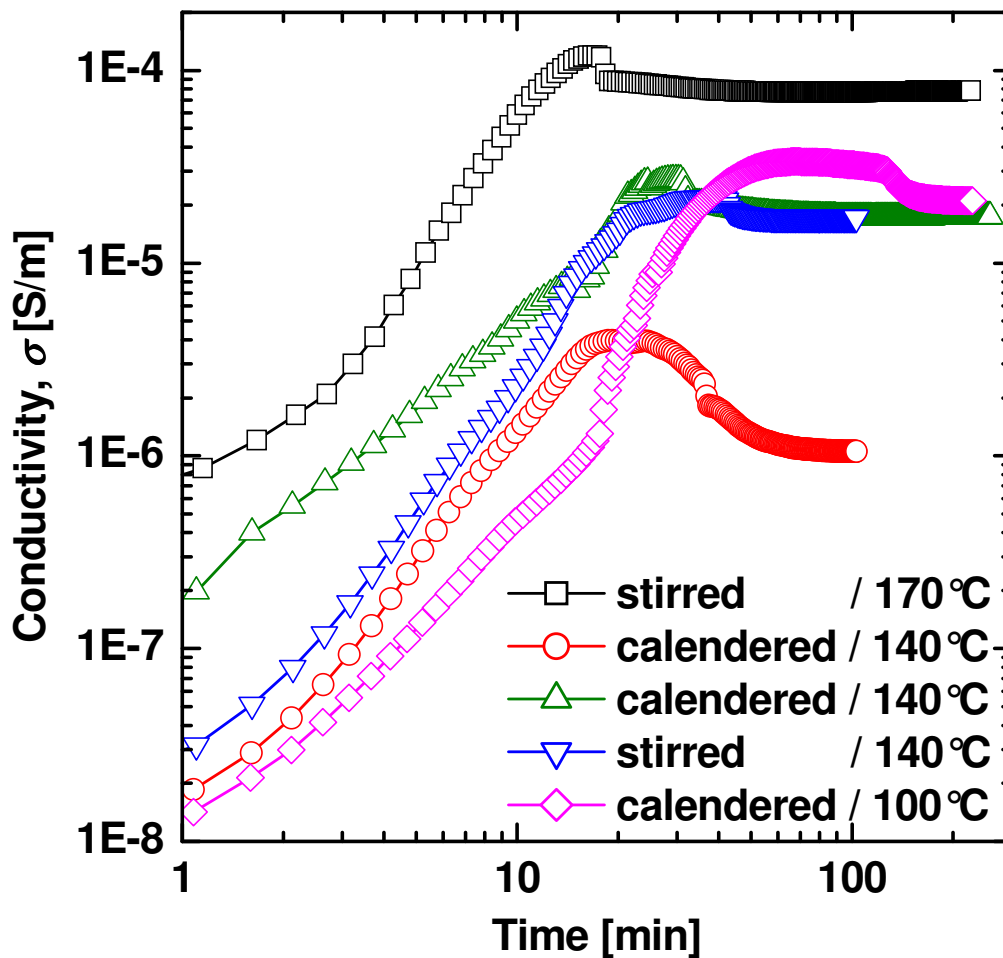
98

Figure 5-9 Curing experiments with in situ conductivity monitoring. 0.01 wt% Nanocyl CNT suspended in the LY556/XB3473 system were aligned by an electric field $E = 11$ V_{rms}/mm during the curing process. The suspensions were either stirred or calendered and then cured at the specified temperatures.

Processing-induced residual stresses in thermosets are due to the uneven distribution of the resin components and the presence of foreign elements (e.g. reinforcing fibres), which leads to conversion and thermal gradients at the different stages of the curing cycle. These gradients are responsible for irregular volumetric shrinkage of the resin during the crosslinking reaction (resulting in chemically induced stresses) and during the cooling to room temperature (resulting in thermally induced stresses). The stress field affects significantly the

mechanical strength of the material in a variety of ways, and has to be taken into account for the product design [251-255].

Different methods based on both numerical [256,257] and experimental [257-265] approaches have been suggested to characterise the evolution of cure and thermally induced residual stresses in thermoset resins and composites through changes in density, volume and stiffness over time. For example, Lange et al. [258,259] utilised a bilayer-beam bending technique and parallel-plate rheometry to investigate the onset of stresses in epoxy films. In combination with predictions based on elastic theory, it was found that only stresses occurring while cooling below the glass transition temperature T_g yield an important contribution to the overall residual stress state at the end of the cure schedule.

In thermoset composites, an alternative approach involves the use of conductive macroscopic- and nano-fibres which can act as self-strain sensors as well as reinforcing elements. For example, single carbon fibre/epoxy composites were prepared by Wang et al. [257] and Park et al. [265] and studied regarding their electrical resistivity as a function of curing time and temperature. When heated/cooled in association with a polymer matrix, stresses build up across the fibre surface because of relatively large differences in the thermal expansion coefficient of the two components. The new "strained" state of the fibre at the end of the curing cycle yields a difference in conductivity from its original value, which was found to be larger for higher processing temperatures due to more extensive formation of interfacial thermal stresses.

In recent years, SWCNT have become the focus of attention in many studies [266-270] regarding strain and pressure sensing in the micro- and nano-scale. Early Raman spectroscopic investigations carried out by Wagner and collaborators [267,268] demonstrated the sensitivity of the D*-band (also named G'-band) of SWCNT to the pressure exerted by different liquid and viscous media. Further studies performed independently by Wagner [268] and Young

[269,270] dealt with a Raman response to applied mechanical deformations of SWCNT cured within thermoset polymer matrices. The knowledge of the stress-strain and Raman shift-strain relationships of the composites made it possible to develop high resolution strain mappings in the vicinity of defects or stress concentrators. The microscale sensing characteristics of SWCNT enables their utilisation to monitor the evolution of residual stresses during curing and thermal annealing of epoxy resins.

5.6.2 Experimental procedure

Elicarb SWCNT (see Section 2.2.4) were used such that the loading in the final composite was 0.2 wt%. The SWCNT were dispersed in the resins of the LY556/XB3473, LY564/A2954 and L135/H137 systems (see Section 2.1) by a three-roll-mill procedure previously reported by Gojny et al. [95]. The respective hardener was distributed within each SWCNT/epoxy mixture by means of mechanical agitation. The mixture was degassed in a vacuum oven and cured according to the schedule presented in Table 2-1.

For the production of the samples for the sensing experiments, the liquid mixture of SWCNT/epoxy/hardener was spin-coated onto a glass substrate with gold electrodes attached. Tinned copper wires were soldered onto the electrodes and used as electrical contacts for the conductivity measurements. The HP 4284A LCR meter was attached to the programmable oven (Linkam THMS600) to monitor the conductivity evolution during polymer curing cycles. The electrical conductivity of the composite was determined according to the method described in Section 4.2.2.

5.6.3 Chemically induced stresses

The curing curves obtained by Raman and impedance spectroscopy for the three composite systems are presented in Figure 5-10. In contrast to other study cases [267-270], in this analysis the G-band was preferred over the G'-band for monitoring the SWCNT response to the changes of temperature and pressure exerted by the curing resin. Although the G'-band possesses twice the

wavenumber sensitivity of the G-band, its scattering for different sampling positions on the composites was found to be five times higher than that of the G-band (Figure 5-11). Changing the sampling spot is an unavoidable effect of the in situ curing, as the sample moves slightly when adjusting a different temperature.
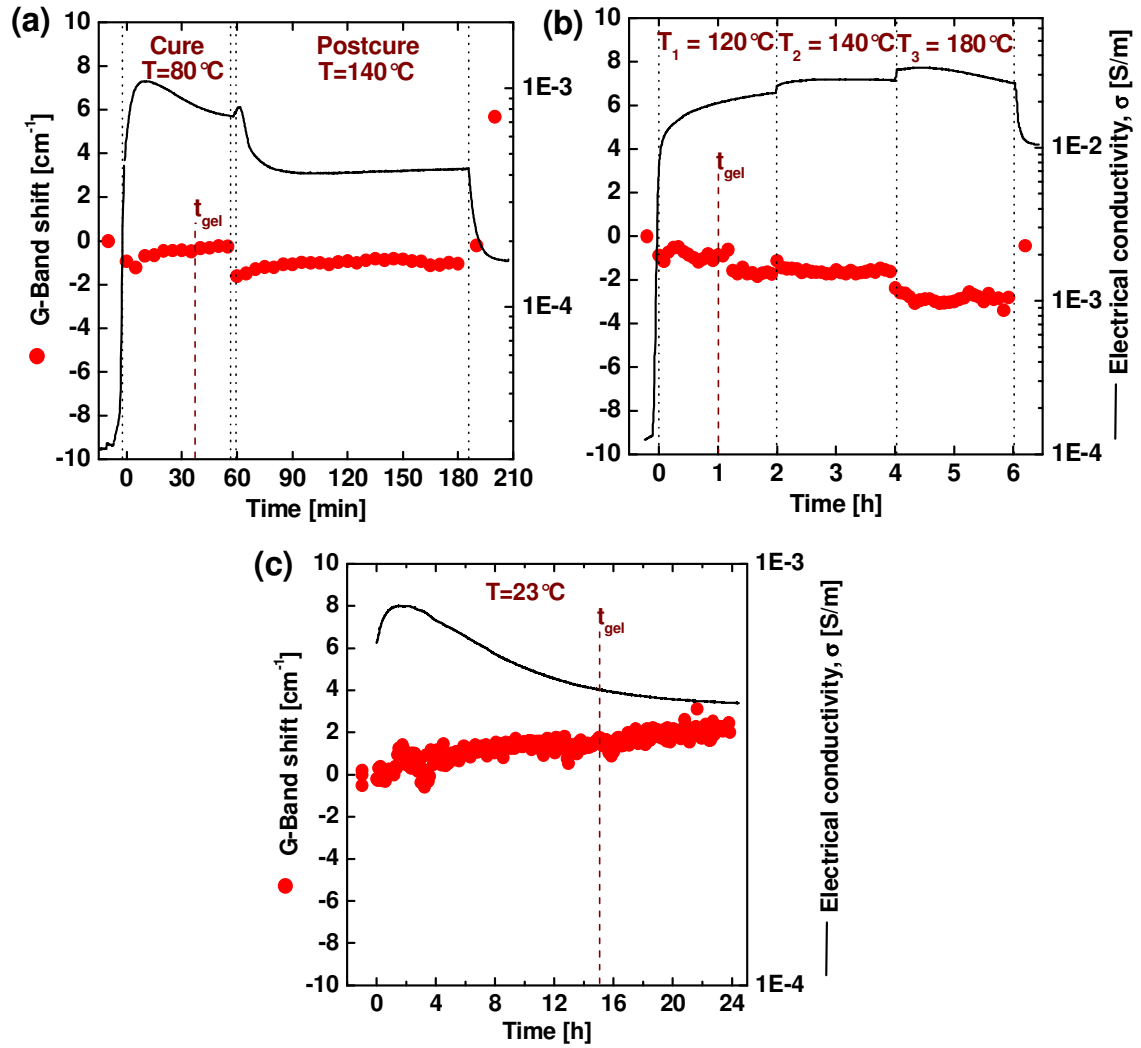

Figure 5-10 Curing experiments with in situ Raman and conductivity analyses for (a) the LY564/A2954 system, (b) the LY556/XB3473 system and (c) the L135/H137 system, each with 0.2 wt% Elicarb SWCNT filler concentration. The time regions before the first isotherm and after the second (a) or third (b) isotherm show the band positions at room temperature before and after the curing cycle, respectively.
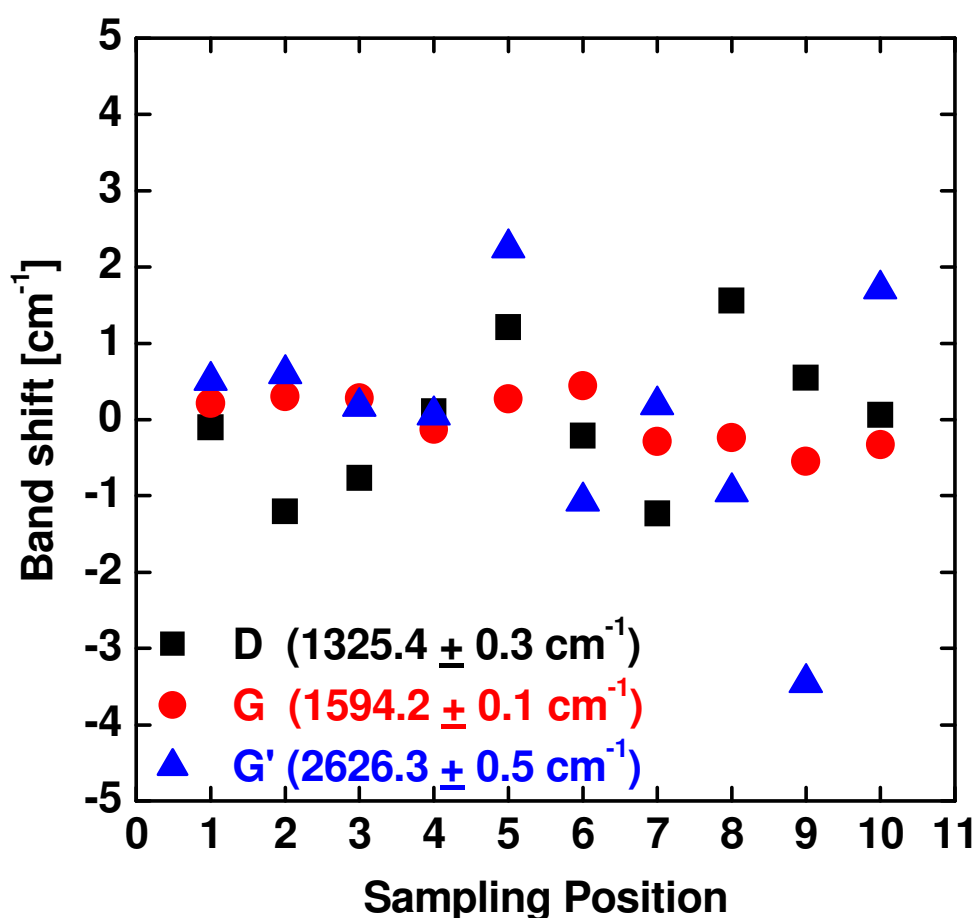
Figure 5-11 Band shift vs. beam position for a fully cured composite sample (L135/H137 + 0.2 wt% Elicarb SWCNT). The values reported between parenthesis are the average values of each band fitted through a Lorentzian-Gaussian function, as well as their respective standard errors.

It can be seen in Figure 5-10 that all three composite systems reach their gelation time t_{gel} without showing any significant changes in the Raman signal. The time to gelation refers to the point after which the crosslinking density of the curing resin becomes sufficiently high to hinder reversible deformation of the network. In oscillatory rheology, t_{gel} is normally taken as the crossover point between the storage and the loss modulus.[7] This transition is associated with the onset of chemical residual stresses because volumetric shrinkage occurs

---

[7] The same method was used here to determine the gelation time.

subsequently in a highly entangled structure with extremely reduced mobility. The time to vitrification t_{vit} is reached when the curing temperature becomes essentially the same as T_g, and the reaction becomes diffusion- rather than chemically-controlled. At this point, the storage modulus becomes virtually constant in the rheological measurements. t_{vit} was determined to be roughly twice t_{gel} for the hot curing systems [271] and therefore is not reached before the second temperature step. But even after this step, no changes in the Raman signal are visible except a slight decrease of the band position which is attributed to the temperature increase. Even for the room temperature curing system–which was chosen for analysing the build-up of residual stresses independently from thermal influences–a G-band shift of only 2 cm^{-1} is detected which is most likely caused by a wavelength drift of the spectrometer within a day-long measurement. All these results suggest that no chemical shrinkage is present–or at least detectable–in the analysed systems.

The conductivity measurements offer additional and complementary information about the curing behaviour of the systems. A comparison between the initial conductivity of the liquid dispersion and the final conductivity of the cured composite (both at room temperature) reveals an increase of one order of magnitude for the LY564/A2954 system and of two orders of magnitude for the LY556/XB3473 system. This improvement is attributed to the CNT network formed during the curing process. However, the conductivity development during the curing process seems to be different for the aliphatic polymer composites (Figure 5-10a,c) compared to the aromatic one. All three materials have in common that the conduction process is determined by electrons tunnelling between neighbouring SWCNT. As expected for a tunnelling process, the sample conductivity increases with increasing temperature (visible at each heating step in Figure 5-10a,b) and decreases with decreasing temperature. However, the tunnelling processes within the aliphatic polymer composites seem to be dominated by another mechanism which lowers the sample conductivity to a constant value. The decreasing mobility of the suspended ions

with increasing crosslinking density would explain this behaviour [272,273], but more experiments are necessary in order to validate this assumption.

5.6.4 Thermally induced stresses

After their curing cycle, the hot curing systems were re-heated stepwise in order to identify the shift contributions from different physical regions (Figure 5-12). In the Raman measurements of the two systems, a change of the slope can be clearly identified when crossing the glass transition temperature. It is inferred that above this temperature a "stress releasing" effect arises from the enabled movement of the molecular chains. The fact that such an inflection point is not found for the electrical conductivity measurements suggests that the CNT network is not largely influenced by the build-up of residual stresses.

The Raman shift in the region above the glass transition is attributed to the temperature dependence of the SWCNT immersed in a resin medium which is, given the more constricting environment for their free expansion [267], lower than for SWCNT in air (see Figure 5-5).

For the LY564/A2954 system significantly higher shift rates with temperature are found than for the LY556/XB3473 system. The thermal expansion coefficients of both systems are to equal to explain this difference (Table 2-1). Another explanation might be a difference in the bonding strength at the interface of the two types of composites. It is presumed that the LY564/A2954 system could have an enhanced interfacial strength because of the epoxy/cycloaliphatic chemistry of this system. In liquid state, strong intermolecular forces act between the molecular chains of the epoxy monomer and the CNT. The initial interaction of the SWCNT with the hardener is expectedly lower, since it does not contain benzene rings in its structure. Therefore, a preferential growth of the polymer chains could occur near to the SWCNT surface.
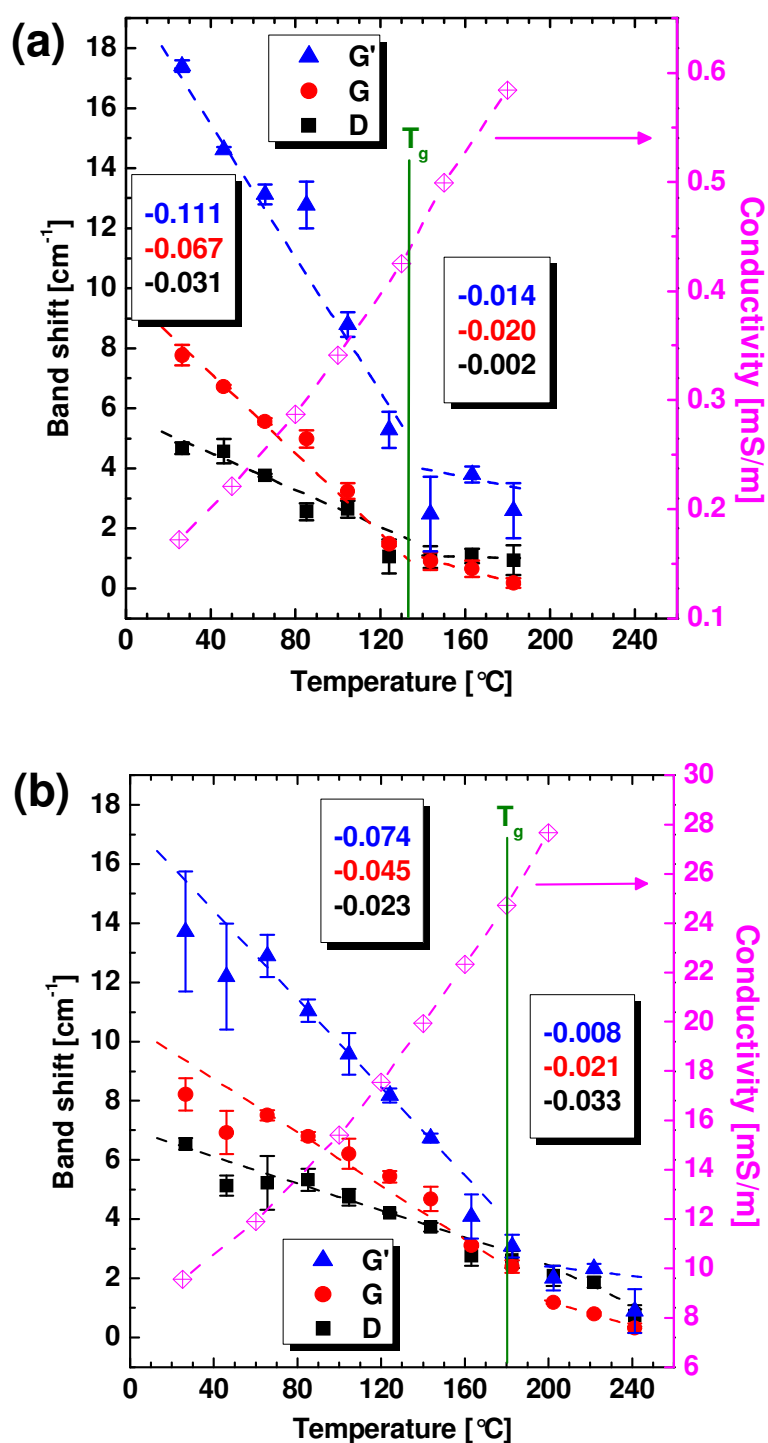
Figure 5-12 Temperature (controlled by oven) dependence of the Raman bands of 0.2 wt% Elicarb SWCNT embedded (a) in the LY564/A2954 system and (b) in the LY556/XB3473 system. The inset display the slopes (in $cm^{-1}K^{-1}$) of this dependence below (left inset) and above (right inset) the glass transition temperatures T_g. The laser intensity was kept constant at 1%.

Initially (i.e. within the first isotherm), the concentration of hardener at the zones far from the CNT is expected to be higher, leading to an inhomogeneously cross-linked network. This "inhomogeneous" curing process is completed during the post-curing process, in which the residual epoxy groups closely located to the surface of the SWCNT and the residual amine groups are able to react, with further bonding of the matrix to the interphase. The result is a material with enhanced interfacial strength. Evidence for the existence of such mechanism has been provided by Wise et al. [274] and Star et al. [275], however, its validity for the systems presented here still has to be verified. In the case of the LY556/XB3473 system, both the resin and hardener are aromatic compounds for which no "inhomogeneous" curing process is expected to take place.

5.7 Summary and conclusion

The Raman spectra of CNT were analysed under various aspects. It was found that SWCNT and DWCNT yield up to 100 times more intense Raman signals than MWCNT. The Stokes/anti-Stokes method for determining the temperature in the laser focus was shown to be applicable and accurate for the analysed CNT.

Polarised Raman spectroscopy was successfully applied to aligned CNT in order to assess the potential of determining their orientation distribution. However, difficulties arise from the waviness of the CNT as well as from not knowing whether the CNT are excited resonantly or non-resonantly by the laser light.

The stress sensing capabilities of Elicarb SWCNT in epoxy resin was demonstrated. Changes attributed to the ongoing chemical and physical transitions of the curing resins were monitored by means of Raman and impedance spectroscopy. For all analysed systems it was found that chemically induced stresses produce a negligible effect on the overall residual stress state of the cured product and/or are far too low to be detected by Raman

spectroscopy. Recent experiments using HiPco SWCNT (Unidym Inc., USA) as stress sensors [276] yield better Raman signals and confirm these statements.

The Raman response of the Elicarb SWCNT to temperature was found to be also dependant on the surrounding medium, showing a more pronounced shift rate for SWCNT in air, as for those immersed in a polymer matrix. In the latter case, a sudden change of the shift rate could be clearly identified around the glass transition temperature of the polymer system.

In contrast to the Raman measurements, a change in slope was not observed for the conductivity of the cured samples reheated up to their ultimate processing temperature. It is assumed that the magnitude of thermal stresses that developed under the studied conditions is not sufficiently high to affect the integrity of the established CNT network. The only explanation for the initially presented conductivity drop at the end of the curing cycles of various nanoparticle/epoxy composites remains the decreasing ionic conductivity of the system with progressive curing. This seems to lower the conduction between adjacent CNT and finally lead to tunnelling conduction when the vitrification time is reached.[8]

---

[8] Private communication: Ingo Alig (Deutsches Kunststoff-Institut, Darmstadt, Germany; 10. September 2007)

6 Rheological analyses

The huge impact of shear forces on the agglomeration of CNT, the formation of a conducting network and the resulting steep increase of the electrical conductivity of the suspension is introduced in Section 4.3. So far, shear forces were exerted by the standard mixing equipment, a dissolver disk. It produces a rather complicated shear state in the suspension which is hard to analyse. Controlled shear states are found in a rheometer, which is most suitable for analysing the influence of shear forces on the network formation of CNT in a polymer.

The rheometer used in this thesis allows monitoring the CNT/epoxy suspension optically (Section 6.3.1), electrically (Section 6.3.2) and rheologically (Section 6.4) at same time. This is a unique possibility worldwide. The group of Erik Hobbie at NIST [213] reported in 2004 for the first time on rheological and optical studies of flow-induced clustering inside of CNT/polyisobutylene suspensions–performed on two different devices, one for the rheological and the other for the optical measurements. The same holds for the group of Alan Windle [281] who analysed CNT/epoxy suspensions rheologically and optically in 2006. Later on, Hobbie's group impressively demonstrated the break-up of an individual CNT agglomerate with increasing shear rate [277].

6.1 Rheology of fibre suspensions

Rheological parameters such as viscosity, storage and loss modulus of fibre suspensions deviate from the pure matrix parameters if the fibres start to interact physically with each other. Three liquid states are discriminated, depending on fibre diameter d, length ℓ and volume concentration ϕ^{vol} [278].

In dilute suspensions, the average distance between the fibres is much larger than their length. The fibres do not interact with each other. In semidilute suspensions, the fibres are still separated far enough not to touch each other. However, this holds only for the static case. If the fibres are subjected to movement or rotation, they are likely to touch each other. In concentrated suspensions, the fibres are likely to touch each other even in the static case because their excluded volumes ($d\ell^2$) overlap. Typical CNT aspect ratios $\ell/d = 8{,}000 - 600$ as used throughout this thesis yield:

Dilute region
$$\phi^{vol} \ll \frac{\pi}{4}\left(\frac{d}{\ell}\right)^2 = 10^{-6} - 10^{-4} \text{ vol\%}$$

Semidilute region
$$\frac{\pi}{4}\left(\frac{d}{\ell}\right)^2 \ll \phi^{vol} \ll \frac{\pi}{4}\left(\frac{d}{\ell}\right)$$

Concentrated region
$$\phi^{vol} \gg \frac{\pi}{4}\left(\frac{d}{\ell}\right) = 0.01 - 0.1 \text{ vol\%}$$

Interactions between the suspended fibres seem to be likely for the whole concentration region (0.001-1 wt%) analysed in this thesis. These interactions are believed to be necessary for observing a kinetic percolation threshold as described in Section 4.3. In the concentrated region (above ~ 0.1 wt%) however the interactions are too intense to allow any kinetic processes and therefore yield a statistical percolation (Section 4.3).

The balance between hydrodynamic and Brownian forces is described by the rotational Peclet number $Pe_r = \dot{\gamma}/D_r$ with the shear rate $\dot{\gamma}$ and the rotational diffusivity $D_r = \dfrac{3kT(\ln(\ell/d) - 0.8)}{\pi\eta\ell^3}$ [213,278]. The parameter range used in this thesis yields $D_r = 10^{-9} - 10^{-3} \text{ s}^{-1}$ and $\dot{\gamma} = 0.01 - 100 \text{ s}^{-1}$. This means that Brownian forces can always be neglected when compared to the hydrodynamic forces that act on the suspended fibres.

The shear flow between the rheometer plates is characterized by the Reynolds number $Re = \dot{\gamma} s^2 \rho / \eta$, s being the separation length of the plates, ρ and η the density and the viscosity of the matrix [213]. Below $Re = 2{,}000$ the shear flow is laminar and above it turbulent. In this thesis, the Reynolds number ranges between 10^{-6} and 10, thus, laminar flow is sustained under any conditions.

6.2 Experimental procedure

Rheological properties were measured with a stress controlled rheometer (StressTech HR Fluid Rheometer) from Rheologica Instruments AB, Sweden, with 30 mm parallel plates and gap sizes between 0.5 and 1.3 mm. The lower plate is made of quartz glass and allows looking inside the gap using an optical microscope which is attached to a digital camera system. Various plate systems furthermore allow the in-situ measurement of electrical conductivity. One system, which is denoted as *bottom-bottom electrodes* (Figure 6-1a), consists of a lower quartz plate with two gold electrodes (5 × 10 mm) deposited on it and an insulating upper plate made of glass. It allows to exert electric fields and to measure conductivity along the shear flow direction. The optical microscope can be adjusted to monitor the 2 mm gap between the electrodes. Another plate system, denoted as *top-bottom electrodes* (Figure 6-1b), consists of a lower quartz plate with an annular, gold electrode (with 10 and 30 mm inner and outer diameter, respectively) deposited on it and an upper plate made of metal. The upper plate is electrically insulated at the top of its shaft and possesses a mechanism below the insulation which allows electrical contacting. With this system, electrical fields and conductivity measurements can be accomplished perpendicular to the shear flow in direction of the velocity gradient.

The suspensions analysed with the rheometer were produced following various routines, which are addressed individually in the following sections.
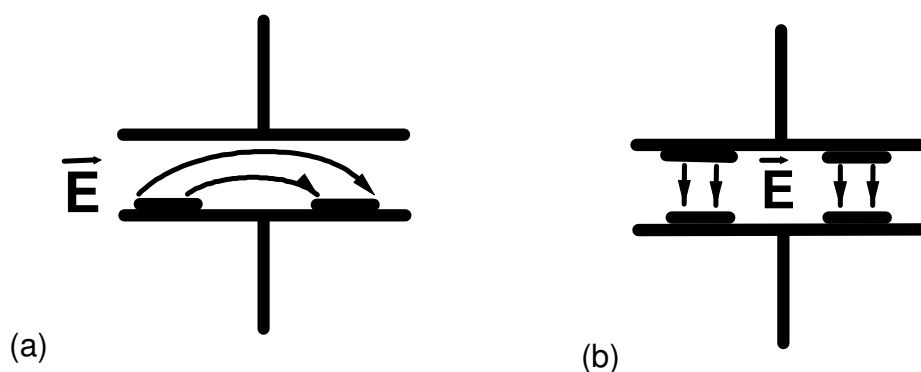
(a)   (b)

Figure 6-1 Sketch of the (a) bottom-bottom electrode and the (b) top-bottom electrode plate systems.

6.3 Shear induced network formation and destruction

6.3.1 Optical analyses

For the optical analyses, a suspension of 0.05 wt% Nanocyl CNT in LY556 epoxy resin was produced following the routine described in Section 4.2.1.1. The routine however was stopped before adding the hardener to the suspension. Instead, 1 ml of the suspension was transferred to the rheometer, heated to a constant temperature and then exposed to various shear rates. Images of the suspension were taken during the shearing process with the built-in optical microscope of the rheometer every 30 sec. Each image could later be related to a certain shearing condition by the time stamps of both, the images and the shearing program.

Figure 6-2 illustrates the built-up of agglomerates while the suspension is sheared with 0.1 s^{-1} and later with 1 s^{-1}. A shear rate of 10 s^{-1} however seems to be already too high for the established agglomerates, they start decomposing into smaller ones. Increasing the shear rate to 100 s^{-1} instantaneously decreases the agglomerates sizes even more. Figure 6-3 displays what happens if the shear rate is now decreased again. At 10 s^{-1} the agglomerates gather together to form bigger ones which–interestingly–match

112

the size of the agglomerates from Figure 6-2 at the end of their 10 s^{-1} shearing (which was a destructive shear process). Further lowering of the shear rate to 1 s^{-1} and later 0.1 s^{-1} reassembles the agglomerates to sizes found in Figure 6-2 at the end of the respective shear conditions. This finding proves the agglomeration process to be reversible.

It is important to note that the estimation of the maximum shear rate exerted by the dissolver disk used in the experiments in Section 4.3 amounts to ~ 1 s^{-1} when rotating with 50 rpm. This rotational speed proved to form agglomerates efficiently while 2000 rpm did not. As reported in the previous paragraph, 1 s^{-1} is the maximum shear rate that is able to build up agglomerates in a rheometer and it perfectly coincides with the shear rate from the estimation.

Successive optical analyses focus on the influence of temperature (6.3.1.1) and shear rate (6.3.1.2) on the agglomeration speed and maximum agglomerate size. The image series recorded during these analyses were automatically evaluated with respect to the visible agglomerate sizes and numbers using an in-house developed Matlab program. The program comprises two image processing steps (Figure 6-4): the original image (a) is first binarised using the mean grey value as threshold and then inverted (b). Agglomerates that outreach the image and those that are smaller than the mean agglomerate size determined in (b) are then eliminated (c). Removing agglomerates that are not completely visible should avoid errors in estimating the mean agglomerate size. Removing agglomerates smaller than the size threshold should allow analysing the growth of bigger agglomerates by monitoring the mean agglomerate size. Without size threshold–which usually is ~ 0.005 % of the image–the huge number of small agglomerates would severely decrease the mean agglomerate size. The grey threshold and the size threshold are determined only once for each image series using an image taken prior to shearing.
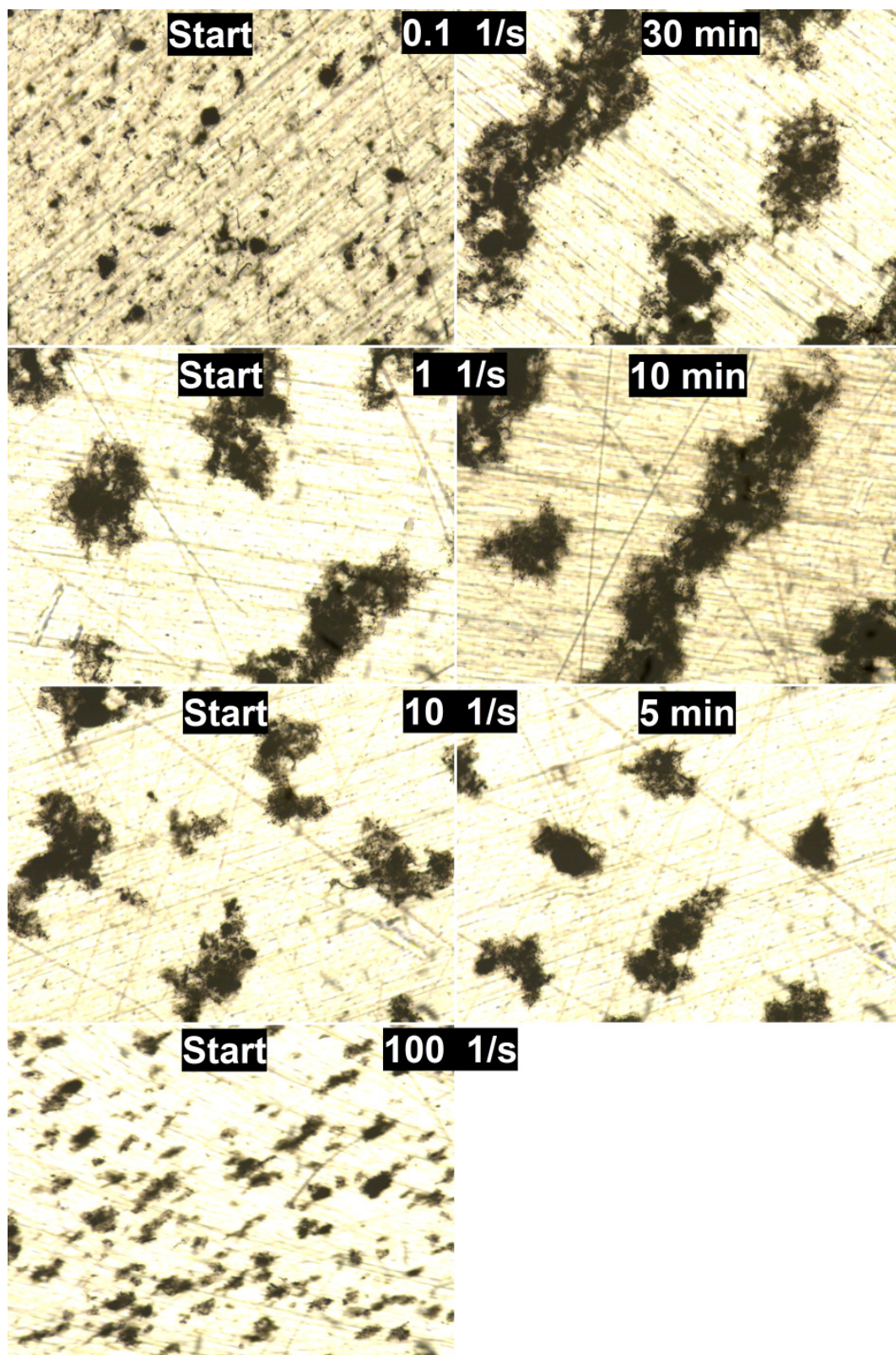
Figure 6-2 Images taken in situ while shearing a 0.05 wt% Nanocyl CNT/LY556 epoxy suspension with stepwise increasing shear rates at 70℃. The width of each image is 1 mm.
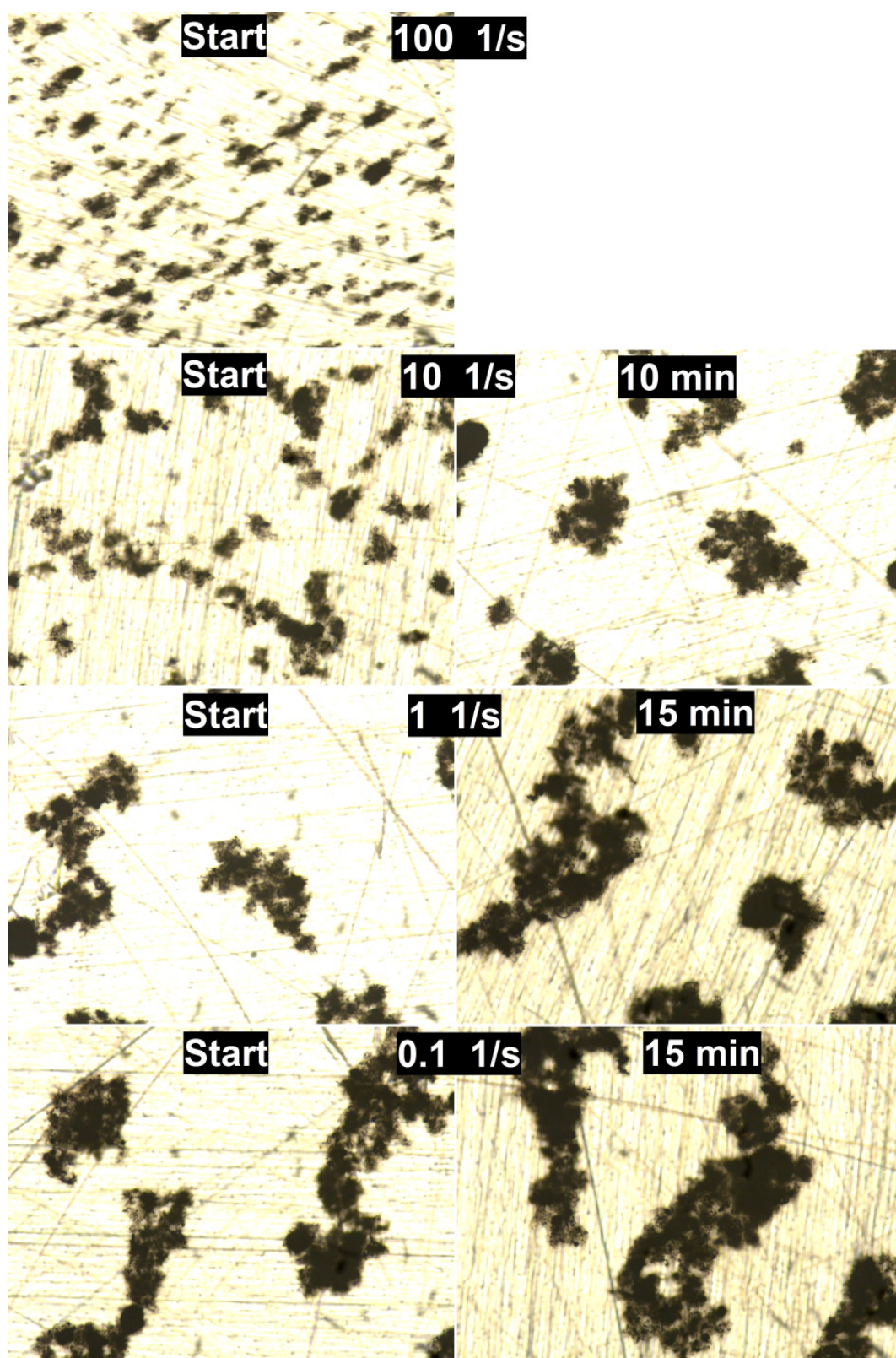
Figure 6-3 Images taken in situ while shearing the 0.05 wt% Nanocyl CNT/LY556 epoxy suspension from the state obtained in Figure 6-2 with stepwise decreasing shear rates at 70 ℃. The width of each image is 1 mm.
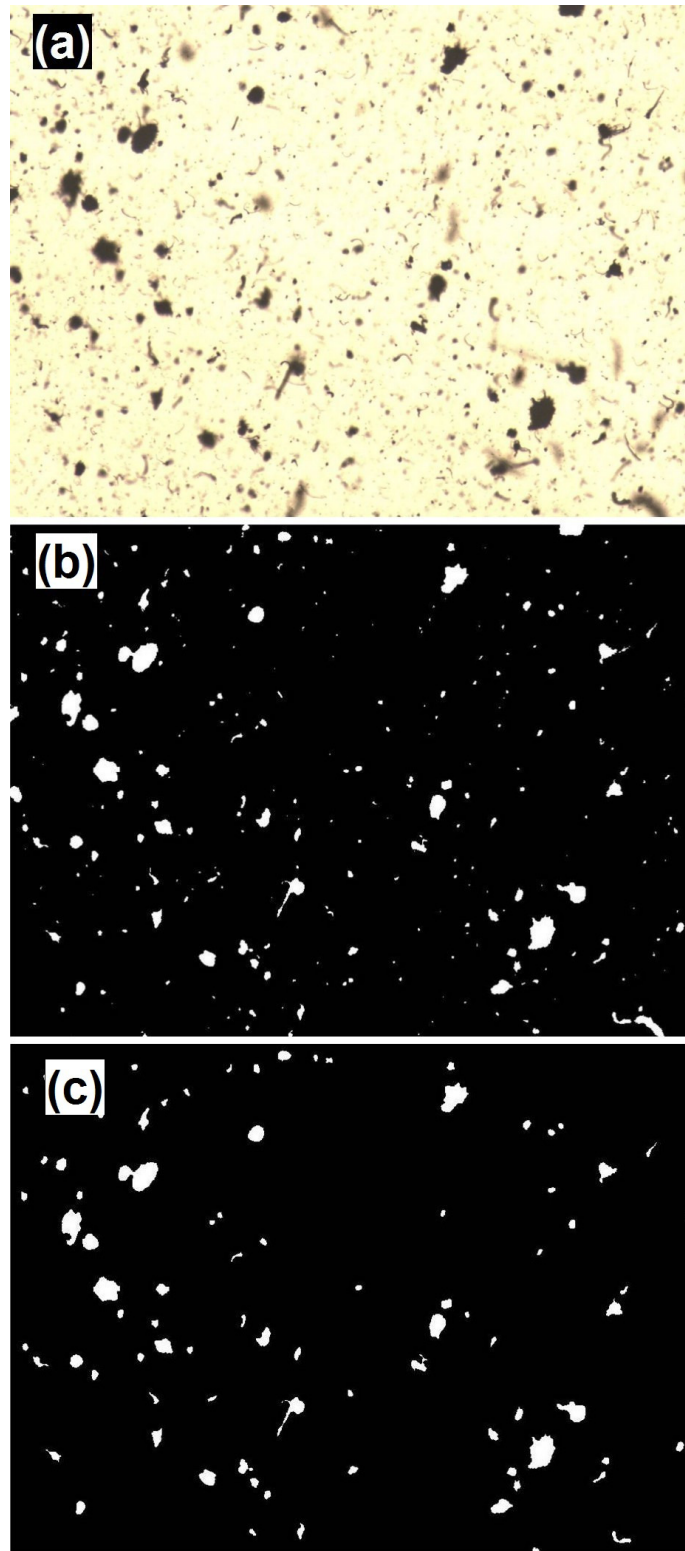
Figure 6-4 Automatic image evaluation using a Matlab program. Original image (a) is first binarised and inverted (b). Agglomerates that outreach the image and those that are smaller than the mean agglomerate size determined in (b) are then eliminated (c).

6.3.1.1 Temperature dependence

The experiment presented in Figure 6-2 was repeated for shear rates between 0.1 and 5 s^{-1} for various suspension temperatures. The evolution of the number of agglomerates and their mean size for a suspension at 30°C is shown in Figure 6-5a. The speed of the agglomerate built-up and destruction is extracted from the mean agglomerate size evolution at 0.1 s^{-1} and above 1 s^{-1}, respectively. The same procedure is repeated for suspension temperatures of 50°C and 70°C. The extracted slopes are summarized in Figure 6-5b. The destruction of agglomerates in the suspension at 70°C was too fast to be fitted accurately.

As expected, the formation of agglomerates is promoted through high temperatures. However, it seems that the destruction of agglomerates is also promoted through high temperatures. This finding contradicts the common assumption that high shear forces–optimally transferred to the agglomerates through high viscosity fluids, thus low temperatures–are necessary to disrupt agglomerates. It seems that there is a difference between agglomerates that need to be disrupted for the first time and re-agglomerated structures, so called flocks (see Section 4.3). The former need high shear forces while the latter do not.
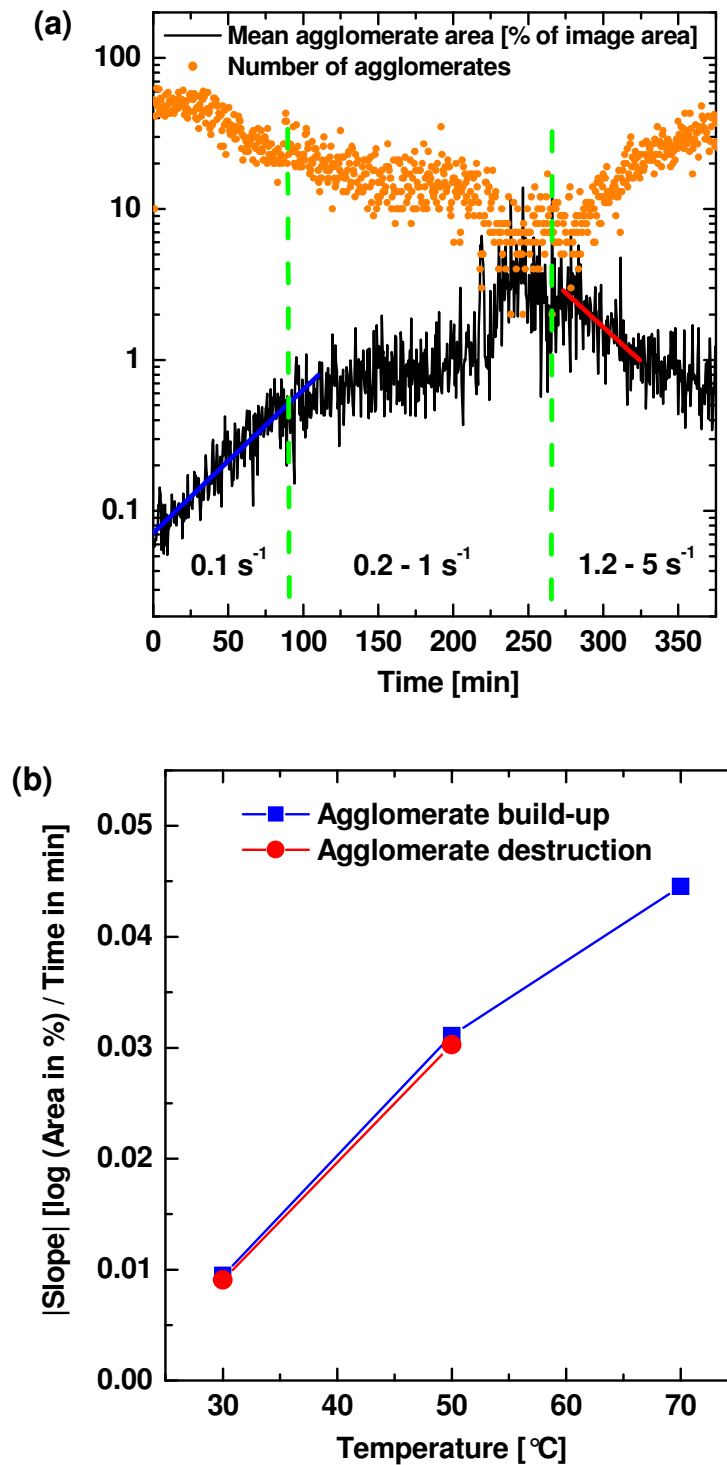
Figure 6-5 (a) Evolution of the number of agglomerates and their mean size as function of an increasing shear rate (0.1-5 s^{-1}) at 30°C. (b) Absolute values of the agglomerate build-up and destruction velocity–measured in log(agglomerate area [%]) per time [min]–for various suspension temperatures. The suspension consists of 0.05 wt% Nanocyl CNT in LY556 epoxy resin.

6.3.1.2 Shear rate dependence

Figure 6-6 presents experiments performed on 0.05 wt% Nanocyl CNT/LY556 epoxy suspensions at 30 °C and various constant shear rates in order to find the shear rate that yields the fastest agglomeration. The mean agglomerate size is found to increase under shearing and to reach an equilibrium size where saturation takes place. The slopes from the growth period and the saturated mean agglomerate sizes are summarized in Figure 6-7.
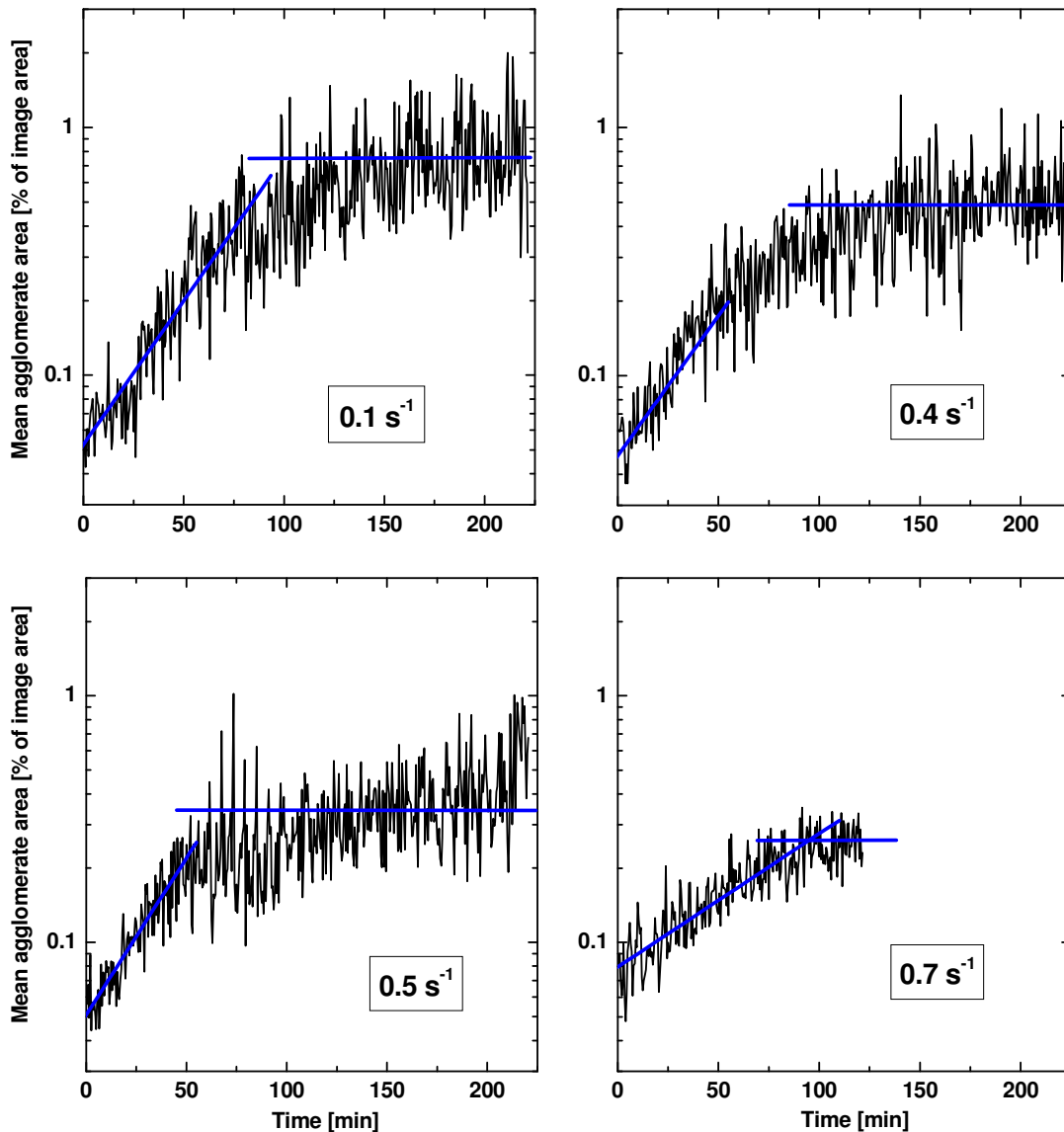

Figure 6-6 Mean agglomerate area evolution with time for various constant shear rates (inset) at 30 °C suspension temperature. The suspension consists of 0.05 wt% Nanocyl CNT in LY556 epoxy resin.
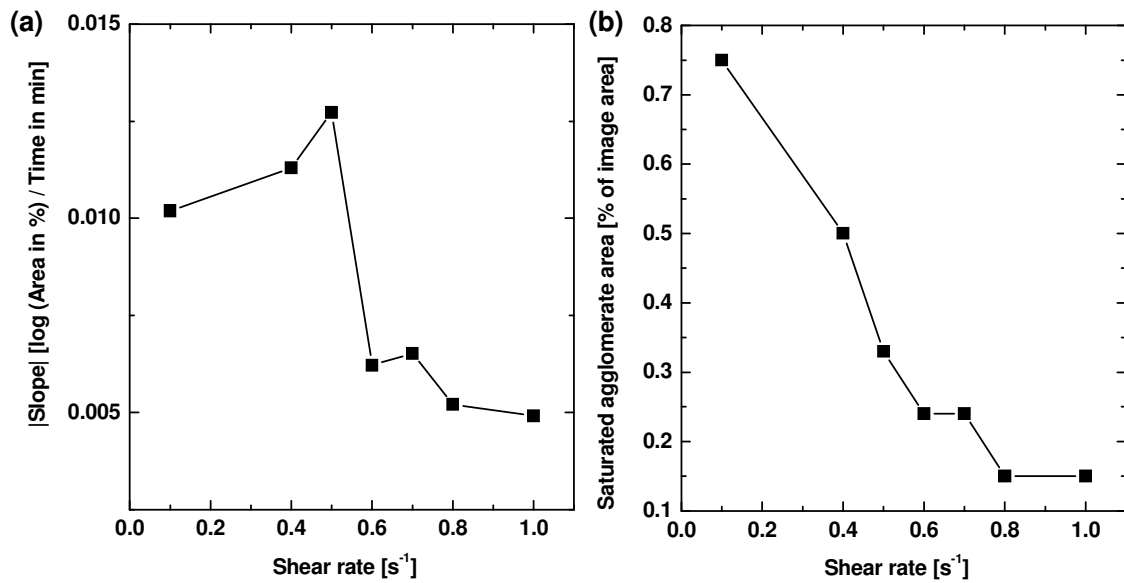
Figure 6-7 Agglomerate (a) build-up velocity–measured in log(agglomerate area [%]) per time [min]–and (b) saturation area [%] for various shear rates at 30°C suspension temperature. The data are taken from the fits in Figure 6-6.

The efficiency in building up agglomerates (Figure 6-7a) does not increase with decreasing shear rate–at least for suspensions at 30°C. Instead, an optimum shear rate at 0.5 s^{-1} is identified with decreasing efficiencies for higher and lower shear rates. The steep drop of efficiency already at 0.6 s^{-1} demonstrates how sensitive the agglomeration process is.

In contrast to the build-up velocity, the saturated mean agglomerate size seems to be inversely proportional to the shear rate (Figure 6-7b). The lowest shear rates produce the biggest agglomerates. In fact, each shear rate seems to be able to produce and maintain only a certain agglomerate size, irrespective of the production method (destruction at 10 s^{-1} in Figure 6-2 and build-up at 10 s^{-1} in Figure 6-3).

6.3.2 Electrical analyses

6.3.2.1 Analyses of calendered suspensions

A suspension containing 0.12 wt% Nanocyl CNT in LY556 epoxy was produced following the routine described in Section 4.2.1.1. The routine however was stopped before adding the hardener to the suspension. The suspension was processed without hardener in a three roll calender [95,96], then 1 ml was extracted and transferred to the rheometer, heated to 50°C and then exposed to various shear rates. The electrical conductivity of the suspension was recorded every 10 sec via the built-in electrodes of the rheometer. Each conductivity data could later be related to a certain shearing condition by the time stamps of both, the conductivity measurement and the shearing program. The CNT concentration was too high to monitor the agglomerates in the 1 mm gap optically.

The suspension was exposed to a shearing routine similar to the one used in Figure 6-2 and Figure 6-3. The arrows in Figure 6-8 assign the adjustment of certain shear rates which are maintained up to the next arrow. Although the initial shear rate of 0.5 s^{-1} was shown to be able to build up agglomerates, no increase in conductivity was observed during 10 min of shearing. Increasing the shear rate stepwise to 100 s^{-1} did not alter the conductivity. It seems that either no agglomerates were formed or there is no correlation between the agglomerates and the suspension conductivity.

When the shear rate was lowered again, the conductivity was found to increase within minutes for each step. Back at 0.5 s^{-1} (for the bottom-bottom electrode configuration) or at 0.001 s^{-1} (for the top-bottom electrode configuration) the conductivity increased by one order of magnitude compared to the initial value. Adjusting higher shear rates once again decreases the conductivity to the values previously found for the respective shear rates. Adjusting lower shear rates increases the conductivity again. The suspension conductivity seems to

behave analogical to the mean agglomerate sizes in Section 6.3.1: each shear rate seems to be related to a certain conductivity level which is recovered every time the respective shear rate is adjusted.

It should be noted that the conductivity measurements yield similar characteristics for the bottom-bottom as well as for the top-bottom electrode configurations, although the latter setup does not allow a permanent contact between the CNT network and the rotating plate.

It should also be noted that viscosity is not decreasing during any of the 10 min shear processes at constant shear rate, which indicates that the suspension does not behave thixotropic. A thixotropic behaviour is expected when individually dispersed CNT align due to shearing and decrease the suspension viscosity [279,280]. Obviously, either no alignment of the CNT takes place or alignment has a negligible effect at the present CNT concentration or matrix viscosity. Experiments from Rahatekar et al. [281] on a similar CNT suspension suggest the latter case to be true.

These results could be indicative for the stabilisation mechanisms (electrostatic and/or steric) present in calendered CNT/epoxy suspensions. High shear forces could be necessary to overcome the stabilisation forces of individual CNT or small agglomerates, as no conductivity increase is visible for low shear rates. In contrast, big agglomerates as found in the non-calendered suspensions seem to be able to overcome the stabilisation forces already at low shear rates, as proven by optical (Section 6.3.1) and electrical analyses (Section 6.3.2.2). As long as high shear rates are present in the calendered samples, the CNT seem to be brought together but also torn apart again. It seems that CNT agglomerates can survive only if the shear rate is lowered moderately so that the agglomerates formed at high shear rates are not torn apart again. This conclusion is supported by the observation of a conductivity increase when the rheometer plate is stopped from 1 s^{-1} shear rates. This increase is not observed when the plate is stopped from 10 s^{-1} (Figure 6-8a).
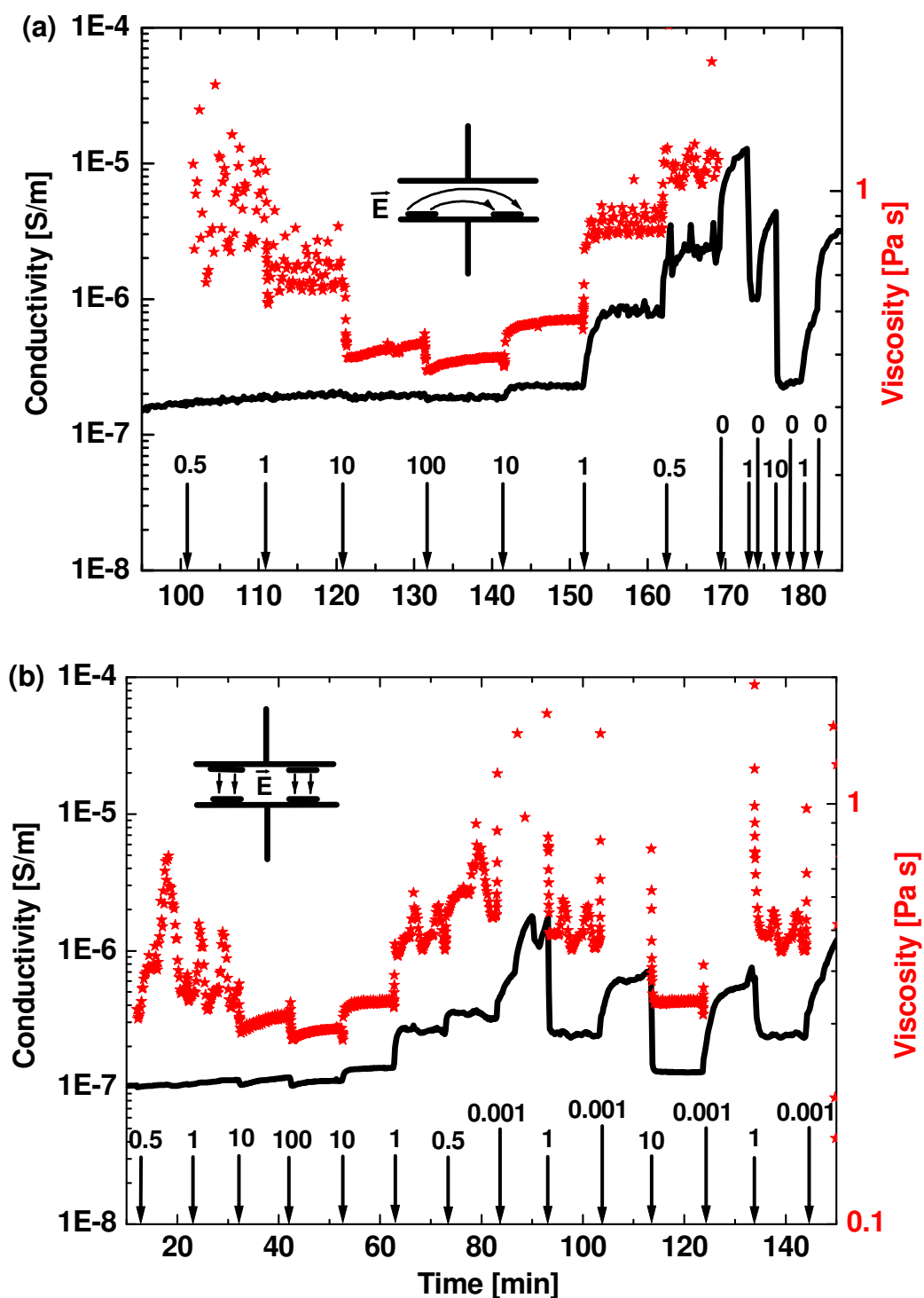
Figure 6-8 Conductivity (line) and viscosity (asterisk) evolution of a calendered 0.12 wt% Nanocyl CNT/LY556 epoxy suspension at 50°C for various shear rates (the given value in s^{-1} was adjusted at the respective arrow on the time axis). The electrode setup used for the conductivity measurement is depicted in the inset: (a) bottom-bottom electrodes, (b) top-bottom electrodes.

6.3.2.2 Analyses of non-calendered suspensions

Suspensions containing various concentrations (0.006-0.6 wt%) of CCVD-aligned-grown CNT were produced following the routine described in Section 4.2.1.3. However, instead of pouring the CNT/LY556/XB3473 suspension into the cavities of the PTFE block, 1 ml was transferred to the rheometer, heated to a constant temperature (20°C or 50°C) and then exposed to various shear rates. The electrical conductivity of the suspension was recorded every 10 sec via the built-in electrodes (bottom-bottom configuration) of the rheometer. Each conductivity data could later be related to a certain shearing condition by the time stamps of both, the conductivity measurement and the shearing program. The suspensions in the 1 mm gap of the rheometer were optically transparent only below a CNT concentration of 0.025 wt%, therefore no optical analyses could be performed.

The suspensions were exposed to a shearing routine similar to the one presented in Section 6.3.2.1. Shear rate sweeps were performed by applying a shear rate of 0.001 s^{-1} for 10 min while taking 10 measurement points, then increasing the shear rate to 0.01 s^{-1} within 10 sec and then again measuring for 10 min. This sequence was repeated up to a shear rate of 100 s^{-1} (measured values are referred to as *pre-100*) and then decreased stepwise to 0.001 s^{-1} again (measured values are referred to as *post-100*). The electrical and rheological measurements for three CNT concentrations, each measured at 20°C and 50°C, are presented in Figure 6-9. Generally, conductivity and viscosity behave similar for all samples with CNT concentrations above the electrical percolation threshold, which is 0.04 wt% for suspensions at 20°C and 0.008 wt% at 50°C (see Section 6.4 for more details on electrical and rheological percolation). Conductivity and viscosity both drop with increasing shear rate[9] and increase when the shear rate is lowered again. However, they basically stay constant for every shear rate for suspensions with a CNT concentration below the electrical threshold (e.g. the 0.025 wt% CNT/epoxy

---

[9] The suspension conductivity drops only until the pure polymer conductivity around 10^{-7} S/m is reached.

suspension at 20℃ in Figure 6-9). Obviously, the incorporation of CNT turns the epoxy from a Newtonian liquid into a shear thinning one. Shear thinning liquids have to be distinguished from thixotropic liquids: while the viscosity of the former only decreases with increasing shear rate (which is indicative for breaking of interconnected networks between CNT), the viscosity of the latter decreases with time while the shear rate is constant (which is indicative for CNT alignment).

However, differences become obvious when conductivity and its behaviour during the 10 min shearing process are analysed in detail. [10] Eleven suspensions with CNT concentrations between 0.006 and 0.6 wt% were included in the analysis. If the suspensions are heated to 20℃, conductivity is found to stay constant during any of the 10 min shearing processes in the pre-100 regime. In the post-100 regime, a steady increase of conductivity is observed for shear rates below 0.01 s^{-1} (e.g. the 0.158 wt% CNT/epoxy suspension in Figure 6-9). This increase gets more and more step-like for higher CNT concentrations. The post-100 conductivity values usually do not reach the respective pre-100 values at the same shear rates, although they get closer to them as the shear rate is decreased (e.g. the 0.62 wt% CNT/epoxy suspension in Figure 6-9). If the suspensions are heated to 50℃, conductivity usually increases at low shear rates for both, the pre-100 (e.g. the 0.158 wt% CNT/epoxy suspension in Figure 6-9) and the post-100 regime (e.g. the 0.025 wt% CNT/epoxy suspension in Figure 6-9). As for the 20℃ suspensions, the increase in the post-100 regime gets more and more step-like for higher CNT concentrations. But this time the post-100 conductivity values usually exceed the respective values found in the pre-100 regime at the same shear rates (e.g. the 0.158 wt% CNT/epoxy suspension in Figure 6-9).

---

[10] The viscosity data are less sensitive than the conductivity data and therefore are excluded from the discussion.
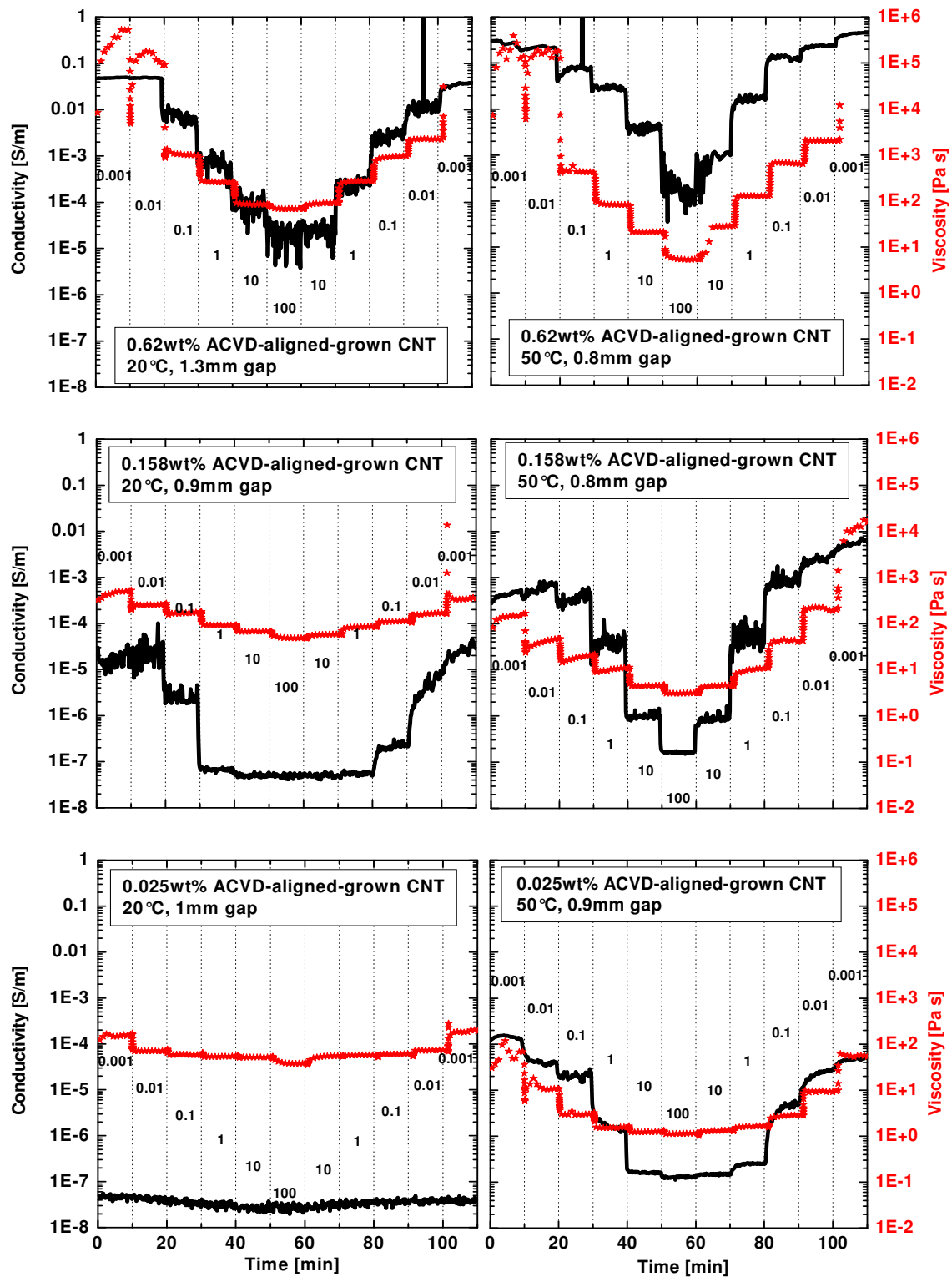
Figure 6-9 Shear rate sweep with in situ measurement of viscosity (asterisk) and electrical conductivity (line) of CCVD-aligned-grown CNT/LY556/XB3473 suspensions for various CNT concentrations (rows) at 20°C (left column) and 50°C (right column). The shear rate values are given in s^{-1}.

From the observed conductivity behaviour two conclusions can be drawn. First, calendered and non-calendered suspensions seem to behave different when subjected to shear forces. For the non-calendered suspensions discussed here, no increase of conductivity at low shear rates in the post-100 regime was observed without a preceding increase in the pre-100 regime. The bigger agglomerates present in the non-calendered suspensions do not seem to need pre-shearing of the suspension in order to form electrically conductive paths within the suspension. The second conclusion is that high temperatures and low shear rates seem to promote the network formation.

6.4 Electrical vs. rheological percolation threshold

The dependences of rheological parameters–such as viscosity, storage and loss modulus–on filler concentration yield a rheological percolation threshold which, in general, occurs at lower concentrations than electrical percolation. Filler particles can interact with each other via polymer chains whereas direct contact between them is required for electrical conduction.

The electrical and rheological data presented in Section 6.3.2.2 are replotted as a function of CNT concentration for the CCVD-aligned-grown CNT/epoxy suspensions at 20°C (Figure 6-10) and 50°C (Figure 6-11). Conductivity and viscosity are averaged from the values measured during the 10 min shearing process at 0.1 s^{-1}. The rheological percolation threshold–the concentration where viscosity vs. CNT concentration suddenly changes slope [282]–is found to be 0.1 wt% for both, the 20°C and 50°C suspension. The electrical percolation threshold–determined according to the procedure described in [162]–is found to be 0.04 wt% for the 20°C suspension and 0.008 wt% for the 50°C suspension.
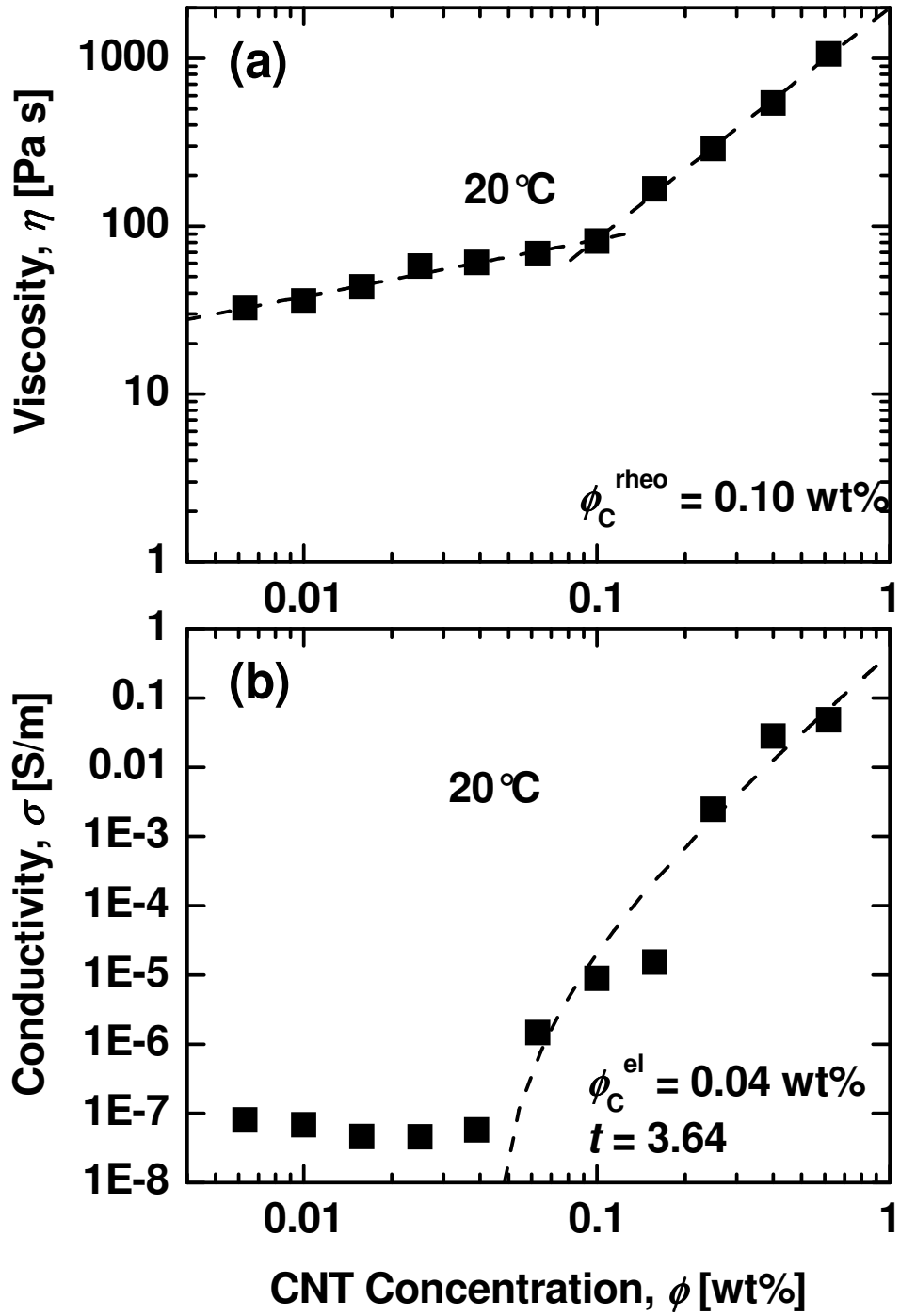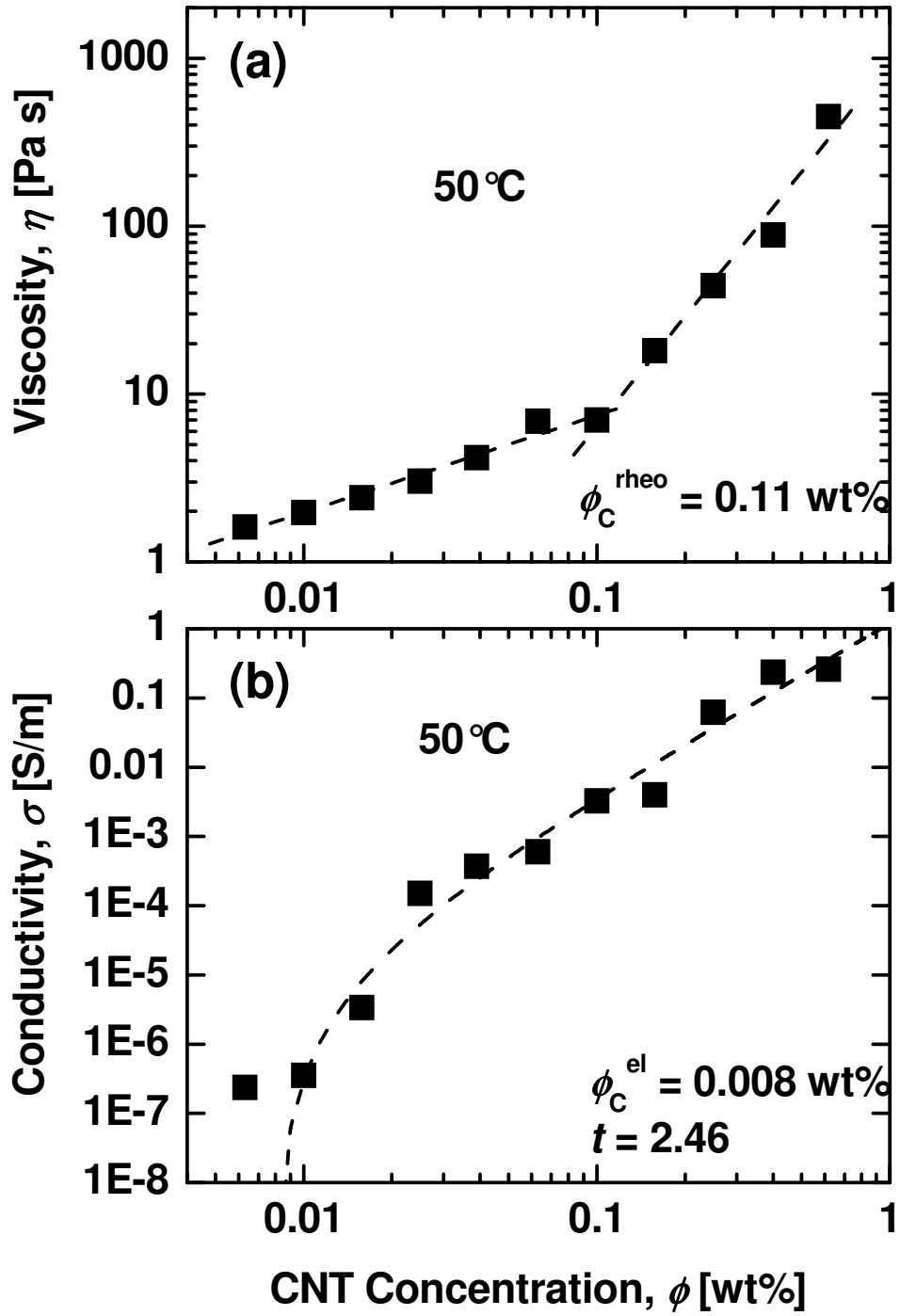
Figure 6-10 Simultaneous measurement of the composite (CCVD-aligned-grown CNT/LY556/XB3473) viscosity (a) and electrical conductivity (b) as function of the CNT weight fraction, performed in the liquid state prior to curing at 0.1 s^{-1} and 20 °C. The rheological percolation threshold ϕ_C^{rheo} is found at 0.1 wt% and the electrical percolation threshold ϕ_C^{el} at 0.04 wt%.

Figure 6-11 Simultaneous measurement of the composite (CCVD-aligned-grown CNT/LY556/XB3473) viscosity (a) and electrical conductivity (b) as function of the CNT weight fraction, performed in the liquid state prior to curing at 0.1 s^{-1} and 50 °C. The rheological percolation threshold ϕ_C^{rheo} is found at 0.1 wt% and the electrical percolation threshold ϕ_C^{el} at 0.008 wt%.

It seems that the electrical percolation threshold occurs at lower concentrations than the rheological one for both temperatures. This behaviour is common to thermoset systems which do not have polymer chains before the crosslinking process started. In contrast, for the thermoplastic system SWCNT/PMMA, Du et al. [25] indeed observe a rheological threshold at 0.12 wt% well below the electrical threshold at 0.39 wt%.

Evaluating the effect of suspension temperature it is found that the electrical threshold decreases with increasing temperature while the rheological threshold stays constant. The rheological threshold indicates the onset of a strong physical interaction between the filler particles, which obviously should not depend on temperature. The behaviour of the electrical percolation threshold is more interesting. One explanation could involve the contribution of ions. Electrical conduction through a CNT network suspended in a liquid could partly be accomplished through ions in the liquid. They could establish electrical contacts between CNT that are nearby but not in direct contact. Increasing the temperature of the suspension would increases the mobility of the ions, which then would be able to bridge bigger distances between the CNT, effectively lowering the electrical percolation threshold.

However, this does not explain the results summarized in Figure 6-12. One would expect the electrical percolation threshold to increase again as soon as the polymer vitrifies in the course of its curing process. But this does not happen. The electrical percolation threshold of the solid composite–which was cured at 120°C–matches the one of the liquid suspension at 50°C. This result suggests that the ions are at least not the only reason for the temperature dependence of the electrical threshold. It seems that the polymer sheathing layer [193] around each CNT controls the network conduction mechanism. The large interfacial area of the CNT binds a considerable amount of polymer. The mobility of the polymer in this layer is low near the CNT, increases with increasing distance to the CNT and approaches the mobility of the freely suspended polymer. It seems that a high suspension temperature alters the mobility gradient within the

sheathing layer, effectively reducing its thickness. This allows adjacent CNT to get closer to each other, thereby reducing the CNT contact resistance and the electrical percolation threshold.

The reduced layer thickness lasts until the polymer vitrifies, which explains why the electrical percolation threshold of the solid composite matches the one of the liquid at 50 °C and not at 20 °C. The reason why the electrical threshold of the solid composite–cured at 120 °C–is not lower than the one of the liquid at 50 °C could still be found in the ion conduction which lowers the percolation threshold in the liquid polymer but ceases to work in the solid composite.
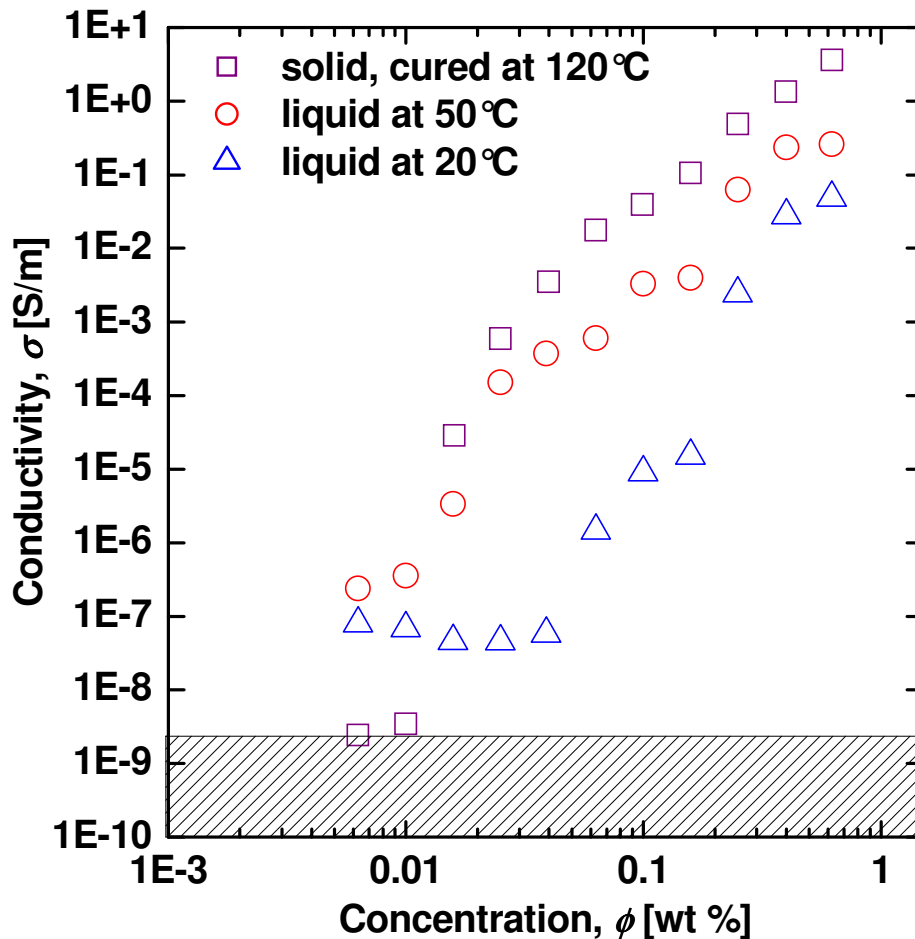

Figure 6-12 Compilation of the conductivity results for the no-stir CCVD-aligned-grown CNT as presented in Figure 4-12 for the solid composite and in Figure 6-10 and Figure 6-11 for the liquid composites at 20 °C and 50 °C.

6.5 Summary and conclusion

The CNT network formation in an epoxy liquid due to shear forces was studied under controlled conditions in a rheometer. Rheological, electrical and optical parameters could be monitored and analysed simultaneously.

Shearing with low shear rates (0.001-0.1 s^{-1}) was found to produce agglomerates while shearing with high shear rates (1-100 s^{-1}) destroyed them. Shearing again with low shear rates re-established the former agglomerates, proving the reversibility of this agglomeration process.

High temperatures were found to promote the agglomeration as well as the destruction of agglomerates. At 30 °C, an optimum shear rate for agglomerate formation was identified at 0.5 s^{-1} with decreasing efficiencies for higher and lower shear rates. The size of the established agglomerates seems to increase with decreasing shear rate. In fact, each shear rate seems to be able to produce and maintain only a certain agglomerate size.

The formation of electrically conductive networks was different for calendered and non-calendered CNT/epoxy suspensions. The calendered samples needed a pre-shearing step at high shear rates and a gradual lowering of the shear rate in order to establish a network. In contrast, non-calendered suspensions did not seem to need pre-shearing.

The electrical and rheological percolation thresholds of the CNT/epoxy suspensions were determined. The electrical threshold was found to be lower than the rheological, as expected for thermoset systems which do not posses polymer chains prior to crosslinking. The electrical threshold decreased with increasing temperature, which was attributed to the ionic conduction in the liquid matrix and to the effect of a polymer layer sheathing the CNT. The rheological threshold remained constant while the temperature was increased, indicating that physical interactions between filler particles are temperature independent.

7 Summary and conclusion

This thesis analyses the network formation of CNT in epoxy matrices using scanning electron microscopic, electrical, Raman spectroscopic and rheological techniques.

A non-destructive method for determining the real CNT shapes and distributions in a composite over several length scales was developed. The different electrical conductivities of the CNT and the matrix were exploited to generate a voltage (or charge) contrast which could be imaged by scanning electron microscopy–provided that the composite surface is not covered with a conductive layer as usual. The effect of several parameters (such as magnification, scanning speed, acceleration voltage, sample conductivity and dispersion quality) on the voltage contrast were investigated.

Conductivity measurements over up to three decades of CNT concentration with narrow increments revealed two percolation thresholds, the lower one attributed to a kinetic and the higher one to a statistic network formation process. The kinetic percolation threshold was found to be sensitive to temperature and the shear forces present in the liquid composite. For every CNT type, length and thickness analysed in this thesis, the respective kinetic percolation threshold was shown to be approximately one order of magnitude lower that the statistic one. CNT with higher aspect ratios were found to have lower statistic and kinetic percolation thresholds, meaning that the influence of the aspect ratio on the kinetic percolation threshold is dominating the influence of shearing. While the entanglement state of the CNT does not influence the kinetic or statistical percolation threshold, it (or the higher aspect ratio) seems to increase the conductivities considerably at high CNT concentrations. In contrast to this, shearing was not able to increase the conductivities at high concentrations.

Processing of the CNT/epoxy suspension with a calender was found to be disadvantageous for both, the percolation threshold and the maximum achievable composite conductivity.

Raman spectra were utilised to determine the temperature, orientation and stress state of CNT in epoxy resins. The waviness of some CNT types was shown to restrict determining the CNT orientation. Stresses induced by the thermal expansion coefficient of the matrix and their relief at the glass transition temperature could be monitored accurately by Raman spectroscopy. Simultaneous conductivity measurements revealed that the thermal stresses were not sufficiently high to affect the integrity of the established CNT network. Chemically induced stresses during the curing process of the epoxy were found to have a negligible effect on the sample stress state–or to be far too low to be detected by Raman spectroscopy.

The CNT network formation in an epoxy liquid due to shear forces was studied under controlled conditions in a rheometer. Rheological, electrical and optical parameters could be monitored and analysed simultaneously. Shearing with low shear rates was found to produce agglomerates while shearing with high shear rates destroyed them, both being reversible processes. High temperatures were found to promote the agglomeration as well as the destruction of agglomerates. The size of the established agglomerates was shown to increase with decreasing shear rate. The formation of electrically conductive networks was different for calendered and non-calendered CNT/epoxy suspensions. The calendered samples needed a pre-shearing step at high shear rates and a gradual lowering of the shear rate in order to establish a network. The electrical and rheological percolation thresholds of the unsheared, liquid CNT/epoxy suspensions were determined. While the electrical percolation threshold was found to be sensitive to temperature (attributed to the ionic conduction of the liquid matrix and to a polymer layer sheathing the CNT) the rheological threshold was not (indicating a temperature independent onset of physical interactions between the filler particles).

8 Outlook

The scanning electron microscope proved to be a valuable tool for analysing the CNT distribution and shape within polymer matrices. However, it holds the potential to deliver much more information on the CNT/polymer system. Techniques like capacitive coupling voltage contrast or resistive contrast imaging–known and used in semiconductor industry for a long time [283]–could be employed to gain knowledge on

- o which CNT contribute how to the overall network conductivity,
- o how deep the CNT are embedded in the polymer and
- o the electric resistance of the CNT and their mutual contact.

After all, the network of CNT within a polymer very much resembles the circuit paths of a chip.

The electrical characterisation of composites containing CNT of different types and geometries should be continued in order to confirm or contradict the results and conclusions presented in this thesis. Especially CNT with huge diameter are worth a detailed examination as their electrical behaviour deviated from that of the other CNT:

- o no plateau was observed between the kinetic and statistic percolation threshold
- o shearing was able to increase the composite conductivity even above the statistic percolation threshold

For all analyses, it is important to keep the processing conditions constant while varying the CNT type and to use a setup that is able to prevent unintended shearing through e.g. convection.

The differences between calendered and non-calendered CNT suspensions should be explored in more detail as the former are necessary for all Raman analyses and showed interesting features in the rheological investigations.

Deviant behaviour was found for the two polymer systems analysed by Raman spectroscopy, presumably due to the different bonding strength at the CNT/polymer interface. These results should be compared to the mechanical performance of the composites in order to assess the above mentioned assumption. If the results turn out to be correlated to the Raman ones, Raman spectroscopy would constitute a fast and non-destructive method for assessing the mechanical properties of various CNT/polymer systems. The potential of Raman spectroscopy to determine the orientation degree of CNT in a composite should be verified using CNT that are not wavy.

The shear dependent network formation is still not fully understood. Discrepancies arise for calendered and non-calendered suspensions. The effects of various CNT types and geometries–as already evaluated electrically–need to be evaluated rheologically. The electrical and rheological percolation thresholds should be monitored for various temperatures (including the polymer curing temperature) in order to quantify the contributions from shearing, ionic conduction and the CNT sheathing layer. The systematic electro-rheological analyses–as introduced in this thesis–is perfectly suitable for this purpose.

List of abbreviations

ACVD	aerosol chemical vapour deposition
ADA	aminododecanoic acid
AHA	aminohexanoic acid
AIBN	azoisobutyronitrile
APTS	aminopropyltriethoxy silane
ASTAA	alkoxysilane terminated amide acid
BKC	benzalkonium chloride
BSE	backscattered electron
CCVD	catalytic chemical vapour deposition
CNT	carbon nanotube
CoMoCAT®	cobalt-molybdenum catalyst process
CVD	chemical vapour deposition
DLA	diffusion-limited aggregation
DPD	dissipative particle dynamics
DWCNT	double-wall carbon nanotube
e	entangled
EMA	effective medium approach
ET	Everhart-Thornley detector
GA	gum Arabic
HiPco®	High pressure carbon monoxide process
MEK	methyl ethyl ketone
MWCNT	Multi-wall carbon nanotube
ne	non-entangled
OP	polyoxyethylene octyl phenyl ether
P3HT	poly 3-hexylthiophene
P3OT	poly 3-octylthiophene
PA-6	polyamide-6

PANI	polyaniline
PAT	polyhexadecyl thiophene
PBT	polybutylene terephthalate
P(BuA)	polybutyl acrylate
PC	polycarbonate
PCL	polycaprolactone
PE	polyethylene
PEE	polyphenylene ethynylene
PEO	polyethylene oxide
PET	polyethylene terephthalate
PFA	polyfurfuryl alcohol
PI	polyimide
PLA	poly(lactic acid)
PMMA	polymethyl methacrylate
PmPV	poly-m-phenylenevinylene
PP	polypropylene
PPV	polyparaphenylene vinylene
PS	polystyrene
PTFE	polytetrafluorethylen
PU	polyurethane
PVA	polyvinyl acetate
PVC	polyvinyl chloride
PVDF	polyvinylidene difluoride
SE	secondary electron
SDBS	sodium dodecylbenzenesulfonate
SDS	sodium dodecyl sulphate
S-I-Latex	styrene-isoprene copolymer latex
SPPA	sulfonated polyphenylacetylene
SWCNT	single-wall carbon nanotube
UPR	unsaturated polyester resin
VE	vinylester
VMQ	methylvinyl silicone rubber

List of symbols

Symbol	Unit	Meaning
A	m^2	area
A_r	g/mole	atomic weight
c	$2.998 \cdot 10^8$ m/s	light velocity
C	F	capacitance
d	m	fibre diameter
D_r	s^{-1}	rotational diffusivity
E	eV	electron beam energy
E	Pa	Young's modulus
F^{hyd}	N	hydrodynamic force
h	$6.626 \cdot 10^{-34}$ Js	Planck constant
I	m^4	second moment of area
I_D	-	D-band intensity of nanotubes
I_G	-	G-band intensity of nanotubes
k_B	$1.381 \cdot 10^{-23}$ J/K	Boltzmann constant
ℓ	m	fibre length
M	Nm	bending moment
Pe	-	Peclet number
r	-	fibre aspect ratio
R	Ω	resistance
R_C	Ω	contact resistance
R_{KO}	m	Kanaya and Okayama electron range
Re	-	Reynolds number
s	m	length

t	-	critical exponent of scaling law
t_{gel}	s	gelation time
t_{vit}	s	vitrification time
T	K	temperature
T_g	K	glass transition temperature
V	m^3	volume
Y^*	S	complex admittance
Z	-	atomic number
γ	rad, °	angle
$\dot{\gamma}$	s^{-1}	shear rate
ε_0	$8.854 \cdot 10^{-12}$ F/m	vacuum permittivity
ε_r	-	relative static permittivity
η	Pas	viscosity
λ	m	wavelength
ν	m^{-1}	wavenumber
ν_i	m^{-1}	incident laser wavenumber
ν_p	m^{-1}	phonon wavenumber
ρ	g/m^3	density
σ	S/m	conductivity
ϕ	vol%, wt%	filler content
ϕ_C	vol%, wt%	percolation threshold
ϕ_C^{el}	vol%, wt%	electrical percolation threshold
ϕ_C^{rheo}	vol%, wt%	rheological percolation threshold
ω	rad/s	angular velocity

List of figures

List of tables

References

[1]   Goodman SH. Handbook of Thermoset Plastics. Noyes Publications, 1st edition. New Jersey, US: 1986.

[2]   Ellis B (editor). Chemistry and Technology of epoxy resins. Blackie Academic & Professional, 1st edition. Glasgow, UK: 1993.

[3]   Davis WR, Slawson RJ, Rigby GR. An unusual form of carbon. *Nature* 1953; 171(4356): 756.

[4]   Oberlin A, Endo M. Filamentous growth of carbon through benzene decomposition. *Journal of Crystal Growth* 1976; 32(3): 335-49.

[5]   Nesterenko AM, Kolesnik NF, Akhmatov YS, Sukhomlin VI, Prilutski OV. Metals 3 UDK 869.173.23. *News of the Academy of Science, USSR*; 1982, p.12-6.

[6]   Iijima S. Helical microtubules of graphitic carbon. *Nature* 1991; 354(7): 56-8.

[7]   Thess A, Lee R, Nikolaev P, Dai H, Petit P, Robert J, Xu C, Lee YH, Kim SG, Rinzler AG, Colbert DT, Scuseria GE, Tomanek D, Fischer JE, Smalley RE. Crystalline ropes of metallic carbon nanotubes. *Science* 1996; 273(5274): 483-7.

[8]   Wei BQ, Vajtai R, Ajayan PM. Reliability and current carrying capacity of carbon nanotubes. *Applied Physics Letters* 2001; 79(8): 1172-4.

[9]   Cahill DG, Goodson K, Majumdar A. Thermometry and thermal transport in micro/nanoscale solid-state devices and structures. *Journal of Heat Transfer* 2002; 124(2): 223-41.

[10]   Krishnan A, Dujardin E, Ebbesen TW, Yianilos PN, Treacy MMJ. Young's modulus of single-walled nanotubes. *Physical Review B* 1998; 58(20): 14013-9.

[11] Yu MF, Lourie O, Dyer MJ, Moloni K, Kelly TF, Ruoff RS. Strength and breaking mechanism of multiwalled carbon nanotubes under tensile load. *Science* 2000; 287(5453): 637-40.

[12] Bacsa RR, Laurenta Ch, Peigney A, Bacsa WS, Vaugien Th, Rousset A. High specific surface area carbon nanotubes from catalytic chemical vapor deposition process. *Chemical Physics Letters* 2000; 323(5-6): 566-71.

[13] Prehn K, Adelung R, Heinen M, Nunes SP, Schulte K. Catalytically active CNT-polymer-membrane assemblies: From synthesis to application. *Journal of Membrane Science* 2008; 321(1): 123-30.

[14] Sussiek M, Müller J, Lehmann U. Carbon nanotubes as adsorbent in packed columns for a miniaturised gas chromatograph. *Proc. Sensor - 12th International Conference* 2005; 2: 117-9.

[15] Wang YH, Lin J, Huan CHA, Chen GS. Synthesis of large area aligned carbon nanotube arrays from C_2H_2-H_2 mixture by rf plasma-enhanced chemical vapor deposition *Applied Physics Letters* 2001; 79(5): 680-2.

[16] Sandler J, Shaffer MSP, Prasse T, Bauhofer W, Schulte K, Windle AH. Development of a dispersion process for carbon nanotubes in an epoxy matrix and the resulting electrical properties. *Polymer* 1999; 40(21): 5967-71.

[17] Martin CA, Sandler JKW, Shaffer MSP, Schwarz MK, Bauhofer W, Schulte K, Windle AH. Formation of percolating networks in multi-wall carbon-nanotube-epoxy composites. *Composites Science and Technology* 2004; 64(15): 2309-16.

[18] Martin CA, Sandler JKW, Windle AH, Schwarz MK, Bauhofer W, Schulte K, Shaffer MSP. Electric field-induced aligned multi-wall carbon nanotube networks in epoxy composites. *Polymer* 2005; 46(3): 877-86.

[19] Allaoui A, Bai S, Cheng HM, Bai JB. Mechanical and electrical properties of a MWNT/epoxy composite. *Composites Science and Technology* 2002; 62(15): 1993-8.

[20]   Haggenmueller R, Gommans HH, Rinzler AG, Fischer JE, Winey KI. Aligned single-wall carbon nanotubes in composites by melt processing methods. *Chemical Physics Letters* 2000; 330(3-4): 219-25.

[21]   Andrews R, Jacques D, Minot M, Rantell T. Fabrication of carbon multiwall nanotube/polymer composites by shear mixing. *Macromolecular Materials and Engineering* 2002; 287(6): 395-403.

[22]   Safadi B, Andrews R, Grulke EA. Multiwalled carbon nanotube polymer composites: Synthesis and characterization of thin films. *Journal of Applied Polymer Science* 2002; 84(14): 2660-69.

[23]   Hobbie EK, Wang H, Kim H, Lin-Gibson S, Grulke EA. Orientation of carbon nanotubes in a sheared polymer melt. *Physics of Fluids* 2003; 15(5): 1196-203.

[24]   Du F, Fischer JE, Winey KI. Coagulation method for preparing single-walled carbon nanotube/poly(methyl methacrylate) composites and their modulus, electrical conductivity, and thermal stability. *Journal of Polymer Science B* 2003; 41(24): 3333-8.

[25]   Du FM, Scogna RC, Zhou W, Brand S, Fischer JE, Winey KI. Nanotube networks in polymer nanocomposites: Rheology and electrical conductivity. *Macromolecules* 2004; 37(24): 9048-55.

[26]   Kashiwagi T, Du FM, Winey KI, Groth KA, Shields JR, Bellayer SP, et al. Flammability properties of polymer nanocomposites with single-walled carbon nanotubes: effects of nanotube dispersion and concentration. *Polymer* 2005; 46(2): 471-8.

[27]   Brown JM, Anderson DP, Justice RS, Lafdi K, Belfor M, Strong KL, et al. Hierarchical morphology of carbon single-walled nanotubes during sonication in an aliphatic diamine. *Polymer* 2005; 46(24): 10854-65.

[28]   Inam F, Peijs T. Transmission light microscopy of carbon nanotubes-epoxy nanocomposites involving different dispersion methods. *Advanced Composites Letters* 2006; 15(1): 7-13.

[29]   Kovacs JZ, Velagala BS, Schulte K, Bauhofer W. Two percolation thresholds in carbon nanotube epoxy composites. *Composites Science and Technology* 2007; 67(5): 922-8.

[30] Pecastaings G, Delhaes P, Derre A, Saadaoui H, Carmona F, Cui S. Role of interfacial effects in carbon nanotube/epoxy nanocomposite behaviour. *Journal of Nanoscience and Nanotechnology* 2004; 4(7): 838-43.

[31] McNally T, Pötschke P, Halley P, Murphy M, Martin D, Bell SEJ, et al. Polyethylene multiwalled carbon nanotube composites. *Polymer* 2005; 46(19): 8222-32.

[32] Sandler JKW, Kirk JE, Kinloch IA, Shaffer MSP, Windle AH. Ultra-low electrical percolation threshold in carbon-nanotube-epoxy composites. *Polymer* 2003; 44(19): 5893-9.

[33] Bryning MB, Islam MF, Kikkawa JM, Yodh AG. Very low conductivity threshold in bulk isotropic single-walled carbon nanotube-epoxy composites. *Advanced Materials* 2005; 17(9): 1186-91.

[34] Xu XJ, Thwe MM, Shearwood C, Liao K. Mechanical properties and interfacial characteristics of carbon-nanotube-reinforced epoxy thin films. *Applied Physics Letters* 2002; 81(15): 2833-5.

[35] Dufresne A, Paillet M, Putaux JL, Canet R, Carmona F, Delhaes P, et al. Processing and characterization of carbon nanotube/poly(styrene-co-butyl acrylate) nanocomposites. *Journal of Materials Science* 2002; 37(18): 3915-23.

[36] Pötschke P, Fornes TD, Paul DR. Rheological behavior of multiwalled carbon nanotube/polycarbonate composites. *Polymer* 2002; 43(11): 3247-55.

[37] Courty S, Mine J, Tajbakhsh AR, Terentjev EM. Nematic elastomers with aligned carbon nanotubes: New electromechanical actuators. *Europhysics Letters* 2003; 64(5): 654-60.

[38] Watts PCP, Ponnampalam DR, Hsu WK, Barnes A, Chambers B. The complex permittivity of multi-walled carbon nanotube-polystyrene composite films in X-band. *Chemical Physics Letters* 2003; 378(5-6): 609-14.

150

[39] Ramasubramaniam R, Chen J, Liu H. Homogeneous carbon nanotube/polymer composites for electrical applications. *Applied Physics Letters* 2003; 83(14): 2928-30.

[40] Koerner H, Price G, Pearce NA, Alexander M, Vaia RA. Remotely actuated polymer nanocomposites - stress-recovery of carbon-nanotube-filled thermoplastic elastomers. *Nature Materials* 2004; 3(2): 115-20.

[41] Li X, Gao H, Scrivens VA, Fei D, Xu X, Sutton MA, et al. Nanomechanical characterization of single-walled carbon nanotube reinforced epoxy composites. *Nanotechnology* 2004; 15(11): 1416-23.

[42] Lau KT, Lu M, Lam CK, Cheung HY, Sheng FL, Li HL. Thermal and mechanical properties of single-walled carbon nanotube bundle-reinforced epoxy nanocomposites: the role of solvent for nanotube dispersion. *Composites Science and Technology* 2005; 65(5): 719-25.

[43] Liu LQ, Wagner HD. Rubbery and glassy epoxy resins reinforced with carbon nanotubes. *Composites Science and Technology* 2005; 65(11-12): 1861-8.

[44] Song YS, Youn JR. Influence of dispersion states of carbon nanotubes on physical properties of epoxy nanocomposites. *Carbon* 2005; 43(7): 1378-85.

[45] Koerner H, Liu WD, Alexander M, Mirau P, Dowty H, Vaia RA. Deformation-morphology correlations in electrically conductive carbon nanotube thermoplastic polyurethane nanocomposites. *Polymer* 2005; 46(12): 4405-20.

[46] Xiao K, Zhang L. Effective separation and alignment of long entangled carbon nanotubes in epoxy. *Journal of Materials Science* 2005; 40(24): 6513-16.

[47] Aarab H, Baitoul M, Wery J, Almairac R, Lefrant S, Faulques E, et al. Electrical and optical properties of PPV and single-walled carbon nanotubes composite films. *Synthetic Metals* 2005; 155(1): 63-7.

[48]   Kim YA, Hayashi T, Endo M, Gotoh Y, Wada N, Seiyama J. Fabrication of aligned carbon nanotube-filled rubber composite. *Scripta Materialia* 2006; 54(1): 31-5.

[49]   Dalmas F, Dendievel R, Chazeau L, Cavaille JY, Gauthier C. Carbon nanotube-filled polymer composites. Numerical simulation of electrical conductivity in three-dimensional entangled fibrous networks. *Acta Materialia* 2006; 54(11): 2923-31.

[50]   Zhu BK, Xie SH, Xu ZK, Xu YY. Preparation and properties of the polyimide/multi-walled carbon nanotubes (MWNTs) nanocomposites. *Composites Science and Technology* 2006; 66(3-4): 548-54.

[51]   Kueseng K, Jacob KI. Natural rubber nanocomposites with SiC nanoparticles and carbon nanotubes. *European Polymer Journal* 2006; 42(1): 220-7.

[52]   Zhu J, Kim JD, Peng HQ, Margrave JL, Khabashesku VN, Barrera EV. Improving the dispersion and integration of single-walled carbon nanotubes in epoxy composites through functionalization. *Nano Letters* 2003; 3(8): 1107-13.

[53]   Cooper CA, Ravicha D, Lips D, Mayer J, Wagner HD. Distribution and alignment of carbon nanotubes and nanofibrils in a polymer matrix. *Composites Science and Technology* 2002; 62(7-8): 1105-12.

[54]   Park C, Ounaies Z, Watson KA, Crooks RE, Smith J, Lowther SE, et al. Dispersion of single wall carbon nanotubes by in situ polymerization under sonication. *Chemical Physics Letters* 2002; 364(3-4): 303-8.

[55]   Lin Y, Zhou B, Fernando KAS, Liu P, Allard LF, Sun YP. Polymeric carbon nanocomposites from carbon nanotubes functionalized with matrix polymer. *Macromolecules* 2003; 36(19): 7199-204.

[56]   Pötschke P, Bhattacharyya AR, Janke A. Carbon nanotube-filled polycarbonate composites produced by melt mixing and their use in blends with polyethylene. *Carbon* 2004; 42(5-6): 965-9.

[57]   Seo MK, Park SJ. Electrical resistivity and rheological behaviors of carbon nanotubes-filled polypropylene composites. *Chemical Physics Letters* 2004; 395(1-3): 44-8.

152

[58]   Meincke O, Kaempfer D, Weickmann H, Friedrich C, Vathauer M, Warth H. Mechanical properties and electrical conductivity of carbon-nanotube filled polyamide-6 and its blends with acrylonitrile/butadiene/styrene. *Polymer* 2004; 45(3): 739-48.

[59]   Grunlan JC, Mehrabi AR, Bannon MV, Bahr JL. Water-based single-walled-nanotube-filled polymer composite with an exceptionally low percolation threshold. *Advanced Materials* 2004; 16(2): 150-3.

[60]   Dalmas F, Chazeau L, Gauthier C, Masenelli-Varlot K, Dendievel R, Cavaille   JY, et al.   Multiwalled   carbon   nanotube/polymer nanocomposites: Processing and properties. *Journal of Polymer Science B* 2005; 43(10): 1186-97.

[61]   Fan ZH, Advani SG. Characterization of orientation state of carbon nanotubes in shear flow. *Polymer* 2005; 46(14): 5232-40.

[62]   Gojny FH, Wichmann MHG, Fiedler B, Schulte K. Influence of different carbon nanotubes on the mechanical properties of epoxy matrix composites - A comparative study. *Composites Science and Technology* 2005; 65(15-16): 2300-13.

[63]   Chen W, Tao XM. Production and characterization of polymer nanocomposite with aligned single wall carbon nanotubes. *Applied Surface Science* 2006; 252(10): 3547-52.

[64]   Hu GJ, Zhao CG, Zhang SM, Yang MS, Wang ZG. Low percolation thresholds of electrical conductivity and rheology in poly(ethylene terephthalate) through the networks of multi-walled carbon nanotubes. *Polymer* 2006; 47(1): 480-8.

[65]   Dalmas F, Chazeau L, Gauthier C, Cavaille JV, Dendievel R. Large deformation mechanical behavior of flexible nanofiber filled polymer nanocomposites. *Polymer* 2006; 47(8): 2802-12.

[66]   Xia HS, Qiu GH, Wang Q. Polymer/carbon nanotube composite emulsion prepared through ultrasonically assisted in situ emulsion polymerization. *Journal of Applied Polymer Science* 2006; 100(4): 3123-30.

[67]   Lee KC, Yu HH, Hwang SJ, Li YS, Cheng MH, Lin CC. Preparation and characterization of the modified carbon nanotubes enhanced epoxy resin composites. *Materials Science Forum* 2006; 505-507(2): 1075-80.

[68]   Goldstein J, Newbury D, Joy D, Lyman C, Echlin P, Lifshin E, et al. Scanning electron microscopy and x-ray microanalysis, 3rd ed. New York: Kluwer Academic / Plenum Publishers, 2003.

[69]   Reimer L. Scanning electron microscopy, 2nd ed. Berlin: Springer-Verlag, 1998.

[70]   Oatley CW, Everhart TE. The examination of p-n junctions with the SEM. *Journal of Electronics* 1957; 2(6): 568-70.

[71]   Chung KT, Reisner JH, Campbell ER. Charging phenomena in the scanning electron microscopy of conductor-insulator composites: A tool for composite structural analysis. *Journal of Applied Physics* 1983; 54(11): 6099-112.

[72]   Loos J, Alexeev A, Grossiord N, Koning CE, Regev O. Visualization of single-wall carbon nanotube (SWNT) networks in conductive polystyrene nanocomposites by charge contrast imaging. *Ultramicroscopy* 2005; 104(2): 160-7.

[73]   Dikin DA, Kohlhaas KM, Dommett GHB, Stankovich S, Ruoff RS. Scanning electron microscopy methods for analysis of polymer nanocomposites. *Microscopy and Microanalysis* 2006; 12(S02): 674-5.

[74]   Lillehei PT, Kim JW, Park C, Crooks RE, Siochi EJ. Optical, electron and probe microscopy characterization of carbon nanotube composites. *NIST practice guide: Measurement issues in single wall carbon nanotubes (Draft)*, December 31, 2005, http://www.msel.nist.gov/Nanotube2/Carbon_Nanotubes_Guide.htm

[75]   Watts PCP, Hsu WK, Randall DP, Kroto HW, Walton DRM. Non-linear current-voltage characteristics of electrically conducting carbon nanotube-polystyrene composites. *Physical Chemistry, Chemical Physics* 2002; 4(22): 5655-62.

[76] Smith JG, Connell JW, Delozier DM, Lillehei PT, Watson KA, Lin Y, et al. Space durable polymer/carbon nanotube films for electrostatic charge mitigation. *Polymer* 2004; 45(3): 825-36.

[77] Smith JG, Delozier DM, Connell JW, Watson KA. Carbon nanotube-conductive additive-space durable polymer nanocomposite films for electrostatic charge dissipation. *Polymer* 2004; 45(18): 6133-42.

[78] Regev O, ElKati PNB, Loos J, Koning CE. Preparation of conductive nanotube-polymer composites using latex technology. *Advanced Materials* 2004; 16(3): 248-51.

[79] Kim YJ, Shin TS, Choi HD, Kwon JH, Chung YC, Yoon HG. Electrical conductivity of chemically modified multiwalled carbon nanotube/epoxy composites. *Carbon* 2005; 43(1): 23-30.

[80] Gojny FH, Wichmann MHG, Fiedler B, Kinloch IA, Bauhofer W, Windle AH, et al. Evaluation and identification of electrical and thermal conduction mechanisms in carbon nanotube/epoxy composites. *Polymer* 2006; 47(6): 2036-45.

[81] Cao Q, Hur SH, Zhu ZT, Sun Y, Wang CJ, Meitl MA, et al. Highly bendable, transparent thin-film transistors that use carbon-nanotube-based conductors and semiconductors with elastomeric dielectrics. *Advanced Materials* 2006; 18(3): 304-9.

[82] Park C, Wilkinson J, Banda S, Ounaies Z, Wise KE, Sauti G, et al. Aligned single-wall carbon nanotube polymer composites using an electric field. *Journal of Polymer Science B* 2006; 44(12): 1751-62.

[83] Melchinger A, Hofmann S. Dynamic double-layer model: Description of time-dependent charging phenomena in insulators under electron-beam irradiation. *Journal of Applied Physics* 1995; 78(10): 6224-32.

[84] Renoud R, Mady F, Ganachaud JP. Monte Carlo simulation of the charge distribution induced by a high-energy electron beam in an insulating target. *Journal of Physics* 2002; 14(2): 231-47.

[85] Grella L, Lorusso G, Niemi T, Adler DL. Simulations of SEM imaging and charging. *Nuclear Instruments and Methods in Physics Research A* 2004; 519(1-2): 242-50.

[86]   Touzin M, Goeuriot D, Guerret-Piecourt C, Juve D, Treheux D, Fitting HJ. Electron beam charging of insulators: A self-consistent flight-drift model. *Journal of Applied Physics* 2006; 99(11): 114110(1-14).

[87]   Dietz C, Roper S, Scherdel S, Bernstein A, Rehse N, Magerle R. Automatization of nanotomography. *Review of Scientific Instruments* 2007; 78(5): 53703(1-5).

[88]   Deng F, Ogasawara T, Takeda N. Evaluating the orientation and dispersion of carbon nanotubes inside nanocomposites by a focused-ion-beam technique. *Materials Letters* 2007; 61(29): 5095-7.

[89]   Jaksch H, Martin JP. High-resolution, low-voltage SEM for true surface imaging and analysis. *Fresenius´ Journal of Analytical Chemistry* 1995; 353(3-4): 378-82.

[90]   Jaksch H. Neues Konzept für ein hochauflösendes Niederspannungs-Schottky-FE-SEM. *Chemie in Labor und Biotechnik* 1996; 10: 452-6.

[91]   Cazaux J. Charging in scanning electron microscopy "from inside and outside". *Scanning* 2004; 26(4): 181-203.

[92]   Dinnis AR. Detectors for quantitative electron beam voltage measurements. *Scanning Microscopy* 1988; 2(3): 1407-18.

[93]   Seiler H. Einige aktuelle Probleme der Sekundärelektronenemission. *Zeitschrift für Angewandte Physik* 1967; 22(3): 249-63.

[94]   Nelson H. Field-enhanced secondary electron emission. *Physical Review* 1940; 57: 560.

[95]   Gojny FH, Wichmann MHG, Köpke U, Fiedler B, Schulte K. Carbon nanotube-reinforced epoxy-composites: enhanced stiffness and fracture toughness at low nanotube content. *Composites Science and Technology* 2004; 64(15): 2363-71.

[96]   Nadler M, Mahrholz T, Riedel U, Schilde C, Kwade A. Preparation of colloidal carbon nanotube dispersions and their characterisation using a disc centrifuge. *Carbon* 2008; 46(11): 1384-92.

[97]   Dotan N. A method for enhancing topography and material contrast in automatic SEM review. Metrology, inspection, and process control for

microlithography XIII. *Santa Clara (California, USA): SPIE* 1999; 3677: 491-8.

[98] Cazaux J. About the role of the various types of secondary electrons (SE1; SE2; SE3) on the performance of LVSEM. *Journal of Microscopy* 2004; 214(3): 341-7.

[99] Bauhofer W, Kovacs JZ. A review and analysis of electrical percolation in carbon nanotube polymer composites. *Composites Science and Technology* 2009; 69(10): 1486-98.

[100] Stauffer D, Aharony A. Introduction to percolation theory. London: Taylor and Francis, 1992.

[101] Sahimi M. Applications of percolation theory. London: Taylor & Francis; 1994.

[102] Coleman JN, Curran S, Dalton AB, Davey AP, McCarthy B, Blau W, Barklie RC. Percolation-dominated conductivity in a conjugated-polymer-carbon-nanotube composite. *Physical Review B* 1998; 58(12): R7492-5.

[103] Winey KI, Kasiwagi T, Mu M. Improving electrical conductivity and thermal properties of polymers by addition of carbon nanotubes as fillers. *MRS Bulletin* 2007; 32(4): 348-53.

[104] Smith JG, Connell JW, Delozier DM, Lillehei PT, Watson KA, Lin Y, Zhou B, Sun YP. Space durable polymer/carbon nanotube films for electrostatic charge mitigation. *Polymer* 2004; 45(3): 825-36.

[105] Kovacs JZ, Mandjarov RE, Blisnjuk T, Prehn K, Sussiek M, Müller J, Schulte K, Bauhofer W. On the influence of nanotube properties, processing condition and shear forces on the electrical conductivity of carbon nanotube epoxy composites. *Nanotechnology* 2009; 20(15): 155703(1-6).

[106] Gojny FH, Wichmann MHG, Fiedler B, Kinloch IA, Bauhofer W, Windle AH, Schulte K. Evaluation and identification of electrical and thermal conduction mechanisms in carbon nanotube/epoxy composites. *Polymer* 2006; 47(6): 2036-45.

[107]   Yu AP, Itkis ME, Bekyarova E, Haddon RC. Effect of single-walled carbon nanotube purity on the thermal conductivity of carbon nanotube-based composites. *Applied Physics Letters* 2006; 89(13): 133102(1-3).

[108]   Moisala A, Li Q, Kinloch IA, Windle AH. Thermal and electrical conductivity of single- and multi-walled carbon nanotube-epoxy composites. *Composites Science and Technology* 2006; 66(10): 1285-8.

[109]   Kim B, Lee J, Yu I. Electrical properties of single-wall carbon nanotube and epoxy composites. *Journal of Applied Physics* 2003; 94(10): 6724-8.

[110]   Barrau S, Demont P, Maraval C, Bernes A, Lacabanne C. Glass transition temperature depression at the percolation threshold in carbon nanotube-epoxy resin and polypyrrole-epoxy resin composites. *Macromolecular Rapid Communications* 2005; 26(5): 390-4.

[111]   Li J, Ma PC, Chow WS, To CK, Tang BZ, Kim JK. Correlations between percolation threshold, dispersion state, and aspect ratio of carbon nanotubes. *Advanced Functional Materials* 2007; 17(16): 3207-15.

[112]   Hu N, Masuda Z, Yamamoto G, Fukunaga H, Hashida T, Qiu J. Effect of fabrication process on electrical properties of polymer/multi-wall carbon nanotube nanocomposites. *Composites Part A* 2008; 39(5): 893-903.

[113]   Du FM, Guthy C, Kashiwagi T, Fischer JE, Winey KI. An infiltration method for preparing single-wall nanotube/epoxy composites with improved thermal conductivity. *Journal of Polymer Science B* 2006; 44(10): 1513-9.

[114]   Barrau S, Demont P, Peigney A, Laurent C, Lacabanne C. DC and AC conductivity of carbon nanotubes-polyepoxy composites. *Macromolecules* 2003; 36(14): 5187-94.

[115]   Zilli D, Goyanes S, Escobar MM, Chiliotte C, Bekeris V, Cukierman AL, Rubiolo GH. Comparative analysis of electric, magnetic, and mechanical properties of epoxy matrix composites with different contents of multiple walled carbon nanotubes. *Polymer Composites* 2007; 28(5): 612-7.

[116]   Bai JB, Allaoui A. Effect of the length and the aggregate size of MWNTs on the improvement efficiency of the mechanical and electrical properties of nanocomposites - experimental investigation. *Composites Part A* 2003; 34(8): 689-94.

[117]   Liu L, Matitsine S, Gan YB, Chen LF, Kong LB, Rozanov KN. Frequency dependence of effective permittivity of carbon nanotube composites. *Journal of Applied Physics* 2007; 101(9): 94106(1-7).

[118]   Yuen SM, Ma CCM, Wu HH, Kuan HC, Chen WJ, Liao SH, Hsu CW, Wu HL. Preparation and thermal, electrical, and morphological properties of multiwalled carbon nanotube and epoxy composites. *Journal of Applied Polymer Science* 2007; 103(2): 1272-8.

[119]   Xu JW, Florkowski W, Gerhardt R, Moon KS, Wong CP. Shear modulated percolation in carbon nanotube composites. *Journal of Physical Chemistry B* 2006; 110(25): 12289-92.

[120]   Cui S, Canet R, Derre A, Couzi M, Delhaes P. Characterization of multiwall carbon nanotubes and influence of surfactant in the nanocomposite processing. *Carbon* 2003; 41(4): 797-809.

[121]   Pecastaings G, Delhaes P, Derre A, Saadaoui H, Carmona F, Cui S. Role of interfacial effects in carbon nanotube/epoxy nanocomposite behavior. *Journal of Nanoscience and Nanotechnology* 2004; 4(7): 838-43.

[122]   Wichmann MHG, Sumfleth J, Fiedler B, Gojny FH, Schulte K. Multiwall carbon nanotube/epoxy composites produced by a masterbatch process. *Mechanics of Composite Materials* 2006; 42(5): 395-406.

[123]   Wang T, Lei CH, Dalton AB, Creton C, Lin Y, Fernando KAS, Sun YP, Manea M, Asua JM, Keddie JL. Waterborne, nanocomposite pressure-sensitive adhesives with high tack energy, optical transparency, and electrical conductivity. *Advanced Materials* 2006; 18(20): 2730-4.

[124]   Dalmas F, Cavaille J-Y, Gauthier C, Chazeau L, Dendievel R. Viscoelastic behavior and electrical properties of flexible nanofiber filled polymer nanocomposites. Influence of processing conditions. *Composites Science and Technology* 2007; 67(5): 829-39.

[125]   Musumeci AW, Silva GG, Liu JW, Martens WN, Waclawik ER. Structure and conductivity of multi-walled carbon nanotube/poly(3-hexylthiophene) composite films. *Polymer* 2007; 48(6): 1667-78.

[126]   Kymakis E, Amaratunga GAJ. Electrical properties of single-wall carbon nanotube-polymer composite films. *Journal of Applied Physics* 2006; 99(8): 84302(1-7).

[127]   Kodgire PV, Bhattacharyya AR, Bose S, Gupta N, Kulkarni AR, Misra A. Control of multiwall carbon nanotubes dispersion in polyamide6 matrix: An assessment through electrical conductivity. *Chemical Physics Letters* 2006; 432(4-6): 480-5.

[128]   Blanchet GB, Fincher CR, Gao F. Polyaniline nanotube composites: a high-resolution printable conductor. *Applied Physics Letters* 2003; 82(8): 1290-2.

[129]   Konyushenko EN, Stejskal J, Trchova M, Hradil J, Kovarova J, Prokes J, Cieslar M, Hwang JY, Chen KH, Sapurina I. Multi-wall carbon nanotubes coated with polyaniline. *Polymer* 2006; 47(16): 5715-23.

[130]   Yoshino K, Kajii H, Araki H, Sonoda T, Take H, Lee S. Electrical and optical properties of conducting polymer-fullerene and conducting polymer-carbon nanotube composites. *Fullerenes, Nanotubes and Carbon Nanostructures* 1999; 7(4): 695-711.

[131]   Nogales A, Broza G, Roslaniec Z, Schulte K, Sics I, Hsiao BS, Sanz A, Garcia-Gutierrez MC, Rueda DR, Domingo C, Ezquerra TA. Low percolation threshold in nanocomposites based on oxidized single wall carbon nanotubes and poly(butylene terephthalate). *Macromolecules* 2004; 37(20): 7669-72.

[132]   Pötschke P, Hornbostel B, Roth S, Vohrer U, Dudkin SM, Alig I. Purification and percolation - unexpected phenomena in nanotube polymer composites. *AIP conference proceedings volume 786: electronic properties of novel nanostructures, Kirchberg, Tirol, Austria* 2005: 596-601.

160

[133] Hornbostel B, Pötschke P, Kotz J, Roth S. Single-walled carbon nanotubes/polycarbonate composites: basic electrical and mechanical properties. *Physica Status Solidi (B)* 2006; 243(13): 3445-51.

[134] Pegel S, Pötschke P, Petzold G, Alig I, Dudkin SM, Lellinger D. Dispersion, agglomeration, and network formation of multiwalled carbon nanotubes in polycarbonate melts. *Polymer* 2008; 49(4): 974-84.

[135] Pötschke P, Abdel-Goad M, Alig I, Dudkin S, Lellinger D. Rheological and dielectrical characterization of melt mixed polycarbonate-multiwalled carbon nanotube composites. *Polymer* 2004; 45(26): 8863-70.

[136] Pötschke P, Dudkin SM, Alig I. Dielectric spectroscopy on melt processed polycarbonate - multiwalled carbon nanotube composites. *Polymer* 2003; 44(17): 5023-30.

[137] Chen L, Pang XJ, Yu ZL. Study on polycarbonate/multi-walled carbon nanotubes composite produced by melt processing. *Materials Science and Engineering A* 2007; 457(1-2): 287-91.

[138] Mitchell CA, Krishnamoorti R. Dispersion of single-walled carbon nanotubes in poly(epsilon-caprolactone). *Macromolecules* 2007; 40(5): 1538-45.

[139] Saeed K, Park SY. Preparation and properties of multiwalled carbon nanotube/polycaprolactone nanocomposites. *Journal of Applied Polymer Science* 2007; 104(3): 1957-63.

[140] Mierczynska A, Mayne-L'Hermite M, Boiteux G. Electrical and mechanical properties of carbon nanotube/ultrahigh-molecular-weight polyethylene composites prepared by a filler prelocalization method. *Journal of Applied Polymer Science* 2007; 105(1): 158-68.

[141] Lisunova MO, Mamunya YP, Lebovka NI, Melezhyk AV. Percolation behaviour of ultrahigh molecular weight polyethylene/multi-walled carbon nanotubes composites. *European Polymer Journal* 2007; 43(3): 949-58.

[142]   Zhu D, Bin YZ, Matsuo M. Electrical conducting behaviors in polymeric composites with carbonaceous fillers. *Journal of Polymer Science B* 2007; 45(9): 1037-44.

[143]   Gorrasi G, Sarno M, Di Bartolomeo A, Sannino D, Ciambelli P, Vittoria V. Incorporation of carbon nanotubes into polyethylene by high energy ball milling: Morphology and physical properties. *Journal of Polymer Science B* 2007; 45(5): 597-606.

[144]   Zhang QH, Rastogi S, Chen DJ, Lippits D, Lemstra PJ. Low percolation threshold in single-walled carbon nanotube/high density polyethylene composites prepared by melt processing technique. *Carbon* 2006; 44(4): 778-85.

[145]   Zhao D, Lei Q, Qin C, Bai X. Melt process and performance of multi-walled carbon nanotubes reinforced LDPE composites. *Pigment and Resin Technology* 2006; 35(6): 341-5.

[146]   McCullen SD, Stevens DR, Roberts WA, Ojha SS, Clarke LI, Gorga RE. Morphological, electrical, and mechanical characterization of electrospun nanofiber mats containing multiwalled carbon nanotubes. *Macromolecules* 2007; 40(4): 997-1003.

[147]   Awasthi K, Awasthi S, Srivastava A, Kamalakaran R, Talapatra S, Ajayan PM, Srivastava ON. Synthesis and characterization of carbon nanotube-polyethylene oxide composites. *Nanotechnology* 2006; 17(21): 5417-22.

[148]   K AA, Agarwal US, Joseph R. Carbon nanotubes-reinforced PET nanocomposite by melt-compounding. *Journal of Applied Polymer Science* 2007; 104(5): 3090-5.

[149]   Lanticse LJ, Tanabe Y, Matsui K, Kaburagi Y, Suda K, Hoteida M, Endo M, Yasuda E. Shear-induced preferential alignment of carbon nanotubes resulted in anisotropic electrical conductivity of polymer composites. *Carbon* 2006; 44(14): 3078-86.

[150]   Ounaies Z, Park C, Wise KE, Siochi EJ, Harrison JS. Electrical properties of single wall carbon nanotube reinforced polyimide

composites. *Composites Science and Technology* 2003; 63(11): 1637-46.

[151] Jiang XW, Bin YZ, Matsuo M. Electrical and mechanical properties of polyimide-carbon nanotubes composites fabricated by in situ polymerization. *Polymer* 2005; 46(18): 7418-24.

[152] Kuan CF, Kuan HC, Ma CCM, Chen CH. Mechanical and electrical properties of multi-wall carbon nanotube/poly(lactic acid) composites. *Journal of Physics and Chemistry of Solids* 2008; 69(5-6): 1395-8.

[153] Schmidt RH, Kinloch IA, Burgess AN, Windle AH. The effect of aggregation on the electrical conductivity of spin-coated polymer/carbon nanotube composite films. *Langmuir* 2007; 23(10): 5707-12.

[154] Chen H, Muthuraman H, Stokes P, Zou JH, Liu X, Wang JH, Huo Q, Khondaker SI, Zhai L. Dispersion of carbon nanotubes and polymer nanocomposite fabrication using trifluoroacetic acid as a co-solvent. *Nanotechnology* 2007; 18(41): 415606(1-9).

[155] Skakalova V, Dettlaff-Weglikowska U, Roth S. Electrical and mechanical properties of nanocomposites of single wall carbon nanotubes with PMMA. *Synthetic Metals* 2005; 152(1-3): 349-52.

[156] Kim HM, Choi MS, Joo J, Cho SJ, Yoon HS. Complexity in charge transport for multiwalled carbon nanotube and poly(methyl methacrylate) composites. *Physical Review B* 2006; 74(5): 54202(1-7).

[157] Benoit JM, Corraze B, Lefrant S, Blau WJ, Bernier P, Chauvet O. Transport properties of PMMA-carbon nanotubes composites. *Synthetic Metals* 2001; 121(1-3): 1215-6.

[158] Du FM, Fischer JE, Winey KI. Effect of nanotube alignment on percolation conductivity in carbon nanotube/polymer composites. *Physical Review B* 2005; 72(12): 121404(1-4).

[159] Dai JF, Wang Q, Li WX, Wei ZQ, Xu GJ. Properties of well aligned SWNT modified poly (methyl methacrylate) nanocomposites. *Materials Letters* 2007; 61(1): 27-9.

[160] Slobodian P, Lengalova A, Saha P. Poly(methyl methacrylate)/multi-wall carbon nanotubes composites prepared by solvent cast technique:

Composites electrical percolation threshold. *Journal of Reinforced Plastics and Composites* 2007; 26(16): 1705-12.

[161]   Curran SA, Ajayan PM, Blau WJ, Carroll DL, Coleman JN, Dalton AB, Davey AP, Drury A, McCarthy B, Maier S, Strevens A. A composite from poly(m-phenylenevinyleneco-2,5-dioctoxy-p-phenylenevinylene) and carbon nanotubes: A novel material for molecular optoelectronics. *Advanced Materials* 1998; 10(14): 1091-93.

[162]   Kilbride BE, Coleman JN, Fraysse J, Fournet P, Cadek M, Drury A, Hutzler S, Roth S, Blau WJ. Experimental observation of scaling laws for alternating current and direct current conductivity in polymer-carbon nanotube composite thin films. *Journal of Applied Physics* 2002; 92(7): 4024-30.

[163]   Kharchenko SB, Douglas JF, Obrzut J, Grulke EA, Migler KB. Flow-induced properties of nanotube-filled polymer materials. *Nature Materials* 2004; 3(8): 564-8.

[164]   Tjong SC, Liang GD, Bao SP. Electrical behavior of polypropylene/multiwalled carbon nanotube nanocomposites with low percolation threshold. *Scripta Materialia* 2007; 57(6): 461-4.

[165]   Gorrasi G, Romeo V, Sannino D, Sarno M, Ciambelli P, Vittoria V, De Vivo B, Tucci V. Carbon nanotube induced structural and physical property transitions of syndiotactic polypropylene. *Nanotechnology* 2007; 18(27): 275703(1-11).

[166]   Sluzarenko N, Heurtefeu B, Maugey M, Zakri C, Poulin P, Lecommandoux S. Diblock copolymer stabilization of multi-wall carbon nanotubes in organic solvents and their use in composites. *Carbon* 2006; 44(15): 3207-12.

[167]   Tchoul MN, Ford WT, Ha MLP, Chavez-Sumarriva I, Grady BP, Lolli GL, Resasco DE, Arepalli S. Composites of single-walled carbon nanotubes and polystyrene: Preparation and electrical conductivity. *Chemistry of Materials* 2008; 20(9): 3120-6.

164

[168] Chang TE, Kisliuk A, Rhodes SM, Brittain WJ, Sokolov AP. Conductivity and mechanical properties of well-dispersed single-wall carbon nanotube/polystyrene composite. *Polymer* 2006; 47(22): 7740-6.

[169] Kim ST, Choi HJ, Hong SM. Bulk polymerized polystyrene in the presence of multiwalled carbon nanotubes. *Colloid & Polymer Science* 2007; 285(5): 593-8.

[170] Poa CH, Silva SRP, Watts PCP, Hsu WK, Kroto HW, Walton DRM. Field emission from nonaligned carbon nanotubes embedded in a polystyrene matrix. *Applied Physics Letters* 2002; 80(17): 3189-91.

[171] Antonucci V, Faiella G, Giordano M, Nicolais L, Pepe G. Electrical properties of single walled carbon nanotube reinforced polystyrene composites. *Macromolecular Symposia* 2007; 247(1): 172-81.

[172] Yu JR, Lu KB, Sourty E, Grossiord N, Konine CE, Loos JC. Characterization of conductive multiwall carbon nanotube/polystyrene composites prepared by latex technology. *Carbon* 2007; 45(15): 2897-903.

[173] Kim YJ, An KJ, Suh KS, Choi HD, Kwon JH, Chung YC, Kim WN, Lee AK, Choi JI, Yoon HG. Hybridization of oxidized MWNT and silver powder in polyurethane matrix for electromagnetic interference shielding application. *IEEE Transactions on Electromagnetic Compatibility* 2005; 47(4): 872-9.

[174] Jang PG, Suh KS, Park M, Kim JK, Kim WN, Yoon HG. Electrical behavior of polyurethane composites with acid treatment-induced damage to multiwalled carbon nanotubes. *Journal of Applied Polymer Science* 2007; 106(1): 110-6.

[175] Wang G, Tan ZK, Liu XQ, Chawda S, Koo JS, Samuilov V, Dudley M. Conducting MWNT/poly(vinyl acetate) composite nanofibres by electrospinning. *Nanotechnology* 2006; 17(23): 5829-35.

[176] Shaffer MSP, Windle AH. Fabrication and characterization of carbon nanotube/poly(vinyl alcohol) composites. *Advanced Materials* 1999; 11(11): 937-41.

[177]   Mamunya Y, Boudenne A, Lebovka N, Ibos L, Candau Y, Lisunova M. Electrical and thermophysical behaviour of PVC-MWCNT nanocomposites. *Composites Science and Technology* 2008; 68(9): 1981-8.

[178]   Seoul C, Kim YT, Baek CK. Electrospinning of poly(vinylidene fluoride)/dimethylformamide solutions with carbon nanotubes. *Journal of Polymer Science B* 2003; 41(13): 1572-7.

[179]   Chen GX, Li YJ, Shimizu H. Ultrahigh-shear processing for the preparation of polymer/carbon nanotube composites. *Carbon* 2007; 45(12): 2334-40.

[180]   Wang L, Dang ZM. Carbon nanotube composites with high dielectric constant at low percolation threshold. *Applied Physics Letters* 2005; 87(4): 42903(1-3).

[181]   Li Q, Xue QZ, Zheng QB, Hao LZ, Gao XL. Large dielectric constant of the chemically purified carbon nanotube/polymer composites. *Materials Letters* 2008; 62(26): 4229-31.

[182]   Ha MLP, Grady BP, Lolli G, Resasco DE, Ford WT. Composites of single-walled carbon nanotubes and styrene-isoprene copolymer latices. *Macromolecular Chemistry and Physics* 2007; 208(5): 446-56.

[183]   Bian CX, Xu XC, Yang GG, Zhao Y, Jin SS, Wang HM, Tang GQ. Studies on conductive properties and mechanism of composites-sulfonated polyphenylacetylene/multiwalled carbon nanotubes. *Acta Chimica Sinica* 2007; 65(6): 525-31.

[184]   Kimura T, Ago H, Tobita M, Ohshima S, Kyotani M, Yumura M. Polymer composites of carbon nanotubes aligned by a magnetic field. *Advanced Materials* 2002; 14(19): 1380-3.

[185]   Gryshchuk O, Karger-Kocsis J, Thomann R, Konya Z, Kiricsi I. Multiwall carbon nanotube modified vinylester and vinylester-based hybrid resins. *Composites Part A* 2006; 37(9): 1252-9.

[186]   Jiang MJ, Dang ZM, Xu HP. Giant dielectric constant and resistance-pressure sensitivity in carbon nanotubes/rubber nanocomposites with

low percolation threshold. *Applied Physics Letters* 2007; 90(4): 42914(1-3).

[187] Celzard A, McRae E, Deleuze C, Dufort M, Furdin G, Marêché JF. Critical concentration in percolating systems containing a high-aspect-ratio filler. *Physical Review B* 1996; 53(10): 6209-14.

[188] Balberg I, Anderson CH, Alexander S, Wagner N. Excluded volume and its relation to the onset of percolation. *Physical Review B* 1984; 30(7): 3933-43.

[189] Behnam A, Guo J, Ural A. Effects of nanotube alignment and measurement direction on percolation in single-wall carbon nanotube films. *Journal of Applied Physics* 2007; 102(4): 44313(1-7).

[190] Connor MT, Roy S, Ezquerra TA, Baltá Calleja FJ. Broadband ac conductivity of conductor-polymer composites. *Physical Review B* 1998; 57(4): 2286-94.

[191] Mott NF, Davis EA. Electronic properties in non-crystalline materials. Oxford: Clarendon; 1979.

[192] Sheng P, Sichel EK, Gittleman JI. Fluctuation-induced tunneling conduction in carbon-polyvinylchloride composites. *Physical Review Letters* 1978; 40(18): 1197-200.

[193] Ding W, Eitan A, Fisher FT, Chen X, Dikin DA, Andrews R, Brinson LC, Schadler LS, Ruoff RS. Direct observation of polymer sheathing in carbon nanotube-polycarbonate composites. *Nano Letters* 2003; 3(1): 1593-7.

[194] Saar MO, Manga M. Continuum percolation for randomly oriented soft-core prisms. *Physical Review E* 2002; 65(5): 56131.

[195] Youngs IJ. A geometric percolation model for non-spherical excluded volumes. *Journal of Physics D* 2003; 36(6): 738-47.

[196] Natsuki T, Endo M, Takahashi T. Percolation study of orientated short-fiber composites by a continuum model. *Physica A* 2005; 352(2-4): 498-508.

[197] Van de Ven TGM. Colloidal hydrodynamics. London: Academic Press, 1989.

[198]   Onsager L. The effects of shape on the interactions of colloidal particles. *Annals of the New York Academy of Sciences* 1949; 51(4): 627-59.

[199]   Foygel M, Morris RD, Anez D, French S, Sobolev VL. Theoretical and computational studies of carbon nanotube composites and suspensions: Electrical and thermal conductivity. *Physical Review B* 2005; 71(10): 104201(1-8).

[200]   Néda Z, Florian R, Brechet Y. Reconsideration of continuum percolation of isotropically oriented sticks in three dimensions. *Physical Review E* 1999; 59(3): 3717-9.

[201]   Kovacs JZ, Andresen K, Pauls JR, Pardo Garcia C, Schossig M, Schulte K, Bauhofer W. Analyzing the quality of carbon nanotube dispersions in polymers using scanning electron microscopy. *Carbon* 2007; 45(6): 1279-88.

[202]   Dalmas F, Dendievel R, Chazeau L, Cavaille J-Y, Gauthier C. Carbon nanotube-filled polymer composites. Numerical simulation of electrical conductivity in three-dimensional entangled networks. *Acta Materialia* 2006; 54(11): 2923-31.

[203]   Berhan L, Sastry AM. Modeling percolation in high-aspect-ratio fiber systems. II. The effect of waviness on the percolation onset. *Physical Review E* 2007; 75(4): 41121(1-7).

[204]   Li C, Chou T-W. Continuum percolation of nanocomposites with fillers of arbitrary shapes. *Applied Physics Letters* 2007; 90(17): 174108(1-3).

[205]   Grujicic M, Cao G, Roy WN. A computational analysis of the percolation threshold and the electrical conductivity of carbon nanotubes filled polymeric materials. *Journal of Materials Science* 2004; 39(14): 4441-9.

[206]   Balberg I. "Universal" percolation-threshold limits in the continuum. *Physical Review B* 1985; 31(6): 4053-5.

[207]   Grimaldi C, Balberg I. Tunneling and nonuniversality in continuum percolation systems. *Physical Review Letters* 2006; 96(6): 66602-1-4.

[208]   Rahatekar SS, Hamm M, Shaffer MSP, Elliott JA. Mesoscale modeling of electrical percolation in fiber-filled systems. *Journal of Chemical Physics* 2005; 123(13): 134702(1-5).

[209]   Wescott JT, Kung P, Maiti A. Conductivity of carbon nanotube polymer composites. *Applied Physics Letters* 2007; 90(3): 33116(1-3).

[210]   Tozzi EJ, Schilling C, Bauhofer W, Klingenberg DJ. Electrical conductivity enhancement in carbon nanotube-polymer composites. *Proceedings of the 79th Annual Meeting of the Society of Rheology, Salt Lake City, Utah, USA* 2007.

[211]   Switzer LH, Klingenberg DJ. Flocculation in simulations of sheared fiber suspensions. *International Journal of Multiphase Flow* 2004; 30(1): 67-87.

[212]   Lebovka NI, Tarafdar S, Vygornitskii NV. Computer simulation of electrical conductivity of colloidal dispersions during aggregation. *Physical Review E* 2006; 73(3): 31402-1-6.

[213]   Lin-Gibson S, Pathak JA, Grulke EA, Wang H, Hobbie EK. Elastic flow instability in nanotube suspensions. *Physical Review Letters* 2004; 92(4): 048302(1-4).

[214]   Lima MD, Andrade MJ, Skakalova V, Bergmann CP, Roth S. Dynamic percolation of carbon nanotubes in liquid medium. *Journal of Materials Chemistry* 2007; 17(46): 4846-53.

[215]   Ezquerra TA, Kulescza M, Santa Cruz C, Baltá-Calleja FJ. Charge transport in polyethylene-graphite composite materials. *Advanced Materials* 1990; 2(12): 597-600.

[216]   Grossiord N, Kivit PJJ, Loos J, Meuldijk J, Yrylyuk AV, van der Schoot P, Koning CE. On the influence of the processing conditions on the performance of electrically conductive carbon nanotube/polymer nanocomposites. *Polymer* 2008; 49(12): 2866-72.

[217]   Luther S, Mewes D. Theoretical study of operating limits for the calendering process. *Kautschuk Gummi Kunststoffe* 2005; 58(4): 149-156.

[218]   Belytschko T, Xiao SP, Schatz GC, Ruoff RS. Atomistic simulations of nanotube fracture. *Physical Review B* 2002; 65(23): 235430,1-8.

[219]   Yamamoto S, Matsuoka T. Dynamic simulation of flow-Induced fiber fracture. *Polymer Engineering & Science* 1995; 35(12): 1022-30.

[220] Ruschau GR, Yoshikawa S, Newnham RE. Resistivities of conductive composites. *Journal of Applied Physics* 1992; 72(3): 953-9.

[221] Flandin L, Bidan G, Brechet Y, Cavaille JY. New nanocomposite materials made of an insulating matrix and conducting fillers: Processing and properties. *Polymer Composites* 2000; 21(2): 165-74.

[222] Sanvito S, Kwon YK, Tománek D, Lambert CJ. Fractional quantum conductance in carbon nanotubes. *Physical Review Letters* 2000; 84(9): 1974-7.

[223] Gao B, Chen YF, Fuhrer MS, Glattli DC, Bachtold A. Four-point resistance of individual single-wall carbon nanotubes. *Physical Review Letters* 2005; 95(19): 196802(1-4).

[224] Pötschke P, Dudkin SM, Alig I. Dielectric spectroscopy on melt processed polycarbonate-multiwalled carbon nanotube composites. *Polymer* 2003; 44(17): 5023-30.

[225] Schwarz M-K, Bauhofer W, Schulte K. Alternating electric field induced agglomeration of carbon black filled resins. *Polymer* 2002; 43(10): 3079-82.

[226] Schwarz MK. Doctoral thesis: Elektrisch leitfähige Füllstoffnetzwerke in Duroplasten auf der Basis von Kohlenstoff-Nanopartikeln, -Nanofasern und -Nanotubes. Cuvillier Verlag, 1st edition. Göttingen, Germany: 2006.

[227] Prasse T, Flandin L, Schulte K, Bauhofer W. In situ observation of electric field induced agglomeration of carbon black in epoxy resin. *Applied Physics Letters* 1998; 72(22): 2903-5.

[228] Prasse T, Cavaillé JY, Bauhofer W. Electric anisotropy of carbon nanofibre/epoxy resin composites due to electric field induced alignment. *Composites Science and Technology* 2003; 63(13): 1835-41.

[229] Cardona M, Merlin R. Light Scattering in Solids IX: Novel Materials and Techniques. 1st ed. Berlin: Springer-Verlag, 2007.

[230] Jorio A, Dresselhaus G, Dresselhaus MS. Carbon Nanotubes: Advanced Topics in the Synthesis, Structure, Properties and Applications. 1st ed. Berlin: Springer-Verlag, 2008.

[231] Hadjiev VG, Arepalli S, Nikolaev P, Jandl S, Yowell L. Enhanced Raman microprobe imaging of single-wall carbon nanotubes. *Nanotechnology* 2004; 15(5): 562-7.

[232] Dresselhaus MS, Dresselhaus G, Saito R, Jorio A. Raman spectroscopy of carbon nanotubes. *Physics Reports* 2005; 409(2): 47-99.

[233] Rao AM, Richter E, Bandow S, Chase B, Eklund PC, Williams KA, Fang S, Subbaswamy KR, Menon M, Thess A, Smalley RE, Dresselhaus G, Dresselhaus MS. Diameter-selective Raman scattering from vibrational modes in carbon nanotubes. *Science* 1997; 275(5297): 187-91.

[234] Maultzsch J, Reich S, Thomsen C. Chirality-selective Raman scattering of the D mode in carbon nanotubes. *Physical Review B* 2001; 64(12): 121407(1-4).

[235] Brown SDM, Jorio A, Corio P, Dresselhaus MS, Dresselhaus G, Saito R, Kneipp K. Origin of the Breit-Wigner-Fano lineshape of the tangential G-band feature of metallic carbon nanotubes. *Physical Review B* 2001; 63(15): 155414(1-8).

[236] Jorio A, Souza AG, Dresselhaus G, Dresselhaus MS, Swan AK, Unlu MS, Goldberg BB, Pimenta MA, Hafner JH, Lieber CM, Saito R. G-band resonant Raman study of 62 isolated single-wall carbon nanotubes. *Physical Review B* 2002; 65(15): 155412(1-9).

[237] Dresselhaus MS, Dresselhaus G, Jorio A, Souza AG, Saito R. Raman spectroscopy on isolated single wall carbon nanotubes. *Carbon* 2002; 40(12): 2043-61.

[238] Lupo F, Rodríguez-Manzo JA, Zamudio A, Elías A, Kim YA, Hayashi T, Muramatsu M, Kamalakaran R, Terrones H, Endo M, Rühle M, Terrones M. Pyrolytic synthesis of long strands of large diameter single-walled carbon nanotubes at atmospheric pressure in the absence of sulphur and hydrogen. *Chemical Physics Letters* 2005; 410(4-6): 384-90.

[239]   Huong PV, Cavagnat R, Ajayan PM, Stephan O. Temperature-dependent vibrational-spectra of carbon nanotubes. *Physical Review B* 1995; 51(15): 10048-51.

[240]   Zhang L, Li HD, Yue KT, Zhang SL, Wu XH, Zi J, Shi ZJ, Gu ZN. Effects of intense laser irradiation on Raman intensity features of carbon nanotubes. *Physical Review B* 2002; 65(7): 73401(1-4).

[241]   Li HD, Yue KT, Lian ZL, Zhan Y, Zhou LX, Zhang SL, Shi ZJ, Gu ZN, Liu BB, Yang RS, Yang HB, Zou GT, Zhang Y, Iijima S. Temperature dependence of the Raman spectra of single-wall carbon nanotubes. *Applied Physics Letters* 2000; 76(15): 2053-5.

[242]   Huang FM. Yue KT, Tan PH, Zhang SL, Shi ZJ, Zhou XH, Gu ZN. Temperature dependence of the Raman spectra of carbon nanotubes. *Journal of Applied Physics* 1998; 84(7): 4022-4.

[243]   Brown SDM, Corio P, Marucci A, Dresselhaus MS, Pimenta MA, Kneipp K. Anti-Stokes Raman spectra of single-walled carbon nanotubes. *Physical Review B* 2000; 61(8): R5137-40.

[244]   Jorio A, Souza AG, Brar VW, Swan AK, Unlu MS, Goldberg BB, Righi A, Hafner JH, Lieber CM, Saito R, Dresselhaus G, Dresselhaus MS. Polarized resonant Raman study of isolated single-wall carbon nanotubes: Symmetry selection rules, dipolar and multipolar antenna effects. *Physical Review B* 2002; 65(12): 121402(1-4).

[245]   Saito R, Takeya T, Kimura T, Dresselhaus G, Dresselhaus MS. Raman intensity of single-wall carbon nanotubes. *Physical Review B* 1998; 57(7): 4145-53.

[246]   Gommans HH, Alldredge JW, Tashiro H, Park J, Magnuson J, Rinzler AG. Fibers of aligned single-walled carbon nanotubes: Polarized Raman spectroscopy. *Journal of Applied Physics* 2000; 88(5): 2509-14.

[247]   Rao AM, Jorio A, Pimenta MA, Dantas MS, Saito R, Dresselhaus G, Dresselhaus MS. Polarized Raman study of aligned multiwalled carbon nanotubes. *Physical Review Letters* 2000; 84(8): 1820-3.

[248]   Hwang J, Gommans HH, Ugawa A, Tashiro H, Haggenmueller R, Winey KI, Fischer JE, Tanner DB, Rinzler AG. Polarized spectroscopy

of aligned single-wall carbon nanotubes. *Physical Review B* 2000; 62(20): 310-3.

[249] Frogley MD, Zhao Q, Wagner HD. Polarized resonance Raman spectroscopy of single-wall carbon nanotubes within a polymer under strain. *Physical Review B* 2002; 65(11): 113413(1-4).

[250] Kannan P, Eichhorn SJ, Young RJ. Deformation of isolated single-wall carbon nanotubes in electrospun polymer nanofibres. *Nanotechnology* 2007; 18(23): 235707(1-7).

[251] Hull D, Clyne TW. An Introduction to composite materials. Cambridge University Press, 2nd edition. Cambridge, UK: 1996.

[252] Ehrenstein GW. Polymeric materials. Carl Hanser Verlag, 1st edition. Munich, Germany: 2001.

[253] Antonucci V, Cusano A, Giordano M, Nasser J, Nicolais L. Cure-induced residual strain build-up in a thermoset resin. *Composites Part A* 2006; 37(4): 592-601.

[254] Merzlyakov M, McKenna GB, Simon SL. Cure-induced and thermal stresses in a constrained epoxy resin. *Composites Part A* 2006; 37(4): 585-91.

[255] Zhao LG, Warrior NA, Long AC. A thermo-viscoelastic analysis of process-induced residual stress in fibre-reinforced polymer-matrix composites. *Materials Science and Engineering A* 2007; 452: 483-98.

[256] Plepys A, Vratsanos MS, Farris RJ. Determination of residual-stresses using incremental linear elasticity. *Composite Structures* 1994; 27(1-2): 51-6.

[257] Wang XJ, Chung DDL. Residual stress in carbon fiber embedded in epoxy, studied by simultaneous measurement of applied stress and electrical resistance. *Composite Interfaces* 1998; 5(3): 277-81.

[258] Lange J, Toll S, Manson JAE, Hult A. Residual-stress buildup in thermoset films cured above their ultimate glass-transition temperature. *Polymer* 1995; 36(16): 3135-41.

[259] Lange J, Toll S, Manson JAE, Hult A. Residual stress build-up in thermoset films cured below their ultimate glass transition temperature. *Polymer* 1997; 38(4): 809-15.

[260] Case SL, O'Brien EP, Ward TC. Cure profiles, crosslink density, residual stresses, and adhesion in a model epoxy. *Polymer* 2005; 46(24): 10831-40.

[261] Holst M, Schänzlin K, Wenzel M, Xu JJ, Lellinger D, Alig I. Time-resolved method for the measurement of volume changes during polymerization. *Journal of Polymer Science B* 2005; 43(17): 2314-25.

[262] Zarrelli M, Partridge IK, D'Amore A. Warpage induced in bi-materials specimens: Coefficient of thermal expansion, chemical shrinkage and viscoelastic modulus evolution during curing. *Composites Part A* 2006; 37(4): 565-70.

[263] Giordano M, Laudati A, Russo M, Nasser J, Persiano GV, Cusano A. Advanced cure monitoring by optoelectronic multifunction sensing system. *Thin Solid Films* 2004; 450(1): 191-4.

[264] Zhao F, Jones FR. Thermal loading of short fibre composites and the induction of residual shear stresses. *Composites Part A* 2007; 38(11): 2374-81.

[265] Park JM, Lee SI, Choi JH. Cure monitoring and residual stress sensing of single-carbon fiber reinforced epoxy composites using electrical resistivity measurement. *Composites Science and Technology* 2005; 65(3-4): 571-80.

[266] Li CY, Chou TW. Strain and pressure sensing using single-walled carbon nanotubes. *Nanotechnology* 2004; 15(11): 1493-6.

[267] Wood JR, Wagner HD. Single-wall carbon nanotubes as molecular pressure sensors. *Applied Physics Letters* 2000; 76(20): 2883-5.

[268] Zhao Q, Wood JR, Wagner HD. Stress fields around defects and fibers in a polymer using carbon nanotubes as sensors. *Applied Physics Letters* 2001; 78(12): 1748-50.

[269]   Cooper CA, Young RJ, Halsall M. Investigation into the deformation of carbon nanotubes and their composites through the use of Raman spectroscopy. *Composites Part A* 2001; 32(3-4): 401-11.

[270]   Lucas M, Young RJ. Raman spectroscopic study of the effect of strain on the radial breathing modes of carbon nanotubes in epoxy/SWNT composites. *Composites Science and Technology* 2004; 64(15): 2297-302.

[271]   de la Vega A, Kovacs JZ, Bauhofer W, Schulte K. Combined Raman and dielectric spectroscopy on the curing behaviour and stress build up of carbon nanotube-epoxy composites. *Composites Science and Technology* 2009; 69(10): 1540-6.

[272]   Alig I, Johari GP. Relaxations in Thermosets. 19. Dielectric effects during curing of diglycidyl ether of bisphenol-A with a catalyst and the properties of the thermoset. *Journal of Polymer Science B* 1993; 31(3): 299-311.

[273]   Kazilas MC, Partridge IK. Exploring equivalence of information from dielectric and calorimetric measurements of thermoset cure-a model for the relationship between curing temperature, degree of cure and electrical impedance. *Polymer* 2005; 46(16): 5868-78.

[274]   Wise KE, Park C, Siochi EJ, Harrison JS. Stable dispersion of single wall carbon nanotubes in polyimide: the role of noncovalent interactions. *Chemical Physics Letters* 2004; 391(4-6): 207-11.

[275]   Star A, Han TR, Gabriel JCP, Bradley K, Gruner G. Interaction of aromatic compounds with carbon nanotubes: Correlation to the Hammett parameter of the substituent and measured carbon nanotube FET response. *Nano Letters* 2003; 3(10): 1421-3.

[276]   de la Vega A, de A Prado LAS, Kovacs JZ, Bauhofer W, Schulte K. SWCNT as cure-induced stress sensors in epoxy nanocomposites. *Solid State Phenomena* 2009; 151: 48-53.

[277]   Start PR, Hudson SD, Hobbie EK, Migler KB. Breakup of carbon nanotube flocs in microfluidic traps. *Journal of Colloid and Interface Science* 2006; 297(2): 631-6.

[278] Doi M, Edwards SF. The theory of polymer dynamics. Oxford University Press, 1st edition. Oxford, UK: 1986.

[279] Advani SG, Fan Z. Effect of dispersion state on the rheology of multi-walled carbon nanotube suspensions in shear flow. *AIP Conference Proceedings – Materials Processing and Design: Modeling, Simulation and Applications* 2004; 712(1): 1619-23.

[280] Xiao K, Zhang L. Effective separation and alignment of long entangled carbon nanotubes in epoxy. *Journal of Materials Science* 2005; 40(24): 6513-6.

[281] Rahatekar SS, Koziol KKK, Butler SA, Elliott JA, Shaffer MSP, Mackley MR, Windle AH. Optical microstructure and viscosity enhancement for an epoxy resin matrix containing multiwall carbon nanotubes. *Journal of Rheology* 2006; 50(5): 599-610.

[282] Wu G, Zheng Q. Estimation of the agglomeration structure for conductive particles and fiber-filled high-density polyethylene through dynamic rheological measurements. *Journal of Polymer Science Part B* 2004; 42(7): 1199-205.

[283] Soden JM, Anderson RE. IC failure analysis - Techniques and tools for quality and reliability improvement. *Microelectronics and Reliability* 1995; 35(3): 429-53.

176

List of own publications

Reviewed publications

Kovacs JZ, Velagala BS, Schulte K, Bauhofer W. Two percolation thresholds in carbon nanotube epoxy composites. *Composites Science and Technology* 2007; 67(5): 922-8.

Kovacs JZ, Andresen K, Pauls JR, Pardo Garcia C, Schossig M, Schulte K, Bauhofer W. Analyzing the quality of carbon nanotube dispersions in polymers using scanning electron microscopy. *Carbon* 2007; 45(6): 1279-88.

Bauhofer W, Kovacs JZ. A review and analysis of electrical percolation in carbon nanotube polymer composites. *Composites Science and Technology* 2009; 69(10): 1486-98.

de la Vega A, Kovacs JZ, Bauhofer W, Schulte K. Combined Raman and dielectric spectroscopy on the curing behaviour and stress build up of carbon nanotube-epoxy composites. *Composites Science and Technology* 2009; 69(10): 1540-6.

de la Vega A, de A Prado LAS, Kovacs JZ, Bauhofer W, Schulte K. SWCNT as cure-induced stress sensors in epoxy nanocomposites. *Solid State Phenomena* 2009; 151: 48-53.

Kovacs JZ, Mandjarov RE, Blisnjuk T, Prehn K, Sussiek M, Müller J, Schulte K, Bauhofer W. On the influence of nanotube properties, processing condition and shear forces on the electrical conductivity of carbon nanotube epoxy composites. *Nanotechnology* 2009; 20(15): 155703(1-6).

Proceedings

Kovacs JZ, Schulte K, Bauhofer W. Visualizing carbon nanotubes inside polymer composites by scanning electron microscopy. *Proceedings of the 16th International Conference on Composite Materials*, Kyoto, Japan, 2007.

Kovacs JZ, Schulte K, Bauhofer W. The influence of shearing and electric fields on the percolation threshold in carbon nanotube epoxy composites.

Proceedings of the 16th International Conference on Composite Materials, Kyoto, Japan, 2007.

de la Vega A, de A Prado LAS, Kovacs JZ, Bauhofer W, Schulte K. SWCNT as cure-induced stress sensors in epoxy nanocomposites. *E-MRS.Proceeding, European Materials Research Society*, Warsaw, Poland, 2008.

Kovacs JZ, Bauhofer W. The influence of the dispersion quality of carbon nanotubes in an epoxy matrix on the electrical conductivity of the composite. *Proceedings of the 17th International Conference on Composite Materials*, Edinburgh, UK, 2009.

Fitting HJ, Kovacs JZ. SEM contrast of semi-insulating compound materials. *Proceedings of the Microscopy & Microanalysis Conference*, Richmond, USA, 2009.

Fitting HJ, Kovacs JZ. SEM contrast of semiconducting and semi-insulating samples. *Proceedings of the 9th Multinational Conference on Microscopy*, Graz, Austria, 2009.

Presentations & Abstracts

Kovacs JZ, Bauhofer W. Shear- and ac-field-induced flocculation of nanotubes in an epoxy matrix. *CNT-Net Workshop* 07.-08.10.2004, Szczecin/Poland (Presentation).

Kovacs JZ, Velagala BS, Bauhofer W. Network formation in carbon nanotube epoxy composites. *Carbon Nanotube/Polymer Composites – International Conference* 04.-07.09.2005, Hamburg/Germany (Poster).

Kovacs JZ, Bauhofer W. Monitoring the network formation of carbon nanotubes in epoxy composites by Raman Spectroscopy. *7th Horiba Jobin Yvon Workshop* 13.-14.03.2007, Bensheim/Germany (Presentation).

Kovacs JZ, Bauhofer W, Schulte K. Visualizing carbon nanotubes inside polymer composites by scanning electron microscopy. *16th International Conference on Composite Materials* 08.-13.07.2007, Kyoto/Japan (Presentation).

Kovacs JZ, de la Vega A, Schulte K, Bauhofer W. Combined Raman and dielectric spectroscopy on the curing behaviour of carbon nanotube epoxy composites. *Carbon Nanotube/Polymer Composites – International Conference* 10.-12.09.2007, Cambridge/UK (Presentation).

Supervised student research projects

Velagala Bala, Analysis of nanotube-epoxy composites over a wide filler concentration regime, 2005.

Andresen Kjer, Herstellung dünner, leitfähiger Epoxidschichten durch Spin Coating unter Zugabe von Carbon Nanotubes, 2006.

Binev Momchil, Light Microscopy Investigations of Carbon Black, Chopped Fibers and Nanofibers dispersed in an Epoxy Matrix, 2006.

Pauls Jan Roman, Herstellung, Charakterisierung und Optimierung der phys. Eigenschaften elektrisch leitfähiger Schichten aus Kohlenstoffnanoröhrchen-haltigen Epoxidharzen, 2006.

Oncken Hendrick, Ramanspektroskopische Untersuchung verschiedener Carbon Nanotube-haltiger Epoxydharz-Gemische, 2006.

Rein Jens, Nachweis von Kohlenstoff-Nanoröhrchen mit einem Rasterkraftmikroskop, 2006.

Bechtle Sabine, Rheologische, Optische und Elektrische Untersuchung der Carbon Nanotube – Strukturbildung in Epoxidharz, 2006.

Löwe Heinrich, Entwicklung einer Bildanalyse-Software zur Lageerfassung von Kohlenstofffasern in einer Epoxidharzmatrix, 2007.

Manuello Daniel, Einfluss von elektrischen Feldern auf Kohlenstofffasern in einer Epoxydharzmatrix, 2007.

Blisnjuk Thomas, Einflüsse von Dispersionsqualität, Scherung und Härtertyp auf die Netzwerkbildung von MWCNT in einer Epoxidharzmatrix, 2008.

Supervised diploma theses

Lindstaedt Florian, Simulating Systems of Highly Conducting Flexible Fibers in Electric Fields, 2005.

Djaja Dicky Tirta, Einfluss eines elektrischen Wechselfeldes auf die Leitfähigkeit von PAni/Epoxidharz-Mischungen bei der Vernetzung, und von lösungsmittelhaltigen PAni-Dispersionen bei der Filmbildung, 2006.

Ponnam Balaji, Flocculation of nanotubes in epoxy resin induced by shearing and electric fields, 2006.

Pardo Garcia Claudia, Investigations on the rotation of carbon fibers under the influence of an AC electric field and on the network formation of carbon nanotubes in an epoxy matrix, 2006.

Velagala Bala, Rheo-Optical Studies of Carbon Nanotube Agglomeration in Epoxy Composites, 2007.

Schilling Christian, Simulation of Systems of Highly Conductive Carbon Nanotubes Using Tunneling Model, 2007.

Mandjarov Roman, Analysis of shear induced percolation in carbon nanotube epoxy composites, 2008.

Curriculum vitae

Name	Josef-Zoltan Lott, né Kovacs
Date of birth	2 November 1976
Place of birth	Timisoara, Romania

Education

09.1987 – 10.1990	Secondary school, Timisoara, Romania
11.1990 – 07.1991	Secondary school, Runkel, Germany
09.1991 – 06.1997	Secondary school, Weilburg, Germany
	Qualification: University-entrance diploma
07.1997 – 07.1998	Community service, Wetzlar, Germany
10.1998 – 12.2003	Studies of physics, University of Marburg, Germany
	Major: Semiconductor physics, solid state physics
	Diploma thesis: Spatiotemporal dynamics of optical excitations in semiconductors

Experience

04.2004 – 09.2008	Research associate, Institute for Optical and Electronic Materials, Hamburg University of Technology, Germany
04.2009 – present	Project leader, Heraeus Noblelight GmbH, Hanau, Germany